Evaluation of Oxygen-Enhanced MRI for the identification of hypoxia induced treatment resistant tumours in patients with head and neck cancer

Thesis submitted to the University of Nottingham for the degree of Doctor of Philosophy

November 2024

Alastair Leslie George McCabe
Student ID: 20327552

Supervisors: Prof Stewart Martin, Dr Rafal Panek

University of Nottingham
UK | CHINA | MALAYSIA

Abstract

Tumour hypoxia is a recognised cause of radiotherapy treatment resistance in head and neck squamous cell carcinoma (HNSCC). Although potential hypoxia modification therapeutic strategies exist, they are not widely used in clinical practice in part due to a lack of a readily available method to identify patients who may benefit from such treatments. Imaging of tumour hypoxia is an appealing solution to this issue due to its ability to repeatedly provide information on the spatial distribution of oxygen. This thesis evaluates the potential use of the hypoxia imaging technique of oxygen-enhanced MRI (OE-MRI) for the assessment of tumour hypoxia in HNSCC.

A scoping review of the use of OE-MRI for the assessment of tumour hypoxia revealed strong pre-clinical evidence of the utility of OE-MRI in assessing tumour hypoxia but limited clinical translation of this work with no published clinical studies of the use of OE-MRI in HNSCC at the start of this research.

A volumetric OE-MRI protocol for dynamic T_1 relaxation time mapping was developed and implemented on 1.5T clinical scanners using only routinely available clinical equipment. Initial testing of the protocol yielded results that were considered adequate to proceed to a clinical study. 25 participants were scanned breathing room air and during high flow oxygen administration. Oxygen induced changes in T_1 times (ΔT_1) and R_2^* rates (ΔR_2^*) were measured in malignant tissue and healthy organs. Patients were surveyed on their experience of the OE-MRI protocol.

The developed OE-MRI sequence took only 10 mins to acquire and was well tolerated. A non-rigid image co-registration approach was

applied and its effect on OE-MRI derived data evaluated. A total of 15 histologically confirmed primary tumours and 41 malignant nodal masses were identified in the scanned participants. The OE-MRI sequence was able to discern differing response of healthy tissues and tumours to oxygen challenge. Estimates of tumour hypoxic fractions were obtained in all patient participants with a statistically non-significant greater magnitude of hypoxic fractions present for radiotherapy treatment resistant tumours. Exploratory analysis was performed to investigate potential novel OE-MRI derived biomarkers and to explore the feasibility of using OE-MRI derived hypoxic maps to aid radiotherapy treatment planning contouring.

In summary, a well-tolerated clinical implementation of dynamic, volumetric OE-MRI of the head and neck region using only routinely available equipment that allows discernment of differing oxygen responses within biopsy confirmed HNSCC is presented. Novel OE-MRI analysis methods are discussed and suggestions made for future work in order to fully translate this technique into a clinically utilised resource in the management of HNSCC.

Trial registration: ClinicalTrials.gov, NCT04724096.
Registered 26 January 2021.
https://www.clinicaltrials.gov/study/NCT04724096

Dedicated to the loving memory of my Dad.
To Rhiann, Isla, Abigail and my Mum; without your patience, love and support this thesis would never have been completed.

Acknowledgements

I would like to express my thanks to the many people who have helped me during the conduct of this research.

To my supervisors Prof Stewart Martin, Dr Rafal Panek and Dr Judy Christian I thank you for the support, wisdom and guidance you have given me over the course of these PhD studies and beyond. This project has been an incredibly exciting opportunity for me to combine my interest and knowledge in head and neck cancer, radiotherapy treatments, and MRI physics. Your help and hard work in obtaining funding and guiding the direction of the research has been fundamental to its success.

I am grateful for the help and support of the staff in the ENT and Maxillofacial departments at NUH for the identification and recruitment of patient participants and to the MRI radiographers and booking team at NUH, as without you this research would quite simply not have happened. I would also like to acknowledge the support and computing expertise of Dr Damian Borys who assisted with developing the data analysis pipeline for the image registration.

Finally I would like to thank all of the patients at Nottingham University Hospitals who agreed to discuss this research with me and all of those who took part in the study. All the patient participants knew that there would be no direct benefit to them from their participation, yet freely gave their time and energy during a very stressful period in their lives to participate in research that they hope will ultimately help develop more effective and better tolerated treatments for head and neck cancer in the future. The humanity shown by all participants is humbling and should never be taken for granted.

COVID-19 Impact

The data collection for the research detailed in this thesis was performed between April 2021 and December 2022 after a favourable opinion from the South Central - Berkshire Research Ethics Committee was received on 9 February 2021.

Recruitment occurred during the COVID-19 pandemic within the setting of an acute NHS hospital trust. The approved design of the clinical study required the research MRI scan to be added to patients' routine clinical scans without causing any delay in patients' diagnostic pathways. Despite general enthusiasm for study enrolment from approached patients, recruitment to the study was confounded by a combination of pandemic related consequences including clinical restrictions in the Ear, Nose and Throat (ENT) department, increased demand on the hospital radiology services due to a backlog of clinical scans, social distancing rules and staff absences. As such, the number of patients recruited to this study was significantly below that originally planned which had a negative impact on the power of the study. Nevertheless imaging data was successfully obtained from patients with suspected head and neck squamous cell carcinoma in the clinical setting using only routinely available clinical equipment and is presented in this thesis.

Publications

The following publications and national / international presentations were made during the course of these PhD studies:

Published Papers

1. **McCabe A**, Martin S, Rowe S, Shah J, Morgan PS, Borys D, Panek R. (2024) 'Oxygen-enhanced MRI assessment of tumour hypoxia in head and neck cancer is feasible and well tolerated in the clinical setting.' *Eur Radiol Exp* **8**, 27.

2. **McCabe A**, Martin S, Shah J, Morgan PS, Panek R. (2023) 'T1 based oxygen-enhanced MRI in tumours; a scoping review of current research.' *Br J Radiol* **96**, 20220624.

Conference Presentations

1. **McCabe A**, Martin S, Panek R (2024) 'Can pre-treatment MRI detect head & neck cancers at greater risk of hypoxia induced radioresistance?' European Society for Radiotherapy and Oncology Conference 2024, Glasgow. Oral presentation.

2. **McCabe A** (2023) 'Assessment of Head and Neck Cancer Tumour Hypoxia in the Clinical Setting'. Invited speaker at the National Head and Neck Oncology Meeting, York September 2023.

3. **McCabe A**, Panek R (2023) 'Patient reported experiences of medical imaging during the workup for radical radiotherapy treatment of head and neck cancer' British Association of Head & Neck Oncologists (BAHNO) conference 2023, London. Oral presentation.

4. **McCabe A**, Panek R (2023) 'Can pre-treatment MR imaging identify hypoxic regions in head and neck squamous cell carcinomas?' European Congress on Head and Neck Oncology (ECHNO) 2023, Lisbon, Portugal. Oral presentation.

5. **McCabe A**, Christian J, Panek R (2022) 'Oxygen-induced MRI T1 changes in head and neck anatomical structures' Clin Radiol. **77:e1–2**. Oral presentation in person Birmingham, UK. Winner of the George and Vera Ansell abstract competition.

6. **McCabe A**, Borys D, Christian J, Pereira S *et al.* (2022) 'Oxygen induced T1 changes in head and neck anatomical structures' Proc Intl Soc Mag Reson Med. **Abstract 2923**. Digital poster presented in person.

7. **McCabe A**, Christian J, Panek R (2022) 'Initial experience of oxygen enhanced MRI in determining regions of hypoxia in head and neck cancer' The joint International Congress on Innovative Approaches in Head and Neck Oncology (ICHNO) and the European Congress on Head and Neck Oncology (ECHNO) 2022, Online. Poster presentation.

8. **McCabe A**, McGrath D, Blockley N, Panek R. (2021) 'Does hypocapnia affect oxygen induced changes in brain T1 times at 3T?' European Society of Magnetic Resonance in Medicine and Biology (ESMRMB) Conference 2021, Online. Oral presentation. Awarded a magna cum laude award.

Acronyms

2D two-dimensional

3D three-dimensional

AAPM American association of physicists in medicine

AI artificial intelligence

ANTs advanced normalization tools

AP-1 activator protein 1

ARCON accelerated radiotherapy with carbogen and nicotinamide

ASCO American society of clinical oncology

ATP adenosine triphosphate

BER base excision repair

BOLD blood oxygen level dependent MRI

CAIPIRINHA controlled aliasing in parallel imaging results in higher acceleration

CAIX carbonic anhydrase 9

CI confidence interval

CoG centre of gravity

COPD chronic obstructive pulmonary disease

CoV coefficient of variation

CRT concurrent chemo-radiotherapy

CRUK cancer research UK

CSF cerebrospinal fluid

CT diagnostic computed tomography

CTLA-4 cytotoxic T-lymphocyte associated protein 4

DAHANCA Danish Head and Neck Cancer Group

DCE-MRI dynamic contrast enhanced MRI

DDR DNA damage response

DICOM digital imaging and communications in medicine

DNA deoxyribonucleic acid

DNA-PK DNA dependent kinase

DSB double-strand breaks

DSC Dice similarity coefficients

DWI diffusion weighted imaging

EBV Epstein-Barr virus

EGFR epidermal growth factor receptor

eIF-4E eukaryotic translation initiation factor 4E

EMT epithelial-to-mesenchymal transition

EORTC European Organisation for Research and Treatment of Cancer

ER endoplasmic reticulum

ESTRO European Society for Radiotherapy and Oncology

ETL echo train length

F_iO_2 fraction of inspired oxygen

F-HX4 flortanidazole

FA flip angle

FAZA fluoroazomycin arabinoside

FDG-PET ^{18}F-fluoro-2-deoxy-D-glucose-PET

FFT fast Fourier transform

FID free induction decay

FIH factor inhibiting HIF

FMISO fluorinated-misonidazole

FoV field of view

FSE fast spin echo

GAD-7 generalised anxiety disorder assessment

GADD45 growth arrest and DNA-damage-inducible protein 45

GBM glioblastoma multiforme

GE gradient echo

GLCM grey level co-occurrence matrix

GLUT-1 glucose transporter 1

GLUT-3 glucose transporter 3

GMC general medical council

HADS hospital anxiety and depression scale

Hct haematocrit

HER2 human epidermal growth factor receptor 2

HIF hypoxia-inducible factor

HNSCC head and neck squamous cell carcinoma

HPV human papillomavirus

HR homologous recombination

HRE hypoxia response elements

ICA independent component analysis

IHC immunohistochemistry

IR inversion recovery

ISMRM International Society of Magnetic Resonance in Medicine

IV intravenous

K^{trans} transfer rate constant

MAPK mitogen-activated protein kinases

MDT multidisciplinary team

MHC-1 major histocompatibility complex class 1

MMR mismatch repair

MOBILE mapping of oxygen by imaging lipids relaxation enhancement

MOLLI modified Look-Locker inversion recovery

mpMRI multiparametric MRI

MRI magnetic resonance imaging

MRI-AQ magnetic resonance imaging-anxiety questionnaire

mRNA messenger ribonucleic acid

MRS magnetic resonance spectroscopy

mTOR mammalian target of rapamycin

NADPH nicotinamide adenine dinucleotide phosphate

NER nucleotide excision repair

NF-κB nuclear factor κB

NHEJ non-homologous end joining

NHS National Health Service

NIfTI neuroimaging informatics technology initiative

NIHR National Institute for Health and Care Research

NK natural killer

NMR nuclear magnetic resonance

NUH Nottingham University Hospitals NHS trust

OE-MRI oxygen-enhanced MRI

OER oxygen enhancement ratio

OPN osteopontin

PD proton density

PD-1 programmed cell death protein 1

PD-L1 programmed death-ligand 1

PET positron emission tomography

PHD prolyl hydroxylase domain

planning-CT radiotherapy treatment planning computed tomography

PRISMA-ScR preferred reporting items for systematic reviews and meta-analyses extension for scoping reviews

PTEN phosphatase and tensin homolog

qDixon Siemens quantitative multi-echo Dixon protocol

Rb retinoblastoma

RF radio-frequency

ROI regions of interest

SCC squamous cell carcinoma

SE spin echo

SNR signal to noise ratio

SOS stack of stars

Sp1 specificity protein 1

SPGR spoiled gradient echo

SPM12 statistical parametric mapping version 12

SSB single-strand breaks

SyN symmetric diffeomorphic

TE echo time

TI inversion time

TOLD tissue oxygenation level dependent MRI

TR repetition time

TSE turbo spin echo

UPR unfolded protein response

USPIO ultrasmall superparamagnetic iron oxide

$\mathbf{v}_e$ extravascular extracellular volume fraction

VEGF vascular endothelial growth factor

VFA variable flip angle

VHL Von Hippel-Lindau

VIBE volumetric interpolated breath-hold examination

VOI volume of interest

WHO World Health Organisation

Contents

1 Introduction **1**

1.1 The Issue of Hypoxia 1

1.1.1 Radiobiology and oxygen 11

1.2 Head and Neck Cancers 14

1.2.1 Human papillomavirus 15

1.2.2 Epstein-Barr Virus 17

1.2.3 Therapeutic approaches 19

1.3 Modification of Hypoxic Radioresistance in Head and Neck Cancers 22

1.4 Modifying Radiotherapy Treatment Plans to Overcome Hypoxia . 27

1.5 Determining Tumour Hypoxia 29

1.5.1 Direct O_2 measurement 29

1.5.2 Bioreductive compounds 30

1.5.3 Hypoxia induced gene and protein expression 31

1.5.4 Hypoxia Imaging 34

1.5.4.1 Hypoxia MRI 39

1.6 Conclusion 45

2 MRI Physics **46**

2.1 Introduction 46

2.2 Signal Creation 46

2.3 Spin Echo 50

2.4 Gradient Echo 53

2.4.1 Spoiled Gradient Echo 53

2.5 Measurement of T_1 Relaxation Times 55

2.5.1 Inversion Recovery 55

2.5.2 Look-Locker . . . 56
2.5.3 Variable Flip Angle . . . 56
2.6 Conclusion . . . 58

3 T_1 based oxygen-enhanced MRI in tumours; a scoping review of current research 59
3.1 Abstract . . . 59
3.2 Introduction . . . 60
3.3 Methods . . . 61
3.4 Results . . . 62
3.4.1 Research focus . . . 62
3.4.2 Preclinical Studies . . . 65
3.4.3 Human studies . . . 68
3.4.4 Technical considerations . . . 69
3.4.5 Oxygen delivery . . . 74
3.5 Discussion . . . 75
3.5.1 Update of literature search . . . 77
3.6 Limitations . . . 79

4 OE-MRI in HNSCC Clinical Study Design 81
4.1 Hypothesis, aims and objectives . . . 81
4.2 Study overview . . . 82
4.3 Eligibility Criteria . . . 84
4.3.1 Inclusion Criteria . . . 84
4.3.2 Exclusion criteria . . . 86
4.4 Study Sample Size . . . 87
4.5 Ethical Approval . . . 88
4.6 Recruitment . . . 88
4.7 Data handling . . . 88

5 OE-MRI Study Development 91
5.1 OE-MRI sequence development . . . 91
5.2 Participant Setup . . . 95
5.3 Phantom assessment of VIBE OE-MRI sequence . . . 98

5.3.1 Method . . . 98
5.3.2 Results . . . 99
5.3.3 Discussion . . . 102
5.4 Data analysis code . . . 103
5.5 CSF based F_iO_2 estimation . . . 105
5.5.1 Method . . . 107
5.5.2 Results . . . 108
5.5.3 Discussion . . . 110
5.6 Conclusion . . . 111

6 Dynamic OE-MRI image co-registration 112
6.1 Abstract . . . 112
6.2 Introduction . . . 113
6.3 Method . . . 117
6.4 Results . . . 121
6.5 Discussion . . . 129

7 Clinical outcomes 135
7.1 Abstract . . . 135
7.2 OE-MRI in HNSCC Clinical Study . . . 136
7.2.1 Method . . . 136
7.2.2 Results . . . 137
7.2.3 Discussion . . . 149
7.2.4 Limitations . . . 153
7.2.5 Conclusion . . . 155
7.3 Exploratory analysis . . . 155
7.3.1 Method . . . 158
7.3.2 Results . . . 159
7.3.3 Discussion . . . 162
7.4 Radiotherapy . . . 164
7.4.1 Method . . . 165
7.4.2 Results . . . 165
7.4.3 Discussion . . . 166

8 Tolerability of Oxygen Enhanced MRI **169**
8.1 Abstract 169
8.2 Background 170
8.2.1 Patients' experience of medical imaging 172
8.3 Method 173
8.4 Results 175
8.5 Discussion 176

9 Overall Conclusions and Suggestions for Future Work **181**

References **187**

A Supplementary Figures **233**

B Supplementary Tables **238**

C ANTs Code **245**

Chapter 1

Introduction

1.1 The Issue of Hypoxia

Oxygen is essential in the human body for the process of aerobic respiration; the generation of the cellular energy source adenosine triphosphate (ATP) through oxidative phosphorylation. If a discrepancy arises between the supply of and cellular demand for oxygen then tissue hypoxia arises which can compromise normal cellular functions. Room air has a partial pressure of oxygen of 160 mmHg (21% concentration) however by the time oxygen has traversed the pulmonary system and exited the lungs, this pressure has dropped to typical arterial blood oxygen partial pressures of 70 mmHg (9.5%) (McKeown 2014). Exact definitions of levels of oxygen that constitute normal physiological oxygen levels (physoxia) are difficult to state given the differing metabolic requirements and vascular supplies of different tissues however end organs have typical partial oxygen pressures ranging from 70 mmHg (9.5%) in kidneys to 41 mmHg (5.4%) in liver and 34 mmHg (4.4%) in the brain (Carreau et al. 2011) with peripheral tissues having an average partial oxygen pressure of 46 mmHg (6%) (McKeown 2014). Physiological hypoxia is the lower level at which cellular hypoxia responses occur and is stimulated at partial oxygen pressures of approximately 15 mmHg (2%) with pathological hypoxia occurring at oxygen pressures < 8 mmHg ($< 1\%$) when normal homeostatic mechanisms have been disrupted (McKeown 2014).

Although there are healthy tissues in the human body that routinely reside in low oxygen levels, such as regions of bone marrow that can have oxygen levels of

approximately 10 mmHg (1.5% oxygen) (Spencer et al. 2014) and the lumen of the gut where commensal obligate anaerobic bacteria reside at oxygen pressures < 1 mmHg (Albenberg et al. 2014), these hypoxic regions are restricted to a limited number of specific locations. The presence of biologically significant hypoxia in tumours however is much more widely observed and has been recognised since the work of Thomlinson & Gray (1955). Tumours show on average significantly lower levels of oxygen than their corresponding normal tissues; for example healthy breast tissue has median partial pressures of oxygen of around 65mmg compared to 10 mmHg in breast cancer, normal cervix tissue has median oxygen pressure of 42 mmHg compared to 9 mmHg in squamous cell carcinoma (SCC) of the cervix (Vaupel et al. 2007) and HNSCC have median tumour oxygen levels ranging from 10 mmHg to 14.6 mmHg compared to 40 mmHg to 51.2 mmHg for healthy pharyngeal tissue (McKeown 2014). Studies in a range of tumours have shown that the presence of oxygen concentrations below 10 mmHg results in significantly worse survival outcomes (Vaupel et al. 2007, McKeown 2014, Hughes et al. 2019). These observations have been explicitly confirmed in clinical studies in HNSCC (Brizel et al. 1997, 1999, Lyng et al. 1999, Overgaard 2011).

Cellular hypoxia is generally considered to consist of two components; chronic (diffusion limited) hypoxia and intermittent hypoxia, also known as cycling hypoxia. Chronic tumour hypoxia is a manifestation of the limited diffusion distance of molecular oxygen combined with the high and uncontrolled proliferation rates of highly metabolically active and therefore oxygen consuming tumour cells (Zhao et al. 2017). Cells geographically closer to perfused blood vessels utilise the available oxygen resulting in cells more distal from the vasculature residing in environments with lower oxygen tension. A broadly stable oxygen concentration gradient is established with cells further away from blood vessels being increasingly hypoxic (Thomlinson & Gray 1955, Hughes et al. 2019). Although pro-angiogenic factors are produced by cancer cells in response to regions of tissue hypoxia, tumours are characterised by disorganised and non-functional vascular proliferation thus confounding the issue of tumour hypoxia (Nagy et al. 2010). Non-cancer components of the tumour microenvironment also play a part in modulation of tumour vasculature and thus oxygenation with the activation

and proliferation of stromal cells leading to vascular compression (Chen et al. 2023).

In addition to tumour oxygen gradients, cyclical changes in tumour hypoxia occur as a consequence of alterations in the blood perfusion and erythrocyte flux through the characteristically disorganised and low density tumour vasculature (Dewhirst et al. 2008, Delprat et al. 2020). This unstable blood flow leads to periods of marked hypoxia followed by periods of reoxygenation over timescales that can vary from minutes to days and can lead to the partial pressure of oxygen in regions of tumours up to 130μm away from micro-vessels varying periodically by approximately 20 mmHg (Cárdenas-Navia et al. 2008, Dewhirst et al. 2008, Matsumoto et al. 2010, Panek et al. 2017). The wide range of cycling frequencies observed has been attributed to different underlying aetiologies; higher frequencies being associated with thermoregulatory mechanisms including acute changes in perfusion and erythrocyte flux as well as intermittent vascular occlusion, whereas the lower frequency components of the order of days are linked to changes in the vascular supply secondary to neoangiogenesis (Dewhirst et al. 2008, Matsumoto et al. 2010). Chronic and cycling hypoxia are both important when it comes to the activation of hypoxia driven cellular adaptive methods as well as in regards treatment resistance and tumour aggressiveness. However pre-clinical studies have shown that chronic and intermittent hypoxia may cause different changes in deoxyribonucleic acid (DNA) repair pathways and cell-cycle control; chronic hypoxia can suppress the homologous recombination (HR) DNA double-strand breaks (DSB) repair pathway as well as decreasing mismatch repair (MMR) function leading to increased cellular resistance to platinum-based chemotherapies as well as leading to genomic instability, whereas intermittent hypoxia can increase DNA damage-associated checkpoint cell-cycle arrest and DSB repair via non-homologous end joining (NHEJ) (Bristow & Hill 2008, Klein & Glazer 2010).

The DNA damage response (DDR) pathways in cells are responsible for maintaining genomic integrity. For damage induced by ionising radiation, the repair mechanisms are broadly divided into those responsible for repairing single-strand breaks (SSB) and those for fixing the potentially more catastrophic DSB, although other forms of DNA damage do exist including base damage, sugar damage, DNA

cross-linking and clustered damage sites (Huang & Zhou 2021). SSB are repaired by either base excision repair (BER), nucleotide excision repair (NER) or MMR depending on the nature of the DNA damage. BER is the simplest of these three, capable of repairing 1 to 10 nucleotides only whereas NER is more complex and can repair lesions that include cisplatin-induced DNA adducts. DSBs on the other hand are principally repaired by one of two main pathways; the high-fidelity but time consuming HR repair, or the quicker but more error prone NHEJ. HR requires the presence of the sister chromatid and so can only happen during the S/G2 phase of the cell cycle as opposed to NHEJ that can repair DSBs throughout the cell cycle (Huang & Zhou 2021).

On the cellular level, the response to hypoxia is mediated by hypoxia-inducible factor (HIF) dependent and independent pathways that have differing sensitivities to the extent and duration of hypoxia and modify both gene transcription and messenger ribonucleic acid (mRNA) translation of target proteins to modulate cells' responses to differing oxygen levels (Wouters & Koritzinsky 2008). The HIF pathway is possibly the best known modulator of a cell's response to hypoxia. First discovered in the 1990's (Semenza & Wang 1992), HIF is composed of two subunits known as α and β with 3 versions of each subunit known to exist. Although both the α and β subunits are constitutively synthesised, the HIF-α component is sensitive to increased expression from a number of cellular pathways including the PI3K/AKT/mTOR and RAS/RAF/MEK/ERK pathways as well as being subject to oxygen dependent proteasomal degradation (McGettrick & O'Neill 2020). The most important oxygen sensing mechanism that regulates HIF-α levels is that of the prolyl hydroxylase domain (PHD) enzymes (figure 1.1). PHDs are enzymes that are dependent on oxygen as a co-factor and catalyse the hydroxylation of two proline residues, Pro402 and Pro564 on the HIF-α subunits. In normoxic conditions these hydroxylations are recognised by Von Hippel-Lindau (VHL) E3 ubiquitin ligase leading to VHL mediated poly-ubiquitination and subsequent rapid proteasomal degradation resulting in a half-life in normoxic conditions of HIF-1α of the order of 5-10 minutes (Ratcliffe 2007, Hanahan & Weinberg 2011).

In hypoxic conditions the HIF-α subunit is not marked for degradation and can then translocate to the nucleus and dimerises with the HIF-β subunit and

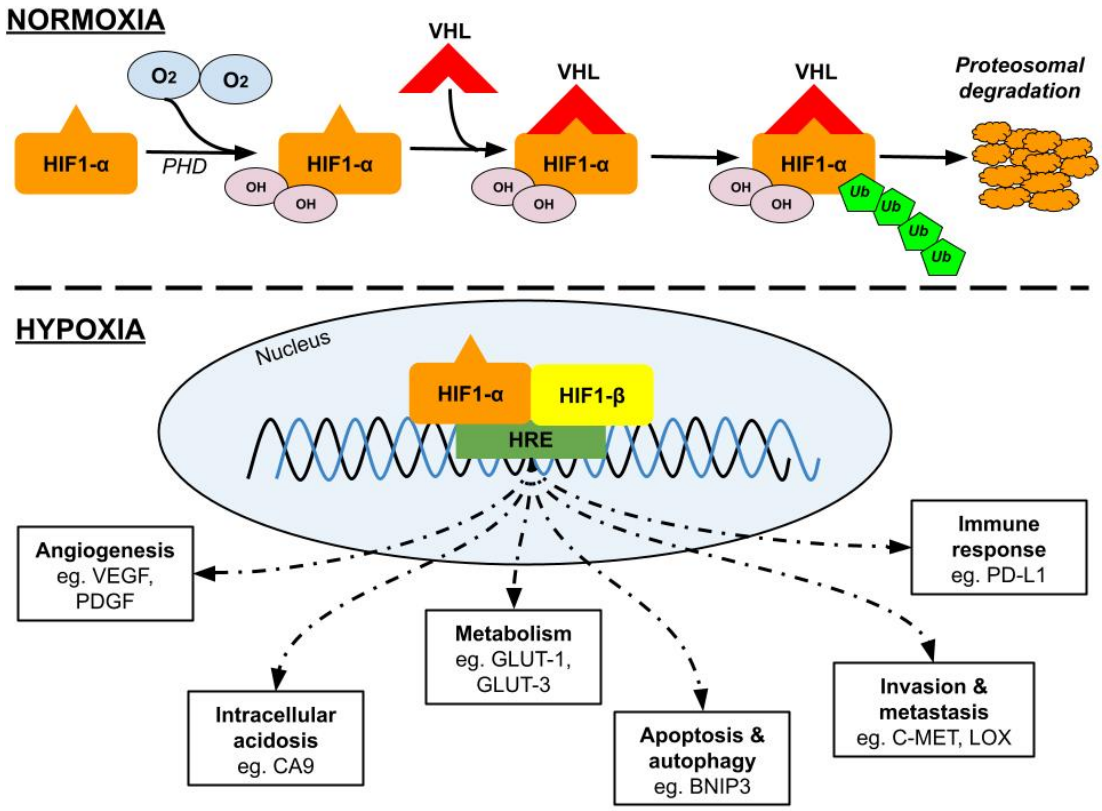

Figure 1.1: Hypoxia Inducible Factor - Diagrammatic illustration of the regulation of HIF-1α by PHD in normoxic and hypoxic conditions. In normoxic conditions HIF-1α is hydroxylated by PHD allowing binding of VHL causing polyubiquitination and subsequent proteasomal degradation. Under hypoxic conditions, HIF-1α is stable and forms a heterodimer with HIF-1β. This complex translocates to the nucleus where (with co-factors) it binds to hypoxia response elements (HRE) and acts to initiate transcription of the HIF target genes. *HIF1* - hypoxia inducible factor 1, *PHD* - prolyl hydroxylase domain protein, *VHL* - Von Hippel-Lindau protein, *Ub* - ubiquitin protein, *HRE* - hypoxia response elements, *VEGF* - vascular endothelial growth factor, *PDGF* - platelet-derived growth factor, *CA9* - carbonic anhydrase 9, *GLUT* - glucose transporter, *BNIP3* - Bcl2 interacting protein 3, *C-MET* - mesenchymal-epithelial transition factor, *LOX* - lysyl oxidase, *PD-L1* - programmed death-ligand 1. Adapted from figure 3 Semenza (2003), figure 2 Sørensen & Horsman (2020) and figure 3 Mallikarjuna et al. (2022).

subsequently bind to hypoxia response elements (HRE) within the promoter regions of target genes (Hanahan & Weinberg 2011). Along with the co-activator proteins p300 and CBP, this HIF complex activates the transcription of genes that mediate the cellular response to hypoxia (Krock et al. 2011). In addition, to the PHD mediated oxygen sensing regulation of HIF, the binding of the HIF associated co-factors is subject to oxygen sensing control. Factor inhibiting HIF (FIH) is an oxygen dependent enzyme that in normoxic conditions hydroxylates an asparagine residue on HIF-1α preventing the binding of p300/CRB. However in hypoxic conditions, this asparagine hydroxylation does not proceed and thus the co-factors can bind to HIF allowing it to function as a transcription activator (McGettrick & O'Neill 2020).

In total the HIF proteins are known to regulate well over 1,000 gene targets under hypoxic conditions, affecting a wide range of cellular functions including metabolic adaptation, apoptosis resistance, angiogenesis, cell survival and proliferation and in the case of cancer also driving invasion and metastasis (Semenza 2003, Kizaka-Kondoh & Konse-Nagasawa 2009, Dengler et al. 2014). These downstream targets of HIF include vascular endothelial growth factor (VEGF) with a role in angiogenesis, glucose transporter 1 (GLUT-1) and glucose transporter 3 (GLUT-3) affecting glycolysis (the principal method of energy generation in cancer cells) and carbonic anhydrase 9 (CAIX) with a role in pH regulation (figure 1.1). The increased expression of these proteins by cells residing in hypoxic conditions have been investigated as surrogate markers of tumour hypoxia (see section 1.5.3).

Non-HIF dependent hypoxic signalling can occur through regulation of the kinase mammalian target of rapamycin (mTOR) and through activation of the unfolded protein response (UPR). The UPR is activated at lower levels of oxygen concentration ($< 0.2\%$) than HIF ($< 2\%$) and leads to changes in transcription and translation due to endoplasmic reticulum (ER) stress, mediated by the master regulator HSPA5 (figure 1.2) (Wouters & Koritzinsky 2008, Price et al. 2022). The hypoxic signalling through mTOR occurs through hypoxic inhibition of the mTOR-C1 complex which through its increased association with the protein eukaryotic translation initiation factor 4E (eIF-4E) prevents translation initiation (Wouters & Koritzinsky 2008).

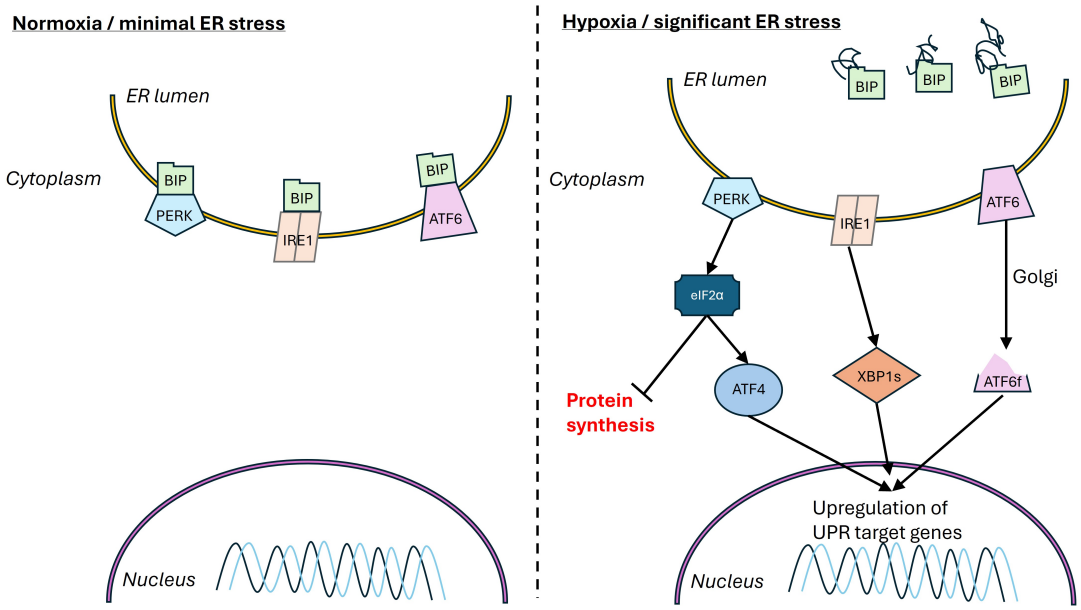

Figure 1.2: Unfolded Protein Response - In normoxic conditions with minimal ER stress, the master regulator of the Unfolded Protein Response, HSPA5 (also known as Binding Immunoglobulin Protein (BIP)) is bound to sensor proteins making them inactive. These sensor proteins include PERK, IRE1, AFT6. Under hypoxia induced ER stress, misfolded proteins in the ER lead to BIP/HSPA5 dissociating from these sensors. PERK then phosphorylates eIF2α which inhibits protein synthesis as well as allowing for the transcription of ATF4 which acts as a transcription factor and upregulates genes associated with apoptosis, autophagy and amino acid metabolism. IRE1 activation produces XBP1s and ATF6 is cleaved to ATF6f following translocation to the Golgi apparatus. This leads to the induction of proteins that lead to increased function of the ER and/or the removal of mis or unfolded proteins. Adapted from Wouters & Koritzinsky (2008), Bolland et al. (2021) and Price et al. (2022)

In addition to HIF and the UPR mediated responsive elements, other transcription factors that can be activated by hypoxia include activator protein 1 (AP-1), nuclear factor κB (NF-κB), specificity protein 1 (Sp1), Myc and the tumour suppressor protein p53 (Druker et al. 2021). AP-1 is a transcription factor that consists of homo and heterodimers of proteins from the Jun, Fos and ATF families (Yoshitomi et al. 2021). Cellular hypoxia can lead to the accumulation of reactive oxygen species which can promote the activation of mitogen-activated protein kinases (MAPK) pathways which in turn phosphorylate the c-jun/c-fos subunits of AP-1 consequentially activating AP-1 as a transcription factor. This activated form of AP-1 principally acts in conjunction with HIF and NF-κB and leads to the expression of a range of hypoxia responsive genes including those that promote angiogenesis and cellular adaptation to the hypoxic environment (Druker et al. 2021, Yoshitomi et al. 2021). Overexpression of AP-1 has also been described in a range of epithelial malignancies and lymphomas (Song et al. 2023). Hypoxia induced increased expression of Sp1 occurs in a HIF dependent manner and can act synergistically to enhance the promoter role of HIF as well as directly driving expression of hypoxia adaptation genes including VEGF (Deacon et al. 2012, Druker et al. 2021).

Severe hypoxia or anoxia leads to cell death and regions of necrosis but the multitude of genetic and proteomic cellular changes mediated by survivable hypoxia can drive cells to develop the hallmarks of cancer as well as develop more aggressive and treatment resistant tumour cell phenotypes (McKeown 2014, Verduzco et al. 2015, Thiruthaneeswaran et al. 2021). One such hallmark of cancer that is driven by hypoxia is that of genomic instability, with lower levels of tumour oxygenation correlating with greater tumour mutational burden and increased prevalence of oncogene and tumour suppressor gene mutations (Bhandari et al. 2020). However as hypoxia itself does not directly cause DNA damage, the presence of such genomic instability in hypoxic environments implies decreased functionality of the DDR pathways (Kaplan & Glazer 2020). Indeed HR repair is suppressed in hypoxia due to the reduction in transcription of the HR factors BRCA1 and RAD51, MMR is reduced via the hypoxic suppression of MLH1 and MSH2 factors and BER is decreased in hypoxia due to the downregulation of a number of BER related factors (Kaplan & Glazer 2020). Although the effect of

hypoxia on NHEJ and NER are less clear, the overall effect of hypoxia is to reduce the ability of cells to make effective repair of DNA lesions thereby contributing to genomic instability.

In addition although severe hypoxia leads to the induction of apoptosis via the upregulation of prop-apoptotic factors such as BNIP3 via HIF mediated pathways, under less severe hypoxic conditions increased resistance of cells to apoptosis is observed through increased expression of anti-apoptotic proteins such as IAP-2 whose activity is upregulated via increased transcription of NF-κB (Tang et al. 2021). The decrease in expression of pro-apoptotic proteins such as p53 has also been noted in tumours subject to cycling hypoxia implying that lower level hypoxic environments select tumour clones more likely to withstand apoptotic signalling (Bhandari et al. 2020). This reduction in apoptosis in regions of moderate hypoxia leads to cell proliferation despite the potential presence of DNA damage and therefore further drives genomic instability.

It is well characterised that hypoxic tumour regions display increased resistance to radiotherapy treatments (see section 1.1.1) but they also display greater resistance to both classic cytotoxic chemotherapy treatments and the more recently developed checkpoint inhibitor (immunotherapy) treatments. The erratic and poorly organised tumour vasculature and reduced pH of hypoxic regions leads to reduced intracellular delivery of cytotoxic medications as well as causing a lack of nutrient delivery that tends to reduce cell turnover therefore protecting against chemotherapy agents. In addition, a reduction in free radical generation in hypoxic regions can reduce the cytotoxicity of some chemotherapy treatments (Cosse & Michiels 2008, Dewhirst et al. 2008). Both 5-fluorouracil and cisplatin are chemotherapy treatments routinely used in the management of HNSCC that have been found to be less effective *in vivo* in hypoxic cells, although interestingly this effect was not noted *in vitro* suggesting a more complex interplay between the chemotherapy drugs and the hypoxic tumour microenvironment (Horsman et al. 2021).

Tumour hypoxia also has a significant effect on the immune system within the tumour microenvironment with consequential impact on the efficacy of immunotherapy treatments. The tumour microenvironment contains a range of different immune cells including cytotoxic CD8+ T-cells, CD4+ T-cells, regulatory

T-cells, natural killer (NK) cells, tumour associated macrophages and dendritic cells. The relative abundance and activity of these different immune cells can be modulated by hypoxia. In addition to decreased immune cell extravasation through disorganised tumour vasculature, tumour hypoxia exerts a net immunosuppressive effect through a reduction in macrophage and T-cell infiltration and activation as well as an increase in tumour cell resistance to the cytotoxic activity of the immune system (Barsoum et al. 2014). The more acidic and glucose deprived conditions in hypoxic tumours leads to a survival advantage for regulatory T-cells due to their resistance to high lactate levels but a reduction in cytotoxic activity of other immune cells (Bigos et al. 2024). In addition, tumour hypoxia can drive increased expression of cytokines and chemokine including CCL28 which leads to increased recruitment of regulatory T-cells to the tumour microenvironment further inhibiting the activity of the cytotoxic cells and contributing to the immunosuppressive effect of hypoxia (Facciabene et al. 2011). NK cells also undergo reduced activation in hypoxic environments due to decreased expression of activating cell surface receptors (Bigos et al. 2024). Tumour hypoxia can also drive immune invasion by inhibiting the expression of major histocompatibility complex class 1 (MHC-1) whose normal function is to present peptide fragments to cytotoxic T-cells and contribute to activating their cytotoxic function. Hypoxia driven suppression of MHC-1 therefore contributes to tumour immune invasion. The suppression of MHC-1 has been found to occur in tumours in both a HIF dependent manner (Sethumadhavan et al. 2017) and via the activation of autophagy via the PERK arm of the UPR (figure 1.2) (Estephan et al. 2025). It has also been identified that severe hypoxia can contribute to the state of T-cell exhaustion that is frequently seen in cancers and chronic infections (Scharping et al. 2021).

Tumour hypoxia also increases tumour cell resistance to the cytotoxic activity of the immune system by upregulating expression of co-inhibitory molecules such as programmed death-ligand 1 (PD-L1) and cytotoxic T-lymphocyte associated protein 4 (CTLA-4) that result in the down-regulation of the immune system in the tumour microenvironment. These important immune regulatory proteins are targets for a number of clinically used immunotherapy drug therapies including the programmed death receptor targeting therapies of Pembrolizumab and

Nivolumab that are both licensed for routine clinical use in metastatic or locally recurrent HNSCC (Barsoum et al. 2014, Noman et al. 2014). Of note, although some patients with metastatic HNSCC can obtain significant and long lasting response to immunotherapy treatment, the overall objective response rate of these medications in HNSCC is only of the order of 20% (Ferris et al. 2016, Burtness et al. 2019). It has been suggested that tumour hypoxia may play a role in this low response rate due to its immunosuppressive effects (Horsman et al. 2021).

Pre-clinical and clinical studies in cervical carcinoma (Hockel et al. 1996) and soft-tissue sarcoma (Nordsmark et al. 2001) have also shown that hypoxic environments increase the risk of developing distant metastatic disease by the upregulation of metastasis-related genes (Hammond et al. 2014, McKeown 2014). This metastatic potential is also in part driven by the hypoxia caused angiogenic drive that both produces the vasculature required for distant spread of malignant cells as well as the HIF driven suppression of E-cadherin that increases epithelial-to-mesenchymal transition (EMT) to promote metastases generation (Thiruthaneeswaran et al. 2021).

The impact of hypoxia in tumours is therefore complicated, multifaceted and a clear potential target for therapeutic gains.

1.1.1 Radiobiology and oxygen

One of the major concerns with tumour hypoxia is its effect on radiotherapy treatment. Radiotherapy is the use of high energy photons, electrons or other charged particles to kill cells by causing excitations and ionizations of atoms of exposed tissues. Although such ionizations can damage cellular lipids and protein, the damage caused to DNA is generally considered the most important cellular target of radiation. The resulting DNA lesions caused range from base damage and SSB to the more lethal DSB and clustered DNA lesions that consist of mixtures of SSB and DSB (Fabbrizi & Parsons 2020). Depending on the severity of the damage and the functioning or not of DNA damage repair mechanisms in the irradiated cancer cells, these lesions can be either lethal or sublethal. The phase of the cell cycle that radiation is delivered in affects the sensitivity of the cell to the damage with irradiations occurring immediately prior to or during

mitosis being more likely to decrease cell survival than irradiations performed in late S-phase. Decreased repair of sublethal damage is more commonly seen in cancer cells due to both their higher replication rate and the frequent presence of defects in the DDR pathway (Price et al. 2022).

One of the hallmarks of ionising radiation exposure is the presence of clustered DNA damage. This refers to the presence of multiple DNA lesions within close proximity of each other, generally considered to be within a few helical turns (Sutherland et al. 2001). As the majority of radiation induced DNA damage is mediated via reactive oxygen species generation, most of these DNA lesions are single-strand damage including SSBs, oxidative base damage, abasic sites and DNA crosslinks. These damaged sites can be on the same DNA strand or on opposing strands. In addition, DSBs can also constitute lesions in clustered DNA damage however the chance of such damage occurring is a couple of orders of magnitude smaller than the odds of single-strand lesions for a given delivered radiation dose (Nickoloff et al. 2020). The simplest type of clustered DNA lesion is a DSB caused by two SSBs on opposing strands occurring in close vicinity to each other. However, clustered lesions can be significantly more complex due to variability in the number and type of DNA lesions as well as different spatial distribution of damage within clusters. Clustered DNA damage is often difficult for cells to repair. This is in part due to the close proximity of different types of lesions making it more complex for repair proteins to recognise and simultaneously access all of the damaged sites whilst selecting the most appropriate repair mechanism in addition to distortion in DNA structures caused by the clustered lesions reducing the ability of DNA repair mechanisms to align and repair damage (Sutherland et al. 2001, Sage & Shikazono 2017). A significant reason for the cytotoxicity of ionising radiation is therefore due to the weakness of DNA repair mechanisms to process clustered DNA damage (Nickoloff et al. 2020).

The most commonly used radiotherapy modality for treating head and neck tumours worldwide is high energy photon radiotherapy using electromagnetic radiation in the energy range around 6MV. When high energy photons are incident on tissue they liberate so-called secondary electrons. It is the deposition of dose from these secondary electrons that mediates cell damage either by direct DNA

damage, or in 70% to 80% of the time by the production of free radicals in water. These highly damaging free radicals, usually denoted as $R^{\cdot}$, are unstable and can have one of two fates; reaction with oxygen to eventually yield a stable compound (ROOH) that makes the damage permanent or "fixed", or reaction with H^+ to restore the DNA to its original form. The latter primarily happens in areas of low oxygen. This is known as the oxygen fixation hypothesis and explains the critical role of oxygen in mediating radiotherapy cell killing (Brown & Wilson 2004, Grimes et al. 2017). The generation of reactive oxygen species by ionising radiation can also cause cellular effects separate from DNA damage including promoting cell apoptosis or senescence or stimulating cell proliferation (Price et al. 2022).

The influence of oxygen on radiotherapy outcomes has been recognised since the 1950's (Gray et al. 1953) but experimental evidence to support the oxygen fixation hypothesis was first generated in the 1970s where it was shown that oxygen had to be present within microseconds of radiation exposure for radiation damage to be observed (Michael et al. 1973). In order to quantify the effect of oxygen on cell kill likelihood, radio-biologists use the oxygen enhancement ratio (OER):

$$\text{OER} = \frac{\text{Radiation dose in hypoxia}}{\text{Radiation dose in air}}, \tag{1.1}$$

where the radiation doses are those required to produce equivalent biological effect (Joiner & van der Kogel 2009). For most cell types the OER is around 3 however this ratio does not vary linearly with oxygen concentration (Grimes et al. 2017). It is generally suggested that the level of oxygenation that results in radiobiological hypoxia is the half maximal value of the OER versus oxygen concentration curve. This equates to between 2.5 mmHg and 3 mmHg oxygen (Vaupel et al. 2007, McKeown 2014, Grimes et al. 2017). A meta-analysis of studies in cervix, head and neck and breast cancer found that the median oxygen concentration in tumours was 10 mmHg with the mean radiobiological hypoxic fraction being approximately 25% (Vaupel et al. 2007). Head and neck tumours have between a 3 and 4.5 fold decrease in oxygenation levels compared to surrounding healthy tissue (McKeown 2014). There is however significant heterogeneity of oxygen levels within tumours (Adam et al. 1999, Vaupel et al. 2007, Hammond et al.

2014) and the full impact of this on cancer prognosis and treatment outcomes is still under assessment.

Hypoxic tumour environments can also drive more radio-resistant phenotypes by acidification of the extracellular matrix through the upregulation of CAIX and the increase in glycolysis metabolism primarily through the HIF pathway. Such changes in pH and rates of glycolysis metabolism leads to increased production of reducing compounds such as pyruvate, lactate, glutathione and nicotinamide adenine dinucleotide phosphate (NADPH) which tend to protect DNA from radiation induced free radical production (Meijer et al. 2012).

One of the fundamental tenets of radiobiology is the principle of re-oxygenation whereby previously hypoxic cells can become re-oxygenated during fractionated radiotherapy due to the death of surrounding tumour cells leading to improved vascular supply as well as reductions in intratumoural pressure amongst other factors (Pajonk et al. 2010). This re-oxygenation is considered to lead to radiosensitisation of previously radioresistant areas thereby increasing the cell kill likelihood of subsequent fractions of radiotherapy thus improving treatment outcomes. However, this schema would suggest that baseline tumour oxygenation levels should be less clinically relevant than studies have observed, as tumour hypoxia may be expected to resolve during therapy. Pre-clinical studies suggest this discrepancy may be due to hypoxia inducing some tumour cells to enter a state of cell quiescence, a state that continues even after re-oxygenation thereby perpetuating increased radioresistance (Menegakis et al. 2021). Indeed it may well be these hypoxic cells that are present at the beginning of a course of radiotherapy that are responsible for tumour relapse after radiation treatment possibly due to this hypoxia induced quiescence (Menegakis et al. 2023). The impact of oxygenation on tumours' responses to radiation is therefore clearly a complex one.

1.2 Head and Neck Cancers

The term head and neck cancer covers a range of different tumour types that arise from one of 6 major sites: oral cavity, pharynx, larynx, nasal cavity, paranasal sinuses and salivary glands. For the purposes of staging, prognosis and treatment,

these major sites are broken down to further anatomical subsites. The pharynx for example is divided into nasopharynx, oropharynx and hypopharynx, all of which have different tumour staging rules and different therapeutic approaches (James D. Brierley, Mary K. Gospodarowicz, Christian Wittekind 2017). Although there are a wide range of different tumour types found in head and neck cancer, over 90% of malignant pathologies found here are SCC that arise from the mucosal lining. The majority of the other malignant subtypes arise from salivary glands or are metastatic deposits from non local primary tumours (Hanna et al. 2008). The majority of head and neck cancers arise in the pharynx and larynx and the incidence is increasing. According to Cancer Research UK, there were approximately 8,800 cases of head and neck cancer in 2010 increasing to around 12,400 cases annually in 2018. Men are twice as likely to develop head and neck cancer as females with the majority of cases being in people over the age of 50 (*Cancer statistics* 2018). These demographics are changing however due to the increasing prevalence of human papillomavirus (HPV) infection.

1.2.1 Human papillomavirus

Historically, HNSCC were caused by tobacco smoking and alcohol consumption. In recent years, a new distinct clinical and pathological variant of HNSCC that affects the oropharynx has emerged, caused by HPV infection. HPV is a sexually transmitted virus that has a worldwide prevalence meaning that an estimated 80% of people will be infected by the virus at some stage of their adult life (Winer & Koutsky 2004). Oropharyngeal HPV infection occurs following oral-genital transmission and HPV related cancers are often seen in younger patients without any history of smoking. The abundant lymphoid tissue in the oropharynx facilitates the ready passage of lymphocytes and antigen presenting cells from the immune system through the basement membrane enabling the efficient functioning of the immune system. However it also allows HPV to traverse the basement membrane and consequently infect the oropharynx (Scott-Wittenborn & Fakhry 2021).

HPV is a DNA virus encoding up to 8 genes (Cosper et al. 2021). There are over 200 different subtypes of HPV but only a relatively small number have been determined to be high-risk for causing human cancers. The most common

carcinogenic clones are HPV-16 and HPV-18 (Göttgens et al. 2019) which are well known for causing cervical cancer and are amongst the HPV subtypes that the HPV vaccination and cervical screening program target (NICE 2022). HPV can also cause vulvar, penile and anal cancers in the anogenital region (Scott-Wittenborn & Fakhry 2021). Once infected with HPV in the cervical region, most women will clear the virus however 10% to 20% of women will develop a persistent infection that can lead to carcinogenesis (Winer & Koutsky 2004, Scott-Wittenborn & Fakhry 2021). Despite increasing rates of HPV vaccination, it is projected that the incidence of HPV associated oropharyngeal cancer will continue to increase due to older people who are at greater risk of cancers in general not having been vaccinated against HPV (Zhang et al. 2021). The burden of HNSCC is therefore likely to continue to increase in the foreseeable future.

HPV genes are divided into *early* genes that are involved in replication of the viral genome and *late* genes that produce the viral capsid proteins. Of the early genes, two known as E6 and E7 are known to be oncogenes (Ruttkay-Nedecky et al. 2013). In brief, E6 is known to bind the tumour suppressor protein p53 and mark it for proteasomal degradation. In a similar manner, E7 binds the tumour suppressor protein retinoblastoma (Rb) and marks this for degradation. The net result of the loss of these regulating proteins is that infected cells lose the ability to arrest the cell cycle or apoptose or become senescent, helping to establish replicative immortality, one of the hallmarks of cancer (Göttgens et al. 2019).

One of the most interesting facets of HPV related oropharyngeal malignancies is that despite often presenting with grossly enlarged, cystic cervical lymph nodes, these cancers have a significantly better prognosis than non-HPV related tumours (Kimple et al. 2013, Lassen et al. 2014, Mehanna et al. 2019, Daniels et al. 2020, Riaz et al. 2021). Overall HPV related HNSCC has a more immunogenic tumour micro environment, a lower mutation rate with fewer p53 mutations, higher radiosensitivity and consequently improved prognosis (Göttgens et al. 2019). Such improvements in clinical outcomes have generated significant interest in investigating if HPV positive cancers can be successfully managed with reduced intensity treatment in order to reduce acute and late toxicities whilst maintaining cure rates. Despite promising results from early trials, de-escalation strategies have

yet to be routinely adopted into clinical practice due to mixed results from phase 3 studies (Rühle et al. 2021*a*). In the UK, the De-ESCALaTE study caused significant concern where the substitution of the monoclonal antibody cetuximab for the standard chemotherapy drug cisplatin in patients being treated with radical chemoradiotherapy caused significantly worse 2 year overall survival (hazard ratio 5.0 (95% confidence interval 1.7 to 14.7) (Mehanna et al. 2019). Although HPV positive cancers are suspected to have a lower hypoxic burden than their HPV negative counterparts (Lassen et al. 2014, Sørensen et al. 2014), this does not equate to all HPV induced cancers being normoxic and it may potentially be this subgroup of hypoxic HPV related tumours that is confounding the outcomes of de-escalation studies.

The 30 ROC trial provides evidence as to the importance of hypoxia in the HPV positive subgroup of oropharyngeal cancers. This study randomised HPV positive oropharynx participants to standard chemoradiotherapy versus a dose reduced radiotherapy arm in those patients in whom hypoxia positron emission tomography (PET) imaging at baseline revealed no hypoxia. All patients in the intervention arm then underwent a planned neck dissection with a high rate of complete pathological response found despite the de-escalated treatment (Riaz et al. 2021). This has led to subsequent clinical phase 2 studies of this de-escalated regimen (section 1.4) (Lee et al. 2024*a*,). The importance of hypoxia status as well as HPV status should therefore not be dismissed when stratifying patients into prognostic categories especially when such groupings are used to guide therapy.

1.2.2 Epstein-Barr Virus

Another virus that has an aetiological role in the development of carcinomas of the head and neck region is Epstein-Barr virus (EBV). EBV is a double-stranded DNA herpes virus (human herpes virus 4 (HHV-4)) with a global prevalence in adults of greater than 90%. Its most common clinical manifestation is infectious mononucleosis (also known as Glandular fever) that commonly affects teenagers and young adults (NICE 2024), however latent EBV infection is known to be

linked with a number of epithelial and lymphoid malignancies including EBV-associated subtypes of gastric cancer and rarely breast, thyroid, salivary gland and hepatobiliary cancers as well as Burkitt lymphoma and Hodgkin lymphoma. The most common EBV associated epithelial cancer is however nasopharyngeal carcinoma, a head and neck malignancy (Han et al. 2021).

Nasopharyngeal carcinomas arise from the epithelial lining of the nasopharynx and are histologically classified by the World Health Organisation into 3 subtypes; keratinizing squamous cell carcinoma, non-keratinizing carcinoma and basaloid squamous cell carcinoma with EBV infection being strongly associated with the undifferentiated subtype of non-keratinizing carcinomas, which have a better prognosis than other nasopharyngeal carcinoma subtypes (Badoual 2022). There is significant geographical variation in nasopharyngeal carcinoma diagnosis with East and Southeast Asia having the highest prevalence of the disease with over 70% of global incidence of nasopharynx cancer occurring in this region. This, combined with the fact that lifelong persistent EBV infection is known to occur in over 90% of the world's population (Su et al. 2023) suggests a multifactorial role for the pathogenesis of the disease with higher rates of smoking, consumption of preserved foods with high levels of salt and underlying genetic predisposition also being implicated as risk factors in addition to EBV infection (Wei & Sham 2005, Chua et al. 2016).

Studies have demonstrated a clear clonal origin for EBV infections in nasopharynx caner with epidemiological research indicating early childhood EBV infections also being significant for nasopharynx carcinogenesis (Poh et al. 2016) implying that EBV is involved in the early initiation of nasopharynx cancer (Su et al. 2023). Following the initial EBV infection, a life-long latent infection occurs in memory B cells. The principle genes expressed in this latency are the viral protein-encoding genes EBNA1, LMP1 and LMP2 in addition to two non-coding RNAs and some micro RNAs (Nakanishi et al. 2017, Kraus et al. 2017). These proteins have a wide range of effects on the host cells including inducing genetic instability through suppressing NER via the PI3K pathway as well as dysregulation of cell cycle checkpoints and causing epigenetic changes including DNA hypermethylation and histone modifications. In addition LMP1 and the expressed RNAs can trigger inflammatory responses with EBNA1 additionally

altering the balance of the tumour immune micro-environment in favour of immunosuppressive cells helping the developing cancer to evade the host immune system. EBNA1 can also increase the expression of VEGF thus promoting tumour angiogenesis (Nakanishi et al. 2017, Su et al. 2023).

It has also been proposed that the development of hypoxic regions within developing nasopharyngeal carcinomas may actually drive lytic EBV infections in these areas via HIF-1α mediated activation of the EBV viral gene BZLF1. Such lytic infections then lead to the secretion of a range of both host and viral factors that can drive the further growth of the nasopharynx tumour (Kraus et al. 2017).

The role of EBV infection in the development of nasopharynx cancer is therefore complex with the exact molecular mechanism still to be fully elucidated. Nevertheless the association of EBV with undifferentiated non-keratinizing nasopharynx carcinoma is so marked that measurements of plasma EBV DNA levels post radiotherapy may be sensitive enough to identify those patients with an increased risk of both local and distant disease recurrence. Such levels may also correlate to overall survival duration. There are therefore on-going trials evaluating whether post-treatment plasma EBV DNA levels may guide the use of additional (adjuvant) chemotherapy treatment post completion of curative intent radiotherapy in order to increase cure rates (Kim et al. 2017, Chan et al. 2018).

1.2.3 Therapeutic approaches

Treatment options for head and neck cancers include both surgical and non-surgical options with the choice of therapeutic approach being dictated by factors including the tumour site, staging, baseline functional status of involved organs, patient co-morbidities and patient choice. The ultimate aim of treatment is to render patients cancer free with good quality of life and preservation of organ function. However despite significant advances in treatment approaches, 5 year survival rates still range from only 25% to 61% depending upon tumour subsite (Machiels et al. 2020). Investigating ways to improve these rates, through targeting issues such as hypoxia mediated treatment resistance are therefore crucial.

Surgically, HNSCC operations can range from localised laser therapy for early stage glottic cancers through to extensive resections including total laryngo-pharyngectomy and bilateral neck dissection. Depending upon the final surgical pathology results, patients may be recommended to receive adjuvant radiotherapy or adjuvant concurrent chemo-radiotherapy (CRT) (Bernier et al. 2004, Hanna et al. 2008). For locally advanced tumours with poor pathological prognostic markers, such as incomplete surgical excision or the presence of extracapsular nodal extension, it is possible for patients to end up receiving triple modality therapy with surgery, radiotherapy and chemotherapy as well as potentially completely losing the function of the affected organ. Such aggressive treatments have substantial short and long term physical, mental and psychological toxicity all of which have a substantial effect on patients' quality of life.

High dose radiotherapy or high dose CRT are treatment options for certain HNSCC tumours that offer the potential for preservation of organ function with at least comparable rates of cure to surgical treatments (Machiels et al. 2020). Standard radiotherapy treatments for HNSCC are delivered daily for a period of between 6 and 7 weeks to an equivalent dose in 2Gy/fraction of 70Gy to the primary tumour and any cervical lymph nodes or cervical lymph node regions either known to contain or with strong clinical suspicion of containing macroscopic deposits of SCC. Cervical nodal drainage basins without macroscopic tumour deposits but that have a 10-15% chance of containing occult metastatic disease based upon extensive surgical series are also routinely treated with lower doses of radiotherapy (equivalent to 50Gy in 2Gy/fraction) in order to eliminate microscopic disease. The choice of treated nodal regions is dependent upon the location and stage of the primary tumour and the presence and extent of metastatic lymph node involvement (Biau et al. 2019).

The majority of HNSCC radiotherapy treatments are delivered using external beam radiotherapy with high energy photon based treatment. Intensity modulated radiotherapy techniques are preferred to older three-dimensional (3D) conformal therapies due to their ability to reduce dose to healthy organs in the head and neck region thus reducing treatment related toxicity (Nutting et al. 2011). There is also increasing interest in the use of proton radiotherapy in HNSCC in order to spare late toxicity however access to proton facilities is highly variable

globally, with the National Health Service (NHS) in the UK only having routine access to two such facilities in 2024. In order to ensure successful treatment of HNSCC, radiation doses must be planned to be delivered to volumes greater in size than the observable gross primary tumour in order to account for microscopic disease spread, tumour movement and errors in daily patient setup (Grégoire et al. 2018). This makes the delivery of radiotherapy to HNSCC a highly complex and technical feat.

Chemotherapy is frequently used alongside radiotherapy. It may be delivered prior to radiotherapy in the form of doublet (cisplatin and 5-fluorouracil) or triplet (cisplatin, 5-fluorouracil and docetaxel) combination neoadjuvant treatment (Vermorken et al. 2007). However as this approach has not been proven in meta-analyses to have an overall survival benefit it is most commonly reserved for cases of rapidly progressive disease that require urgent treatment response. More frequently, single agent chemotherapy most commonly in the form of cisplatin is used in combination with radiotherapy to act as a radiosensitiser and increase the efficacy of the radiation treatment albeit with the cost of increased treatment related toxicity (Blanchard et al. 2011). Cisplatin is a widely used, intravenously administered chemotherapy drug that exerts its cytotoxic effect principally through the formation of crosslinks in DNA. Such damage may be repaired by the cell by for example NER however if this is not possible then cell cycle arrest occurs, leading ultimately to cell death (Martens-de Kemp et al. 2013). In the case of the use of cisplatin as a radiosensitiser, the synergistic relationship requires cells to have a functioning DNA dependent kinase (DNA-PK) dependent NHEJ repair mechanism. This repair pathway normally fixes DNA double-strand breaks but in situations where such repair is not possible, it activates the regulatory protein p53 leading to cell apoptosis. A functioning DNA-PK dependent NHEJ pathway is required for the synergistic effect of cisplatin and ionising radiation to be realised (Boeckman et al. 2005).

In cases where cisplatin is contraindicated, the epidermal growth factor receptor (EGFR) inhibitor cetuximab may be substituted (Bonner et al. 2006). It is known that EGFR expression can modulate tumour cells response to radiotherapy via the RAS-RAF-MEK-ERK pathway which promotes HR DSB repair thus reducing the chance of irradiated cells undergoing apoptosis (Baumann et al.

2007). Cetuximab can thus function as a radiosensitiser. Trials have repeatedly shown though that cetuximab is less potent a radiosensitiser than cisplatin in HNSCC (Mehanna et al. 2019, Gillison et al. 2019, Gebre-Medhin et al. 2021).

Overall, the treatment of HNSCC with CRT is a highly toxic treatment with patients often requiring temporary gastrostomy or nasal feeding tube to support their nutrition. High doses of opiate analgesia alongside a plethora of supportive medications are usually required. In addition, patients need a substantial level of physical and emotional support to tolerate the treatment and a complex medical multidisciplinary team (MDT) consisting of physicians, radiographers, dieticians, speech and language therapists and psychologists is required. Despite these barriers, most patients do manage to complete their treatments however, with the possible exception of HPV associated oropharyngeal cancers, overall survival rates remain poor with significant rates of metastatic disease and local relapse post radiotherapy treatment, in part due to tumour hypoxia driven radioresistance.

1.3 Modification of Hypoxic Radioresistance in Head and Neck Cancers

The potential for hypoxia modification to affect radiotherapy treatment outcomes has been the source of numerous clinical trials in a range of tumours. In a seminal review article published over two decades ago, Overgaard & Horsman (1996) found over 10,000 patients had been enrolled in such trials but only hypoxic modification in head and neck cancers had a significant improvement in post radiotherapy locoregional control (odds ratio 1.31, 95% confidence interval (CI) 1.19 to 1.43).

A further 2011 meta-analysis, specific to HNSCC confirmed the benefit of hypoxia modification for patient outcomes from radiotherapy. Although most of the 32 trials included did not show statistically significant outcomes individually, the authors note that many of these trials were small in size (median number of patients per trial being only 73) and therefore were individually underpowered. The authors grouped the hypoxic modification used into 3 subgroups;

normobaric oxygen, hyperbaric oxygen and hypoxic sensitiser but found that local-regional control rates remained statistically significantly better regardless of method (Overgaard 2011). Despite this result, hypoxia modification of radiotherapy for head and neck cancer has yet to become standard practice in the UK or most of the world.

In a review article on hypoxia in clinical trials, Tharmalingham & Hoskin (2019) suggest that hypoxia modification strategies fall into 4 broad categories:

1. Increased oxygen delivery by the blood
2. Radiosensitising oxygen mimetics
3. Destruction of hypoxic cells
4. Reducing tumour cell oxygen consumption

Attempts at improving the delivery of oxygen to head and neck tumours has been tried using blood transfusions (Hoff et al. 2011) and human recombinant erythropoiesis stimulating drugs (Overgaard et al. 2018). Unfortunately these trials did not show any benefit or resulted in worse patient outcomes. A more successful hypoxia modification approach for the treatment of laryngeal cancer has been the use of accelerated radiotherapy with carbogen and nicotinamide (ARCON) where carbogen is a gaseous mixture of 95% oxygen and 5% carbon dioxide and nicotinamide is an orally deliverable water-soluble form of vitamin B3. The rationale is that carbogen increases arterial oxygen concentration thereby decreasing diffusion limited hypoxia whereas the vasoactive agent nicotinamide decreases perfusion limited hypoxia. Although there was no improvement in local tumour control, regional control was improved in the intervention arm (5 year control rates of 93% versus 86%, p=0.04). Interestingly, a translational aspect of this study revealed a greater impact on outcomes of the ARCON regimen in tumours with greater hypoxic burden as assessed via the exogenous hypoxia marker pimonidazole and provides insight into the need for accurate patient selection for hypoxia modification therapies (Janssens et al. 2012).

The use of bioreductive drugs that become activated in regions of low oxygen tension, to target hypoxic radioresistant regions is illustrated by the results of

the phase 3 HeadSTART trial. This was a randomised control trial investigating the addition of the antitumour drug tirapazamine to patients having radical head and neck chemoradiotherapy. Despite promising early phase trials, the results of this study showed no benefit from the addition of tirapazamine. This trial did not attempt to stratify participants based on tumour hypoxia though and the authors acknowledge the potentially very significant limitation of not doing this (Rischin et al. 2010*a*).

The most widely researched hypoxia modification approach is that of oxygen mimetics, mainly in the form of nitroimidazoles such as misonidazole and the 5-nitromidazole, nimorazole (Wardman 2007, Janssens et al. 2012). These drugs are so called 'electron-affinic' meaning that they increase the radiation sensitivity of hypoxic cells through stabilising free radicals produced by the incident radiation. The DAHANCA-5 trial was the first randomised controlled trial to find that the addition of the hypoxic cell sensitiser nimorazole to standard radiotherapy for supraglottic and pharyngeal tumours improved locoregional control and disease specific survival (Overgaard et al. 1998). Consequently, the Danish national guidelines recommend the routine use of nimorazole (DAHANCA 2020*b*). However, this approach has not been widely adopted outside of Denmark. This may be in part due to the original trial not finding a statistically significant increase in overall survival (Overgaard et al. 1998) and that radiotherapy techniques have made significant improvements in recent years casting doubt on the relevance of this trial for modern day treatments (Thomson et al. 2014). In addition, predecessor drugs of nimorazole caused significant levels of peripheral neuropathy in patients (Saunders et al. 1978, Overgaard et al. 1989) and so although the side effect burden of nimorazole is considered manageable (the most common side effect being nausea and vomiting (Metwally et al. 2014)), without strong evidence of significant clinical benefit with modern day treatment approaches, clinicians have been wary in adopting nimorazole into routine clinical practice (Overgaard 2007, Ang 2010). Nevertheless, there remain on-going clinical trials evaluating the clinical role of nimorazole in the management of HNSCC.

The combined European Organisation for Research and Treatment of Cancer (EORTC) and Danish Head and Neck Cancer Group (DAHANCA) trial (EORTC-1219 / DAHANCA-29) randomised patients with locally advanced HPV

negative HNSCC between accelerated chemoradiotherapy plus/minus nimorazole with the application of a 15-gene hypoxic signature to stratify patients with greater levels of tumour hypoxia (EORTC 2022). Preliminary results of the trial presented at the European Society for Radiotherapy and Oncology (ESTRO) conference in 2021 revealed that recruitment to the trial was closed prematurely due to an interim safety review showing no benefit from the addition of the hypoxia radiosensitiser, although the reduced power of the study trial precludes firm conclusions on the utility of nimorazole (Grégoire et al. 2021). Of note, the radiotherapy treatment planning for all participants of this trial was subject to strict quality control between the study groups in order to minimise the risk of confounding of results based upon radiotherapy treatment quality; a critique that has been levelled at radiotherapy trials in the past (Christiaens et al. 2017, Tol et al. 2019).

Similarly, the UK based NIMRAD study which looked at the addition of nimorazole to radiotherapy for older patients ineligible for concurrent chemoradiotherapy failed to show a benefit from the addition of the hypoxic radiosensitiser (Thomson et al. 2023). This study was initially designed to achieve a power of 90% at the 5% significance level for a hazard ratio benefit of 0.65 but struggled with recruitment meaning a revised recruitment target was devised with a consequential reduction in the power of the study to 80% for an upwardly revised hazard ratio of 0.5. The study did not demonstrate any statistically significant difference in locoregional recurrence or overall survival with the addition of nimorazole within the limitations of the revised study power. The NIMRAD study also used a 26-gene hypoxia classifier to identify more hypoxic tumours although hypoxic tumours were defined as those with a score greater than the median hypoxic signature score of the first 50 participants. The lack of a reference external to the study meant that by definition, approximately 50% of the tumours in whom the signature was obtained were classified as hypoxic (Thomson et al. 2023). In addition, the hypoxic signature was not prognostic for either the overall or HPV-negative cohort which raises questions over the utility of this stratification approach despite the fact that the authors state this gene signature has been previously validated (Eustace et al. 2013). The NIMRAD trial team are also

working with the DAHANCA group to use their alternative 15-gene hypoxic signature on the NIMRAD data; the results of this analysis are awaited (Thomson et al. 2023). The DAHANCA-30 trial is an on-going additional nimorazole trial with a non-inferiority design to assess the hypothesis that nimorazole offers no benefit to less hypoxic tumours as assessed with the 15-gene hypoxic signature (DAHANCA 2021).

An additional approach to overcoming hypoxia induced radioresistance is to modify the oxygen enhancement ratio (Overgaard 2007). It could be considered that proton therapy falls into this category. The TORPEdO trial is currently investigating the benefit of proton therapy over photon therapy in HNSCC (Price et al. 2020) as is a similar Danish study (DAHANCA 2020*a*). Although the influence of hypoxia on treatment outcomes is not a facet of this trial, studies have found that the oxygen enhancement ratio of proton beams are lower than photons implying that proton therapy may offer a radiobiological advantage against hypoxic tumour cells (Iwata et al. 2014). An alternative but less widely available option is the use of carbon ion radiotherapy, which has been shown to have OER close to 1 (Wozny et al. 2020).

Pre-clinical evidence has also suggested that the emerging radiotherapy technique known as FLASH may also overcome hypoxia mediated radioresistance. FLASH radiotherapy refers to the delivery of radiation at significantly greater dose rates (approximately 40 Gy/s compared to 0.5 to 5 Gy/min for conventional radiotherapy) which can increase the radiobiological therapeutic ratio by increasing the radiation tolerance of normal tissues (Matuszak et al. 2022). A pre-clinical study using HNSCC, lung adenocarcinoma and glioblastoma xenografts has found that FLASH was superior to conventional radiotherapy in tumours treated under acute severe hypoxia. The authors present transcriptomic evidence suggesting that this improvement in tumour control was due to inhibition of cell cycle progression, in particular from increased expression of the p53 effector growth arrest and DNA-damage-inducible protein 45 (GADD45) (Leavitt et al. 2024). However current clinical use of FLASH is extremely limited principally due to the radiation dose being delivered using standard energy electrons thereby restricting its use to superficial tumours only (Bourhis et al. 2019, Matuszak et al. 2022). FLASH

therefore remains a theoretical clinical utility for overcoming hypoxia mediated radioresistance.

1.4 Modifying Radiotherapy Treatment Plans to Overcome Hypoxia

Instead of modifying the underlying hypoxic radiation resistance, an alternative approach to managing hypoxia is to boost the radiation dose delivered to the tumour or hypoxic subvolumes (Horsman et al. 2012) with the later approach requiring hypoxic regions to be accurately identified and mapped.

Dose escalation strategies have been previously attempted in HNSCC outside of the consideration of hypoxia, largely driven by poor overall survival rates in patients with higher risk factors, including non-HPV related tumours, those with a heavy smoking history and locally advanced disease stage (Ang et al. 2010). Although these studies have shown that it is feasible to perform dose escalation in HNSCC, the studies tend to be small in size and have shown mixed results regarding locoregional control rates and overall survival (Atwell et al. 2020) hence such treatment strategies have yet to be routinely adopted in clinical practice. The phase 3 ART DECO trial for example randomised patients between standard chemoradiotherapy and a dose escalated and hypofractionated regimen in the treatment of larynx and hypopharynx tumours. Although this was designed as an adequately powered, prospective study it was closed early due to a pre-planned interim futility analysis showing no evidence of a benefit in the intervention arm. Although the dose-escalated arm had worse rates of lower grade pharyngeal mucositis (grade 2), there was no difference in rates of severe (grade ≥ 3) side effects between the arms implying that dose escalations could be safely delivered (Nutting et al. 2021).

Targeted dose escalation studies have therefore been performed looking at restricting escalated doses to tumours or regions of tumours with greater levels of tumour hypoxia. Theoretical dose escalation planning studies have shown the feasibility of using hypoxic PET imaging to guide radiotherapy dose escalations to hypoxic subvolumes whilst maintaining acceptable doses to normal tissues (Grosu

et al. 2007, Lee et al. 2008, Thorwarth & Alber 2010, Hendrickson et al. 2011, Chang et al. 2013, Servagi-Vernat et al. 2015). Clinically, this approach of dose escalating hypoxic PET derived tumour hypoxic subvolumes was investigated in a randomised phase 2 clinical trial evaluating dose escalation to 77Gy to such regions of HNSCC based on pre-radiotherapy treatment imaging. Unfortunately the trial closed early due to slow accrual rates however it found that not only did the presence of pretreatment hypoxia on imaging have a clear, statistically significant prognostic impact on local control rates at 5 years but dose escalation in the hypoxic group also improved local control rates. The dose escalated group had an 84% 5 year local control rate compared to 65% in the control arm albeit not statistically significant (p=0.150) potentially due to the premature closure of the study (Welz et al. 2022).

Nevertheless, there is on-going interest in this area with currently active trials including the DAHANCA-33 trial looking at dose escalated radiotherapy in HPV negative locally advanced HNSCC with pre-treatment hypoxic PET imaging evidence of hypoxia (Saksø et al. 2020) and the German ESCALOX trial where a translational part of this dose escalation study will correlate clinical treatment outcomes to pre-treatment hypoxic PET based tumour hypoxia assessments (Pigorsch et al. 2017).

An alternative approach to radiotherapy treatment dose modification based upon imaged levels of tumour hypoxia has been demonstrated in phase 2 clinical studies in HPV related oropharyngeal HNSCC. As previously discussed, HPV related oropharyngeal tumours are known to have a significantly better prognosis than HPV unrelated cancers although treatment de-intensification trials in this patient group have been unsuccessful so far (section 1.2.1). Lee et al. (2024*a*) postulated that this may be in part due to inappropriate stratification of patients into lower risk groups and therefore this group have looked at only de-escalating therapy in those patients whose tumours do not show baseline tumour hypoxia or in those tumours where hypoxia resolves within the first 1-2 weeks of treatment based on hypoxic PET imaging. This trial treated all primary tumours with upfront surgery and then treated neck nodal disease with chemoradiotherapy. They found that despite heavily dose de-escalating the intervention arm dose to involved lymph node to only 30Gy from the standard dose of 70Gy, the 2

year locoregional control was not compromised (Lee et al. 2024*a*). Crucially, the team have expanded this work in a further phase 2 trial to de-escalate radiation dose to 30Gy to non-hypoxic primary tumours and in an abstract presented at the 2024 American society of clinical oncology (ASCO) meeting, confirm that survival was still preserved in the intervention arm (Lee et al. 2024*b*). This exciting development may help to reduce late toxicity without compromising cure rates and represents a novel application of hypoxia guided therapy, however confirmation of these findings from a phase 3 trial are required.

It is clear to see that one of the likely flaws in older hypoxic modifier trials relates to inadequate stratification of tumours by hypoxic burden consequentially potentially masking or at least reducing the significance of hypoxia modification approaches. Routinely available, widely utilised, quality assured and accurate methods of discriminating HNSCC tumours with greater and lesser hypoxic burden are critical if hypoxia modification strategies are to be widely adopted into routine clinical practice (Horsman et al. 2012, Dewhirst & Birer 2016, Hughes et al. 2019, Busk et al. 2020).

1.5 Determining Tumour Hypoxia

In a review article on the issue of measuring hypoxia in tumours, Overgaard (2007) stated there are 3 principal methods of performing this:

1. Direct measurement of the amount of oxygen
2. Measurement of the ability of hypoxic regions to chemically reduce specific compounds
3. Detection of hypoxia induced gene activation of molecular activity

1.5.1 Direct O_2 measurement

The first studies to measure oxygen levels in head and neck cancers were performed using the Eppendorf electrode. This system directly measures oxygen concentrations through the use of polarographic oxygen electrodes (Busk et al.

2020). Early studies used this method to prove the association between low levels of oxygen in tumours and worse treatment outcomes (Nordsmark et al. 1996, Brizel et al. 1997, 1999, Nordsmark & Overgaard 2000, Rudat et al. 2000, 2001, Dunst et al. 2003, Nordsmark et al. 2005). Although the results from these trials are very compelling, the technique has a number of limitations meaning it has not been adopted into clinical use. The technique is invasive, requiring the insertion of electrodes into the areas of interest. In the case of head and neck cancers, not all tumours are accessible enough to allow this to happen and patient tolerance of such an invasive procedure is likely to be limited especially with respect to repeat assessments. The system also measures interstitial oxygen tension rather than intracellular concentrations and is unable to differentiate between hypoxia and areas of necrosis. In addition, it has its lowest sensitivity in regions of lowest oxygen concentration due to the low amplitude currents associated with hypoxic tissue regions. It is also difficult to produce 3D maps of hypoxic regions using this technique and due to electrochemical reduction, the probe consumes small amounts of oxygen thus altering the molecular environment through performing measurements (Griffiths & Robinson 1999, Busk et al. 2020). An alternative to the Eppendorf probe is a fibre-optic oxygen sensor called OxyLite. Whilst still an invasive measuring device this does overcome some of the limitations of the Eppendorf probe including have a high sensitivity in the 0-15 mmHg oxygen tension level that is of particular interest in tumour hypoxia studies (Griffiths & Robinson 1999). Other, as yet less utilised approaches to directly measuring oxygen concentrations include electron paramagnetic resonance spectroscopy (Schaner et al. 2020) and phosphorescence imaging (Palmer et al. 2010).

1.5.2 Bioreductive compounds

One of the most widely used hypoxia markers are the 2-nitroimidazole compounds and their derivatives which were originally developed as hypoxic cell radiosensitisers. The nitro group present on these compounds can undergo a six-electron intracellular reduction to an amino group (NH_2) but at oxygen partial pressures below approximately 10 mmHg, one of the intermediary products produced is a highly reactive substance that readily forms covalent bonds with intracellular

components in particular with thiol groups in proteins, peptides and amino acids. Regions of intracellular tumour hypoxia can therefore be determined from the distribution of in-vivo administered 2-nitroimidazole compounds either histologically or via labelling the compound with an imaging tracer (section 1.5.4) (Gross et al. 1995, Kizaka-Kondoh & Konse-Nagasawa 2009, Horsman et al. 2012). Pimonidazole is one such 2-nitroimidazole derivative that is available in an intravenous (IV) injectable form. Following IV administration pimonidazole will preferentially accumulates in areas of reduced oxygen tension. If the tumour is then surgical excised or biopsied, usually at least 16-24 hours after pimonidazole administration then the distribution of the pimonidazole and thus tumour hypoxic regions can be determined from immunohistochemistry (IHC) using monoclonal antibodies for pimonidazole (for example, the commercially available Hypoxyprobe (Hypoxyprobe 2024)). This technique has been extensively validated against alternative tumour oxygen measurement techniques (Raleigh et al. 1999, Ljungkvist et al. 2000, Bussink et al. 2000).

Although the extent of tumour hypoxia can be assessed through the whole tumour, this histological approach requires surgical resection of the tumour and thus is of limited clinical use when knowledge about tumour oxygen distributions may be required prior to initiation of therapy and in circumstances where tumours are either unresectable or it is clinically preferred to follow a non-surgical therapeutic approach. Although pimonidazole staining can be performed on tumour biopsies, such results will be confounded by sampling error and thus may have limited clinical utility. In addition, pimonidazole assessments are limited by the requirement for adequate perfusion of the tissue of interest and the fact that the outcome is a binary metric that does not quantify the level of tissue oxygenation. Nevertheless pimonidazole staining has been widely utilised in pre-clinical and clinical studies often as a reference hypoxia indicator for comparison with hypoxia imaging techniques.

1.5.3 Hypoxia induced gene and protein expression

An alternative approach to the measurement of oxygen concentrations is the measurement of the upregulation of genes and proteins in tumours in response to

hypoxia. As previously discussed, the cellular response to hypoxia includes the upregulation of the expression of a number of cellular proteins. IHC techniques to assess the levels of these proteins can therefore serve as a surrogate marker for cellular hypoxia. Such measurements have found levels of tumour hypoxia correlating with IHC expression of CAIX, HIF-1α and p53 (Nordsmark et al. 2007, Sato et al. 2013, Norikane et al. 2014, Nicolay et al. 2020, Rühle et al. 2021*b*).

IHC determined levels of HIF-1α in tumour biopsy samples have been correlated to treatment outcomes in a range of tumours including cervical, lung, breast and HNSCC (Semenza 2003). In oropharyngeal head and neck cancers, Aebersold et al. (2001) found that the degree of HIF-1α immunoreactivity was an independent predictor that inversely correlated with response to radiotherapy in both primary tumours and metastatic lymph nodes. However the use of HIF expression as a marker for hypoxia needs some notes of caution; although hypoxia leads to decreased degradation of HIF-1α, growth factors, cytokines and other signalling molecules can act independently of oxygen levels to increase HIFα synthesis (Semenza 2003). For example mutations in VHL and phosphatase and tensin homolog (PTEN) can act as loss of function mutations (tumour-suppressor genes) and mutations in the gene that encodes for the protein human epidermal growth factor receptor 2 (HER2) as gain of function mutations (oncogene) to increase expression of HIF-1α independent of oxygen concentration (Semenza 2003, Hanahan & Weinberg 2011).

In addition to IHC measurements on tumour biopsies, serum or plasma levels of proteins associated with hypoxia have been investigated as surrogate markers of tumour hypoxia (Sørensen & Horsman 2020). One such protein that has been investigated is osteopontin (OPN) a multifunctional protein that has high levels of expression in chronic inflammatory conditions and autoimmune diseases. It has also been linked to tumour hypoxia with high levels correlating to increase tumour hypoxia and worse prognosis in HNSCC (Overgaard et al. 2005, Petrik et al. 2006). However, there are concerns with inconsistent measured levels of OPN and inconsistent correlations across trials meaning it has yet to garner clinical use (Sørensen & Horsman 2020).

More recently, interest has focussed on the use of hypoxic gene signatures to differentiate tumours with lower and higher hypoxic burdens. Initially, expression of single genes was investigated, but maybe rather unsurprisingly these studies were broadly unsuccessful due to the complex interplay of factors in addition to hypoxia that affect levels of gene expression (Sørensen et al. 2007). As such multi-gene hypoxic signatures have been developed. These are typically built upon a backbone of genes involved in glucose and extracellular matrix metabolism, and apoptosis (Thiruthaneeswaran et al. 2021) in addition to well-recognised hypoxia inducible genes such as CAIX, VEGF and GLUT-1. These backbones are then augmented by additional candidate genes either identified from *in vitro* experiments or clinical gene expression data (Sørensen & Horsman 2020). Correlation of gene expression data derived from tumour biopsy samples to clinical tumour oxygen tension measurements then allows refinement of the gene predictor which is then tested on a clinical validation cohort of patients (Yang & West 2019). In HNSCC, four such hypoxic gene signatures of varying complexity have been developed and tested for prognostic or predictive utility; a 99-gene signature for recurrence free survival (Winter et al. 2007), a 51-gene prognostic signature (Buffa et al. 2010) and a 26-gene modification of this signature for laryngeal cancer (Betts et al. 2013, Eustace et al. 2013), and a 15-gene signature for prediction of response to the radiosensitiser nimorazole (Toustrup et al. 2011, 2012, Deschuymer et al. 2020). The recent large scale NIMRAD (Thomson et al. 2023) and DAHANCA-30 (DAHANCA 2021) clinical trials have used these 15 and 26 gene assays respectively to attempt to stratify tumours as more or less hypoxic (section 1.3).

Gene and protein expression techniques rely on surrogate markers of hypoxia and therefore require well powered, accurate validation studies to negate the possibility of artifactual associations. The majority of tumour hypoxic gene signatures are also disease specific which limits the generalisability of this hypoxia assessment technique. Gene and protein expression techniques are also both invasive approaches, requiring adequate samples of tumour tissue. Although this may be possible to perform on routinely obtained clinical biopsies, it does limit their role in repeated assessment of tumour hypoxia especially if re-assessment

during radiotherapy treatment is required as any changes in the tumour or surrounding tissues' anatomical relations needs to be avoided during treatment to maintain the integrity of the radiotherapy process. In addition, any technique that requires a tissue sample will be inherently sensitive to sampling errors. It is known that tumour hypoxia is heterogeneous and so sampling of one area of the tumour may lead to an under appreciation or overstatement of the true level of tumour oxygenation. Techniques that can offer a map of tumour hypoxia and facilitate re-assessment during therapy to allow for temporal mapping of hypoxia would offer potential solutions to these issues. This leads us to hypoxia imaging.

1.5.4 Hypoxia Imaging

The most widely studied hypoxic imaging techniques are positron emission tomography based (Horsman et al. 2012). PET works on the principle of matter-antimatter annihilation; a radioisotope that decays via positron emission is injected into a patient bound to an appropriate pharmaceutical whose properties determine the distribution of the positron emitter in the body. Emitted positrons interact with surrounding electrons within a couple of millimetres via an annihilation reaction producing two 511keV energy photons that travel in opposite directions. Scintillation crystals connected to photomultiplier tubes detect these photons and if two photons are detected within a few nanoseconds of each other it is assumed that they originated from the same point which will lie along a line joining the points of detection. By detecting large numbers of these so-called events and correcting for attenuation in the photon paths, maps of the distribution of the tracer can be obtained (Vaquero & Kinahan 2015). The power of PET is that the contrast is governed by the relative abundance of tracer accumulation, which depends upon the pharmacokinetic properties of the tracer used and thus can provide functional information pertaining to the underlying tissue. The most commonly used positron emitter in clinical imaging is ^{18}F, a radioactive isotope of fluorine that decays 96.73% of the time by positron emission, with a physical half-life of 109.77 mins (S. Y. F. Chu & Firestone 1998).

The most commonly used PET imaging in oncology is ^{18}F-fluoro-2-deoxy-D-glucose-PET (FDG-PET). This positron emitting glucose analogue detects cancer

cells via their energy dependency on glycolysis and their consequential abnormal utilisation of glucose (Warburg effect). One such driver of tumour glycolysis is the upregulation of glucose transporters and glycolytic enzymes through activation of HIF. Clearly, HIF activation is related to tumour hypoxia however it can also be activated via other non-hypoxic means including genetic mutations and stimulation from growth factors (Dierckx & Van de Wiele 2008). Consequently, although FDG-PET uptake may indirectly reflect tumour hypoxia the interaction is complex and unreliable (Dierckx & Van de Wiele 2008, Gouel et al. 2023).

In hypoxic PET imaging, the ^{18}F positron emitter is attached to 2-nitroimidazole derived bioreductive drugs that preferentially accumulate in hypoxic regions of the body (section 1.5.2). Fluorinated-misonidazole (FMISO) was the first and therefore the most widely studied 2-nitroimidazole based PET tracer, however it has a number of clinical limitations principally due to the relatively slow clearance of unbound tracer from normoxic cells which limits the achievable contrast to noise ratio and prolongs the time required between tracer injection and imaging. Newer, less lipophilic tracers such as the second generation tracer fluoroazomycin arabinoside (FAZA) and the third generation agent flortanidazole (F-HX4) have a faster rate of unbound tracer clearance and therefore help to overcome these limitations (Chen et al. 2012, Busk et al. 2020). FMISO however remains the most frequently used hypoxic PET radiopharmaceutical globally. Table 1.1 compares different hypoxic PET tracers and alternative magnetic resonance based techniques for tumour hypoxia assessment.

The accuracy of hypoxia PET has been compared to histological specimen hypoxia staining in preclinical studies (Rasey et al. 1996, Horsman et al. 2012, Hughes et al. 2019). A significant number of trials have been published showing the utility of hypoxia PET imaging in head and neck cancer. The majority of these trials have looked at using pre-treatment hypoxia PET in a prognostic role by correlating measures of tumour hypoxic burden to outcomes from standard HNSCC therapy (Rajendran et al. 2006, Welz et al. 2017, Thorwarth et al. 2019, Sörensen et al. 2020, Zschaeck et al. 2020, Carles et al. 2021). These studies have confirmed the adverse prognosis of tumour hypoxia. Other studies have looked at assessing change in hypoxia during chemoradiotherapy (Zschaeck et al. 2015, Zegers et al. 2016, Löck et al. 2017). A 2019 systematic review of this topic

suggested that the optimal timing of such functional imaging to assess response to treatment is between 2 and 3 weeks into treatment (Martens et al. 2019). This suggests that it is the failure of hypoxia to resolve rather than the presence of hypoxic regions per se that is most important to treatment outcomes and is consistent with the radiobiological phenomenon of re-oxygenation. However, as previously discussed (section 1.1) hypoxic tumour regions may harbour quiescent tumour cells that can retain a radioresistant phenotype despite re-oxygenation. This suggests that there may be two different processes at play; one related to failure of tumour regions to re-oxygenate during treatment and the other relating to baseline hypoxia induced radioresistance.

Table 1.1: Comparison of hypoxic PET tracers and alternative MR methods of imaging or measuring tumour hypoxia. *ATSM* diacetyl-bis(N4-methylthiosemicarbazone), *EPR* Electron Paramagnetic Resonance, *FAZA* fluoroazomycin arabinoside, *FMISO* fluorinated-misonidazole, *MOBILE* Mapping of Oxygen By Imaging Lipids relaxation Enhancement, *MRS* Magnetic Resonance Spectroscopy.

Type	*Method*	*Mechanism*	*Advantages*	*Disadvantages*	*References*
PET	^{18}F-FMISO	Based on hypoxia selectivity of 2-nitroimidazole compounds (section 1.5.2). Administered in IV form.	• Most widely studied and available hypoxia PET tracer. • Correlation to alternative tumour hypoxia markers and treatment outcome predictions. .	• Relatively slow clearance from blood means long latency between injection and imaging. • Relatively long image acquisitions. • Ionising radiation dose which may limit repeat assessments.	Horsman et al. (2012), Gouel et al. (2023), Perez et al. (2023)
PET	^{18}F-FAZA	More hydrophilic 2-nitroimidazole compound than FMISO.	• Faster vascular clearance and improved image contrast between hypoxic and normoxic tissue compared to FMISO. .	• Less widely available and less studied than FMISO. • Ionising radiation dose which may limit repeat assessments.	Horsman et al. (2012), Gouel et al. (2023), Perez et al. (2023)
PET	^{64}Cu-ATSM	Tracer diffuses into cells due to high membrane permeability and is reduced under hypoxic conditions leading to increased intracellular concentrations in areas of low oxygen tension. Uses ^{64}Cu as positron source.	• Fast clearance from normal tissues. • Easier production than other hypoxic PET tracers.	• Mechanism of hypoxia selectivity is complex and not fully characterised. • Can accumulate in necrotic tissue. • Tracer not widely available. • ^{64}Cu decays via both positron emission and beta decay. • Ionising radiation dose which may limit repeat assessments.	Horsman et al. (2012), Gouel et al. (2023), Perez et al. (2023)
MR	Proton MRS	Proton spectroscopic assessment of lactate intensity as a surrogate marker for tumour hypoxia due to increased production in oxygen poor environments. Can also assess other metabolites, for example choline/creatine ratio as marker of cell turnover.	• Can be performed with standard clinical MR equipment. • Can assess range of metabolites (tumour metabolome). • Potential to perform spectroscopic imaging to map distribution of metabolites.	• Mixed outcomes from studies regarding correlation of lactate levels to tumour oxygenation in head and neck cancer. • Single-voxel approach limits spatial distribution assessments.	Star-Lack et al. (2000), Bezabeh et al. (2005), Le et al. (2008)
MR	^{19}F MR oximetry	R_1 relaxation rate of perfluorocarbons increases linearly with dissolved oxygen concentration. Administration of ^{19}F containing perfluorocarbons as IV emulsions or direct tumoural injection can measure tumour oxygen levels.	• Quantitative assessment of oxygen partial pressures. • Can be performed alongside standard proton MR imaging.	• Requires MR coil tuned to ^{19}F. • Direct tumoural injection of perfluorocarbons yields better SNR.	Baete et al. (2011), Hallac et al. (2014)

Table 1.1 continued.

MR	^{19}F MRS of fluorinated 2-nitroimidazoles	MR based alternative to PET to assess intracellular accumulation of fluorinated 2-nitroimidazoles in hypoxic conditions based on spectroscopic assessment of ^{19}F.	• High specificity for ^{19}F. • No use of ionising radiation. • Repeat assessments possible.	• Magnitude and rate of detection of ^{19}F is relatively low resulting in lower sensitivity compared to PET. • Requires MR coil tuned to ^{19}F.	Seddon et al. (2002), Lee et al. (2009)
MR	^{31}P MRS	Spectroscopic assessment of tumour energetics via high-energy phosphate metabolites such as nucleoside triphosphates and phosphocreatine whose production is dependent upon cellular glucose and oxygen availability. Can also assess cellular pH levels via chemical shift of inorganic phosphate.	• Provides quantification of tumour metabolism which is related to both cellular energy and oxygenation status. • Can be readily repeated to monitor changes with treatment.	• Lower relative sensitivity than proton MRS limiting spatial resolution and sensitivity in small tumours and those with lower metabolic activity. • Complex interpretation as phosphate metabolites influenced by multiple factors in addition to hypoxia. • Requires MR coil tuned to ^{31}P .	Tozer & Griffiths (1992), Abdel Razek & Poptani (2013), Lin & Chung (2014)
MR	MOBILE	Change in tumour lipid T_1 relaxation time with supplemental oxygen (section 3.4.4).	• Greater solubility of oxygen in lipid than water makes it more sensitive to changes in tumour oxygen levels than global T_1 change (OE-MRI).	• Sensitive to the lipid content of tumours and therefore may not be applicable to tumours with low lipid levels.	Colliez et al. (2017)
MR	EPR oximetry	Utilises spin-exchange interaction between the unpaired electrons of molecular oxygen and a paramagnetic EPR spin-probe to derive oxygen concentrations.	• Can derive actual partial pressure of oxygen levels. • Can perform repeat assessments. • Rapid measurements possible.	• Requires placement of oxygen-sensing paramagnetic probe which can be soluble probes, carbon particulates or crystalline materials (eg. OxyChip). • Requires EPR scanner. • Limited information on spatial distribution of oxygenation. • Limited to more superficial tumours.	Gallez et al. (2004), Swartz et al. (2014), Schaner et al. (2020)

1.5.4.1 Hypoxia MRI

An alternative imaging technique that can use functional information to generate contrast is magnetic resonance imaging (MRI). The physics underpinning MRI is reviewed in chapter 2. One of the strengths of clinical MRI is its potential ability to generate image contrast based upon underlying functional information rather than purely anatomical information. There are a range of acquisition techniques that provide differing functional information as well as differing spatial anatomical information. It is common for a single patient imaging session to consist of multiple different MR imaging techniques, known as multiparametric MRI (mpMRI) (McRobbie et al. 2017). The use of mpMRI has proven particularly useful in oncological imaging and is now generally considered the standard of care for prostate cancer diagnostic investigations for example (Stabile et al. 2020).

One of the most studied functional MRI approaches to the issue of hypoxia and a routine component of mpMRI is dynamic contrast enhanced MRI (DCE-MRI). It is routine clinical practice to use the rare earth metal gadolinium as a contrast agent in standard oncological MR imaging. Gadolinium is strongly paramagnetic and therefore reduces T_1 relaxation times. Following IV administration of gadolinium the contrast agent enters a tumour's microcirculation through feeding arteries before entering the tumour capillaries. However tumour angiogenesis tends to produce blood vessels that lack normal physiological control with the capillaries being particular 'leaky' (Bernstein et al. 2014). As such gadolinium tends to concentrate in tumours thereby producing a marked shortening of T_1 times and thus appearing with increased signal intensity on T_1 weighted imaging. DCE-MRI is a contrast agent based MRI technique most commonly with gadolinium that uses dynamic image acquisitions over the order of minutes to track the changing distribution of contrast in an area of interest. By fitting mathematical models to the distribution of contrast agent concentration with time, parameters can be derived that correlate with physiological factors including blood perfusion and vascular permeability that in turn govern tumour hypoxia. The most commonly used model in the clinical setting is that of the two compartment model of Tofts et al. (1999) where the parameters used include the contrast agent concentration as a factor of time (which also requires a model of the arterial input),

haematocrit (Hct), extravascular extracellular volume fraction (v_e), and a factor known as the transfer rate constant (K^{trans}) which reflects the rate at which gadolinium contrast moves from the blood plasma into the tissue extravascular extracellular space, the vascular permeability (Gaustad et al. 2020).

Pre-clinical models have shown correlations between DCE-MRI parameters, in particular K^{trans} with tumour hypoxic fractions, metastatic potential and tumour sensitivity to ionising radiation (Gaustad et al. 2020). There are also clinical studies in a range of tumour sites illustrating the utility of DCE-MRI in hypoxia imaging (Perez et al. 2023), including in nasopharynx head and neck cancer where DCE-MRI parameters have been correlated with IHC markers of hypoxia (HIF-α) and cell proliferation (Huang et al. 2021). However, DCE-MRI does not directly measure oxygen concentrations but instead provides parameters that describe oxygen delivery and consumption; namely blood perfusion and permeability (Perez et al. 2023). This therefore has implicit limitations for assessing tumour tissue hypoxia.

Other potential indirect MRI approaches to determining hypoxia include magnetic resonance spectroscopy (MRS) and diffusion weighted imaging (DWI). MRS uses the principles of magnetic resonance to produce spectra of the concentration of metabolites. Although not used to detect tissue oxygenation directly, it can detect metabolic products that are increased in hypoxic environments such as lactate as well as associated changes in tissue pH levels (Ratai et al. 2018). DWI uses the Brownian motion of water to determine tissue cellularity based upon the apparent degree of water diffusivity. Combining DWI and DCE-MRI derived parameters in mpMRI may yield more reliable surrogate markers for tumour hypoxia than DCE-MRI alone, as evidenced in HNSCC by Wiedenmann et al. (2020) who found that mpMRI parameters differed significantly between normoxic and hypoxic tumour regions. However neither imaging method directly measures oxygenation levels but instead rely on surrogate markers of tumour hypoxia relating to blood perfusion, permeability and cell density (Perez et al. 2023). As such, correlations between these parameters and tumour hypoxia need to be interpreted with caution and the risk of significant confounding be carefully considered.

An MRI technique that is more directly reliant on oxygen concentrations is blood oxygen level dependent MRI (BOLD) where contrast is generated in proportion to the level of oxygen saturation of haemoglobin. Oxyhaemoglobin has no unpaired electrons and therefore is weakly diamagnetic in contrast to deoxyhaemoglobin which has 4 unpaired electrons and is therefore strongly paramagnetic (McRobbie et al. 2017). Changes in the oxy to deoxyhaemoglobin ratio can thus alter the MRI parameter of T_2^* relaxation time (R_2^* relaxation rate) thus measuring local perturbations in T_2^* relaxation times can provide information about local blood oxygenation levels which can be used as a surrogate marker of tumour oxygenation.

Pre-clinical studies in non head and neck tumours have linked changes seen on BOLD with tumour oxygenation levels (Rickard et al. 2019). In head and neck cancers, this technique has been used to demonstrate cycling hypoxia in human tumours (Panek et al. 2017). Dynamic imaging of ten patients with HNSCC was performed to map temporal changes in R_2^* relaxation rates over 1 hour (with a temporal resolution of 30s). By performing voxel-wise power spectrum analysis, underlying periodicities of fluctuations were derived which the authors proposed are linked to impaired tumour vasculature and thus cycling hypoxia. There was however no correlation identified from the metrics in this study and levels of chronic hypoxia as determined by pimonidazole staining. The extended imaging time required in this study is worthy of note as this would significantly hamper any future routine clinical application. BOLD measurements are also limited in their tumour hypoxia assessment due to being susceptible to motion artefacts and the fact that the effect itself is modulated by intravascular oxygen concentration and not tissue oxygen levels, which is the parameter that is of ultimate interest when considering the effect of tumour hypoxia on cell metabolism and treatment response. In addition, BOLD measurements are heavily influenced by blood volume with interpretation of BOLD imaging in the context of tumour hypoxia being highly challenging without this parameter. Studies have shown markedly different R_2^* relaxation rates with changes in tumour blood volume (Taylor et al. 2001, Rodrigues et al. 2004, Min et al. 2016).

OE-MRI, also known as tissue oxygenation level dependent MRI (TOLD) is an alternative MRI technique for imaging hypoxia whereby image contrast

is generated in proportion to changes in T_1 relaxation times in direct response to *tissue* oxygen concentrations (figure 1.3). Due to the presence of unpaired

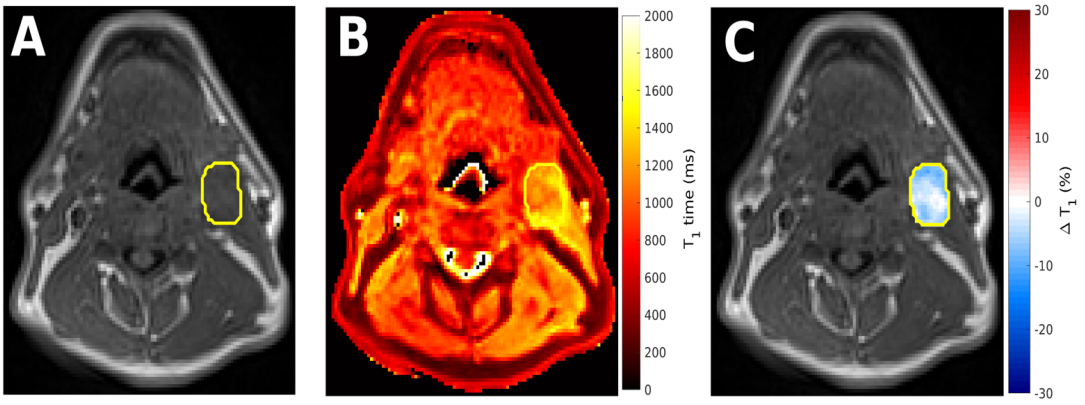

Figure 1.3: Illustrative example of different types of T_1 based MR imaging - Example images from a patient with head and neck squamous cell carcinoma illustrating the difference between conventional T_1 weighted imaging (**A**), corresponding quantitative map of T_1 relaxation times (**B**) and oxygen induced quantitative ΔT_1 map (**C**). Within the highlighted malignant nodal mass (yellow contour), regions of oxygen induced T_1 shortening (blue) implying normoxia are clearly seen. Distinct oxygen refractory regions (white/red) are also identifiable which imply either hypoxic or non-perfused areas.

electrons, molecular oxygen is weakly paramagnetic thus elevated concentrations of dissolved oxygen in blood plasma increase the longitudinal relaxation rate ($\mathrm{R}_1 = 1/T_1$) of tissues including tumours (Tadamura et al. 1997, Arnold et al. 2007). In well oxygenated tumour regions, haemoglobin is well saturated. If the patient were to breath high concentration oxygen this would result in increased dissolved molecular oxygen both in blood plasma and interstitial tissue fluid with a consequential reduction in T_1 times / increase in R_1 relaxation rates:

$$\Delta R_1 = R_{1(t)} - R_{1(0)} = \Delta[O_2].r_{1,O_2} + \Delta[Hb].r_{1.Hb}, \tag{1.2}$$

where $R_{1(0)}$ is the initial R_1 rate, $R_{1(t)}$ the R_1 rate at time t after commencing high concentration oxygen, $\Delta[O_2]$ and $\Delta[Hb]$ the change in concentration of dissolved oxygen and haemoglobin and r_{1,O_2} and $r_{1,Hb}$ the corresponding relaxivity constants. In reality the haemoglobin component is very small and therefore ΔR_1

can be considered to be proportional to the change in dissolved oxygen concentration (O'Connor et al. 2019). In regions of tumour hypoxia where haemoglobin is less well saturated, the administration of high concentration oxygen preferentially leads to an increase in oxy-haemoglobin concentration over dissolved molecular oxygen levels. Consequently T_1 times are relatively invariant but R_2^* rates may decrease due to the decrease in deoxyhaemoglobin concentration by virtue of the BOLD effect.

Thus by administering high concentration oxygen to patients and performing dynamic T_1 mapping, areas of hypoxia can be identified from a lack of change in T_1 times (figure 1.4). This theory has been validated in pre-clinical models and early clinical studies (Hallac et al. 2014, Linnik et al. 2014, Dewhirst & Birer 2016, O'Connor et al. 2016, Salem et al. 2019). A scoping review of the role of OE-MRI in the assessment of tumour hypoxia is presented in chapter 3.

MRI scans offer many potential advantages over PET scans. From a health economics perspective the cost of establishing OE-MRI scanning is significantly less than hypoxic PET. The National Institute for Health and Care Research (NIHR) cost tool lists the basic cost of a partial body PET scan as £1,484 as opposed to a head and neck MRI scan with contrast at £389 (NIHR 2020). The additional cost of oxygen and a mask for OE-MRI is negligible relative to that of an additional radio-pharmaceutical for hypoxic PET. From a patient perspective, MRI scans do not result in additional radiation exposure and are often shorter in total duration than PET once the delay between having the radioisotope injected and imaging is considered (usually between 1 and 4 hours) (Grimes et al. 2017).

From a technical perspective one of the limitations of any medical imaging technique is matching the spatial resolution to the scale of changes of clinical interest. The typical in-plane resolution of a clinical PET scan is of the order of $\sim$4mm^2 to 1cm^2 whereas MRI can achieve 3D spatial resolutions down to $<$1mm^3 (Vaquero & Kinahan 2015, Dewhirst & Birer 2016, Grimes et al. 2017). Molecular oxygen has a diffusion distance of the order of 80 to 100μm (Thomlinson & Gray 1955) and pre-clinical animal experiments have shown that oxygenation levels can change from normoxic to radiobiologically significant hypoxia within distances of this order. The oxygen level represented by a single imaging voxel therefore represents a composite of the true underlying heterogeneous oxygen distribution.

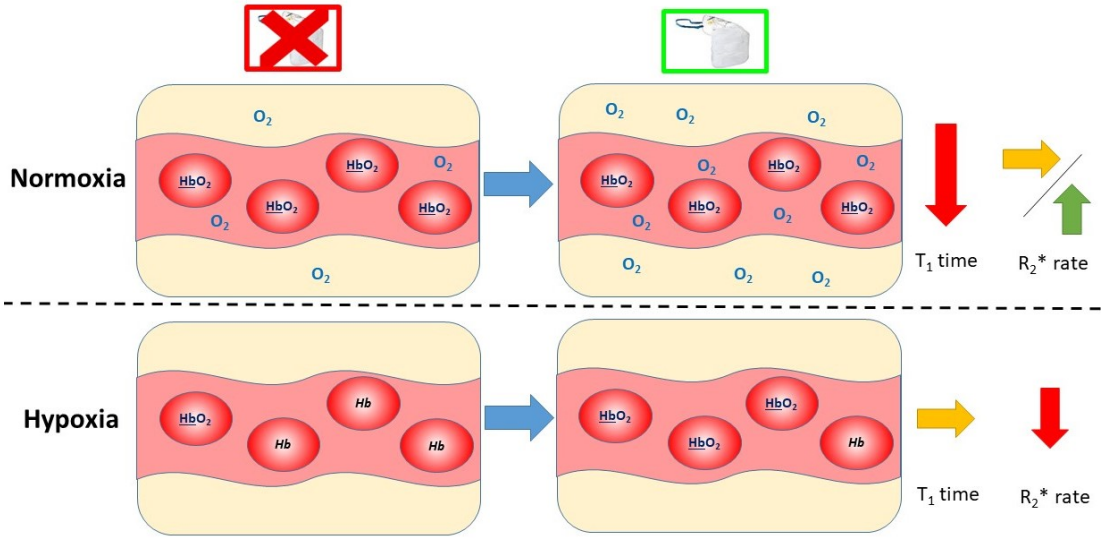

Figure 1.4: Diagrammatic representation of theory behind OE-MRI - Theoretical basis of OE-MRI. Top row shows a normoxia situation whereby whilst breathing room air (left), the haemoglobin (Hb) is essentially saturated with oxygen (O_2) forming oxyhaemoglobin (HbO_2) meaning that when supplemental oxygen is administered the additional oxygen manifests as molecular oxygen dissolved in tissue fluid and blood plasma (right). This consequently reduces the T_1 relaxation time due to the weakly paramagnetic property of dissolved oxygen but has minimal impact on the R_2^* rate due to the relative invariance of the oxy to deoxyhaemoglobin ratio. Conversely in hypoxic regions the haemoglobin is unsaturated on room air and therefore additional oxygen preferentially binds to form oxyhaemoglobin resulting in an unchanged T_1 time but a reduction in the R_2^* rate due to the relative increase in oxyhaemoglobin concentration.

This partial voluming effect means we run the risk of missing significant, but small areas of hypoxia on PET which may be more reliably assessed on MRI (Grimes et al. 2017).

1.6 Conclusion

In summary, hypoxia is a crucial factor that drives the development of more aggressive tumour phenotypes that display increased resistance to chemotherapy, immunotherapy and radiotherapy treatments. Tumour hypoxia is a particular issue for the radiotherapy treatment of HNSCC that confers a significantly worse prognosis. Techniques to overcome hypoxia mediated radioresistance either via medications that reduce its significance such as hypoxic radiosensitisers and bioreductive drugs, or via increased radiation doses exist but trials of such techniques have had mixed results. Stratification of patients by tumour hypoxia extent or location may improve appropriate patient selection for such trials. Hypoxic imaging is an appealing approach to this issue due to its non-invasive nature and potential to provide spatial information on the distribution of hypoxia as well as the ability to repeat the imaging during treatment. Whilst hypoxia imaging techniques exist, they are not widely available in clinical practice. A hypoxia imaging technique based on changes directly related to tissue oxygen concentration that has the potential to be readily deployed in cancer centres worldwide due to its lack of additional specialist equipment is OE-MRI.

The research detailed in subsequent chapters of this thesis assess the utility of performing OE-MRI in patients with head and neck cancer for the assessment of tumour hypoxia using equipment available in a standard NHS hospital. Chapter 2 reviews the basic physics behind MRI acquisitions before a scoping review of the current research landscape of OE-MRI in tumours is presented in chapter 3. Chapter 4 presents the research hypothesis, aims and objectives and details the clinical study design with the results of the initial assessments performed in developing the OE-MRI technique for use in HNSCC presented in chapter 5. Results from the clinical study are presented in chapters 6 to 8 with final conclusions drawn together in chapter 9 along with suggestions for future work.

Chapter 2

MRI Physics

2.1 Introduction

The physical principles of nuclear magnetic resonance were first elucidated during the middle part of the 20^{th} century. The application of these principles to the production of medical images and the creation of the field of MRI ultimately led to the award of the 2003 Nobel Prize in Physiology or Medicine to Paul Lauterbur and Sir Peter Mansfield. In this chapter a brief overview of the underlying physics principles governing the generation of MRI is presented along with a review of the principles of quantitative T_1 determination which is fundamental to tumour hypoxia assessment via OE-MRI.

2.2 Signal Creation

MRI is based on the principle of nuclear magnetic resonance (NMR) and in particular, due to its abundance in the form of water in the human body, the magnetic resonance of the hydrogen nucleus (equivalent to the subatomic particle of the proton, ^{1}H). The fundamental principles of MRI are based on subatomic quantum-mechanical phenomena, however a working knowledge of MRI can be obtained using a classical mechanics approximation which will be the focus of this brief introduction. However the generation of the initial magnetic moment that is manipulated to generate the MRI signal does require a brief consideration

of quantum mechanics.

All atomic and subatomic particles possess a property called spin. Like charge, spin is a fundamental property of nature whose magnitude cannot be changed (although its direction can be altered). Spin confers intrinsic angular momentum ($\boldsymbol{\rho}$) and also a magnetic moment ($\boldsymbol{\mu}$) on particles such that:

$$\boldsymbol{\mu} = \gamma\boldsymbol{\rho} = \gamma\hbar m, \tag{2.1}$$

where γ is the gyromagnetic ratio ($\gamma/2\pi = 42.56$MHz/T for a proton), $\hbar$ is Planck's constant and m is the nuclear angular momentum quantum number.

The magnitude of spin is quantised implying it takes discrete values only. In the case of the proton, spin is discretised to 2 values; $m = \frac{1}{2}$, known as "spin-up" and $m = -\frac{1}{2}$ known as "spin-down". In thermal equilibrium these spin states are degenerate. However in the presence of an external magnetic field (B_0) this degeneracy breaks down with the resulting energy states E_m given by:

$$E_m = -m\gamma\hbar B_0. \tag{2.2}$$

The difference between proton states is thus:

$$\Delta E = \gamma\hbar B_0. \tag{2.3}$$

In classical statistical mechanics, the distribution of protons between the two spin states is described via the Boltzmann distribution:

$$\frac{\text{Number spin down}}{\text{Number spin up}} = \exp\left(\frac{\Delta E}{kT}\right) = \exp\left(\frac{\gamma\hbar B_0}{kT}\right), \tag{2.4}$$

where k is the Boltzmann constant ($1.38 \text{ x } 10^{-23}$ JK^{-1}) and T is the absolute temperature. At body temperature and with a standard clinical MRI field strength of 1.5T, we find that this ratio is 1.00001. This difference, although small, is what generates the net magnetic moment M_0 that is manipulated to generate the MR signal.

By applying a radio-frequency (RF) pulse (B_1) orthogonal to the direction of B_0 at the resonant frequency of protons ($f = \gamma B_0 = 63$MHz at 1.5T) the orientation of the initial longitudinal magnetisation (M_0) is tilted away from the orientation of B_0 (longitudinal axis, M_z). The magnitude of this tilt is known as

the flip angle (FA) and is proportional to the strength and duration of B_1. A 90° pulse tips M_0 fully into the transverse plane (M_{xy}). When B_1 is turned off, the protons return to their initial state through two independent processes:

1. Loss of energy from the spins to surrounding tissues causing gradual recovery of the longitudinal magnetization to achieve thermal equilibrium. This is known as spin-lattice relaxation and is characterised by the relaxation time T_1 (or relaxation rate $R_1 = 1/T_1$) such that:

$$M_z(t) = M_0(1 - e^{(-t/T_1)}). \tag{2.5}$$

2. Rapid dephasing of spins in the transverse plane due to small perturbations in the spin precessional frequencies. This spin-spin relaxation is characterised by the relaxation time T_2 (or relaxation rate $R_2 = 1/T_2$) such that:

$$M_{xy} = M_0 e^{(-t/T_2)}. \tag{2.6}$$

   However inhomogeneities in the main magnetic field accelerate T_2 decay, characterised by the relaxation time T_2^* such that:

$$\frac{1}{T_2^*} = \frac{1}{T_2} + \gamma\frac{\Delta B_0}{2}, \tag{2.7}$$

   where γ is the gyromagnetic ratio and ΔB_0 is the inhomogeneity in the primary magnetic field.

Although recovery of magnetisation along the longitudinal axis (T_1 recovery) and decay of magnetisation in the transverse plane (T_2 decay) are independent of each other, they do occur simultaneously although typical tissue T_1 values are several times longer than T_2 times meaning that for a 90° RF pulse, the transverse magnetisation fully decays significantly before the longitudinal magnetisation returns to its baseline value (McRobbie et al. 2017). Figure 2.1 illustrates typical T_1 recovery and T_2 decay curves.

The magnitude of the relaxation time for a particular tissue of interest can be manipulated in clinical practice through the administration of contrast agents. The vast majority of clinically used contrast agents are IV administered gadolinium based. Gadolinium is a rare-earth metal that has seven unpaired electrons

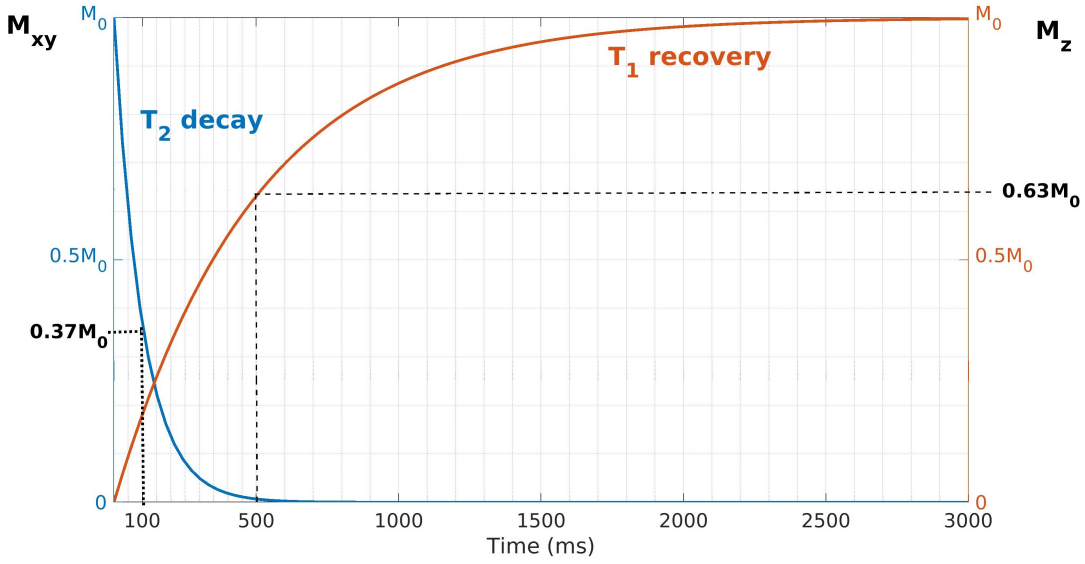

Figure 2.1: T_1 and T_2 relaxation curves - Example T_1 recovery and T_2 decay curves for a representative tissue with a T_1 time of 500ms and T_2 time of 100ms. T_1 recovery and T_2 decay occur simultaneously but independently of each other. T_1 recovery is characterised by the T_1 time which is the time required for the longitudinal magnetization (M_z) to return to $(1 - 1/e)$ (approximately 63%) of its initial value (M_0). T_2 decay is characterised by the T_2 time which is the time taken for the transverse magnetisation (M_{xy}) to decay to $1/e$ (approximately 37%) of its maximum value. Figure adapted from Chapter 8, McRobbie et al. (2017) with curves plotted using MATLAB based on equations 2.5 and 2.6.

meaning that it is strongly paramagnetic; when placed in a magnetic field the gadolinium forms induced magnetic fields in the same direction as the main field. This results in the shortening of T_1 times for tissues in the vicinity of the contrast agent in proportion to the concentration of accumulated gadolinium which in turn is governed by a range of factors including a tissue's vasculature and perfusion characteristics as well as the pharmacokinetics of the contrast agent (McRobbie et al. 2017). In a similar physical manner, molecular oxygen (O_2) has two unpaired electrons and is therefore also paramagnetic and will thus also tend to reduce T_1 times, albeit to a significantly smaller magnitude than is achievable with gadolinium (Tadamura et al. 1997).

The basic MRI signal is obtained by detecting a voltage induced in a receiver coil by the transverse component of the magnetization. This is known as a free induction decay (FID). However, in order to make this an imaging technique additional magnetic fields (known as gradient fields) are required to spatially encode the magnetisation precession frequencies before measuring the magnetic resonance signal by creating what is known as an echo.

2.3 Spin Echo

Figure 2.2 shows an illustration of a basic spin echo (SE) pulse sequence. Following an initial 90° RF pulse, an additional 180° 'refocussing' RF pulse is applied to reverse the dephasing of the spins in the transverse plane and thus generate an echo. As the 180° refocusing RF pulse completely reverses the spatially invariant decay caused by magnetic field perturbations, SE sequences are governed by genuine T_2 decay.

The signal is acquired in what is known as frequency-space (k-space) meaning that in order to create the final image, the frequency domain data is transformed into the spatial domain using the two-dimensional (2D) fast Fourier transform (FFT). This means that to spatially locate the magnitude of an MR signal, we need to locate this in frequency space. Thus, by manipulating the frequency and phase of the measured signal before the application of the refocussing pulse, the MR signal can be spatially encoded in the frequency domain.

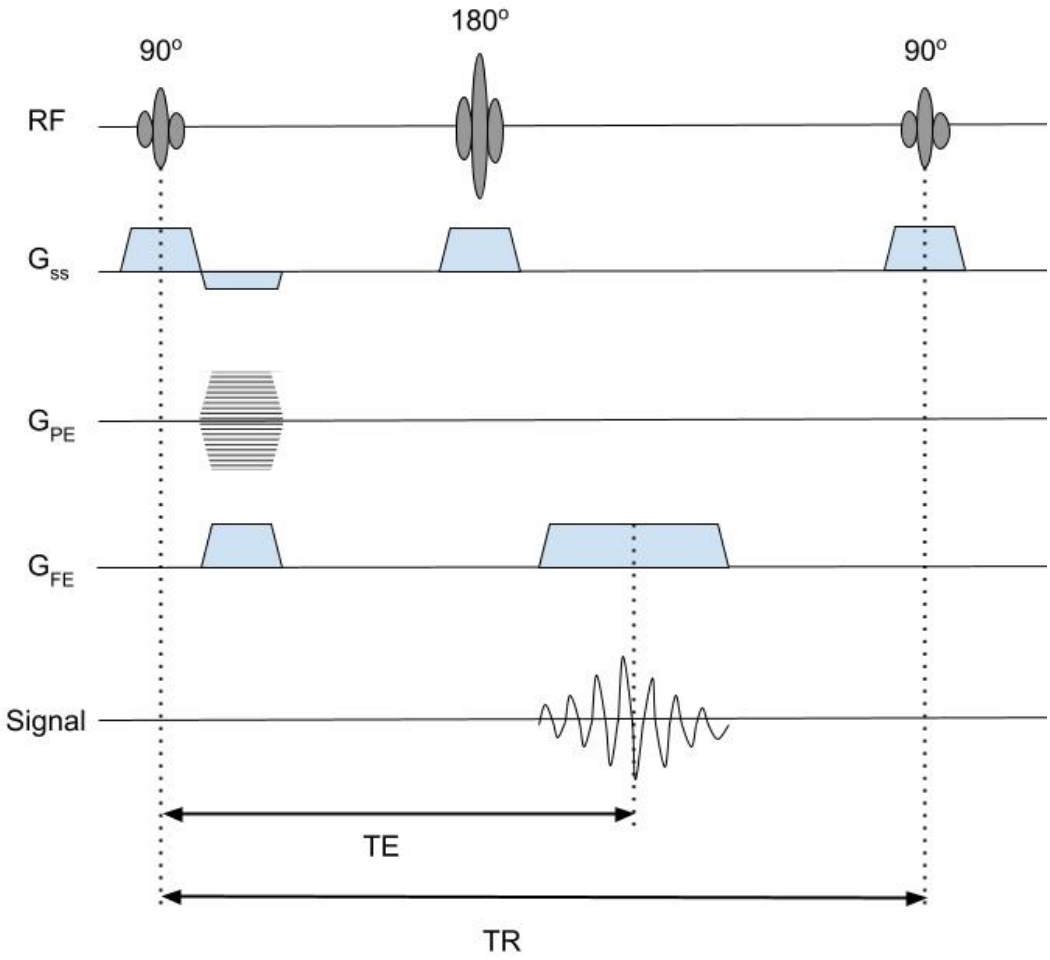

Figure 2.2: Basic Spin Echo Pulse Sequence - Illustration of a standard 2-dimensional spin echo pulse sequence where G_{ss} is the slice select gradient, G_{PE} is the phase encode gradient and G_{FE} is the frequency encode or readout gradient. TE = echo time and TR = repetition time.

By applying a gradient along the imaging slice direction (G_{SS}) concurrent with the RF pulses, a slab of tissue can be selected for excitation where the precessional frequencies of the spins in the slab match the RF frequency. This process is repeated for each required 2D slice. Phase and frequency encoding gradients can then be applied in discrete steps for the phase encoding (G_{PE}) and as a continuous field during the signal readout for the frequency encoding (G_{FE}) in order to fully spatially encode the signal. It is possible to phase encode a signal in multiple directions and thus a true 3D image can be constructed via phase encoding in 2 orthogonal directions with frequency encoding performed in the final direction. However, due to the requirement to perform phase encoding in discrete steps, this significantly prolongs the imaging acquisition time.

The level of contrast in the acquired MR image is dependent upon both the underlying properties of the imaged tissue (tissues T_1 and T_2 relaxation times and the proton density (PD)) and the imaging parameters used to acquire the sequence. Two key parameters of the imaging sequence are the repetition time (TR) and the echo time (TE).

The TR refers to the gap between successive RF excitation pulses (90° RF pulses in the case of SE) and is a major determinant of the overall imaging acquisition time as it determines the wait that must be endured between successive excitations to allow recovery of the longitudinal magnetization. Techniques exist to allow faster acquisitions (such as turbo spin echo (TSE) / fast spin echo (FSE)) but a review of these techniques is beyond the scope of this discussion. TE refers to the time from the initial RF pulse to the centre of the acquired echo and thus dictates how much T_2 decay occurs before the signal is acquired.

Thus for a SE sequence, image acquisitions with short TR and short TE tend to minimise T_2 decay and T_1 recovery and thus produce images where the contrast is principally T_1 weighted. Conversely, sequences with long TR and TE allow significant T_1 recovery for the range of T_1 times in a tissue but have significant T_2 decay and thus produce predominantly T_2 weighted images.

2.4 Gradient Echo

In contrast to SE, gradient echo (GE) uses a single initial excitation RF pulse. The frequency encoding magnetic field gradient is then used on its own to generate the echo (figure 2.3). There is an initial dephasing of the spins by applying the readout gradient in the opposite direction before it is switched to the full readout gradient.

As previously discussed, T_1 mediated relaxation after the RF pulse results in recovery of longitudinal magnetization. However if the TR is less than that required for full T_1 recovery, repeated RF pulses eventually result in a situation where recovery of the longitudinal magnetisation for each TR interval is equivalent to that tilted into the transverse plane. This is the definition of steady state formation. One of the benefits of GE imaging is the ability to reduce the TR using this steady state approach, thus allowing more rapid image acquisition than is possible with SE. Considering the transverse magnetization in this situation, if the TR is not significantly greater than the T_2^* time there will be residual transverse magnetization present when subsequent RF pulses are applied which would contribute to the measured signal. There are 3 basic approaches to dealing with this magnetization:

1. Wait for it to fully decay (Unbalanced GE)
2. Utilise it to increase the size of the signal (Balanced GE)
3. Remove it from affecting the final measured signal (Spoiled GE)

2.4.1 Spoiled Gradient Echo

Spoiled gradient echo (SPGR) refers to the removal of residual transverse magnetization by the use of additional spoiler gradient fields and by varying the phase angle of the RF pulses. By spoiling the residual transverse magnetization before the application of subsequent RF pulses, SPGR can be made heavily T_1 weighted. In addition as GE can readily be performed in 3D this makes it an ideal sequence

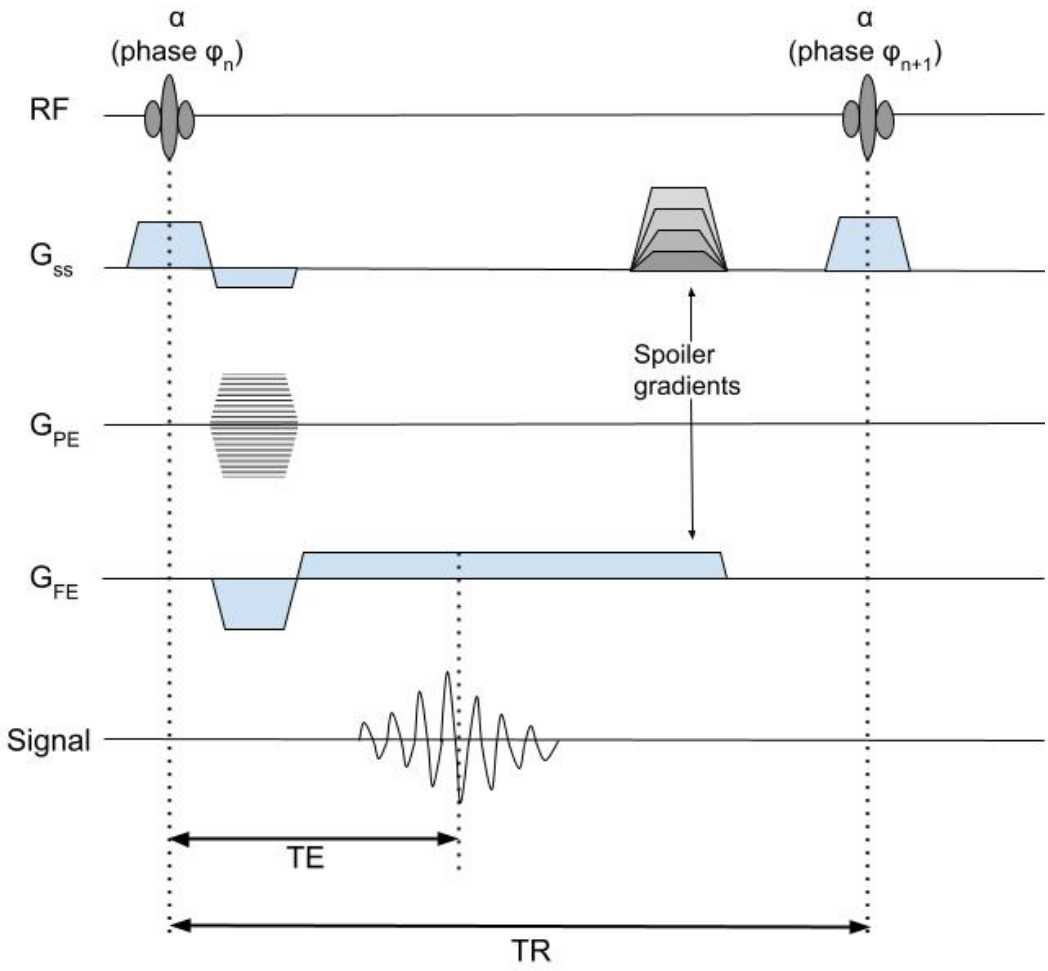

Figure 2.3: Basic Spoiled Gradient Echo Pulse Sequence - Illustration of a 2-dimensional spoiled gradient echo pulse sequence. α = FA of the RF pulse, ϕ = phase angle of the RF pulse. G_{ss} = slice select gradient, G_{PE} = phase encode gradient and G_{FE} is the frequency encode or readout gradient. TE = echo time and TR = repetition time.

for rapid repeated T_1 based volumetric imaging. The equation for the signal intensity for SPGR (S_{SPGR}) is given by (McRobbie et al. 2017):

$$S_{\text{SPGR}} = M_0 \frac{\sin(\alpha) \cdot \left(1 - e^{-TR/T_1}\right) \cdot e^{-TE/T_2^*}}{1 - \cos(\alpha) e^{-TR/T_1}}, \tag{2.8}$$

where α is the RF flip angle.

It can be seen that for a given TR and T_1 time, there exists a FA that maximises the signal intensity. This is known as the Ernst angle and is given by (Ernst & Anderson 1966):

$$\alpha_{\text{Ernst}} = \arccos\left(e^{-TR/T_1}\right). \tag{2.9}$$

2.5 Measurement of T_1 Relaxation Times

The discussion so far has focussed on generating images with the level of contrast present dependent upon the relaxation times amongst other factors. However, it is possible to measure the relaxation times themselves to allow quantitative MRI to be performed. There are a number of different ways to clinically map T_1 times each with their own advantages and disadvantages. We shall briefly mention the three most commonly used methods (Stikov et al. 2015).

2.5.1 Inversion Recovery

As previously discussed, the T_1 time dictates the rate of recovery of longitudinal magnetization following an RF pulse. Formally, this recovery is dictated by the Bloch equation.

If a 180° RF pulse is applied before a standard SE imaging sequence, the transverse magnetization will be completely inverted before the image is acquired. By delaying the application of the imaging sequence for a period of time after this so called inversion pulse, the magnitude of the subsequently measured signal is dependent upon the extent of longitudinal recovery that has occurred between the 180° pulse and the imaging sequence. This time delay is known as the inversion time (TI) and this method of T_1 mapping is known as inversion recovery (IR).

In the situation where the TR is at least 5 times a tissue's T_1 time thus allowing full recovery of the longitudinal magnetization between RF pulses, the measured signal intensity (S_{TI}) from an IR sequence with known TI time for a given tissue T_1 can be simplified to (McRobbie et al. 2017):

$$S_{\mathrm{TI}} = S_0 \left[1 - 2 \cdot \lambda \exp\left(\frac{-\mathrm{TI}}{T_1}\right)\right], \tag{2.10}$$

where λ is known as the inversion efficiency parameter.

It can therefore be seen that the T_1 time of a tissue can be estimated from a non-linear fit of the signal intensity versus the TI time. If dynamic T_1 mapping is required, this can be accomplished via first acquiring a baseline T_1 map using multiple IR times before obtaining the dynamic data using a single IR time. Dynamic T_1 times can then be estimated using the ratio of signal intensities (Huen et al. 2013).

Although often considered the gold standard method for T_1 mapping, IR methods are relatively slow due to the requirements for the TR to be at least five times the T_1 time of interest and for imaging using at least five different TI times.

2.5.2 Look-Locker

A modification to the standard IR methodology of T_1 mapping is the Look-Locker or modified Look-Locker inversion recovery (MOLLI). Essentially, the standard initial inversion pulse is used but rather than acquiring a single reading, data is continuously acquired resulting in measurements at different effective TI times. This data is fitted to an exponential recovery curve with correction factors needing to be applied to determine T_1 times (Aherne et al. 2020). Although widely used in cardiac imaging (Messroghli et al. 2004, Aherne et al. 2020), this technique does not offer the ability to readily produce 3-dimensional T_1 maps and thus its use in tumour T_1 mapping is likely to be limited (Bluemke et al. 2022*a*).

2.5.3 Variable Flip Angle

An alternative to IR based techniques is the variable flip angle (VFA) technique that uses repeat applications of a standard SPGR sequence. As shown by Fram

et al. (1987), it is possible to rearrange equation 2.8 into its linear form:

$$\frac{S_{\mathrm{SPGR}}}{\sin(\alpha)} = \frac{S_{\mathrm{SPGR}}}{\tan(\alpha)} \cdot e^{-TR/T_1} + \rho\left(1 - e^{-TR/T_1}\right), \tag{2.11}$$

where S_{SPGR} is the signal intensity associated with a flip angle α and ρ is a factor proportional to the equilibrium longitudinal magnetization, which in the situation where TE>>T_2^* as is the case in clinical imaging, is equal to M_0.

For an imaging sequence with a fixed TR and TE and acquisitions with FA α, the T_1 time can thus be determined from the gradient of a plot of $S_{\mathrm{SPGR}}/\sin(\alpha)$ against $S_{\mathrm{SPGR}}/\tan(\alpha)$:

$$T_1 = -\frac{\mathrm{TR}}{\ln(\text{gradient})} = \frac{\mathrm{TR}}{|k|}, \tag{2.12}$$

where for two FA α_1 and α_2:

$$k = \ln\left(\frac{dE \cdot \sin(\alpha_2) \cdot \cos(\alpha_1) - \sin(\alpha_1) \cdot \cos(\alpha_2)}{dE \cdot \sin(\alpha_2) - \sin(\alpha_1)}\right), \tag{2.13}$$

and dE is the ratio of the signal intensity from a PD-weighted image (low FA α_1) divided by the signal intensity from a T_1-weighted image (FA α_2).

In order to determine T_1 times in this manner, it is necessary to have at least two acquisitions with different FA. In fact Wang et al. (1987) showed that for a given TR/T_1 ratio there exists a pair of FA that maximises the precision in the T_1 calculation and that this pair of FA produces results that are either comparable or superior to using multiple evenly spaced angles but with the benefit of a decreased acquisition time. This does however assume a single TR/T_1 ratio and also assumes *a priori* knowledge of the T_1 time being measured to determine the optimal FA.

As this technique uses a simple SPGR sequence then it is readily possible to produce 3D T_1 maps in a rapid manner thus allowing repeated T_1 mapping with temporal resolutions of the order of seconds. This technique is however sensitive to spatial variations in the RF pulse angle, a limitation which is particularly pronounced at field strengths of 3T and above. Consequently, for clinical T_1 mapping on 3T scanners and stronger a map of the variations in the FA (B_1 map) is required (Stikov et al. 2015).

For the OE-MRI research study sequence, the VFA approach to T_1 estimation was therefore used to produce 3D T_1 maps in as rapid time as possible thus both

allowing dynamic measurements of T_1 times with oxygen delivery as well as minimising the overall image acquisition time. In addition, as all study acquisitions were performed on 1.5T scanners then in order to avoid unnecessarily extending the imaging time, formal B_1 mapping was not performed.

2.6 Conclusion

In this chapter the principles of NMR and the basic application of this to medical imaging in the form of SE and GE based MRI have been reviewed. An overview of clinical approaches to T_1 mapping has also been presented, with a particular focus on the VFA approach which is the principle methodology used for the clinical OE-MRI experiments presented in this thesis.

Chapter 3

T_1 based oxygen-enhanced MRI in tumours; a scoping review of current research

3.1 Abstract

Background and method

OE-MRI or TOLD is an imaging technique under investigation for its ability to quantify and map oxygen distributions within tumours. The aim of this review was to identify and characterise the research into OE-MRI for characterising hypoxia in solid tumours. A scoping review of published literature was performed on the PubMed and Web of Science databases for articles published before 27th May 2022. Studies imaging solid tumours using proton-MRI to measure oxygen induced T_1/R_1 relaxation time/rate changes were included. Grey literature was searched from conference abstracts and active clinical trials. The search results were updated on 10th March 2024.

Results

49 unique records were identified on the original search that met the inclusion criteria consisting of 34 journal articles and 15 conference abstracts. The updated search identified an additional 5 articles satisfying the inclusion criteria (excluding publications relating to this thesis). The majority of articles were pre-clinical

studies that were performed in a range of tumour types and demonstrated consistent correlation of OE-MRI with alternative hypoxia measurements. No clear consensus on optimal acquisition technique or analysis methodology was found. No prospective, adequately powered, multicentre clinical studies relating OE-MRI hypoxia markers to patient outcomes were identified.

Conclusions

There is good preclinical evidence of the utility of OE-MRI in tumour hypoxia assessment however there are significant gaps in clinical research that need to be addressed to develop OE-MRI into a clinically applicable tumour hypoxia imaging technique.

3.2 Introduction

The presence of biologically significant hypoxia in tumours has been known since the work of Thomlinson and Gray in the 1950's (Thomlinson & Gray 1955). More recently it has been shown in a range of different tumour types that the presence of oxygen concentrations below 10mmHg in tumours results in significantly worse radiotherapy and chemotherapy treatment outcomes as well as increasing the risk of distant metastases (Dewhirst et al. 2008, Hughes et al. 2019). The accurate and reliable assessment of tumour hypoxia to stratify tumours more likely to respond to hypoxia modifying treatments and in monitoring the effect of such interventions is thus not just clinically important for head and neck cancers. Consequently there has been significant interest across tumour subsites in developing tumour hypoxia imaging including via OE-MRI.

In order to assess the evidence base behind OE-MRI and identify areas requiring further research in order to translate OE-MRI into a routinely used clinical technique, a scoping review on the use of magnetic resonance imaging of hypoxia in solid tumours using a supplemental oxygen challenge to induce changes in proton T_1 relaxation rates was performed.

The original literature search for this review was performed in 2022 towards the start of these PhD studies and published in 2023 (McCabe et al. 2023). The results of this original search are presented here in order to place the research

detailed in subsequent chapters of this thesis in the context of the knowledge base at the time of the study design. The literature search strategy used in this scoping review was repeated in March 2024 with the additionally identified papers reviewed in section 3.5.1 of this chapter.

3.3 Methods

This scoping review follows the preferred reporting items for systematic reviews and meta-analyses extension for scoping reviews (PRISMA-ScR) (Tricco et al. 2018) but was not registered on an online database. The original literature search was performed on 27th May 2022 on the PubMed and Web of Science databases using identical search strategies (tables 3.1 and 3.2). There were no limits on publication dates.

Results from the searches were combined, duplicates removed and articles restricted to novel research. References from excluded review articles were manually examined for additional resources. Articles were screened against the following inclusion criteria:

1. Images solid tumours in animal models and/or human participants
2. Uses proton based magnetic resonance imaging
3. Assesses changes in T_1 relaxation times (or R_1 relaxation rates, $R_1 = 1/T_1$) following a supplemental oxygen challenge

A second reviewer (Dr Rafal Panek) screened the identified literature to ensure adherence to the study criteria. Discrepancies between reviewers were discussed and consensus reached. Grey literature was searched by interrogating abstracts from the International Society of Magnetic Resonance in Medicine (ISMRM) annual meeting from 2011 to 2022 and the ClinicalTrials.gov website for currently open trials satisfying the eligibility criteria.

To examine the full scope of OE-MRI in solid tumours, both pre-clinical and clinical research was included and there was no restriction made to a particular tumour subtype. As such, significant heterogeneity was expected in the results with relatively few publications in any one tumour type. Therefore, no plans were

Table 3.1: Results from scoping review search performed on PubMed on 27th May 2022.

#	**Search Terms**	**Results**
#1	(MRI) **OR** ("magnetic resonance")	901,366
#2	(cancer*) **OR** (tumour*) **OR** (tumor*) **OR** (malignan*)	4,174,778
#3	("oxygen enhanced") **OR** ("tissue oxygen level dependent") **OR** ("tissue oxygenation level dependent") **OR** ("oxygen sensitive") **OR** ("O2 sensitive") **OR** (hyperoxi*)	13,141
#4	#1 **AND** #2 **AND** #3	134
#5	#4 **AND** English[lang]	134

made to perform quantitative analysis nor was any predefined critical appraisal criteria constructed to avoid rejecting studies at this stage. The findings were planned to be presented in the form of a descriptive review.

3.4 Results

227 unique records were identified. Following screening, 49 articles were identified for qualitative analysis consisting of 34 journal articles and 15 conference abstracts (figure 3.1). The distribution of the journal articles and published conference abstracts by publication year is shown in figure 3.2. 3 trials satisfying the eligibility criteria that were listed as open to recruitment were identified on the ClinicalTrials.gov website (Choudhury 2021, Datta 2021, Panek & McCabe 2021). All of these studies have corresponding articles or conference abstracts included in the final search results (Bluemke et al. 2022*a*, Datta et al. 2022, McCabe et al. 2022). This includes the published study design and preliminary results from the research that forms the basis of this thesis.

3.4.1 Research focus

The majority of published studies involve animal only research (31 studies, 63.3%) with 15 being human only studies (30.6%) and 3 being mixed studies (6.1%).

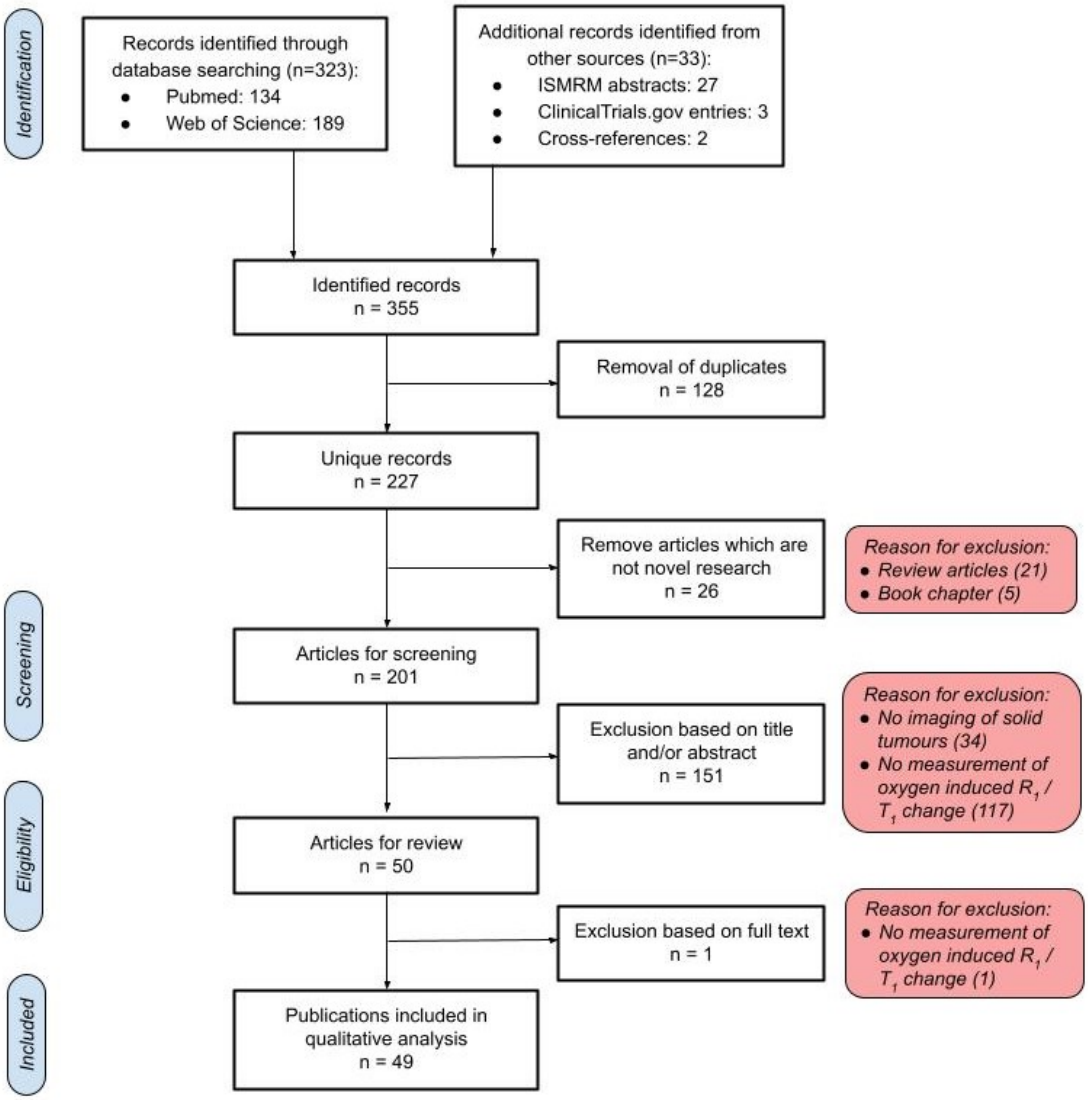

Figure 3.1: PRISMA flow diagram - Flowchart indicating the results obtained from the scoping review search strategies.

Table 3.2: Results from scoping review search performed on Web of Science on 27th May 2022.

#	Search Terms	Results
#1	(MRI) **OR** ("magnetic resonance")	830,038
#2	(cancer*) **OR** (tumour*) **OR** (tumor*) **OR** (malignan*)	4,857,728
#3	("oxygen enhanced") **OR** ("tissue oxygen level dependent") **OR** ("tissue oxygenation level dependent") **OR** ("oxygen sensitive") **OR** ("O2 sensitive") **OR** (hyperoxi*)	16,398
#4	#1 **AND** #2 **AND** #3	189
#5	#4 **AND** English[lang]	189

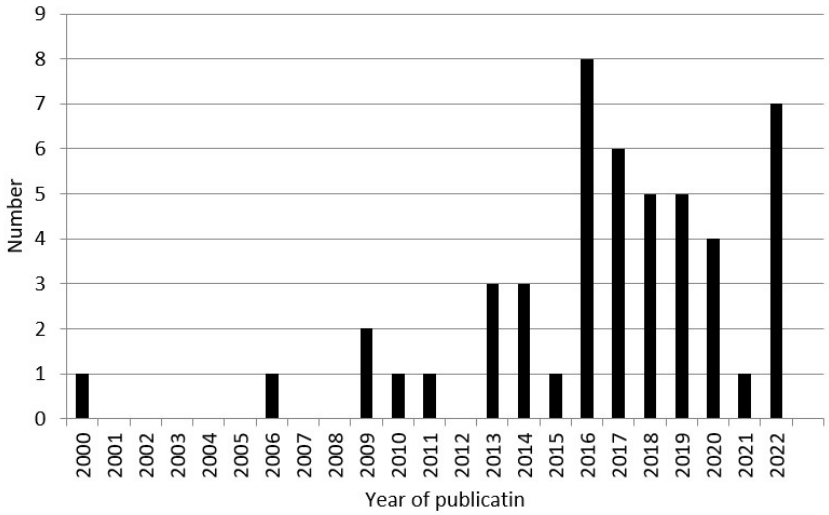

Figure 3.2: Article publication year - Histogram of publication year for journal articles and conference abstracts identified in the scoping review searches.

Of those involving human participants, 4 image intracranial neoplasms and 4 scan head and neck malignancies (22.2% each). Two references image colorectal cancer and hepatocellular cancer (11.1% each) with the remaining results divided between single studies in lung, anal, cervical, renal, prostate and mixed tumour sites.

3.4.2 Preclinical Studies

Four main associations have been tested in preclinical models to validate the ability of OE-MRI in detecting tumour hypoxia:

1. Validation against alternative oxygenation determining techniques including direct measurements and alternative imaging strategies such as hypoxia PET scanning (Pacheco-Torres et al. 2009, Jordan et al. 2013, Colliez et al. 2014, Hallac et al. 2014, O'Connor et al. 2016, Zhou et al. 2019)

2. Verification that the distribution of hypoxic and normoxic areas seen with OE-MRI display intratumoural heterogeneity but with spatially coherent regions in keeping with patterns known to occur biologically (Zhou et al. 2017*a*, Moosvi et al. 2019*a*, Lepicard et al. 2020, Boult et al. 2022, Roy et al. 2022, O'Connor et al. 2009, Winter et al. 2011, Burrell et al. 2013, Remmele et al. 2013, Zhao et al. 2015, Beeman et al. 2016, O'Connor et al. 2016, Rich & Seshadri 2016, Cao-Pham et al. 2017, Zhou et al. 2017*b*, Featherstone et al. 2018, Little et al. 2018, Salem et al. 2019, Zhou et al. 2019, Waschkies et al. 2020)

3. Correlation against histopathological hypoxia indicators such as pimonidazole staining, GLUT-1 expression and HIF-1α expression (Li et al. 2018, Lepicard et al. 2020, Boult et al. 2022, Roy et al. 2022, Linnik et al. 2014, O'Connor et al. 2016, Little et al. 2018, Moosvi et al. 2019*b*, Salem et al. 2019)

4. Verification of OE-MRI's ability to predict tumours more likely to display hypoxia induced treatment resistance (Little et al. 2017, Arai et al. 2021, Hallac et al. 2014, White et al. 2016, Salem et al. 2019)

One of the papers that helped establish the utility of OE-MRI in accurately mapping tumour hypoxia was based on renal and colorectal carcinoma cell lines implanted in mice (O'Connor et al. 2016). The authors correlated OE-MRI data with direct measurements of tissue oxygen concentration and established a correlation between OE-MRI quantified tumour hypoxic fraction and histopathological staining with the hypoxia sensitive marker pimonidazole. The authors also demonstrated that OE-MRI could detect expected increases in tumour hypoxic fractions following administration of the vasodilator drug hydralazine (O'Connor et al. 2016). A separate study in human lung adenocarcinoma xenografts helped biologically validate the OE-MRI technique by demonstrating its ability to detect changes in tumour hypoxic volumes following administration of a bioreductive cytotoxin (Banoxantrone) and an oxygen consumption modifier (Atovaquone) (Little et al. 2017, O'Connor et al. 2024).

The original OE-MRI analysis method calculates the spatial average of T_1/R_1 changes with oxygen over the imaged tumour. However a number of papers fail to show correlations of these spatially averaged values with reference hypoxia markers (O'Connor et al. 2016, Rich & Seshadri 2016, Cao-Pham et al. 2016, Little et al. 2018) or tumour radiosensitivity indicators (Belfatto et al. 2016, Salem et al. 2019, Cao-Pham et al. 2017) possibly due to the heterogeneous distributions of oxygen within tumours resulting in hypoxic regions being masked by the T_1/R_1 changes induced in normoxic areas. O'Connor et al. (2016) proposed combining OE-MRI with a perfusion assessment thereby enabling voxels of interest to be identified as perfused oxygen-enhancing (normoxia), perfused oxygen-resistant (hypoxia) or nonperfused (necrosis). The perfused oxygen-resistant (perfused Oxy-R) biomarker is sensitive to spatial fluctuations in hypoxia and shows correlation with alternative hypoxic markers and clinically relevant tumour hypoxia outcomes in both preclinical (O'Connor et al. 2016, Little et al. 2018, Salem et al. 2019) and human studies (Panek et al. 2018, Little et al. 2019, 2018, Salem et al. 2019). Such perfusion masks have been generated using DCE-MRI (O'Connor et al. 2016, Little et al. 2018, Salem et al. 2019, Panek et al. 2018, Little et al. 2019) and ultrasmall superparamagnetic iron oxide (USPIO) enhanced MRI derived fractional blood volume measurements (Lepicard et al. 2020).

An alternative OE-MRI approach combining R_2^* (BOLD) and R_1 based oxygen-enhanced imaging aims to distinguish blood based oxygen induced changes from tissue based ones. Although increased concentration of dissolved oxygen accelerates R_1 relaxation rates, the net tissue R_1 rate is affected by a number of other factors including being reduced by lower concentrations of deoxyhaemoglobin (Bluemke et al. 2022*b*). Although this influence is generally small compared to the influence of dissolved oxygen, the simultaneous measurement of R_2^* values may yield insights into the cause of observed oxygen-induced tissue R_1 decreases (Burrell et al. 2013, Linnik et al. 2014, Cao-Pham et al. 2017, Yang et al. 2019, O'Connor et al. 2019). In particular, Cao-Pham et al. present a hypothesis based on their work on rhabdomyosarcoma and glioma xenografts where they divide voxels into four classes dependent upon the relative changes in oxygen induced R_1 and R_2^* rates (Cao-Pham et al. 2017):

1. Normoxia: Significantly increasing R_1 (increased molecular oxygen) and stable or mildly increased R_2^* (stable deoxy/oxyhaemoglobin ratio)

2. Mild hypoxia: Slightly increasing R_1 (increased molecular oxygen) with decreasing R_2^* (decreased deoxy/oxyhaemoglobin ratio). Assumes unsaturated baseline haemoglobin changing to near complete saturation.

3. Severe hypoxia: no/mild decreasing R_1 and decreasing R_2^* (decreased deoxy/oxyhaemoglobin ratio)

4. Vascular Steal: decreasing R_1 with increasing R_2^*. Hypothesised to be caused by dilatation of mature blood vessels shunting blood away from tumour regions served by immature vessels resulting in decreased blood volume and molecular oxygen.

The use of a cyclical oxygen challenge combined with independent component analysis (ICA) of the voxel-wise signal traces has been proposed as another method to improve the sensitivity of OE-MRI. Hypoxic regions derived using this approach have been correlated to pimonidazole stained areas in murine squamous cell carcinomas (Moosvi et al. 2019*b*) and shown capable of detecting oxygenation changes in murine tumours following treatment with vascular growth factor

inhibition (Moosvi et al. 2019*a*). However poor correlation with human colorectal xenografts was noted possibly due to the lack of a perfusion assessment meaning that regions of necrosis may have confounded the imaging assessment (Moosvi et al. 2019*b*).

Regarding correlations of OE-MRI parameters with pre-clinical treatment outcomes, three studies in prostate cancer found oxygen induced R_1 changes correlated with outcomes following radiotherapy (Hallac et al. 2014, White et al. 2016, Arai et al. 2021) but one paper found no association between OE-MRI parameters and local tumour control probability (Belfatto et al. 2016). This study used tumour mean oxygen-induced R_1 changes rather than the perfused fraction biomarker. Salem et al. (2019) found that OE-MRI determined biomarkers detected therapy induced changes in hypoxia in glioma xenografts and non-small cell lung cancer but all studies that have looked at correlating OE-MRI biomarkers with treatment outcomes have been with relatively small study sizes.

3.4.3 Human studies

OE-MRI studies on human participants have been performed on all major anatomical regions with no significant difficulties reported with patient tolerability. The principle research foci of the human studies are shown in table 3.3 categorised by domains derived from the cancer research UK (CRUK) and EORTC consensus statement on the clinical translation of imaging biomarkers (O'Connor et al. 2017).

Three studies performed OE-MRI assessments in both pre-clinical and clinical settings and all demonstrate similar patterns between animal and human scans (Linnik et al. 2014, Little et al. 2018, Salem et al. 2019). The studies investigating changes of OE-MRI biomarkers with treatment in patients have been performed in glioblastoma (Zhou et al. 2016), brain metastases (Qian et al. 2020), head and neck cancer (Dubec et al. 2022), non-small cell lung cancer (NSCLC) (Salem et al. 2019), cervical cancer (Datta et al. 2022), rectal cancer (Little et al. 2019) and anal cancer (Bluemke et al. 2020).

Salem et al. (2019) used the perfused hypoxic fraction metric in patients with NSCLC to distinguish tumours that have persistent hypoxia from those

Table 3.3: Summary of principle research focus of tumour OE-MRI studies in humans categorised by domains derived from the Cancer Research UK (CRUK) and European Organisation for Research and Treatment of Cancer (EORTC) consensus statement on the clinical translation of imaging biomarkers (O'Connor et al. 2017).

Clinical research focus	No. studies
Proof of principle including safety, feasibility and tolerability.	15
Repeatability and reproducibility.	5
Correlation with histopathology.	2
Changes of biomarkers with treatment.	7
Initial correlation of biomarkers to clinical outcomes.	1
Prospective, adequately powered studies linking biomarkers to clinical outcomes.	0
Analysis techniques.	7

that demonstrate hypoxia modification with CRT. Similarly, Little et al. (2019) scanned patients with rectal cancer immediately prior to CRT and again at day 7 or day 14 of treatment and found measurable changes in tumour hypoxic burden with treatment using the perfused Oxy-R metric. Reduction in tumour hypoxia was only apparent by day 14 though and not at day 7 (Little et al. 2019). Reduction in hypoxic fractions with treatment is also found in the anal, cervical and head and neck cancer studies with the latter additionally demonstrating the feasibility of performing OE-MRI on the MR-Linac (hybrid MRI scanner and radiotherapy linear accelerator) (Bluemke et al. 2020, Datta et al. 2022, Dubec et al. 2022).

3.4.4 Technical considerations

A range of methodologies have been used in clinical OE-MRI research (tables 3.4 and 3.5). Human studies show a preference for 1.5T (11 studies, 61.1%) over 3T (9 studies, 50.0%) imaging systems (2 studies utilised both field strengths). The most frequently used T_1 measurement technique in human OE-MRI is the VFA

method, used by 50% of studies, closely followed by IR based techniques. An alternative T_1 mapping technique called mapping of oxygen by imaging lipids relaxation enhancement (MOBILE) that exploits the increased solubility of oxygen in lipids over water has also been investigated (Jordan et al. 2013). Studies in tumour models found that oxygen induced changes in lipid R_1 rates were of greater magnitude than changes in water R_1 and global R_1 rates (Jordan et al. 2013, Colliez et al. 2014). This approach however might be sensitive to the amount of lipid present within tumours (Cao-Pham et al. 2016).

Table 3.4: Imaging parameters and setup details for the T_1 based oxygen-enhanced MR scans for the peer-review published in human studies. FFE = Fast Field Echo, SPGR = Spoiled gradient recalled acquisition in the steady state, VFA = Variable Flip Angle, IR-LL = Inversion Recovery Look Locker, IR = Inversion Recovery, MOLLI = Modified Look-Locker Inversion Recovery.

	O'Connor et al. (2009)	**Remmele et al. (2013)**	**Linnik et al. (2014)**	**Bane et al. (2016)**	**Hectors et al. (2017) a**	**Hectors et al. (2017) b**	**Zhou et al. (2017*c*)**
Area	Liver, omentum, pelvis	Brain	Brain	Liver	Liver	Liver	Prostate
B0	1.5T	3T	3T	1.5T	3T	1.5T (3T)	3T
Sequence	3D FFE	2D-SPGR simultaneous R_1/R_2^*	3D FFE	IR-LL	3D VFA	2D IR-LL	FFE
TR/TE (ms)	3.5 / 0.9	103 / 12 echoes	3.5 / 1.1	2.26 / 1.04	10 / 1.2	2.3 / 1.0 (35.1 / 1.2)	
TI (ms)	-	-	-	42 - 1576.5	-	42-1577 (80-1445)	
Flip angles (°)	2, 8, 17	25	2, 5, 10, 16	8	1, 10, 19	8 (10)	2 to 14 (5 angles)
No. slices	25	40	25	1-2	36	1-2	-
Slice (mm)	4	5	4.2	8	5	8	3
FoV (mm)	375	230	230	420x288.75	350x260	420x290 (320x280)	240 to 260mm
Resolution (mm)	2.93	1.8	1.8	3.3	0.9	3.3 (1.0)	0.94
Dynamic/Static	Dynamic	Dynamic	Dynamic	Static	Static	Static	Static
Temp res. (s)	20	2.3	68	-	-	-	-
Hyperoxia	100% (15L/min)	Carbogen: 95% O2	100% (15L/min)	100% / Carbogen	15L/min for 10-15mins	15L/min for 10-15mins	100% for 7 mins
Oxygen delivery device	Non rebreathing circuit with Hudson mask.	Mask	Non-rebreathing mask	Non-rebreathing mask	-	-	Face mask
Coils	Body	Head	Head	Spine and body	Spine and body	Spine and body	Cardiac and endorectal
Duration baseline	24 readings	1min	11 readings	1 reading	1 reading	1 reading	1 reading
Duration oxygen	48 readings	4min	12 readings	1 reading	1 reading	1 reading	1 reading
OE-MRI duration	32mins	7min	26 min	20s per reading	14s per image	18s (10s) per image	-

Table 3.4 continued.

	Little et al. (2018)	**Salem et al. (2019)**	**Bluemke et al. (2020)**	**Qian et al. (2020)**	**Bluemke et al. (2022*a*) a**	**Bluemke et al. (2022*a*) b**
Area	Kidney	Lung	Anus	Brain	Head and neck	Head and neck
B0	1.5T	1.5T	3T	3T	3T	3T
Sequence	IR	IR-prepared 3D-SPGR	MOLLI	FFE	MOLLI	IR-prepared 3D-SPGR
TR/TE (ms)	10,000 / 3.1	2.1 / 0.5	3,000 / 120	32 / 2.0	3.05 / 1.332	4 / 0.656
TI (ms)	50, 200, 500, 10000, 20000, 5000, 1400 (dynamic)	10, 50, 300, 1100 (dynamic), 2000, 5000	11 inversion times	-	11 inversion times	-
Flip angles (°)	45	6	35	7, 16, 37	35	2, 5, 10, 15
No. slices	1	41	1	-	1	-
Slice (mm)	7	5	5	5	10	5
FoV (mm)	375	450	380	240	-	-
Resolution (mm)	2.93	4.69	1.7	1.88	-	-
Dynamic/Static	Dynamic	Dynamic	Static	Static	Static	Static
Temp res. (s)	30	10	-	-	-	-
Hyperoxia	100% (15L/min)	100% (15L/min)	100% until end tidal O2=70%	100% for 3 minutes	100% until end tidal O2=70%	100% until end tidal O2=70%
Oxygen delivery device	Non-rebreathing mask	Non-rebreathing Hudson mask via gas blender	Non-rebreathing mask	Non-rebreathing mask	Non-rebreathing mask	Non-rebreathing mask
Coils	Body	Body	Body	Head	Head	Head
Duration baseline	9 readings	12/18 readings	1 reading	1 reading	1 reading	1 reading
Duration oxygen	-	48 readings	1 reading	1 reading	1 reading	1 reading
OE-MRI duration	-	26mins	-	-	-	-

Table 3.5: Imaging parameters and setup details for the T_1 based oxygen-enhanced MR scans for the conference abstracts of human studies. No imaging parameters were provided for one abstract (Zhou et al. 2016). IR = inversion recovery, SPGR = Spoiled gradient recalled acquisition in the steady state, MOLLI = Modified Look-Locker Inversion Recovery.

	Panek et al. (2018)	**Little et al. (2019)**	**Datta et al. (2022)**	**Dubec et al. (2022)**	**McCabe et al. (2022)**	**Prezzi et al. (2022) a**	**Prezzi et al. (2022) b**
Area	Head and neck	Rectum	Cervix	Head and neck	Head and neck	Rectum	Rectum
B0	3T	1.5T	1.5T	1.5T	1.5T	3T	3T
Sequence	3D SPGR	3D SPGR	IR prepared 3D SPGR	IR prepared 3D SPGR	Dixon	3D SPGR	MOLLI
TR/TE (ms)	4.5 / 2.3	12 / 0.74	2.2 / 0.66	2.8 to 3.0 / 0.9 to 1.0	7.3 / 2.39 & 4.77ms	4.56 / 2.04	280.56 / 1.12
TI (ms)	-	-	100, 500, 1100 (dynamic), 2000, 4300	100, 500, 800, 1100 (dynamic), 4300	-	-	180
Flip angles (°)	3, 16	3, 13, 18	4	6	2, 12	2, 13	35
No. slices	24	25	-	-	72	72	1
Slice (mm)	2.5	4	6	5	2.5	3	8
FoV (mm)	240	375	384	384	200	380 x 309	360 x 307
Resolution (mm)	1.5	2.34	3	3	1.6	1.2	1.4
Dynamic/Static	Dynamic	Dynamic	Dynamic	Dynamic	Static	Static	Static
Temp res. (s)	3	13.9	12	12	-	-	-
Hyperoxia	100%	100%	100%	100%	100% for $\geq$ 7 mins	100% for $\geq$ 3 mins	100% for $\geq$ 3 mins
Oxygen delivery device	Non-rebreathing mask	Non-rebreathing mask	Non-rebreathing mask	Non-rebreathing mask	Non-rebreathing mask	-	-
Coils	Head and neck	-	-	-	Posterior head / anterior flex	-	-
Duration baseline	20 readings	14 readings	25 readings	25 readings	5 readings	6 readings	6 readings
Duration oxygen	210 readings	-	45 readings	45 readings	5 readings	6 readings	6 readings
OE-MRI duration	-	-	19 mins	19 mins	8.6s per reading	40s per reading	8.5s per reading

OE-MRI can be performed statically with T_1 mapping performed before and after oxygen or dynamically during the switch from air to oxygen (tables 3.4 and 3.5). The duration of hyperoxia delivered before repeat imaging in human studies ranges from 2 to 15 minutes. For the 6 human studies that provide a dynamic scan duration, the median OE-MRI acquisition time was 22.5 minutes (range 7 to 32mins).

3.4.5 Oxygen delivery

The oxygen challenge was delivered in the form of 100% oxygen in 35 studies (71.4%) and carbogen (mixture of oxygen and carbon dioxide) in 9 studies (18.4%) with 2 studies using both and 3 unstated. In the human studies, the majority use 100% oxygen (15 studies, 83.3%) with two using carbogen (11.1%) and one using both. Carbogen has been investigated as an alternative to 100% oxygen with the aim of mitigating the vasoconstrictive effect of hyperoxia with the vasodilative influence of carbon dioxide (Winter et al. 2011, Burrell et al. 2013, Colliez et al. 2014, Hallac et al. 2014, Zhao et al. 2015, Beeman et al. 2016, Waschkies et al. 2020, Cao-Pham et al. 2017). However Winter et al. (2011) found that varying the carbon dioxide concentration in administered carbogen had no significant effect on altering blood flow during OE-MRI and Hallac et al. (2014) found similar OE-MRI responses in prostate cancer xenografts with carbogen and 100% oxygen. It should be noted that in animal experiments, high concentration oxygen is also a crucial component of the anaesthetic process therefore potentially affecting baseline oxygenation levels compared to awake animals.

The use of an internal quality control point to provide a quantitative assessment of adequate oxygen delivery has been proposed because inadequate oxygen delivery during an OE-MRI scan could result in inappropriate labelling of regions as oxygen challenge refractory. Such control regions have been located in skeletal muscle (O'Connor et al. 2009), renal cortices (Little et al. 2018), descending thoracic aorta (Salem et al. 2019), uterine body (Datta et al. 2022) and nasal conchae (Dubec et al. 2022).

3.5 Discussion

Overall, there is strong preclinical evidence that OE-MRI can accurately and reliably detect hypoxic regions of solid tumours and monitor how such regions change with anti-cancer therapies. The evidence base for OE-MRI from clinical studies is however much less advanced. Initial results from human trials are promising for the utility of OE-MRI in tumour hypoxia imaging, however due to the early stage nature of this research all of these studies are single institute trials without prospective power calculations and without standardised data acquisition or analysis methodologies. Further work is required on specific tumour sites in patients to optimise and standardise OE-MRI protocols as well as establish the optimum timing to correlate OE-MRI data to clinically relevant outcomes before validating OE-MRI biomarkers in larger multicentre trials.

Currently there is no consensus on the optimal imaging sequence to use in OE-MRI. Given the heterogeneous nature of oxygenation within tumours, it is unsurprising that most researchers have opted for 3D acquisitions in order to map the entire tumour volume. Indeed those clinical studies that opted for single slice acquisitions have struggled with co-registering images acquired during treatment with baseline data (Bluemke et al. 2020, 2022*a*). The accuracy and precision of T_1 determination is not equivalent between different methodologies though; VFA for example consistently overestimates T_1 values in the brain (Stikov et al. 2015, Taylor et al. 2016). However as it is the change in T_1 times that is relevant in OE-MRI, this may mitigate somewhat systematic errors in T_1 measurement. Work to develop a consensus guideline, such as exists in DCE-MRI (Shukla-Dave et al. 2019), balancing the competing demands of acquisition time, spatial coverage, temporal resolution and measurement accuracy is critical in standardising tumour OE-MRI imaging and allowing for comparison of studies.

If OE-MRI were to be added to routine clinical diagnostic protocols, the duration of the OE-MRI sequence is critical with respect to healthcare resources, patient tolerability and the risk of movement and image quality degradation. The extent and nature of movement during OE-MRI scans will vary depending upon the anatomical area of interest however it is clear that appropriate image co-registration techniques are required for robust data analysis (Salem et al. 2019,

Bluemke et al. 2022*a*, McCabe et al. 2022). Currently there is a large range in the duration of clinical OE-MRI scans and variations between dynamic imaging and static acquisitions. The optimal duration of the oxygen challenge in patients is not yet proven and the potential benefits of delivering multiple oxygen challenges during one imaging session thus facilitating ICA techniques has not been proven to outweigh the difficulties of increased scan time.

With regards to the delivery of the oxygen challenge, although there are legitimate concerns regarding the vasoconstrictive effects of hyperoxia confounding the OE-MRI signal, the evidence presented suggests that in practice this is not a significant issue. In addition, inhalation of carbogen gas has been shown to induce unpredictable responses in different organs (O'Connor et al. 2007) as well as not always being well tolerated in humans due to its potential to cause dyspnoea. It therefore seems reasonable for future human studies to use 100% oxygen rather than carbogen, however the risk of hyperoxic vasoconstriction should be considered. In addition, future studies should continue to use quality control points to provide quantitative evidence of adequate tissue oxygen delivery. The location of such points will depend on the anatomical area imaged, the field of view used and the imaging sequence. Standardisation of such markers will be helpful for future multicentre trials.

Novel methods of OE-MRI data analysis continue to be developed and offer the potential to increase the accuracy of OE-MRI in differentiating regions of tumour hypoxia. Although the use of the perfused hypoxic fraction metric has been successfully applied in clinical OE-MRI studies, it does require a co-registered perfusion assessment which may limit its clinical utility. Alternative approaches such as synchronous BOLD and OE-MRI measurements, ICA and novel data clustering techniques may ultimately prove to be more effective hypoxia categorisation tools. Further work is required to correlate data clustering approaches to clinically relevant outcomes and to optimise OE-MRI data processing approaches.

The optimal timing of when to perform OE-MRI assessments of tumours in patients undergoing treatment is not yet clear. Baseline metrics of hypoxic fraction may provide a stratification methodology for the utilisation of novel hypoxia activated drugs or novel radiosensitisers in patients more likely to respond

to them but the more sensitive application of OE-MRI biomarkers may be in identifying regional hypoxia that is invariant to treatment. The initial patient studies looking at such repeat scans in OE-MRI show that the timing of the re-assessments is crucial but this may also be dependent on tumour type and therapy modality and requires further evaluation. In addition, the clinical implication of chronic tumour hypoxia versus transient or cycling hypoxia and the potential for OE-MRI to distinguish between these has not been fully explored as yet. Dynamic or repeated oxygen challenge imaging may allow rapid frequency cycling tumour hypoxia characteristics to be elucidated with OE-MRI whereas repeat assessment on different days is more likely to reveal changes in chronic hypoxia levels (Bader et al. 2020). Separating out these two components of hypoxia may provide a more powerful OE-MRI metric and requires further research.

3.5.1 Update of literature search

The search strategy detailed in tables 3.1 and 3.2 was repeated on 10$^{\text{th}}$ March 2024 in order to identify new published papers relevant to this area that have been published during the course of these PhD studies. A total of 22 new papers were identified of which 2 are publications of work presented in this thesis and are therefore not reviewed further (McCabe et al. 2023, 2024a).

The remaining 20 articles were screened using the scoping review inclusion criteria (section 3.3) with 14 articles excluded; 2 review articles, 4 articles with no imaging of solid tumours and 8 articles with no assessment of changes in T_1 relaxation times following an oxygen challenge. In addition, 1 additionally identified paper was a research study protocol with no experimental data presented (Brighi et al. 2023). This study plans to compare MRI based brain tumour hypoxia assessments (including OE-MRI) with hypoxia-PET scans at multiple time points during treatment. Notably, the authors propose to allow the use of oxygen delivery via nasal prongs in patients for whom an oxygen face mask will not fit comfortably within the head receiver coil. Although the authors present a preliminary measurement suggesting this approach delivers adequate oxygen to induce measureable ΔR_1 relaxation rates in the nasal conchae, it remains to be proven that the lower concentration of oxygen deliverable with such a setup will

yield sufficient magnitude of intra-tumoural R_1 changes to enable reliable tumour hypoxia assessment.

The remaining 5 articles identified in this repeat literature search are divided between 2 pre-clinical and 3 clinical trials. Regarding the 2 pre-clinical papers, Buschmann et al. (2022) continue the previously identified work of Waschkies et al. (2020) in using quantitative T_1 and T_2^* mapping with gas challenges to characterise tumour grafts grown on chorioallantoic membranes. The other pre-clinical paper (Baker et al. 2023) is related to a previous conference abstract included in the original search results (Moosvi et al. 2019*a*). The authors used a repeated gas challenge with ICA to identify hypoxic voxels within murine carcinomas that had been treated with a VEGF inhibitor. In this study, OE-MRI was able to elucidate differing responses to the anti-angiogenic therapy and therefore may be a suitable technique for monitoring tumour response to anti-vascular therapies. Although this paper confirms the utility of ICA technique for OE-MRI, the immediate clinical translational relevance of this is still to be elucidated due to the requirement for a cyclical gas challenge during the dynamic acquisition which significantly prolongs the imaging time.

The additional clinical paper by Lickliter et al. (2023) is related to a previously identified conference abstract (Zhou et al. 2016). In this clinical phase Ib/II study of the addition of a novel oxygen therapeutic dodecafluoropentane emulsion (DDFPe) to the CRT treatment of glioblastoma multiforme (GBM), the authors used OE-MRI in 6 patients to assess for changes in tumour oxygenation induced by the investigative product. OE-MRI was performed before and after treatment with CRT and DDFPe on days 1 and 5 of the first week of treatment using a Look-Locker approach to T_1 mapping on three slice locations in the tumour. They found that tumour tissue showed statistically significant shortening of T_1 times following administration of the trial medication whereas normal brain parenchyma failed to show any significant changes. The authors thereby conclude that this is the first clinical trial of OE-MRI to show a reduction in tumour hypoxia in GBM and highlight the logistical advantages of OE-MRI over hypoxic-PET. The number of patient participants is however small and tumours were only partly imagined. The trial remains therefore in the proof of principle category.

The other 2 additional clinical studies identified on this repeat literature search evaluate OE-MRI in head and neck cancer. The work of Dubec et al. (2023) updates the previously identified conference abstract from the same group (Dubec et al. 2022) on their work on OE-MRI in head and neck cancer in 11 patients on a diagnostic MRI scanner and an MR-Linac. The authors successfully performed OE-MRI in the head and neck, however they only report tumour averaged ΔR_1 rates and no treatment outcomes to correlate these values too. In addition, the MRI protocol used took a total of ∼40mins with the OE-MRI sequence itself taking 18mins. In order to fully translate this into a clinically feasible technique, it is likely that these durations need to be reduced.

The final additional study is by Bluemke et al. (2023) who performed OE-MRI in HPV associated oropharyngeal head and neck cancer on a 3T scanner and attempted to correlate OE-MRI metrics to radiotherapy treatment outcome. This study only had 5 participants who completed the OE-MRI protocol meaning it was not possible to comment on the utility of OE-MRI to predict treatment response. In addition, patient motion caused difficulty with the data quality in this study and therefore tumour averaged OE-MRI metrics were also used.

Both of these clinical head and neck OE-MRI studies are in essence proof of principle studies with low numbers of participants. Both studies were published after the research presented in this thesis was commenced and illustrate the on-going interest in the field of MRI based hypoxia imaging in HNSCC.

3.6 Limitations

There are limitations with this scoping review. Firstly, due to the relatively novel nature of OE-MRI in solid tumours approximately 30% of the originally identified published articles are conference abstracts rather than journal articles. These abstracts have not been through the same level of peer review that journal articles are subject to; however it is important to include this grey literature in order to present the full scope of research being performed in this area. Secondly, the inclusion criteria explicitly limit the included studies to those that quantify oxygen induced T_1 or R_1 changes, however this means at least 3 studies that assessed changes in T_1-weighted signal intensity were excluded from the analysis

(Fan et al. 2017, Lloyd et al. 2019, Liu et al. 2021). Finally, the literature search was focussed on two databases that were considered most likely to yield the greatest number of results. Future reviews may benefit from using alternative databases in order to obtain the most comprehensive search results.

In conclusion, there is strong preclinical evidence of the utility of OE-MRI in assessing and monitoring tumour hypoxia however significant clinical work remains to be completed before OE-MRI derived biomarkers can be utilised as a routine component of cancer imaging.

Chapter 4

OE-MRI in HNSCC Clinical Study Design

4.1 Hypothesis, aims and objectives

The following hypothesis was tested by the research outlined in this thesis:

> *Oxygen enhanced MRI performed on a routine clinical MRI scanner using only routinely available clinical equipment is capable of determining regions of hypoxia that correlate with areas at greater risk of radiotherapy treatment resistance in patients with squamous cell carcinoma of the head and neck.*

The study aims are:

1. Assess the feasibility of deriving estimates of HNSCC tumour hypoxic burden via OE-MRI
2. Develop an OE-MRI scanning protocol for HNSCC hypoxia assessment suitable for implementation in routine clinical NHS practice
3. Test predictive power of OE-MRI derived metrics in identifying patients with HNSCC at greater risk of radiotherapy treatment resistance

4. Investigate the potential for OE-MRI derived tumour hypoxia distributions to guide radiotherapy treatment planning volumes

The study aims will be achieved by the following objectives:

1. Develop an OE-MRI scanning protocol that takes less than 10 minutes to perform on a routine diagnostic MRI scanner using only standard NHS equipment

2. Produce a data processing pipeline to generate clinically relevant tumour hypoxia data from clinical OE-MRI images

3. Survey patients with HNSCC on the clinical experience of undergoing an OE-MRI scan

4. Test for correlations between OE-MRI derived tumour hypoxic metrics and routine clinical treatment response assessments for patients treated with curative intent radiotherapy or chemoradiotherapy.

5. Perform image fusion of OE-MRI derived maps of tumour hypoxia with radiotherapy planning scans

4.2 Study overview

In order to test the aforementioned hypothesis, an observational imaging clinical study was designed. Patients with a high clinical suspicion of HNSCC who were likely to undergo curative intent radiotherapy or chemoradiotherapy were recruited to undergo an extended MRI scan in addition to their routine clinical imaging at Nottingham University Hospitals NHS trust (NUH).

An OE-MRI imaging protocol was developed to produce parametric maps of changes in T_1 relaxation times following the delivery of supplemental oxygen (section 5.1). Dynamic mapping of T_1 times during the transition from normoxic to hyperoxic states was produced on a voxel-by-voxel basis with voxels that failed to show statistically significant shortening of T_1 times classified as hypoxic (figure 1.4). The imaging protocol was developed to take no more than 10mins to acquire

to make this a clinically translatable technique. Only equipment routinely available in the NHS was utilised. All imaging was performed using the NUH clinical Magnetom Sola 1.5T scanners (Siemens Healthineers, Erlangen, Germany).

As discussed in chapter 3, due to a lack of correlation between tumour averaged oxygen induced T_1 changes and reference hypoxia indicators in previous studies in tumours outside of the head and neck, OE-MRI researchers have investigated combining OE-MRI with additional metrics related to tumour perfusion. In clinical studies this has been performed using DCE-MRI to determine the percentage of tumours that are perfused yet show refractory T_1 times with supplemental oxygen (O'Connor et al. 2009, Little et al. 2018, Salem et al. 2019). However, due to the strong paramagnetic properties of IV gadolinium based contrast agent, any sequences requiring such contrast administration must be performed after OE-MRI sequences as otherwise any oxygen induced T_1 time changes would be masked by accumulation of the gadolinium. As the OE-MRI sequence in this study was added to the imaging appointment for a routine clinical head and neck MRI study that contains pre and post contrast enhanced sequences, the study OE-MRI sequence had to be performed prior to the clinical sequence. In addition, due to the differing receiver coil configuration used between the study and routine clinical scan (section 5.2), the need to perform unenhanced sequences as part of the routine clinical scan, the lack of DCE-MRI being a component of the standard NUH head and neck protocol and the need to not alter patients' routine care, it was not possible within the confines of this study to perform DCE-MRI.

An alternative metric that can provide information on the vascular space is obtained via BOLD MRI. The BOLD effect refers to the reduction in R_2^* relaxation rate with the reduction in deoxyhaemoglobin to oxyhaemoglobin ratio within the vascular space as occurs in perfused hypoxic regions following an oxygen challenge. As T_1 relaxation times are also proportional to deoxyhaemoglobin concentrations (Bluemke et al. 2022*a*), the addition of BOLD measurements to T_1-based OE-MRI may refine the characterisation of the oxygenation status of tumours (Cao-Pham et al. 2017, O'Connor et al. 2019). Pre and post supplemental oxygen static mapping of R_2^* relaxation rates was therefore included in the study protocol (section 5.1).

All primary tumours identified in the study were confirmed as squamous cell carcinoma based on routine histopathological analysis of core biopsy specimens as per the routine NUH clinical procedures. Oropharyngeal primary tumours were tested for evidence of HPV as per the local clinical protocols via in situ hybridization for HPV DNA using the INFORM HPV III Family 16 Probe (Ventana Medical Systems, Tucson, AZ, USA). All patients with histologically confirmed HNSCC had their clinical management performed according to the routine clinical procedures at NUH. The study did not affect patients' treatments or follow-up schedules.

For those patients who were treated with curative intent radiotherapy or chemoradiotherapy, treatment response assessment was determined via the standard clinical practice of performing an FDG-PET scan at 12 weeks following completion of treatment (Mehanna et al. 2016, NICE 2018). Primary tumours with a complete metabolic response on this scan were classed as responders. Patients with equivocal imaging findings or radiological evidence of residual disease had subsequent management as per the NUH standard of care treatment. Patients with confirmed residual disease post radiotherapy were classed as non-responders. Associations between OE-MRI derived parameters and treatment outcomes were tested for statistically significant correlations.

A Gantt chart detailing the planned study milestones is shown in figure 4.1.

4.3 Eligibility Criteria

Study inclusion and exclusion criteria for non-patient volunteers and patient participants are detailed below.

4.3.1 Inclusion Criteria

Non-patient Volunteer Inclusion Criteria:

(i) Age 18 years and above

(ii) Signed written informed consent

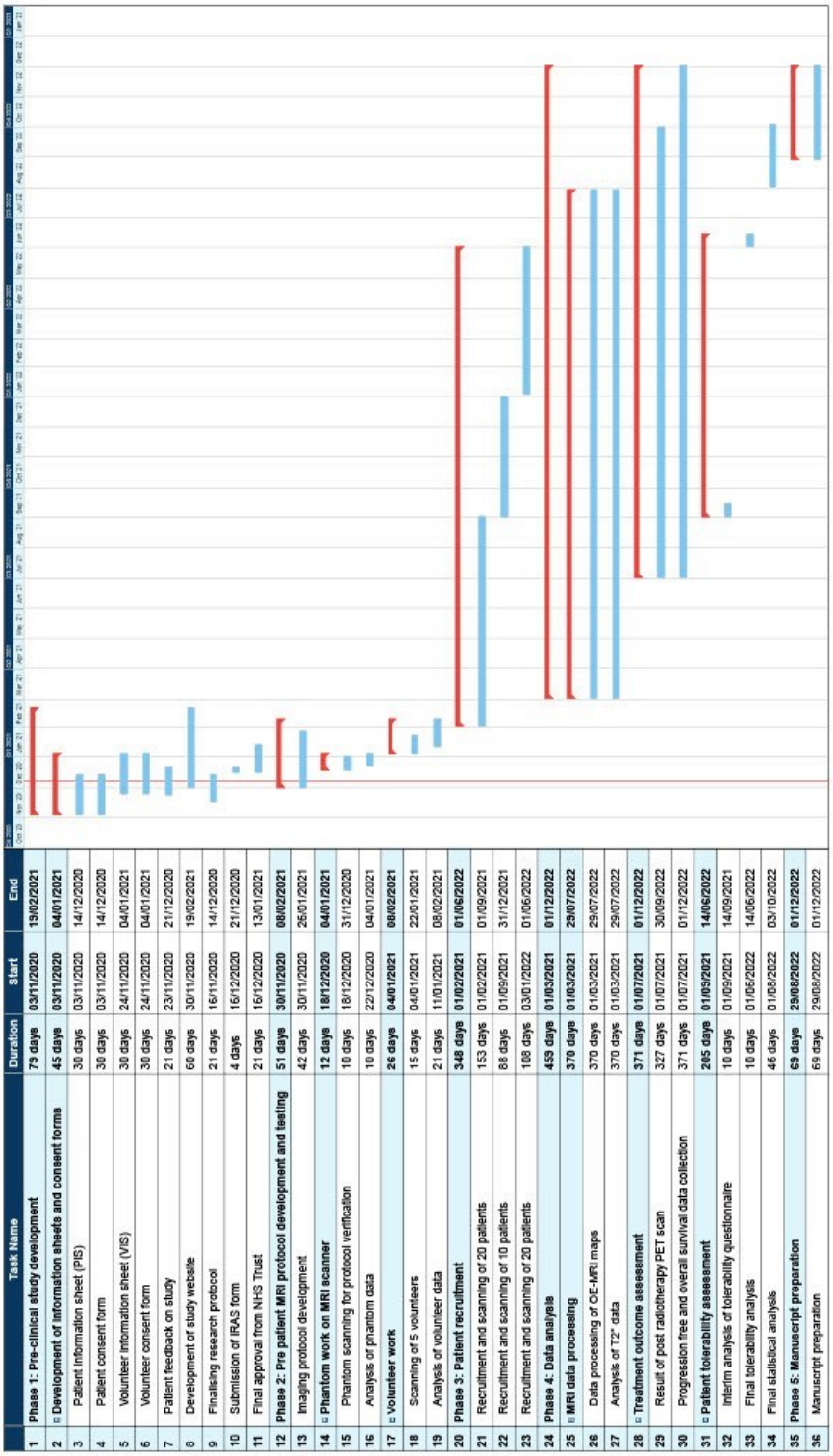

	Task Name	Duration	Start	End
1	**Phase 1: Pre-clinical study development**	**79 days**	**03/11/2020**	**19/02/2021**
2	**Development of information sheets and consent forms**	**45 days**	**03/11/2020**	**04/01/2021**
3	Patient information sheet (PIS)	30 days	03/11/2020	14/12/2020
4	Patient consent form	30 days	03/11/2020	14/12/2020
5	Volunteer information sheet (VIS)	30 days	24/11/2020	04/01/2021
6	Volunteer consent form	30 days	24/11/2020	04/01/2021
7	Patient feedback on study	21 days	23/11/2020	21/12/2020
8	Development of study website	60 days	30/11/2020	19/02/2021
9	Finalising research protocol	21 days	16/11/2020	14/12/2020
10	Submission of IRAS form	4 days	16/12/2020	21/12/2020
11	Final approval from NHS Trust	21 days	16/12/2020	13/01/2021
12	**Phase 2: Pre patient MRI protocol development and testing**	**51 days**	**30/11/2020**	**08/02/2021**
13	Imaging protocol development	42 days	30/11/2020	26/01/2021
14	**Phantom work on MRI scanner**	**12 days**	**18/12/2020**	**04/01/2021**
15	Phantom scanning for protocol verification	10 days	18/12/2020	31/12/2020
16	Analysis of phantom data	10 days	22/12/2020	04/01/2021
17	**Volunteer work**	**26 days**	**04/01/2021**	**08/02/2021**
18	Scanning of 5 volunteers	15 days	04/01/2021	22/01/2021
19	Analysis of volunteer data	21 days	11/01/2021	08/02/2021
20	**Phase 3: Patient recruitment**	**348 days**	**01/02/2021**	**01/06/2022**
21	Recruitment and scanning of 20 patients	153 days	01/02/2021	01/09/2021
22	Recruitment and scanning of 10 patients	88 days	01/09/2021	31/12/2021
23	Recruitment and scanning of 20 patients	108 days	03/01/2022	01/06/2022
24	**Phase 4: Data analysis**	**453 days**	**01/03/2021**	**01/12/2022**
25	**MRI data processing**	**370 days**	**01/03/2021**	**29/07/2022**
26	Data processing of OE-MRI maps	370 days	01/03/2021	29/07/2022
27	Analysis of T2* data	370 days	01/03/2021	29/07/2022
28	**Treatment outcome assessment**	**371 days**	**01/07/2021**	**01/12/2022**
29	Result of post radiotherapy PET scan	327 days	01/07/2021	30/09/2022
30	Progression free and overall survival data collection	371 days	01/07/2021	01/12/2022
31	**Patient tolerability assessment**	**205 days**	**01/09/2021**	**14/06/2022**
32	Interim analysis of tolerability questionnaire	10 days	01/09/2021	14/09/2021
33	Final tolerability analysis	10 days	01/06/2022	14/06/2022
34	Final statistical analysis	46 days	01/08/2022	03/10/2022
35	**Phase 5: Manuscript preparation**	**69 days**	**29/08/2022**	**01/12/2022**
36	Manuscript preparation	69 days	29/08/2022	01/12/2022

Figure 4.1: Gantt chart - Gantt chart indicating the planned milestones and timelines for the study.

Patient Inclusion Criteria:

(i) Histologically proven or strong clinical suspicion of squamous cell carcinoma of the head and neck

(ii) Suitable for undergoing radical radiotherapy or chemoradiotherapy according to local protocols within the head and neck cancer MDT

(iii) Age 18 years and above

(iv) Adequate physical fitness (World Health Organisation (WHO) performance status 0-2)

(v) Signed written informed consent

4.3.2 Exclusion criteria

Non-patient Volunteer Exclusion Criteria:

(i) Contraindications to MRI scans as identified following completion of the NUH standard MRI safety screening questionnaire

(ii) Severe chronic obstructive pulmonary disease (COPD) who are at risk of type 2 respiratory failure or require supplemental oxygen

(iii) Volunteers who are pregnant as identified through the NUH standard MRI safety screening questionnaire

Patient Exclusion Criteria:

(i) Poor physical fitness (WHO performance status > 2)

(ii) Contraindications to MRI scans as identified following completion of the NUH standard MRI safety screening questionnaire

(iii) Severe COPD who are at risk of type 2 respiratory failure or require supplemental oxygen

(iv) Patients who are pregnant or breast-feeding (due to IV contrast use in the routine clinical scan) as identified through the NUH standard MRI safety screening questionnaire

4.4 Study Sample Size

At the time of study development, there were no published OE-MRI studies in HNSCC nor any available data correlating OE-MRI derived parameters to HNSCC treatment outcomes. It was therefore not possible to perform an exact power calculation for this study.

An estimate of the required sample size was performed using data from a conference abstract from Dr Rafal Panek (Panek et al. 2018). Additional detail provided by Dr Panek from this study found that in assumed healthy head and neck region lymph nodes, the mean fraction of perfused imaging pixels refractory to oxygen challenge was 42% (standard deviation 16%). For HNSCC malignant nodes this fraction was 54% (standard deviation 14%).

Assuming healthy nodes are representative of tissues in a normoxic environment and malignant nodes represent tissue in a hypoxic environment, the sample size required to detect a statistically significant difference in oxygenation between normal and diseased lymph nodes can be estimated. Assuming a difference in means of 12% with standard deviation approximately 15% and a parametric distribution with a significance level of 5% (type I error probability of 0.05) then for a power of 95% (type II error probability 0.05), 42 patients will be required (Dupont & Plummer 1990). Assuming a dropout rate of approximately 20% increases the study size to 50 patients.

This sample size is comparable to other research studies looking at assessing differences in quantitative MRI parameters in head and neck cancer between treatment responders and non responders (Falk 2018, Welsh et al. 2015, Guo et al. 2017, Wong et al. 2018). Rates of local recurrence following chemoradiotherapy for locally advanced head and neck cancer suggest that approximately 20% of patients will have evidence of residual disease after treatment (Bhide et al. 2008, Mehanna et al. 2016) equating to approximately 10 patients for a study size of 50 participants. An additional 5 non-patient volunteers were planned to be recruited for protocol testing.

4.5 Ethical Approval

Research ethics approval was obtained from the South Central Berkshire Research Ethics Committee (reference 21/SC/0050) on 9th February 2021. The research sponsor was Nottingham University Hospitals NHS Trust (reference 20MP001) with the Chief Investigator being Dr R. Panek. This study was registered on ClinicalTrials.gov (NCT04724096).

4.6 Recruitment

All participants were prospectively recruited by A. McCabe between August 2021 and November 2022 and provided written informed consent. Patients were recruited according to the flow chart shown in figure 4.2. Patient participants were identified by either the surgical or oncology clinical teams prior to a clinically indicated neck MRI scan for staging of suspected HNSCC. Histological diagnosis was *not* required prior to recruitment to the study if there was a strong clinical suspicion of HNSCC, reflecting the routine clinical diagnostic pathway at NUH and ensuring that recruitment to the study did not delay or alter patients' routine diagnostic pathways.

4.7 Data handling

Patient demographics, tumour staging, treatment plans, post treatment FDG-PET scan outcomes, post-treatment MDT discussion outcomes and histological results of any post-radiotherapy treatment biopsies or surgical interventions were collected for all patient participants and stored in pseudo-anonymised case reporting forms. Patients treated with curative intent radiotherapy had their radiotherapy planning CT scans and treatment volumes pseudo-anonymised and exported from the NUH radiotherapy system to the study data repository.

Electronic study records were developed with backup hard copies printed for all documents and stored in a trial master file that was maintained by A. McCabe. All data was pseudo-anonymised, stored and analysed within NUH and only clinical staff had access to patient identifiable information. All electronic

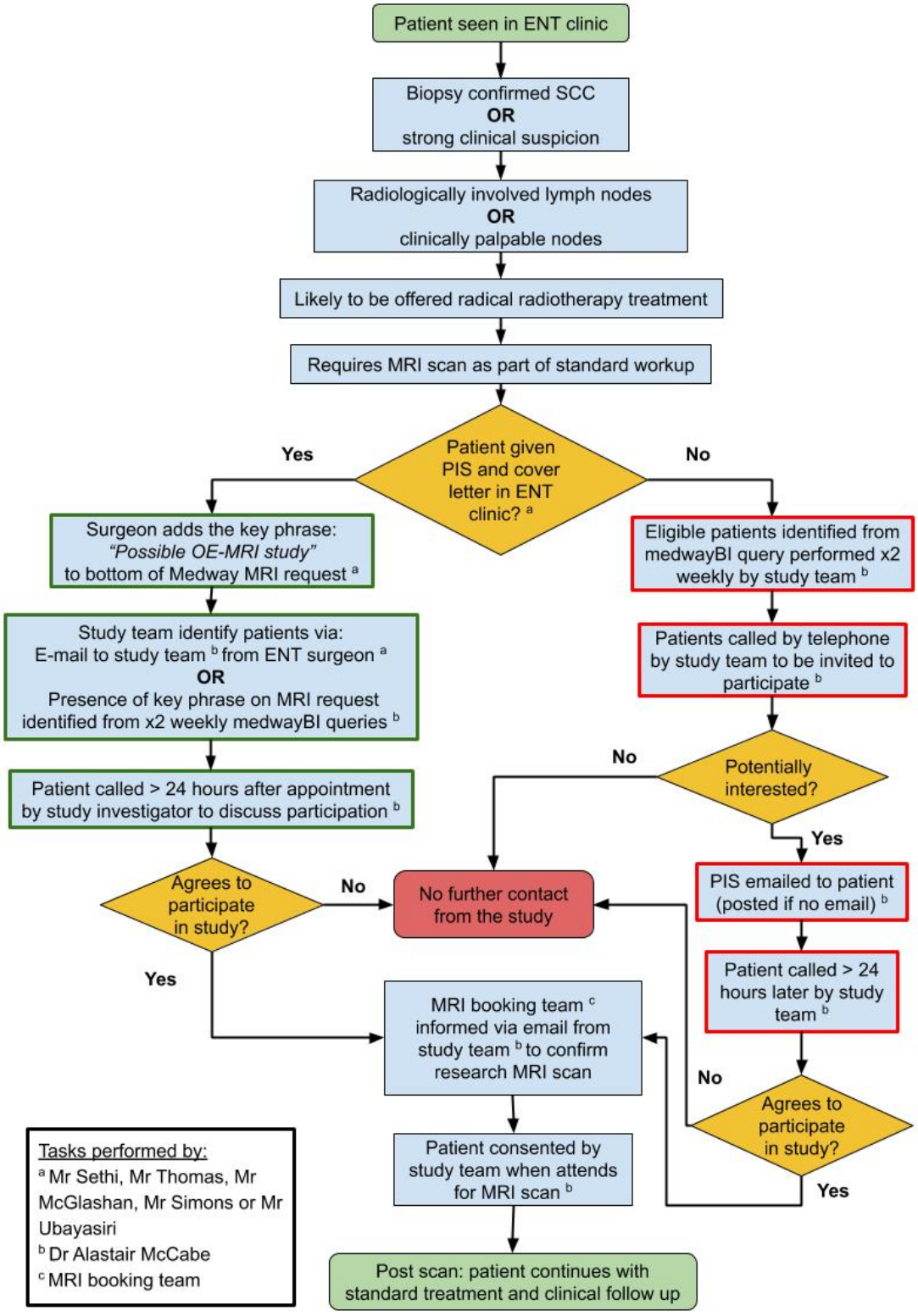

Figure 4.2: Patient recruitment flowchart - Flowchart from the research ethics committee approved study protocol illustrating the patient recruitment process.

data including study images were stored within NUH NHS password protected computers and systems. Paper documents were stored in fireproof, lockable cabinets in a secured NUH building. The study complied with the NUH Privacy Policy and the General Data Protection Regulations (GDPR) at all times.

Chapter 5

OE-MRI Study Development

5.1 OE-MRI sequence development

In order to rapidly and fully map tumour hypoxia via oxygen associated T_1 time shortening, a fat suppressed 3D-SPGR approach was utilised via a volumetric interpolated breath-hold examination (VIBE) sequence as the basis of the OE-MRI protocol. This sequence was chosen due to its rapid acquisition times and ability to be applied in a repeated manner over two different FA in order to dynamically map voxel T_1 times via the VFA approach (section 2.5.3). All participants were scanned on clinical Magnetom Sola 1.5T scanners (Siemens Healthineers, Erlangen, Germany). Parallel imaging techniques using controlled aliasing in parallel imaging results in higher acceleration (CAIPIRINHA) were available on the scanners and were applied to reduce the image acquisition time. Fat suppression was utilised to minimise the risk of off-resonance artefacts. In-plane phase encoding was placed in the anterior-posterior direction to minimise the risk of wrap artefact from the shoulders.

The imaged field of view (FoV) was set to be larger enough to encompass the whole of the clinically relevant neck region. Image resolution was developed to be broadly isotropic in order to facilitate the aim of fusing OE-MRI derived parametric maps with radiotherapy treatment planning computed tomography (planning-CT) scans. Head and neck cancers are routinely planned for radiotherapy using 3mm thick planning-CT slices (Machiels et al. 2020), thus the OE-MRI sequence was built to have a slice thickness below this threshold whilst keeping

the total study imaging time to less than approximately 10 minutes in order to address the research aim of developing an OE-MRI protocol that could be readily implemented into routine clinical practice.

VIBE sequences with two sets of image contrast parameters were constructed; a shorter TR (4.2ms) sequence with higher temporal resolution, and a longer TR of 10ms sequence with a cruder temporal resolution but with predicted higher signal to noise ratio (SNR). There is a consequential decrease in the number of acquired dynamics with the longer TR sequence in order to maintain a comparable overall OE-MRI acquisition time. The FAs of the sequences were set with the aim of maximising the accuracy of the T_1 determination. As shown by Deoni et al. (2003), for a given TR time in a SPGR sequence, the optimised FAs can be determined as a function of the imaged tissues T_1 relaxation time (figure 5.1). Therefore, assuming baseline HNSCC tumour T_1 times of $\approx$ 1200ms at 1.5T (data provided by personal correspondence with the INSIGHT study team (Wong et al. 2016)), the precision in VFA determined T_1 times is optimised with FA of approximately 18° and 2° .

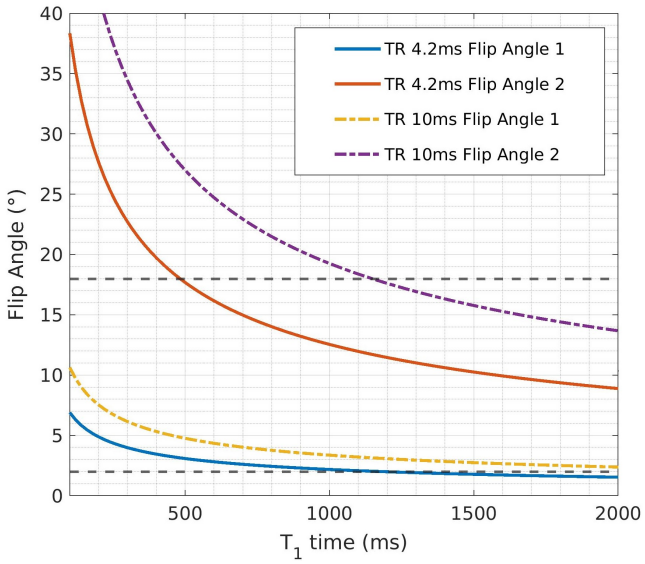

Figure 5.1: Theoretical optimal FA values - Plot of FA against T_1 times for the theoretical two FA required to optimise determination of T_1 times using the VFA methodology for two different TR times (4.2ms and 10ms).

R_2^* mapping was performed in a static manner with a single acquisition performed on room air prior to the T_1 mapping sequence and repeated immediately after the dynamic T_1 acquisition with participants remaining on high flow oxygen for this measurement. A manufacturer supplied sequence based on a multi-echo GE sequence with a multi-step adaptive approach (qDixon) was used to quantify R_2^* relaxation rates (Zhong et al. 2014).

Prior to the OE-MRI sequences, anatomical sequences were used to locate the tumour regions to guide placement of the field of view. A T_2 weighted coronal acquisition (duration 2:08 min:s) was followed by a DWI sequence with two b-values of 50 s/mm^2 and 800 s/mm^2 (duration 1:30 min:s). Due to differences in voxel sizes and imaged volumes between the DWI and VIBE sequences and the presence of signifincant image distortion on the DWI images, it was not possible to compare the DWI and OE-MRI data. The DWI sequence was therefore only used to aid tumour localisation. The order of the study sequences is shown in figure 5.2 with the final acquisition parameters for the Siemens quantitative multi-echo Dixon protocol (qDixon) and VIBE sequence given in table 5.1.

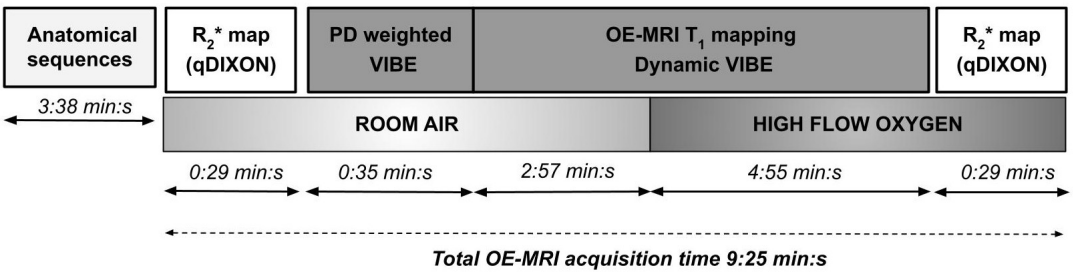

Figure 5.2: Study sequences - Study sequences and timing of switch from room air to high flow oxygen. Sequence parameters for the OE-MRI acquisition are provided in Table 5.1. Anatomical sequences consisted of a T_2 weighted coronal acquisition (duration 2:08 min:s) and a DWI sequence with two b-values (duration 1:30 min:s).

All scans were performed by state registered radiographers and supervised by A. McCabe. Following acquisition of initial anatomical sequences, study imaging volumes were decided upon by A. McCabe and set on the scanners by the radiographers. The scan volume was duplicated for all subsequent study sequences

Table 5.1: Acquisition parameters for the study sequences. Values in parentheses represent the initial imaging protocol reviewed after the first three non-patient volunteers and two patients. *3D* Three-dimensional.

Sequence name	**VIBE**	**qDixon**
Sequence type	3D spoiled gradient-echo	3D multi-echo Dixon
Orientation	Axial	Axial
Repetition time (ms)	10 (4.2)	15.6
Echo time (ms)	1.27 (1.48)	Range 1.10 to 14.28 with 12 echoes
Flip angle (α)	2 / 18	4
Bandwidth (Hz/pixel)	399 (313)	1090
Matrix	128×128	96×96
Field of view (mm^2)	200×200	200×200
Slice thickness (mm)	2.5	2.5
Number slices	72	72
Number acquisitions	Proton density: 3 (5) Dynamic: 40 (60)	1 pre- and post-oxygen
Oxygen on (min:s)	3:32 (2:09)	-
Acquisition time (min:s)	8:27 (5:35)	0:58
Single acquisition (s)	11.8 (5.15)	29

with the radiographers instructed not to make any amendments to the sequence parameters, including FoV size in order to ensure consistent acquisitions across all participants.

5.2 Participant Setup

As discussed in section 3.4.5, the majority of clinical OE-MRI studies use high flow oxygen aiming for as high a concentration of delivered oxygen as possible to maximise the magnitude of the potential induced tumour ΔT_1. However, in routine MRI clinical practice, head and neck cancer patients are scanned using a full head and neck receiver coil which by design comes close to the face making it potentially more difficult to appropriately position a non-rebreathe mask with reservoir bag.

During the study design, two different non-rebreathe masks were available as routine equipment at NUH (figure 5.3). Both masks were trialled inside the standard MRI head and neck receiver coil on non-patient volunteers however due to the different angles between the mask and the reservoir bag on the two brands of mask, only the Hudson RCI mask could fit inside the standard head and neck receiver coil. The fit with this mask was however very tight and would be challenging and likely impossible for patients with an increased body habitus. In addition, the non-patient volunteers who tried the Hudson mask inside the head coil but outside of the scanner bore, reported concerns with claustrophobia. Thus to make the study design as tolerable and ultimately translatable to all patients and different imaging departments with differing standard medical equipment, it was decided to use only the posterior elements of the head and neck receiver coil and to boost the anterior signal detection with an ultraflex large 18-channel coil positioned over the neck region but below the face. This therefore allows for easy positioning of the face mask with the rebreather bag positioned on top of this ultraflex coil to allow for unimpeded inflation of the bag.

In order to satisfy the research aim of making the OE-MRI protocol suitable for routine clinical use with routinely available equipment, it was decided to not use any form of gas mixer. Instead, participants breathed normal room air as opposed to medical air for the pre-oxygen acquisitions in order to avoid the

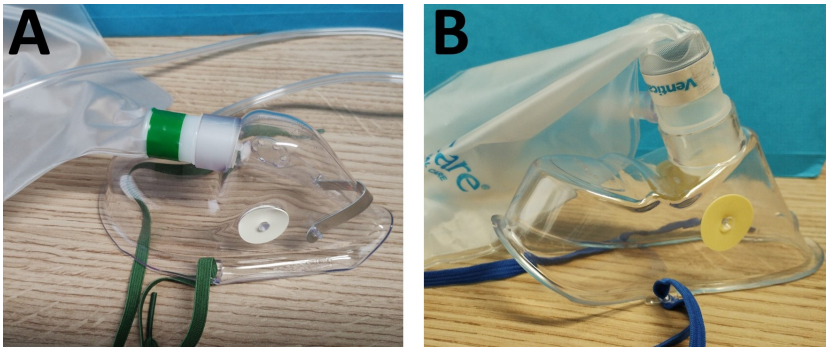

Figure 5.3: Non-rebreathe oxygen masks - **A** Hudson RCI non-rebreathe mask with two pull straps, metallic nose clip and single sided valve with a safety port on the contralateral side. Mask **A** was used for all non-patient volunteers and for the first 17 patient participants. **B** Flexicare non-rebreathe mask with two pull straps, moulded plastic nasal bridge and bilateral valves. Due to a change in local NHS supply chains, the final three patient participants in the study were scanned using non-rebreather mask **B** with one of the valves removed to allow for breathing on room air with no oxygen flow and to emulate the setup with mask **A**.

need for medical gas supply. This was possible due to the safety valves on the side of the non-rebreathe masks meaning that they could be safely used without supplemental gas delivery. Masks were securely fitted to the face of participants prior to the start of the research protocol using the standard straps and nose clips. The switch to room air was accomplished by a member of the research team entering the scanning room during the dynamic acquisition and commencing the high flow oxygen delivery without requiring any participant re-positioning. This did mean that participants did not have the opportunity to become accustomed to the gas delivery before oxygen was commenced. Participants were monitored for adequate inflation of the non-rebreather bag as a surrogate marker for delivery of high flow oxygen to the face mask. All oxygen delivery was supervised by a general medical council (GMC) registered clinician (A. McCabe).

All participants wore ear plugs and ear defenders inside the scanner and had a knee block positioned for comfort. An angled mirror was placed above participants' heads to enable them to see out of the scanner during the image acquisition. A demonstration of the participant setup without this mirror in place is shown in figure 5.4.

Figure 5.4: Participant setup - A member of the research team modelling the participant setup. The posterior component of the head coil is used together with an ultraflex large 18-channel coil positioned over the neck region allowing ready placement of the non-rebreathe oxygen mask. The non-rebreathe bag was positioned on top of the ultraflex coil. Study participants wore ear plugs and ear defenders and did not wear a surgical face mask during the scan.

5.3 Phantom assessment of VIBE OE-MRI sequence

Prior to clinical experiments, the VIBE T_1 mapping sequence was evaluated on an MRI phantom in order to assess the accuracy, temporal stability and spatial uniformity of T_1 determination using the VFA methodology and the study dynamic VIBE sequence.

5.3.1 Method

The accuracy of the VFA T_1 mapping was assessed relative to a reference standard of IR based T_1 determination (section 2.5.1). A Eurospin TO5 phantom with 18 sets of replaceable gel-filled tubes with varying T_1 times (*T1 & T2 EUROSPIN Gels* 2015) was scanned with a single acquisition of the study VIBE sequence (table 5.1) along with a single slice TSE IR sequence (14 TI ranging from 23ms to 2000ms, TR 5000ms, echo train length (ETL) 16, slice thickness 20mm) using the head and neck receiver coil. IR based T_1 values were determined using average signal intensity values from circular regions of interest (ROI) with diameters 80% that of the gel tubes using non-linear least squares curve fitting to equation 2.10. VIBE T_1 values were determined on similarly defined ROI using equations 2.12 and 2.13.

Temporal stability was assessed using the same Eurospin TO5 phantom with 12 gel inserts and the head and neck receiver coil. The full dynamic VIBE sequence was performed and T_1 times determined for each of the 40 dynamic acquisitions in the same manner as per the T_1 accuracy assessment. This was performed on both of the clinical 1.5T MRI scanners that were used in the subsequent clinical study.

Uniformity across the imaged volume of the study VIBE sequence was assessed via imaging a large homogenous phantom using the study VIBE sequence and coil configuration (consisting of the posterior element of the head and neck receiver coil and an anteriorly placed ultraflex large 18-channel coil). Percent integral image uniformity (I) was assessed in accordance with the American association

of physicists in medicine (AAPM) definition:

$$I = \left[1 - \frac{(\overline{S}_{max} - \overline{S}_{min})}{(\overline{S}_{max} + \overline{S}_{min})}\right] \times 100, \tag{5.1}$$

where $\overline{S}_{max}$ is the maximum signal intensity and $\overline{S}_{min}$ is the minimum signal intensity as measured in a homogeneous phantom in a ROI that comprises at least 75% of the cross-sectional area of the phantom. For scanning commissioning of a head receiver coil AAPM recommend that in-plane integral uniformity should be at least 90% on a 1.5T scanner (Jackson et al. 2010).

5.3.2 Results

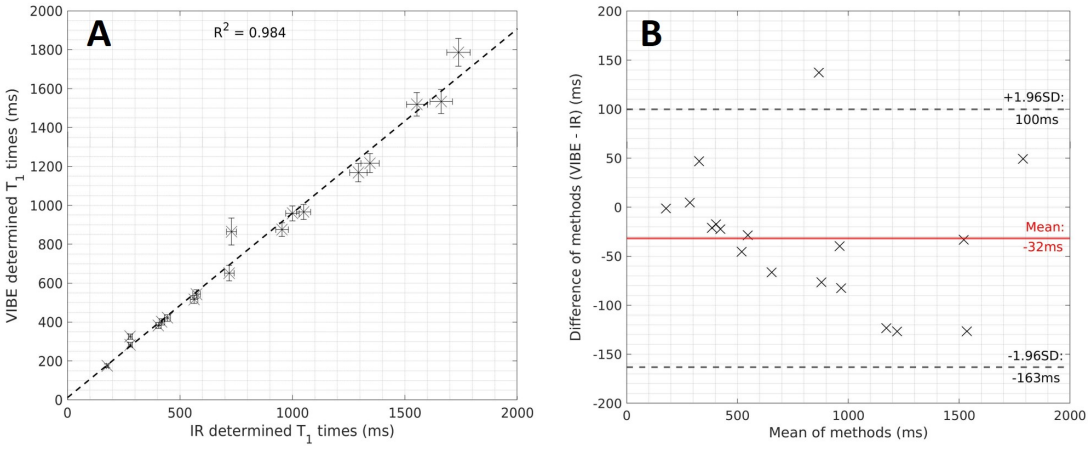

Figure 5.5: T_1 times methodology comparison - Plot of VIBE VFA determined T_1 measurements versus reference IR method for 18 different gel-filled vials scanned in two batches in a Eurospin TO5 phantom with dashed line indicating linear line of best fit with coefficient of determination (R^2) of 0.984 (**A**). Corresponding Bland-Altman plot with difference in T_1 times defined as VIBE minus reference IR (**B**). Mean difference = -32ms (95% CI -65ms to 2ms, p=0.0620 1-sample t-test).

Figure 5.5 shows plots of VFA determined T_1 times versus IR based method and the corresponding Bland-Altman plot. There is a strong linear relationship between the two methods (Pearson's correlation coefficient = 0.992, $p < 0.001$). The VFA method on average underestimates T_1 times relative to IR determined

Table 5.2: Temporally averaged T_1 times from ROI in 12 gel-filled tubes in a Eurospin TO5 phantom with corresponding coefficient of variation (CoV). *CoV* - coefficient of variation.

	Scanner 1		Scanner 2	
Vial	**Mean T_1 (ms)**	**CoV (%)**	**Mean T_1 (ms)**	**CoV (%)**
1	412	0.3	432	0.4
2	878	0.3	913	0.1
3	422	0.2	438	0.2
4	553	0.3	574	0.4
5	159	0.2	158	0.2
6	529	0.2	591	0.3
7	329	0.2	262	0.3
8	877	0.2	702	0.4
9	658	0.3	673	0.4
10	1514	0.4	1613	0.5
11	260	0.1	301	0.3
12	382	0.3	393	0.3
	Median	0.2		0.4
	Range	0.1-0.4		0.2-0.5

Table 5.3: Integral uniformity values based on equation 5.1 in a homogenous phantom using VIBE acquisition with FA = 2° and 18°. Uniformity values were determined using individual voxel minimum and maximum signal intensity values on central slices in all 3 planes for 75% of the phantom area in each plane.

	Integral uniformity (%)	
	PD weighted (FA = 2°)	T_1 weighted (FA = 18°)
Axial	91.7	93.8
Coronal	86.9	90.4
Sagittal	80.2	86.0

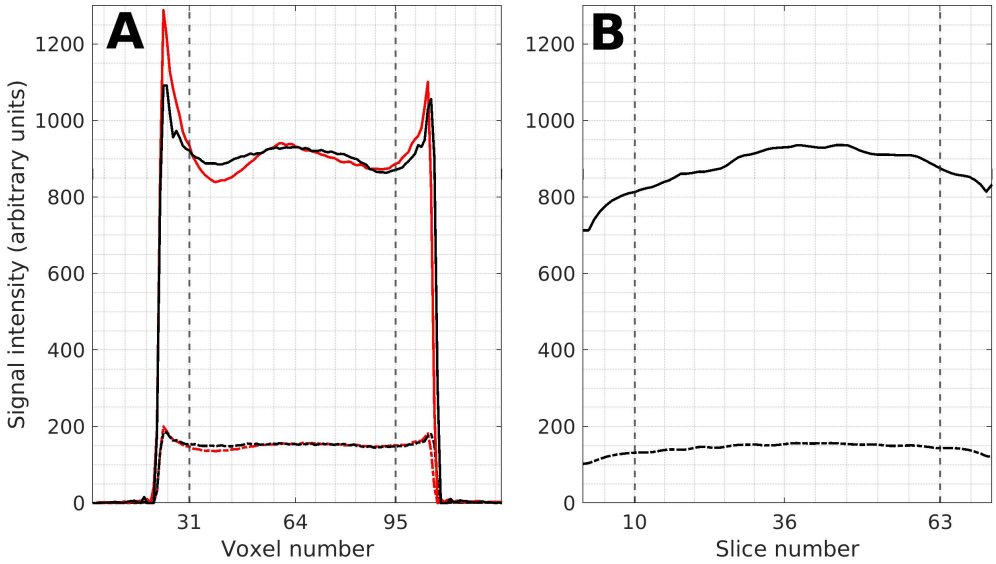

Figure 5.6: Line profiles through homogenous phantom - **A** with black indicating central line profiles in the left-right (frequency encode) direction and red in the anterior-posterior (phase encode) direction. **B** central line profiles in the cranio-caudal (slice) direction. Solid lines refer to acquisitions with flip angle 2° and dashed lines flip angle 18°. Vertical dashed lines indicate the central 75% region.

values by 32ms (95% confidence interval -65ms to 2ms, p=0.062 via 1-sample t-test), albeit with the magnitude of this underestimation tending to increase for longer T_1 times.

coefficient of variation (CoV) for the dynamic T_1 measurements for both of the assessed scanners are presented in table 5.2 with a plot of T_1 values from the dynamic phantom acquisition for all 12 gel phantom inserts for scanner 1 shown in appendix figure A.1. The T_1 values show good temporal stability with median CoV of 0.2% (range 0.1% to 0.4%) for scanner 1 and 0.4% (range 0.2% to 0.5%) for scanner 2.

Line profiles through the homogenous phantom are shown in figure 5.6 with corresponding integral uniformity values in table 5.3. Axial integral uniformity is greater than 90% for both proton density weighted and T_1 weighted VIBE acquisitions.

5.3.3 Discussion

As OE-MRI is dependent upon changes in T_1 times then the absolute accuracy of T_1 values is arguably of lesser importance than the combination of the linearity of the VFA determined times to the reference standard and the temporal stability over the duration of the OE-MRI dynamic acquisition. We found both a strong linear relationship between the VFA and IR methods in the phantom albeit with the VFA methodology on average slightly under-estimating the T_1 times relative to the IR data (statistically non-significant difference of -32ms) as well as temporally stable T_1 times with the greatest observed CoV over the 8:27 min:s that the dynamic VIBE sequence took to acquire being only 0.5%. Although there are apparent differences in the measured T_1 times between the scanners, it should be borne in mind that these measurements were taken on different days in different environmental conditions, with potentially different ambient temperatures which could affect the true value of the individual gel T_1 times.

Regarding image uniformity, for commissioning of a head receiver coil AAPM recommend that integral uniformity should be at least 90% on a 1.5T scanners. Given that the study setup uses only the posterior element of the head coil with the anterior flex coil, it might be expected that image uniformity be negatively

affected. However the axial plane uniformities meet this 90% threshold. The line profiles in figure 5.6 show the expected signal changes at the extreme ends of the field of view. Overall the image uniformity with the VIBE sequence is considered acceptable.

In summary, the VIBE sequence for VFA determined T_1 measurements shows a strong linear response relative to IR based measurement. The measurements indicate very good temporal stability over the duration of the clinical dynamic VIBE sequence with acceptable levels of uniformity using the study receiver coil setup consisting of the posterior part of the head coil with an ultraflex large 18-channel coil anteriorly. The sequence was therefore considered acceptable for utilisation in the clinical study.

5.4 Data analysis code

A schematic diagram of the data processing steps for the imaging acquired in this study is shown in figure 5.7. Initial image pre-processing consisted of converting the acquired imaging data to neuroimaging informatics technology initiative (NIfTI) format from the native digital imaging and communications in medicine (DICOM) standard using statistical parametric mapping version 12 (SPM12), correcting for motion via non-rigid registration using advanced normalization tools (ANTs) (chapter 6) and delineating study volume of interest (VOI) using ITK-SNAP software. Conversion to NIfTI was performed due to the simplified nature of the NIfTI format and its wider compatibility with research based software (Li et al. 2016).

Following the pre-processing, image analysis was performed using software developed by A. McCabe in MATLAB (Mathworks, version R2018b). 3D T_1 maps were generated on a voxel-wise basis using the VFA methodology (section 2.5.3) for each dynamic acquisition in the study sequence. Summary statistics for processed VOIs were automatically determined. Additional processing modules were written by A. McCabe to allow for the processing of acquired R_2^* data, derivation of ΔT_1 statistical maps, derivation of Bootstrap derived statistics and calculation of SNR metrics (section 6.3). In addition, display of parametric maps and plots of T_1 time series were encoded for in the program to allow for interactive

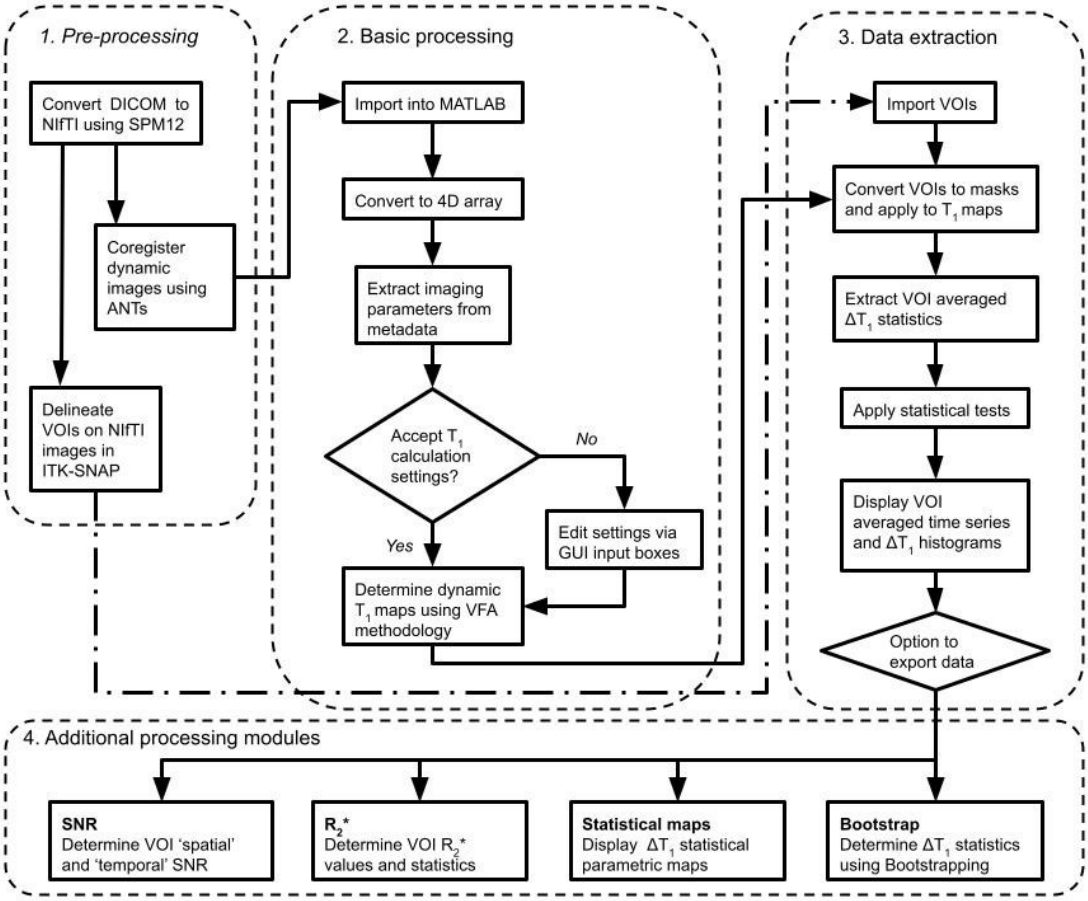

Figure 5.7: Code flow diagram - Study sequence processing flow chart. Section 1 (pre-processing) is performed using publicly available software (as detailed). Sections 2 to 4 are performed using custom written MATLAB scripts. Interaction with the custom written scripts was via a custom written graphical user interface. *ANTs* - Advanced Normalization Tools, *DICOM* - Digital Imaging and Communications in Medicine, *GUI* - Graphical User Interface, *NIfTI* - Neuroimaging Informatics Technology Initiative, *SNR* - Signal to Noise Ratio, *SPM12* - Statistical Parametric Mapping version 12, *VFA* - Variable Flip Angle, *VOI* - Volume of Interest.

exploration of the data. Example screen shots from the developed MATLAB interface are shown in figure 5.8.

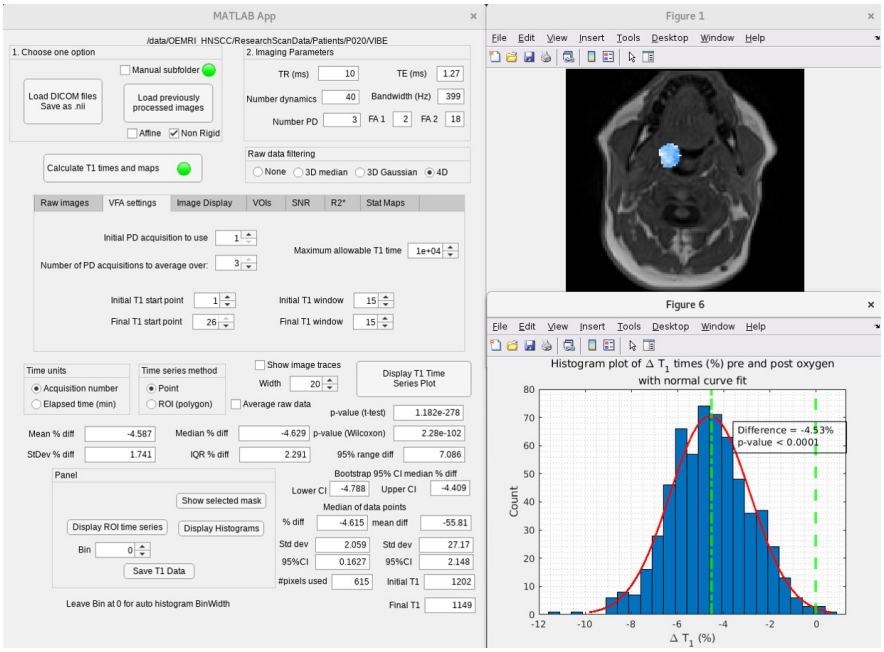

Figure 5.8: Example processing software screenshot - *Left* - Screengrab showing the main graphical user interface for processing the OE-MRI data. Imaging parameters are automatically determined from the image data files with processing parameters adjustable using drop down selection menus and button selection boxes. Data analysis results are presented in text boxes and as graphical outputs. *Right* - two examples of visual outputs from the custom written MATLAB code showing an overlay of an OE-MRI parametric map for a primary tumour on a T_1-weighted MRI scan (*top*) and a histogram of ΔT_1 times from the primary tumour volume (*bottom*).

5.5 CSF based F_iO_2 estimation

The hyperoxic challenge in this study was delivered using non-rebreathe masks with high flow oxygen (15L min^{-1}) as this offers the highest fraction of inspired oxygen (F_iO_2) delivery using routinely available equipment in the NHS (figure 5.3). Non-rebreathe masks have a reservoir bag connected to an oxygen supply

and usually two one-way valves; one between the mask and the reservoir bag and the other from the mask to the outside world. On inhalation the valve to the reservoir bag opens allowing the stored oxygen to be inhaled. On exhalation, the reservoir bag valve closes and the valve to the outside world opens allowing the exhaled gas to escape the mask and not re-enter the reservoir bag. In theory this allows for almost pure oxygen to be inhaled.

However, most clinically used non-rebreathe masks have an additional non-valved air inlet on the side of the mask that serves as a suffocation avoidance safety feature allowing air to enter the mask and be inhaled by the wearer in the absence of an oxygen supply. This results in dilution of the delivered oxygen concentration when the oxygen delivery is on. In addition, although non-rebreathe mask are attached to the wearer's face with pull straps and a nose bridge clip to provide a secure seal between the mask and the face, the obtainable seal is not perfect. This further dilutes oxygen in the reservoir bag with the net result that the actual inspired F_iO_2 concentration is typically between 60% and 90% (Boumphrey et al. 2003, O'Driscoll et al. 2008).

The clinically relevant outcome from OE-MRI is the absence of T_1 shortening during hyperoxia. However an absence of T_1 shortening will also be found if no supplementary oxygen is delivered to the end organ of interest. In addition, the magnitude of any T_1 shortening is proportional to the delivered F_iO_2 and so lower delivered F_iO_2 will result in a smaller magnitude of T_1 shortening, potentially below the minimum measurable level. It is not known what inspired oxygen concentration is required in OE-MRI for head and neck cancer to obtain ΔT_1 times with sufficient sensitivity for the detection of tumour hypoxia. Previous clinical OE-MRI studies in non head and neck sites have principally used high flow oxygen aiming to deliver as close to 100% oxygen as possible (section 3.4.5). The benefit of using a non-rebreathe mask delivery system is that they are universally available in hospitals and are quick and easy to use. However a quality control process to ensure adequate oxygen delivery has been achieved is required.

In order to evaluate the actual delivered oxygen concentration to tissues in the head and neck, a model to estimate delivered oxygen concentration was developed based upon oxygen induced changes in T_1 relaxation times of cerebrospinal fluid (CSF). Although not an organ of interest in relation to HNSCC, typical

CSF oxygen partial pressures and relaxivity coefficients have been documented in previous neuroimaging studies (Zaharchuk et al. 2005, Haddock et al. 2013, Mehemed et al. 2014, Bhogal et al. 2017). The cranial extent of the imaging field of view in this study includes the peri-brainstem CSF and was therefore considered a suitable location to use to derive a model to estimate actual delivered oxygen concentration for the 5 non-patient volunteers and first 5 patients.

5.5.1 Method

Starting with the partial pressure of oxygen in the cerebrovascular space ($P_{CSF}O_2$), Zaharchuk et al. (2005) determined that at 1.5T the linear coefficient $\delta R_1/\delta P_{CSF}O_2$ is $2.7 \times 10^{-4} s^{-1}$/mmHg where R_1 is the longitudinal relaxation rate ($R_1 = 1/T_1$). Assuming a linear relationship between $P_{CSF}O_2$ and P_aO_2, the change in $P_{CSF}O_2$ can be estimated as:

$$\Delta P_{CSF}O_2 = \frac{1/(\text{Hyperoxic } T_1) - 1/(\text{Baseline } T_1)}{2.7 \times 10^{-4}}. \tag{5.2}$$

In addition, the same authors determined that on room air the baseline $P_{CSF}O_2$ in the basilar cisterns is 65 ± 27 mmHg increasing to 130 ± 49 mmHg in the third ventricle. They observed no change in $P_{CSF}O_2$ in the lateral or third ventricles with the administration of 100% oxygen but noted faster R_1 relaxation rates in other CSF spaces (Zaharchuk et al. 2005). This is consistent with the findings from a Nottingham brain OE-MRI study that found hyperoxia induced CSF T_1 changes were significantly greater in the non-lateral ventricle CSF regions (McCabe et al. 2021).

In healthy individuals, P_aO_2 at standard body temperature on room air is 95 mmHg (McLaughlin 2007, Cloutier 2019). Assuming $P_{CSF}O_2$ is directly proportional to P_aO_2, the hyperoxic P_aO_2 can be estimated:

$$P_aO_2 = \frac{(\Delta P_{CSF}O_2 + 65) \times 90}{65}. \tag{5.3}$$

Due to physiological shunting the arterial partial pressure of oxygen (P_AO_2) is lower than alveolar pressure (McLaughlin 2007). This alveolar-arterial partial pressure of oxygen gradient (Aa) increases by approximately 1mmHg per decade of life and can be estimated as $Aa = P_AO_2 - P_aO_2 = \frac{(\text{Age}+10)}{4}$ (Hantzidiamantis &

Amaro 2021). However, the alveolar arterial partial pressure of oxygen gradient also varies with F_iO_2 (Mythen 2010). Assuming an increase in Aa of 6mmHg per 10% increase in F_iO_2, P_AO_2 can be expressed as:

$$P_AO_2 = P_aO_2 + \frac{(\text{Age} + 10)}{4} + \left(\frac{6}{0.1} \times (F_iO_2 - 0.21)\right). \tag{5.4}$$

F_iO_2 can be estimated from the alveolar gas equation:

$$P_AO_2 = P_iO_2 - \frac{P_ACO_2}{R} = (P_B - P_{H_2O}) \times F_iO_2 - \frac{P_ACO2}{R}, \tag{5.5}$$

where R is the Respiratory quotient = 0.8, P_B is normal barometric pressure = 760 mmHg at sea level, P_{H_2O} is water vapour pressure = 47 mmHg at sea level and P_ACO_2 is the alveolar partial pressure of CO_2 = 40mmHg in healthy individuals (Cloutier 2019). Combining equations 5.4 and 5.5 yields:

$$F_{iO_2} = \frac{P_AO_2 + \frac{40}{0.8}}{760 - 47} = \frac{P_AO_2 + 50}{713} = \frac{P_aO_2 + \frac{\text{Age}+10}{4} + 37.4}{653} \tag{5.6}$$

where P_aO_2 can be determined from equations 5.2 and 5.3 to obtain an estimate of the F_iO_2.

Peri-brainstem CSF VOI were constructed on 4 consecutive slices at the caudal end of the brainstem in the 5 non-patient volunteers and first 5 patient participants (figure 5.9) and median pre and post-oxygen CSF VOI T_1 times extracted. F_iO_2 estimations were derived based on equations 5.2, 5.3 and 5.6.

5.5.2 Results

A total of 9 peri-brainstem CSF VOI were constructed on the 5 non-patient volunteers and first 4 patient participants. It was not possible to construct a CSF contour for patient ID 2 due to artefacts in the T_1 maps at the cranial extent. CSF T_1 times and F_iO_2 estimates for the 9 participants are shown in table 5.4. Median F_iO_2 estimates were 54% (range 41% to 66%) across all 9 VOIs with a median of 56% (range 41% to 66%) for non-patient volunteers and 48% (range 47% to 57%) for patient participants.

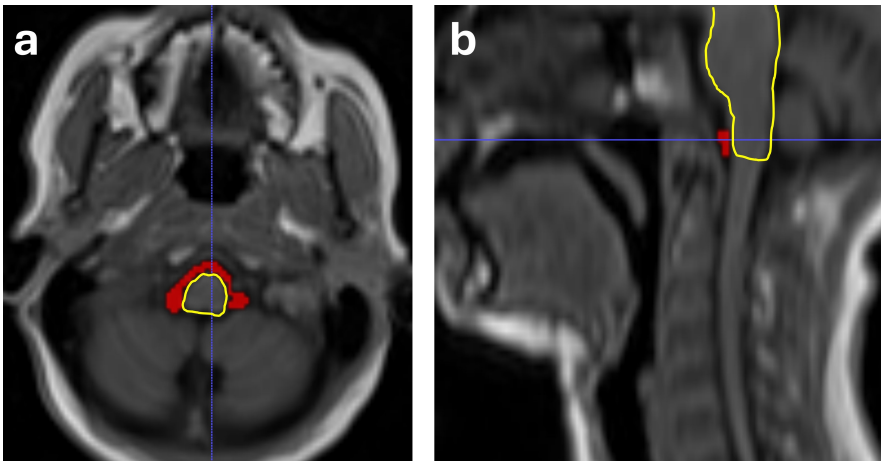

Figure 5.9: Peri-brainstem CSF region - Example from non-patient volunteer V5 of the peri-brainstem region (red) used for the estimation of F_iO_2. Volume is shown in the axial (**a**) and sagittal (**b**) planes and was constructed on the caudal 4 slices containing the brainstem (yellow contour).

Table 5.4: Estimates of F_iO_2 (%) and change in partial pressure of oxygen (ΔO_2, mmHg) derived from participants age and absolute difference in average peri-brainstem T_1 times pre and post supplemental oxygen delivery for the 5 non-patient volunteers (V) and first 5 patient participants (P). Patient ID P2 did not have data available as imaging artefacts were present across the peri-brainstem CSF region.

		CSF T_1 time (ms)		**Estimated values**	
ID	**Age (yrs)**	**Baseline**	**Hyperoxic**	**ΔO_2 (mm/Hg)**	**F_iO_2 (%)**
V1	39	4372	3976	84	41
V2	32	2896	2586	153	56
V3	32	1593	1468	198	66
V4	60	3455	3019	155	58
V5	33	3795	3311	143	54
P1	54	1874	1770	116	49
P2	54	No CSF data		-	-
P3	45	2661	2467	109	47
P4	69	3544	3206	110	48
P5	66	3160	2803	149	57

5.5.3 Discussion

The derived F_iO_2 estimates are lower than the 60% to 90% oxygen delivery concentration that is stated to be achievable with non-rebreathe masks and significantly lower than the 100% F_iO_2 used in some pre-clinical animal OE-MRI studies (section 3.4.5). However, despite the significant assumptions and limitations in the methodology used to derive these estimates the results are broadly similar across all participants suggesting consistency of oxygen delivery with this scanning setup. In addition to the limitations previously detailed, further assumptions made include that there is no impairment of gas exchange or of oxygen transport in any of the participants which is unlikely to be true in smokers, and that P_ACO_2 does not alter with hyperoxia. The FAs used in the T_1 mapping sequence were also optimised for determining the T_1 values of primary tumours and not the longer T_1 times of CSF which may affect the accuracy of the determined T_1 times. The peri-brainstem CSF region is towards the cranial limit of the FoV of the scanning sequence and although it was possible to analyse VOIs in all bar one of the 10 participants that this was attempted on, it may be a region that is outside of the scanning FoV on some patients in clinical practice.

Although this model was used to estimate F_iO_2, the more clinically relevant parameter for OE-MRI is the actual delivery of increased oxygen concentrations to end organs and tissues. Such delivery can be affected by pulmonary and vascular differences between patients that could result in significantly different magnitudes of end organ oxygen delivery for the same F_iO_2, which in turn could affect the sensitivity of OE-MRI for detecting tumour hypoxia. The utility of assessing oxygen induced changes to peri-brainstem CSF as a marker of oxygen delivery to end organs and tumours in the head and neck region is also of uncertain benefit as the physiology of oxygen delivery to CSF is different from that to solid tissues, a phenomena which partly explains the differing responses of distinct CSF regions to hyperoxia (Zaharchuk et al. 2005, Mehemed et al. 2014, Bhogal et al. 2017, McCabe et al. 2021). However, to quantify delivered oxygen concentrations to end organs requires knowledge of the relaxivity of oxygen in the particular tissue of interest, a parameter that is not well characterised for tissues and organs in the head and neck.

The relaxivity of oxygen in CSF value of 2.7×10^{-4} s^{-1}/mmHg used here came from experimental data however Bluemke et al. (2022*b*) have also developed an empirical model to estimate oxygen relaxivity for water, saline, plasma and vitreous fluid based upon field strength, temperature and 4 constants. For a 1.5T scanner, assuming a standard temperature of $37°C$ this model returns an oxygen relaxivity of 2.9×10^{-4} s^{-1}/mmHg, comparable to the experimental CSF relaxivity value previously quoted. As seen in table 5.4 for the patient participants the median increase in oxygen partial pressure in CSF was 113.5mmHg (range 109mmHg to 149mmHg), representing a broadly consistent significant increase of greater than 170% compared to an assumed CSF baseline of 65mmHg (Zaharchuk et al. 2005). The relation of this to changes in head and neck tissue and organ partial pressures is however uncertain. In the absence of reliable knowledge of *tissue* oxygen relaxivity constants, qualitative assessments of adequate end organ oxygen delivery through changes in healthy tissue T_1 times will likely need to suffice as a quality control check in clinical OE-MRI assessments.

In conclusion, the model presented suggests relatively consistent F_iO_2 delivery and consequential increase in CSF partial oxygen pressures with the use of a clinical setup consisting of a non-rebreathe mask and no gas mixer but does not provide a method for confirming definitive increase in oxygen delivery to end organs and tissues in the head and neck.

5.6 Conclusion

An OE-MRI sequence was developed for scanning the head and neck region that takes only 10 minutes to perform and uses only routinely available equipment. The participant setup was carefully designed to ensure that high flow oxygen could be delivered to participants with a range of body habitus using any of the routinely available non-rebreathe masks. The OE-MRI sequence was evaluated using MRI test phantoms and demonstrated adequate performance. In-house written software was developed to process and analyse the OE-MRI data. Measured changes in CSF T_1 times from initial clinical scans were used to estimate concentration of delivered supplemental oxygen.

Chapter 6

Dynamic OE-MRI image co-registration

6.1 Abstract

Background and Method

OE-MRI is susceptible to participant motion generated artefacts due to the nature of the dynamic image acquisition. Image registration approaches to correct for such motion were applied to the imaging datasets of 5 non-patient volunteers and 5 patients with suspected HNSCC using a 3D deformable (non-rigid) and affine registration. Clinically relevant VOI were delineated on initial dynamic images and deformed using inverse transformations into all time points for the dynamic series of images. Deformed VOI were compared using centre of gravity (CoG) displacements, Dice similarity coefficients and Hausdorff distances as well as temporally weighted SNR. Dynamic T_1 times were calculated and maps of change in T_1 time (ΔT_1) derived for unregistered and registered data.

Results

VOIs showed generally larger magnitude of motion compensation with non-rigid registration compared to affine transformation. All VOIs with the exception of brainstem showed statistically significant greater increase in SNR with non-rigid registration compared to affine. ΔT_1 maps show similar VOI averaged ΔT_1 times with all registration approaches but with narrower range of ΔT_1 times for non-rigid registration.

Conclusion
Non-rigid image registration of dynamic OE-MRI results in better motion compensation as evidenced by improvement in VOI SNR values and reduction in the range of derived individual voxel ΔT_1 times compared to affine registration. Non-rigid image registration should be a routine component of the processing pipeline for OE-MRI in the head and neck.

6.2 Introduction

OE-MRI in the head and neck region has the potential to produce 3D maps of the heterogeneous distribution of oxygen within HNSCC. By performing repeated measures during supplementary oxygen delivery, the oxygenation characteristics of individual tumour voxels and dynamic information on the kinetics of oxygen enhancement can be obtained. Such dynamic imaging is performed over multiple minutes and is therefore subject to motion artefact and dynamic image misregistration caused by either gross patient movement or internal motion and local tissue deformation. Misregistration events pose the risk of artifactually increasing or decreasing calculated ΔT_1 times for a particular voxel which could lead to erroneous interpretation of a voxel's oxygenation status and therefore impair the utility of OE-MRI in guiding therapeutic approaches based upon tumour hypoxia.

The risk of misregistration is particularly significant in the head and neck anatomical region due to the combination of the physiology of this region resulting in local tissue deformation and the relatively small size of the clinically relevant volumes of interest (Gurney-Champion et al. 2018, Bruijnen et al. 2019). It also varies significantly by subsite with hypopharyngeal and laryngeal regions showing greater movement than in the oropharynx (Gurney-Champion et al. 2018). An example of uncorrected participant motion for a patient participant in this study is shown in figure 6.1 where significant motion occurring over the duration of the dynamic imaging can be seen with both gradual drift in the participant's position as well as at least one occurrence of abrupt movement despite instructions to the participant to remain as still as possible during the imaging. The corresponding images after the application of non-rigid image registration are shown in figure 6.2.

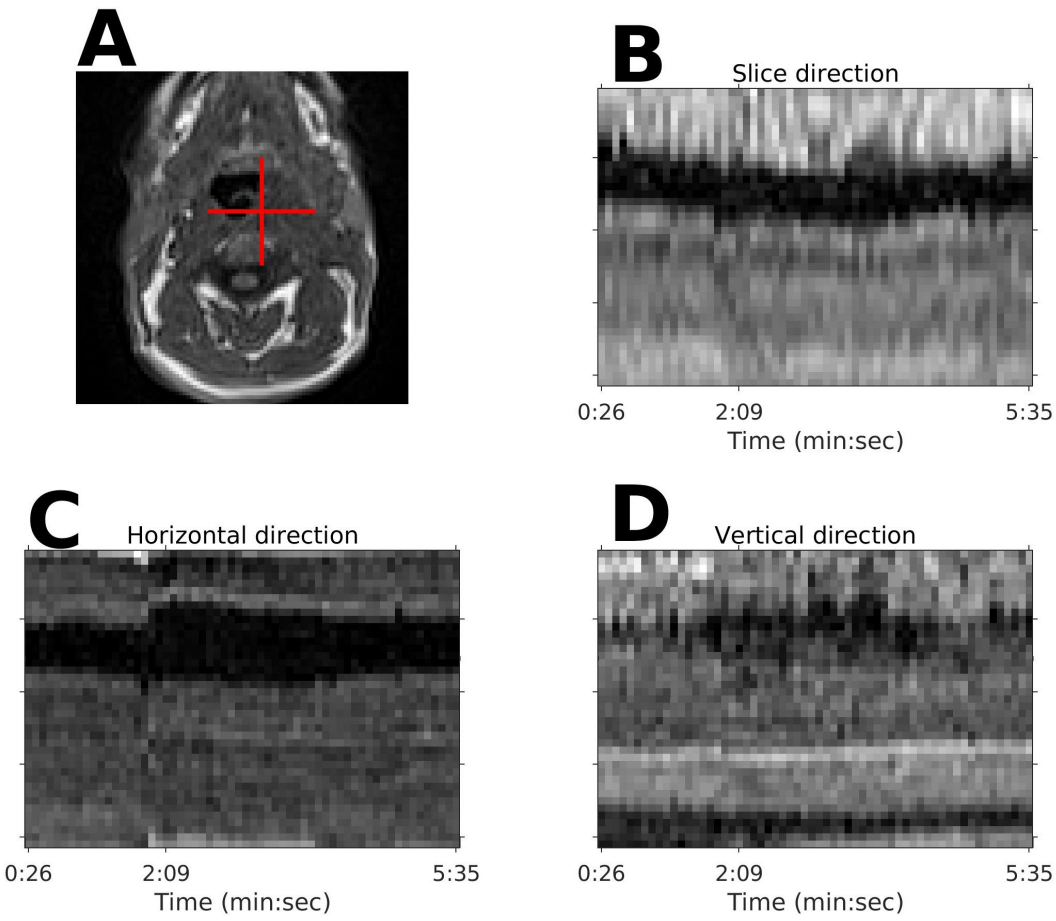

Figure 6.1: Example of uncorrected patient motion - Example of motion during dynamic OE-MRI acquisitions for patient participant ID 1. **A** T_1 weighted image with red cross indicating the voxel of interest through which line profiles for each dynamic acquisition in the slice, horizontal and vertical directions are shown (**B** to **D** respectively). Gradual drift in the participant's position can be appreciated in all 3 planes, with abrupt movement noted at approximately 2min (most clearly seen in panel **C**). Corresponding images after non-rigid image registration in figure 6.2.

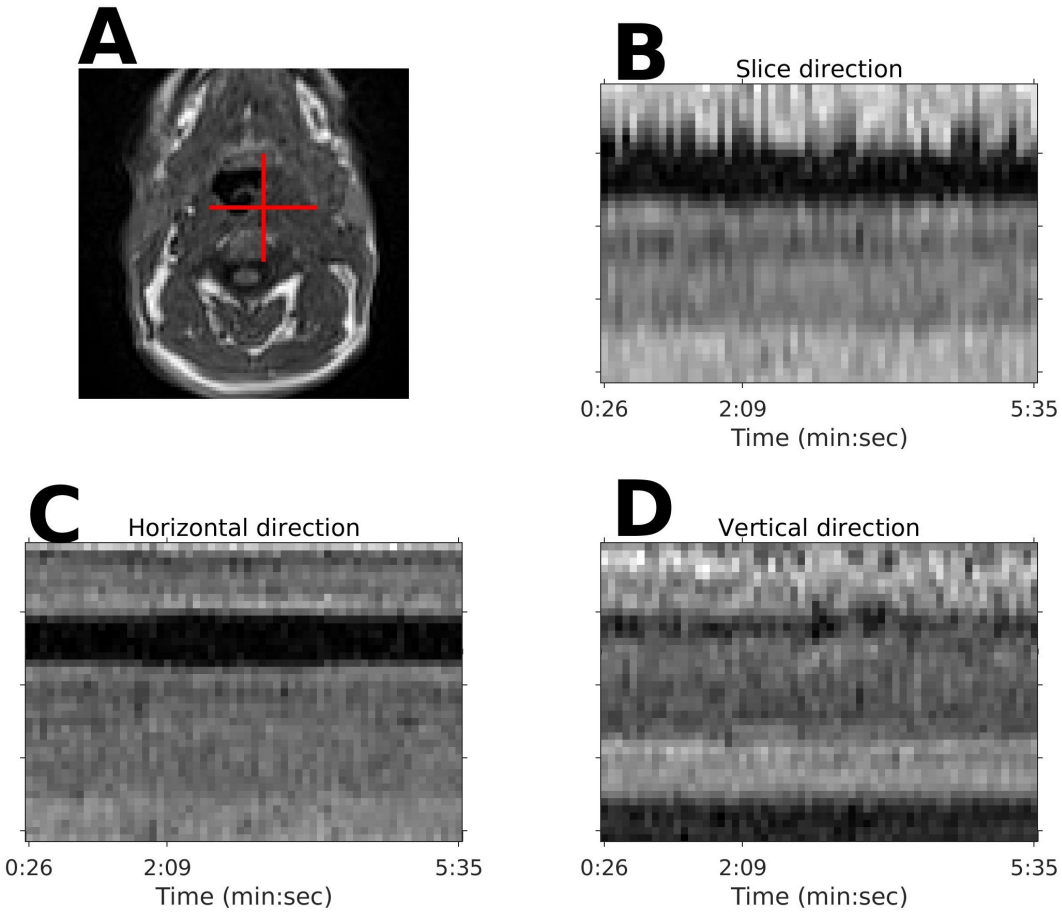

Figure 6.2: Example of corrected patient motion - Example of corrected movement of dynamic Vibe acquisitions for patient participant ID 1. Motion was corrected using nonrigid coregistration of each dynamic acquisition to the first acquired image. **A** T_1 weighted image with red cross indicating the voxel of interest through which line profiles for each dynamic acquisition in the slice, horizontal and vertical directions are shown (**B** to **D** respectively). Corresponding uncorrected images in figure 6.1.

In order to correct for patient motion during acquisitions, it is necessary to apply some form of image registration to align each of the dynamic images. Medical imaging registration approaches are routinely deployed in a range of medical areas including radiotherapy treatment planning in order to co-register planning-CT scans and diagnostic imaging to aid tumour volume delineation as well as motion correction in other dynamic diagnostic imaging modalities such as DCE-MRI (Hamy et al. 2014). One of the significant challenges with image registration in DCE-MRI is that the IV contrast agent that is administered during the image acquisition (gadolinium based compounds), significantly alters the T_1 relaxation time in areas where the agent accumulates meaning that successive images in the dynamic series can have drastically different appearances thus compounding registration approaches reliant on image signal intensity (Jansen et al. 2019, Hamy et al. 2014). In OE-MRI however, the magnitude of the expected change to T_1 times and thus signal intensity change is significantly smaller (O'Connor et al. 2019). Conventional pairwise image registration approaches whereby successive images are coregistered into the imaging space of the initial acquisition may therefore be adequate for OE-MRI.

Different registration approaches exist; rigid registration allows only translation and rotation between the two image sets and is in effect a special case of an affine transformation which additionally allows scaling and shearing of the image set being transformed. In the head and neck region however, localised tissue deformations occur due to physiological functions such as swallowing and breathing. Such localised distortions are unlikely to be adequately corrected using affine transformations and thus require registrations that can deform the image set differentially across the volume. Such deformable or non-rigid registration algorithms exist and although they can be computationally intensive, offer the potential for more accurate image co-registration. The application of 3D image co-registration algorithms as an image pre-processing step in dynamic OE-MRI in the head and neck region has not previously been formally assessed. In this chapter the utility of performing image co-registration on head and neck OE-MRI datasets using a 3D affine and deformable (non-rigid) registration is compared to undertaking no image co-registration.

6.3 Method

Five non-patient volunteers (median age 32 years, range 31 to 60 years) and the first five patients recruited to the study with suspected HNSCC (median age: 54 years, range 45 to 70 years) were included in the registration assessment. All participants were recruited and imaged as per the study protocol detailed in chapters 4 and 5.

Dynamic image acquisitions were corrected for motion using symmetric diffeomorphic (SyN) non-rigid registration algorithm implemented in ANTs (version 2.3.5) (Avants et al. 2011). 3D registrations were performed to the first dynamic acquisition of the dynamic VIBE series for each participant using the predefined script `antsRegistrationSyN.sh` with a three stage transformation type; rigid, affine, deformable (Appendix C). VOIs corresponding to 6 anatomical structures relevant for head and neck radiotherapy (brainstem, epiglottis, parotid glands, spinal cord, submandibular glands and thyroid gland) were outlined on the first dynamic of each acquisition using ITK-SNAP software (Yushkevich et al. 2006). Published guidelines on the delineation of normal structures in the head and neck region for radiotherapy planning were used to guide VOI delineation (Brouwer et al. 2015) (figure 6.3). VOIs were transformed to the original non-corrected image sets using the ANTs derived inverse transformations for both the three stage transformation (non-rigid) and the two stage transformation (affine) for each dynamic acquisition (figure 6.4).

Affine and non-rigid transformed VOIs along with original and corrected dynamic images were imported into MATLAB (R2018b, Mathworks). Dynamic data sets were initially inspected qualitatively for motion using cine images and intensity profiles (example in figure 6.1). Image registrations were quantitatively assessed using custom written MATLAB code for three metrics derived from the contoured VOIs:

1. Volume-based metrics using Dice similarity coefficients (DSC)

$$DSC = \frac{2|A \cap B|}{|A| + |B|}, \tag{6.1}$$

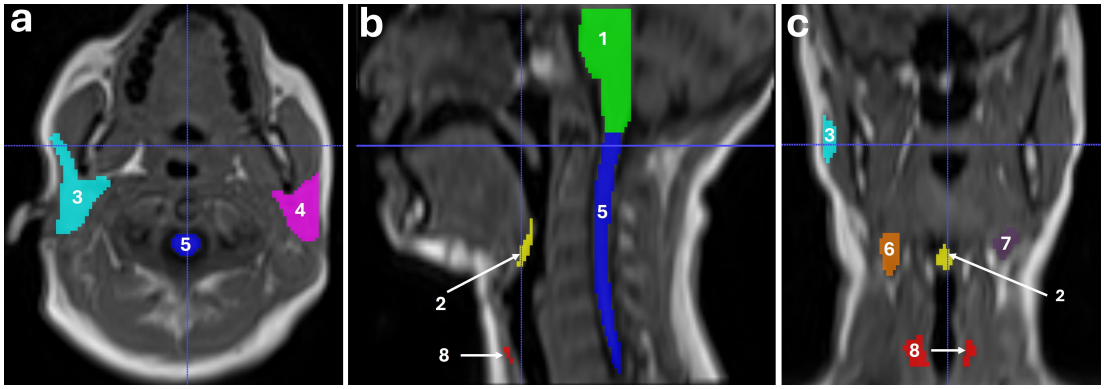

Figure 6.3: VOI delineation - An example from non-patient volunteer V005 of the delineated anatomical structures used for image registration assessment. VOIs for the brainstem (1), epiglottis (2), right and left parotid glands (3, 4), spinal cord (5), right and left submandibular glands (6, 7) and thyroid gland (8) are shown in the axial (**a**), sagittal (**b**) and coronal (**c**) planes.

where A and B represent the reference and transformed data sets and the DSC can take values between 0 and 1 (with 1 representing perfect overlap) (Dice 1945, Sherer et al. 2021).

2. Moment-based measurements using CoG displacement

3. Surface-based assessments via the Hausdorff distance; defined as the largest value from the set of distances generated from determining the closest distance from each point in the reference volume to the transformed volume with 0mm representing perfect overlap (Sherer et al. 2021).

The qualitative comparison of volumetric contours is a routine component of radiotherapy contouring studies including research using artificial intelligence (AI) to perform auto-contouring. The most commonly used metric to compare AI generated contours to a reference contour is the DSC with Mackay et al. (2023) finding that 96.6% of such research studies used this metric. DSC is appealing due to its ease of computation and quantification of the difference between entire volumes, however it has a lower sensitivity to complex boundary changes and is affected by volume bias whereby the DSC for a larger sized VOI is greater than for a smaller volume VOI for the same magnitude of contouring error. In addition,

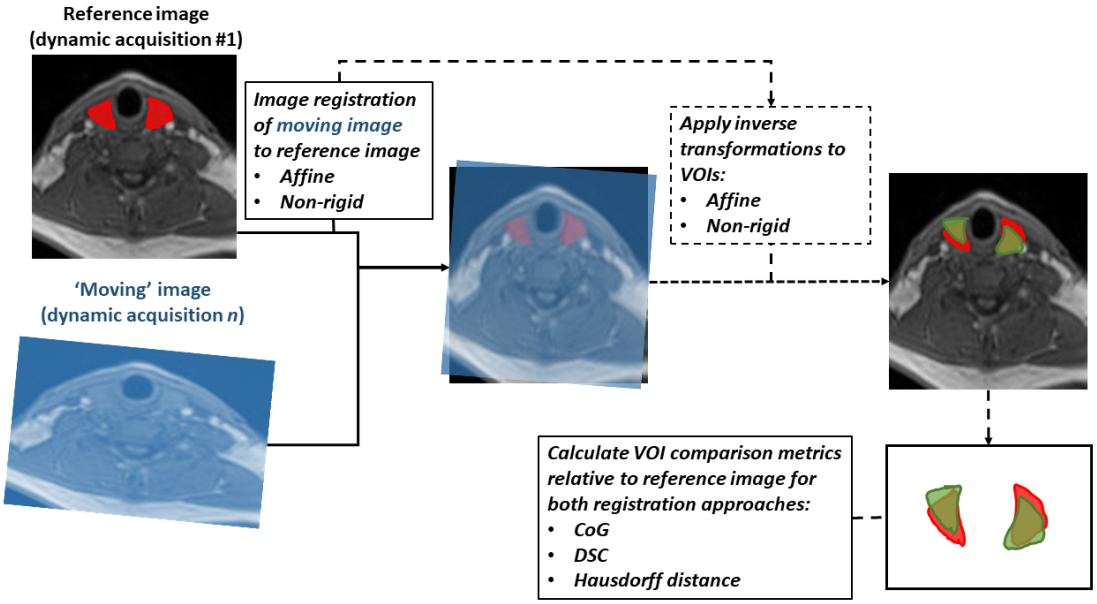

Figure 6.4: Registration assessment schematic - Diagram illustrating the registration assessment methodology. Dynamic images (exaggerated illustrative example shown in blue wash) were registered to initial dynamic acquisitions in a pairwise manner using affine and non-rigid registration via ANTs. Inverse registration transformations were then applied to VOIs that had been contoured on reference images. Example thyroid VOI shown in red for the reference VOI and green for a transformed version. Registration assessment metrics were calculated comparing the transformed VOIs to the reference VOIs.

there is evidence that DSC has mixed correlation with expert clinical opinion and as such caution is required in its use (Thor et al. 2011, Rohlfing 2012, Sherer et al. 2021). Consequently, DSC metrics were supplemented by CoG measurements to quantify changes to the central location of VOIs as well as Hausdorff distances as a sensitive indicator of changes in individual points on a contour (Sherer et al. 2021). The three registration metrics were determined for each dynamic acquisition and VOI for affine and non-rigid transformations relative to the initial acquisition. Differences between affine and non-rigid transformations were assessed via a paired t-test.

It is reasonable to assume that SNR parameters determined over the duration of a dynamic acquisition will show an increase in magnitude with increasing accuracy of image registration due to a reduction in motion induced voxel wise signal intensity variability. Although absolute SNR values are dependent upon a wide range of parameters including individual patient body composition and receiver coil setup location, relative increases in SNR values between unregistered and coregistered image datasets can give an indication of the utility of the registration approach. Therefore, as an indication of registration quality temporally weighted dynamic SNR measurements (SNR_T) were determined for each VOI and registration approach (Kousi et al. 2016, Bradley 2022):

$$\mathrm{SNR}_T(x, y, z) = \frac{\overline{A_R}(x, y, z)}{\sigma_{A_R}(x, y, z)}, \tag{6.2}$$

where $\overline{A_R}$ is the temporally averaged signal intensity for the central voxel of a ROI R consisting of 5 voxels, σ_{A_R} is the signal intensity standard deviation for R across all spatial and temporal dimensions. SNR values were determined in MATLAB using code modified from that kindly provided by Joe Bradley (Bradley 2022). Median SNR_T values were determined for each VOI and registration approach with registered data normalised to the unregistered data. Differences in the percentage change in SNR_T values between affine and non-rigid transformations for each anatomical structure set were compared using the Wilcoxon signed rank test. In order to account for repeated tests on the same data sets, Bonferroni correction was used to set the p-value for statistical significance to values

less than $p < \frac{0.05}{4} = 0.0125$ (based upon 1 SNR_T and 3 registration magnitude metrics).

Finally, as a measure of the impact of differing registration approaches on OE-MRI based tumour hypoxia assessment, oxygen induced ΔT_1 maps were produced as per the methodology in section 7.2.1 for each unregistered and registered data set for each participant. Median and 95% range of VOI oxygen induced ΔT_1 times were compared across the unregistered, affine and non-rigid registration data sets using repeated measures analysis of variance with statistical significance set at $p < \frac{0.05}{2} = 0.025$.

6.4 Results

All ten participants were scanned according to the protocol with adequate non-rebreather bag inflation recorded for all. VOI segmentation of the brainstem (n=10), epiglottis (n=10), vocal cords (n=10), parotid glands (n=20), spinal cord (n=10), submandibular glands (n=19) and thyroid gland (n=10) was performed. The right and left parotid and submandibular glands were segmented and analysed independently. One participant had a single submandibular gland due to previous surgery. Visual inspection of the dynamic images revealed evidence of participant movement in most cases.

Figures 6.5 to 6.10 shows box plots of CoG, DSC and Hausdorff distances for the 6 VOIs for the affine and non-rigid registrations along with boxplots of transformed VOI averaged SNR values relative to unregistered data sets and median and 95% range ΔT_1 times for all data sets.

The median (range) of displacements over all VOI and participants for affine transformations are 0.9mm (0 to 4.9mm) for CoG, 0.916 (0.519 to 1.000) for DSC and 1.6mm (0 to 6.7mm) for Hausdorff distance. For non-rigid transformations these values are 1.2mm (0 to 7.4mm) for CoG, 0.888 (0.430 to 1.000) for DSC and 2.2mm (0 to 10.6mm) for Hausdorff distance. For all VOI and assessment metrics with the exception of CoG for submandibular glands, the magnitude of the average transformation was greater with non-rigid registration than with affine transformations ($p < 0.0125$ level). The VOIs with the largest displacement in transformed volumes are the epiglottis and thyroid gland.

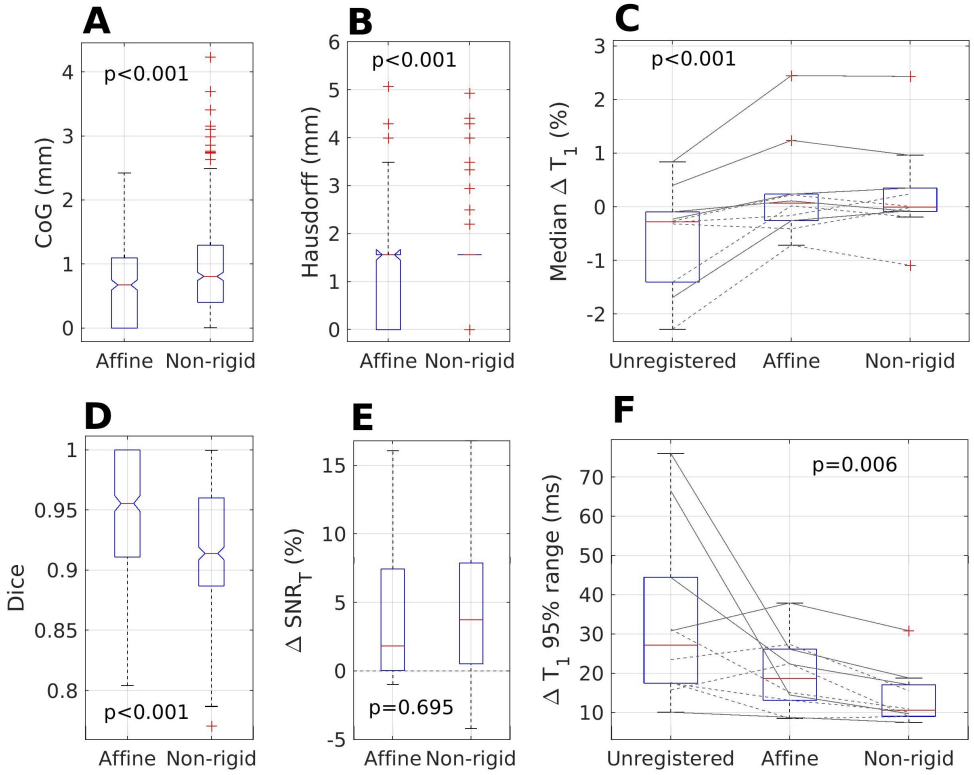

Figure 6.5: Brainstem registration assessment - VOI registration assessment metrics (**A**, **B**, **D**, **E**) and ΔT_1 time medians and 95% range (**C**, **F**) for unregistered and registered brainstem VOI data. Solid lines indicate patient participants and dashed lines non-patient volunteers. Greater magnitude of CoG shifts and Hausdorff distance and lower magnitude Dice similarity coefficients imply greater motion compensation.

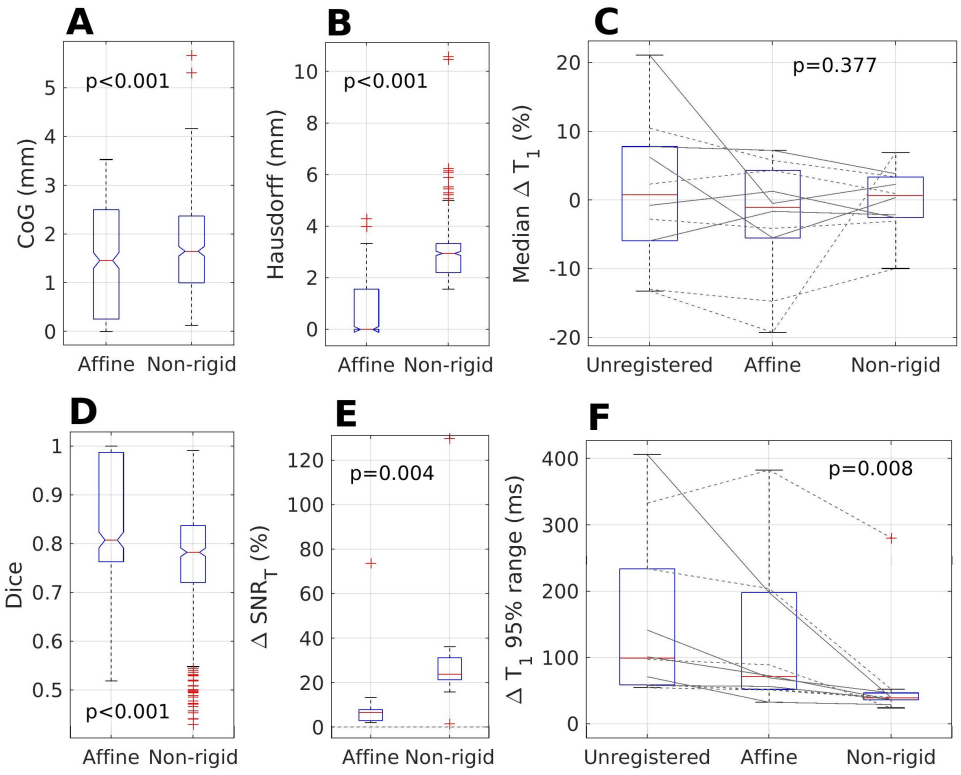

Figure 6.6: Epiglottis registration assessment - VOI registration assessment metrics (**A**, **B**, **D**, **E**) and ΔT_1 time medians and 95% range (**C**, **F**) for unregistered and registered epiglottis VOI data.

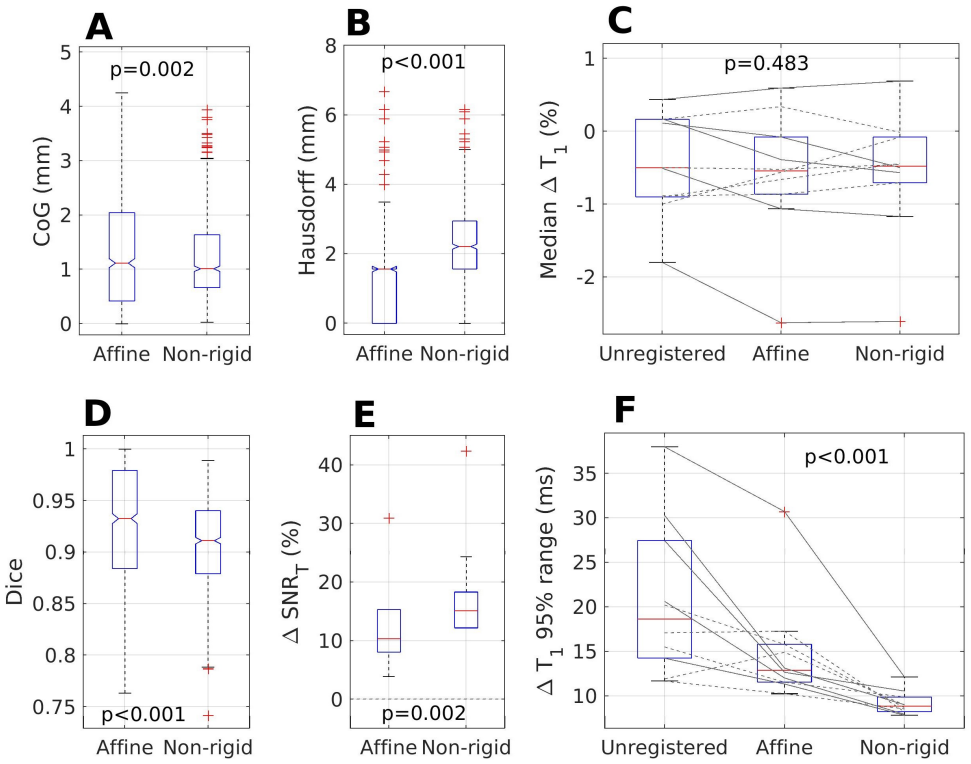

Figure 6.7: Parotid glands registration assessment - VOI registration assessment metrics (**A**, **B**, **D**, **E**) and ΔT_1 time medians and 95% range (**C**, **F**) for unregistered and registered parotid gland VOI data.

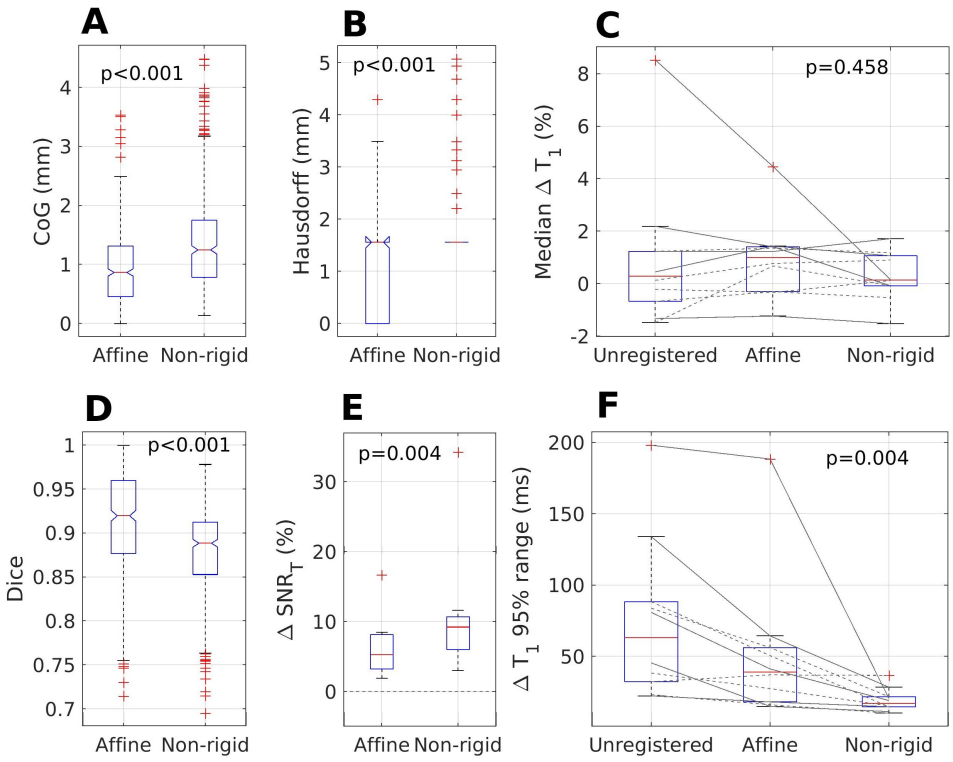

Figure 6.8: Spinal cord registration assessment - VOI registration assessment metrics (**A**, **B**, **D**, **E**) and ΔT_1 time medians and 95% range (**C**, **F**) for unregistered and registered spinal cord VOI data.

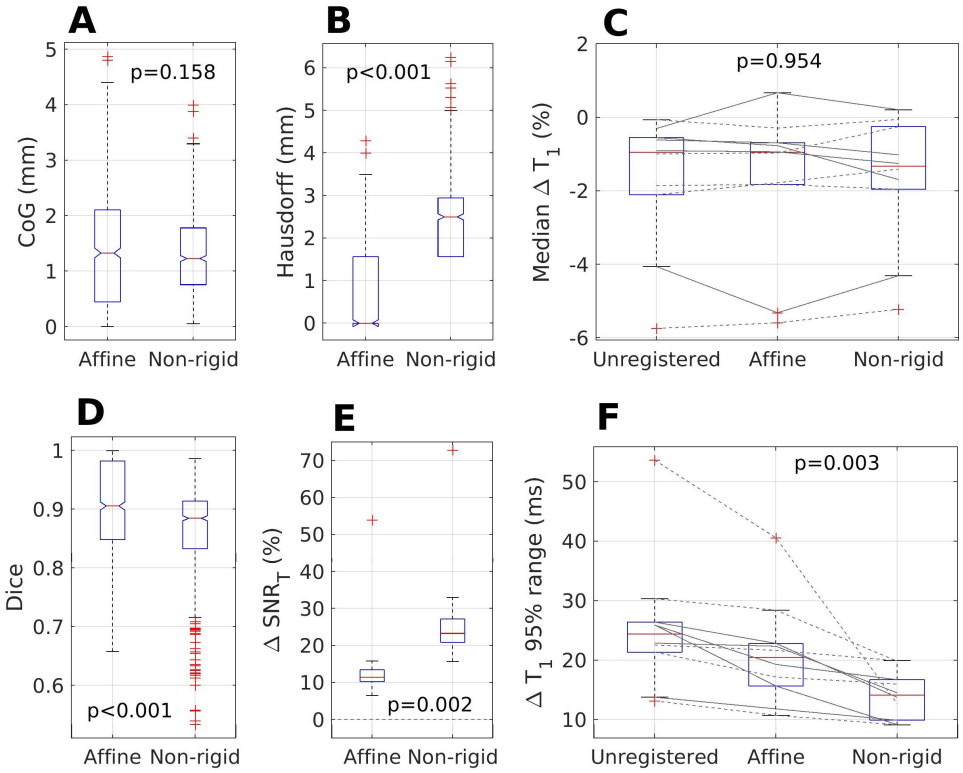

Figure 6.9: Submandibular glands registration assessment - VOI registration assessment metrics (**A**, **B**, **D**, **E**) and ΔT_1 time medians and 95% range (**C**, **F**) for unregistered and registered submandibular gland VOI data.

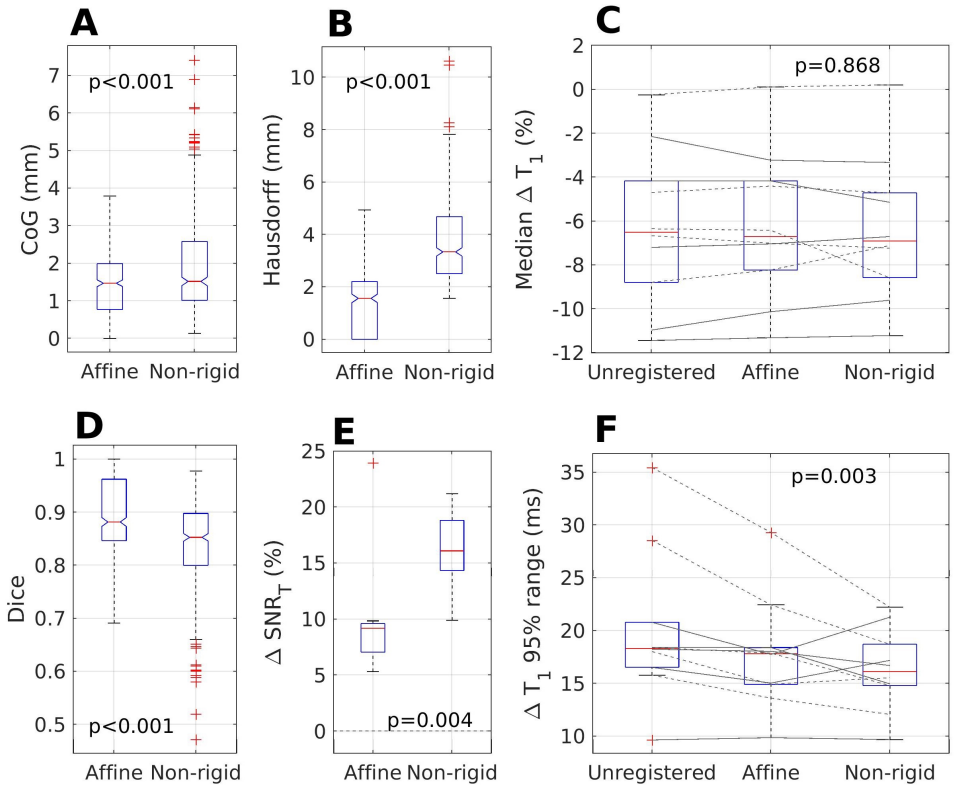

Figure 6.10: Thyroid gland registration assessment - VOI registration assessment metrics (**A**, **B**, **D**, **E**) and ΔT_1 time medians and 95% range (**C**, **F**) for unregistered and registered thyroid gland VOI data.

Table 6.1: Comparison of median VOI averaged ΔT_1 times for unregistered, affine registration and non-rigid registration datasets for 5 non-patient volunteers and 5 patients. p-values from repeated measures analysis of variance with significant values ($p < 0.025$) highlighted in bold.

	Median ΔT_1 % mean (standard deviation)			
	Unregistered	Affine	non-rigid	p-value
Brainstem	-0.5 (1.0)	0.3 (0.9)	0.3 (0.9)	**<0.001**
Epiglottis	1.2 (10.7)	-2.7 (8.6)	0.0 (4.7)	0.377
Parotid glands	-0.5 (0.7)	-0.6 (0.9)	-0.6 (0.9)	0.483
Spinal cord	1.0 (2.9)	0.9 (1.5)	0.3 (0.9)	0.458
Submandibular glands	-1.7 (1.8)	-1.7 (2.1)	-1.7 (1.8)	0.954
Thyroid	-6.3 (3.6)	-6.2 (3.4)	-6.3 (3.3)	0.868

Regarding changes in VOI averaged SNR_T values, at the $p < 0.0125$ there is statistically greater average values for all VOIs except the brainstem with non-rigid registration compared to affine registration. Compared to unregistered data, 2 brainstem VOIs showed worse volume averaged SNR_T values with affine registration than unregistered data (patient ID 2 has 0.2% decrease and patient ID 3 has 1.0% decrease)) and 1 brainstem VOI had reduced SNR_T with non-rigid registration (non-patient volunteer 4 with 4.2% decrease).

ΔT_1 maps were successfully produced for all 10 participants for co-registered and unregistered data sets. Tables 6.1 and 6.2 display VOI median ΔT_1 times and 95% ranges. With the exception of the brainstem VOI that showed greater median ΔT_1 times for both co-registered data sets compared to unregistered data, at the $p < 0.025$ level there was no statistically significant trend for change in median VOI ΔT_1 times. The VOI 95% range of ΔT_1 times did however show consistent reduction in magnitude across all VOIs in the order of unregistered to affine to non-rigid registrations.

Table 6.2: Comparison of 95% range of VOI averaged ΔT_1 times for unregistered, affine registration and non-rigid registration datasets for 5 non-patient volunteers and 5 patients. p-values from repeated measures analysis of variance all significant at $p < 0.025$ level.

	ΔT_1 **95% Range (ms) mean (standard deviation)**			
	Unregistered	Affine	non-rigid	p-value
Brainstem	33.4 (22.4)	19.6 (9.3)	13.9 (7.1)	0.006
Epiglottis	156 (126)	121(110)	62.4 (77.1)	0.008
Parotid glands	20.7 (8.7)	15.0 (6.0)	9.2 (1.3)	< 0.001
Spinal cord	74.8 (56.2)	51.1 (19.4)	19.4 (8.1)	0.004
Submandibular glands	25.6 (11.3)	21.1 (8.7)	14.2 (4.0)	0.003
Thyroid	20.0 (7.2)	17.7 (5.3)	16.3 (3.8)	0.003

6.5 Discussion

The issue of misregistration in the assessment of tumour hypoxia is particularly pertinent due to the heterogeneous distribution of oxygen within tumours (Evans et al. 2007, Panek et al. 2017, Featherstone et al. 2018). In the hypothetical case of a significantly large VOI with homogeneous oxygen distribution, the average change in T_1 time over the VOI could be argued to be a sufficient marker of oxygen status and as such small magnitude misregistrations would be unlikely to have a significant effect on the interpretation of overall oxygenation status. However given that tumour oxygen levels can change from normoxic to radiobiologically significant hypoxia within distances of the same order as the diffusion distance of molecular oxygen (approximately 100 μm (Thomlinson & Gray 1955)) then misregistration of dynamic OE-MRI acquisitions could mask potentially clinically relevant underlying tumour oxygen distribution. Conversely, accurate image registration allows the known heterogeneous oxygenation patterns within tumours to be mapped and correlations of such textural features to clinical outcomes to be investigated.

The spatial resolution in this study is an order of magnitude different to the diffusion distance of oxygen and so even in the absence of any misregistration,

each voxel already represent a spatial average of oxygenation. In contrast to hypoxic PET imaging where the interpretation of the voxel signal intensity is complicated by the non-linearity of the PET signal to local oxygen concentration and the dependence of the signal on local cellularity and tissue perfusion (Grimes et al. 2017), in OE-MRI the change in longitudinal relaxation rate (R_1) is linearly proportional to the plasma partial pressure of oxygen (Zaharchuk et al. 2006). Although the in vivo relationship between tissue oxygen partial pressures and relaxation rate is complicated by dependences on factors including the ratio of oxygenated to deoxygenated haemoglobin, blood volume, haematocrit level and tissue oxygen extraction fraction (Blockley et al. 2008, Bluemke et al. 2022*a*), the mean change in a voxel's R_1 value can be directly related to the magnitude of the underlying average hypoxic subvolume. Accurate image coregistration of dynamic OE-MRI therefore facilitates voxel wise based interpretation of tumours' hypoxic subvolumes in HNSCC.

By imaging over a volume of 200x200x180mm, sufficient data was acquired to facilitate applying both affine and deformable image registration algorithms to the entirety of the clinically relevant head and neck region. The magnitudes of clinically relevant VOI transformations caused by using a non-rigid co-registration algorithm are statistically significantly different than with an affine transformation implying that overall there is variable motion throughout the imaged volume that is not amenable to correction solely by affine registration.

The VOIs with the greatest magnitude of change, epiglottis (figure 6.6) and thyroid gland (figure 6.10), correspond to anatomical regions routinely subject to locally deformable movement from breathing and swallowing. Although the magnitude of the differences in centre of gravity shifts between the affine and non-rigid transformations are small for all VOIs, the differences in the average Hausdorff distances are comparable to the in-plane image resolution of the images (1.6mm). This implies that although the non-rigid transformation registration is not resulting in large differences in the gross shifts of the VOI compared to the affine transformation, there are regions of the VOI that are being deformed to a greater extent with the non-rigid transformation compared to the affine transformation on the scale of the image resolution.

As the magnitude of relaxation time shortening caused by molecular oxygen is relatively small, optimising SNR within a VOI is crucial to detect oxygen induced ΔT_1 changes. The SNR_T results clearly show a general pattern of increasing relative SNR for all VOIs with both affine and non-rigid registrations. In addition, the non-rigid registration showed statistically significant greater improvements in SNR compared to affine registration between all except 2 of the non-rigid and affine registrations across all 6 VOI ($p < 0.01$). The epiglottis VOI showed the largest magnitude of median SNR improvement, consistent with this being an anatomically small region that is prone to significant physiological movement. The non-rigid approach is therefore more likely to account for additional internal movement of this structure relative to the patient contour. Although there were two SNR measurements that had lower values with non-rigid registration compared to unregistered data, these were small magnitude compared to the improvement noticed in all other measurements. It should be noted that increases in SNR values with co-registered data sets compared to unregistered data may be influenced by the bilinear interpolation used in constructing the deformed image sets which could result in apparent increases in VOI SNR values relative to unregistered data independent of co-registration accuracy. However, the relative greater increase in SNR values with non-rigid registration compared to affine registration is less likely to be influenced by this effect. Overall these results demonstrate that the non-rigid registration approach is both feasible in head and neck OE-MRI as well as offering SNR improvements over affine registered data implying greater accuracy of motion correction.

Considering the result of differing registration approaches on the end result of ΔT_1 times, it can be seen that although for 5 / 6 volumes there was no statistically significant change in VOI averaged ΔT_1 times (table 6.1), the range of individual voxel ΔT_1 times within the volumes did significantly change. The 95% range of ΔT_1 times was smaller for all VOI with the non-rigid registration compared to both unregistered and affine registered data (table 6.2). This implies that non-rigid registration is more powerful at reducing the magnitude of outlier values of individual voxel ΔT_1 times as it is reasonable to assume that within these normal head and neck structures, ΔT_1 times are likely to be relatively homogeneous. Although image registration has minimal impact on VOI averaged values, it does

change the appearance of the derived ΔT_1 maps and thus parameters derived from interrogating individual voxel values.

At the time that the data presented in this chapter was collected, there were no published papers on performing OE-MRI in the head and neck region. In addition to the work presented in this thesis, two additional papers performing OE-MRI in the head and neck region have subsequently been published. Although both studies used volumetric acquisitions, the 3T study by Bluemke et al. (2023) also attempted to perform single-slice pre and post-oxygen T_1 mapping using MOLLI. The authors report that patient motion in the slice direction was a nontrivial concern resulting in unusable data from the MOLLI acquisitions due to the T_1 maps being in different geometric locations. Although Dubec et al. (2023) do not explicitly comment on the extent of overall participant movement in their study, they do note that one dataset was unusable due to uncorrectable motion. Such intra-scan movement is consistent with that observed of the participants in the current study although as detailed in chapter 7, usable data was obtained from *all* patient participants in the full clinical part of this OE-MRI study (McCabe et al. 2024a). Whilst Bluemke et al. (2023) make no comment on image registration, Dubec et al. (2023) adopted a deformable registration approach using the toolbox Elastix, an approach broadly equivalent to the non-rigid registration used in this study.

An alternative image registration approach would be to restrict the registered area to that of the contoured tumour and its immediate environs. Such an approach may in theory return more accurate tumour registration even with the use of a multistep deformable approach as the accuracy of the initial rigid registration is likely to be greater thus reducing the magnitude of non-rigid deformations required. However, this would not facilitate the generation of hypoxic maps over the entire clinically relevant head and neck area which was one of the goals of this project but may be an approach that could be used in situations where participant motion is in excess of that correctable by the registration approaches detailed in this chapter. It is also worth noting that the predefined ANTs registration script was used. Images were thus deformed using mutual information as the optimisation metric however there are additional approaches contained with

ANTs that could be explored such as cross-correlation and MRI sequence specific methods (Avants et al. 2011).

There are a number of limitations with this analysis and the non-rigid image registration process. Firstly, there is no ground truth with which to compare the transformed data sets to. Although there is a statistically significant difference between affine and non-rigid registered data in terms of the magnitude of the transformations and resulting improvements in SNR, it is not possible to comment on the absolute truth of the final transformed data. Although it is conceivable to construct a *ground truth* by re-contouring each VOI on every acquired image, due to the lower spatial resolution and image quality of the dynamic OE-MRI images compared to diagnostic quality scans, there is the potential for significant errors in this process thereby negating this as an absolute reference.

Non-rigid registration is a computationally more complicated technique than affine registration. As such, the processing of the image sets took longer using the non-rigid approach. However, as the process was automated through scripting and could therefore run in the background or overnight, the magnitude of this time difference was not quantified. The increases in processing time with non-rigid registration are likely to be clinically irrelevant though as tumour hypoxia imaging would at best influence the long term management of HNSCC rather than guide the immediate, emergency management of a patient.

This analysis comprises data from an equal number of non-patient volunteers and patients with suspected HNSCC. There is an inherent selection bias for patients who are willing to undergo an extended MRI scan and potentially tolerate the MRI scan process thereby reducing the magnitude of gross motion during the imaging. Although the non-rigid image registration algorithm was successfully applied to all participants, larger magnitudes of observed movement as may occur in an unselected patient cohort may not be as readily correctable.

In addition, the magnitude of patient movement and therefore the extent of the registration correction required may vary significantly from that observed in this cohort of participants depending on the clinical application and therefore patient setup used. For example if the OE-MRI were performed as an adjunct to an MRI scan performed for the principle purpose of planning radiotherapy treatment for HNSCC, it is conceivable that the scan could be performed with the patient

immobilised in the radiotherapy treatment shell; a custom made thermoplastic mask designed to restrict patient movement during radiotherapy treatment and allow accurate and repeatable daily patient positioning. Such a scanning setup is used for radiotherapy planning purposes to significantly reduce the magnitude of any bulk patient motion during the scan (Paulson et al. 2015), albeit with reduced or minimal impact on internal motion. Such a scan setup may therefore reduce the need for the use of the more computationally intensive non-rigid registration approaches for dynamic OE-MRI.

It is also important to note that the non-rigid co-registration algorithm cannot correct for variations in signal intensity caused by any migration of the receiver coil during the dynamic scan. This study used a large flex coil positioned on the chest of participants to allow easy fitting of the high flow oxygen mask. However as this is not fixed to a rigid structure then there is a greater risk of a change in the relative position of the coil and the participant which can cause changes in signal intensities. Such changes would result in regions of abrupt change in T_1 times principally in the anterior portion of the head and neck that fails to be corrected with image co-registration. This would be detectable on visual inspection of the ΔT_1 maps and would also cause regions of reduced SNR. Such areas should not be used for quantitative purposes. Finally, although no transformation specific artefacts were detected in the datasets given the deformable nature of the registration technique, this should be monitored for in all clinical data.

In conclusion, the use of non-rigid image co-registration is both practically possible and a necessary step in the processing pipeline for dynamic OE-MRI of the head and neck due to the risk of gross movement and local tissue deformation.

Chapter 7

Clinical outcomes

7.1 Abstract

Background

Tumour hypoxia is a recognised cause of radiotherapy treatment resistance in HNSCC however current PET-based hypoxia imaging techniques are not routinely available in the NHS or in many cancer centres worldwide. The results presented in this chapter were obtained from a clinical study investigating if the imaging technique of OE-MRI could be performed using routine clinical equipment in patients with HNSCC.

Methods

A volumetric OE-MRI protocol for dynamic T_1 relaxation time mapping was implemented on 1.5T clinical scanners using only routinely available clinical equipment. Participants were scanned breathing room air and during high flow oxygen administration. Oxygen induced changes in T_1 times (ΔT_1) and R_2^* rates (ΔR_2^*) were measured in malignant tissue and healthy organs. Voxel-wise statistical testing using unequal variance t-test was used to derive estimates of tumour hypoxic fractions that were compared between radiotherapy treatment responsive and non-responsive groups. Additional exploratory analysis using a Bootstrapping approach to generate normoxia likelihood maps for textural analysis was performed. In addition, the potential of fusing OE-MRI derived parametric maps with radiotherapy treatment planning CT scans was explored.

Results

Fifteen patients with HNSCC (median age 59 years, range 38 to 76) and 10 non-HNSCC subjects (median age 46.5 years, range 32 to 62) were scanned; the OE-MRI acquisition took less than 10 min. Fifteen histologically confirmed primary tumours and 41 malignant nodal masses were identified. Median (range) of ΔT_1 times and hypoxic fraction estimates for primary tumours were -3.5% (-7.0% to -0.3%) and 30.7% (6.5% to 78.6%) respectively. Radiotherapy responsive and resistant primary tumours had mean estimated hypoxic fractions of 36.8% (95% CI 17.4% to 56.2%) and 59.0% (95% CI 44.6% to 73.3%), respectively (p = 0.111). Textural features of Energy, Entropy and Cluster Shade were extracted from hypoxia likelihood maps but did not show any statistically significant differences between responding and non-responding tumours.
Conclusion
An implementation of dynamic, volumetric OE-MRI of the head and neck region using routinely available clinical equipment allowed the discernment of differing oxygen responses within biopsy confirmed HNSCC.

7.2 OE-MRI in HNSCC Clinical Study

Recruitment to the evaluation of OE-MRI in HNSCC study detailed in chapter 4 was performed between April 2021 and December 2022 at Nottingham University Hospitals NHS Trust. Study imaging was performed using the setup and scan protocol detailed in chapter 5. The details of the study execution and analysis of the acquired OE-MRI imaging data is presented in this section.

7.2.1 Method

All patients were scanned using the study imaging sequences as per figure 5.2 using the imaging parameters in table 5.1. VIBE images were corrected for motion relative to the first dynamic acquisition via non-rigid registration (chapter 6). The water image from the qDixon sequence was similarly registered for each participant and the resulting registration transformation applied to derived qDixon parametric maps.

A four-dimensional median filter was applied to dynamic images before producing voxel-wise T_1 maps for each dynamic acquisition using the VFA methodology (section 2.5.3). An initial room air period was defined from 0:35 to 3:32 min:s and hyperoxic phase from 5:30 min:s until the end of the dynamic sequence. Mean voxel-wise room air T_1 times (T_1Air) and hyperoxic T_1 times (T_1O_2) were determined and voxel-wise changes in T_1 times defined as:

$$\Delta T_1(voxel) = \frac{(T_1O_2 - T_1Air)}{T_1Air} \times 100 \tag{7.1}$$

Histologically confirmed primary tumours were contoured on the first acquisition of the VIBE images. Malignant nodes were defined as nodal masses in patients with biopsy proven HNSCC whose radiological appearance was deemed malignant by the local head and neck MDT. Contoured volumes less than 0.25 mL were excluded. Parotid, submandibular and thyroid glands were contoured in accordance with radiotherapy contouring guidelines (Brouwer et al. 2015). All contouring was performed using ITK-SNAP (version 3.4.0) (Yushkevich et al. 2006).

Average VOI ΔT_1 times and ΔR_2^* rates were defined as the median of $\Delta T_1(voxel)$ times and voxel R_2^* rate differences with statistical significance against the null hypothesis of no change in median value assessed via Wilcoxon signed-rank test, with p-values lower than 0.05 as significant. Individual voxels within VOIs were interrogated for significant ΔT_1 via a two-tailed unequal variance t-test, with p-values lower than 0.05 as significant. Estimates of hypoxic fractions were defined as percentage of voxels not showing statistically significant negative ΔT_1. Estimated hypoxic fractions and VOI averaged ΔT_1 were compared for responding and nonresponding groups via two-tailed unequal variance t-test, with p-values lower than 0.05 as significant. Parcellation analysis of primary tumours and malignant nodes was performed using VOI averaged ΔT_1 times and ΔR_2^* rates (Cao-Pham et al. 2017). Statistical analysis was performed using MATLAB version R2018b.

7.2.2 Results

A total of 5 non-patient volunteers (median age 32 years, range 31 to 60) and 20 patients with suspected HNSCC (median age 57 years, range 36 to 76) were

recruited of whom 15 received histological diagnoses of HNSCC (median age 59 years, range 38 to 76). Out of the 5 patients who did not have HNSCC, 1 had lymphoepithelial cyst (patient 2), 1 benign cystic lesions (patient 18), and 3 had no radiological abnormality identified (patients 8, 12, 17).

Adequate inflation of the oxygen mask non-rebreathe bag was recorded for all participants. One patient (patient 12) terminated the study early following dynamic acquisition 32. ΔT_1 maps were produced with the hyperoxic phase defined using the final 7 dynamic measurements.

The first 3 non-patient volunteers and first 2 recruited patients were scanned using the VIBE sequence with TR of 4.2ms (table 5.1). However following a qualitative review of the imaging quality the subsequent 20 participants (2 non-patient volunteers and 18 patients) were scanned using the VIBE sequence with TR of 10ms to increase the SNR of the acquired images to both enable more accurate VOI contouring and decrease the noise noted in the images.

Normal structures

OE-MRI data from all 25 participants was used to determine VOI averaged ΔT_1 times for normal structures in the head and neck region. Median (range) ΔT_1 times were -0.6% (-2.6% to 1.0%) for parotid glands, -1.3% (-4.7% to 2.7%) for submandibular glands and -8.1% (-14.1% to 0.4%) for thyroid glands (figure 7.1). Figure 7.2 shows example ΔT_1 parametric maps, VOI averaged T_1 time series and total VOI ΔT_1 histogram for an example thyroid gland.

Malignant tissue

Fifteen primary tumours (median volume 5.04 mL, range 0.54 to 33.70 mL) and 41 distinct malignant nodal masses (median volume 2.62 mL, range 0.26 to 20.56 mL) were contoured (table 7.1). Median baseline tumour T_1 times and R_2^* rates were 1200ms (range 716 to 1417ms) and $29.6s^{-1}$ (range 20.1 to $144.8s^{-1}$) respectively for primary tumours and 1322ms (range 577 to 1674ms) and $14.0s^{-1}$ (range 6.9 to $30.9s^{-1}$) for malignant nodal masses.

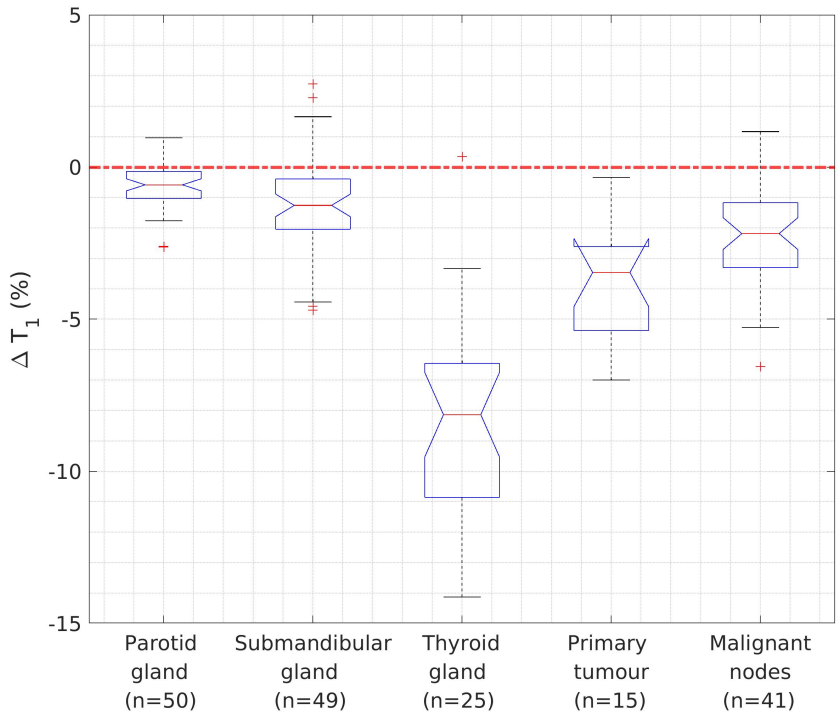

Figure 7.1: VOI median ΔT_1 times - Notched box plots of oxygen induced ΔT_1 (%) times for all 25 participants for the parotid, submandibular and thyroid glands and for the 15 patients with head and neck squamous cell carcinoma for the primary tumour and malignant nodal masses. The single outlier point showing positive ΔT_1 in the thyroid gland came from non-patient volunteer V3.

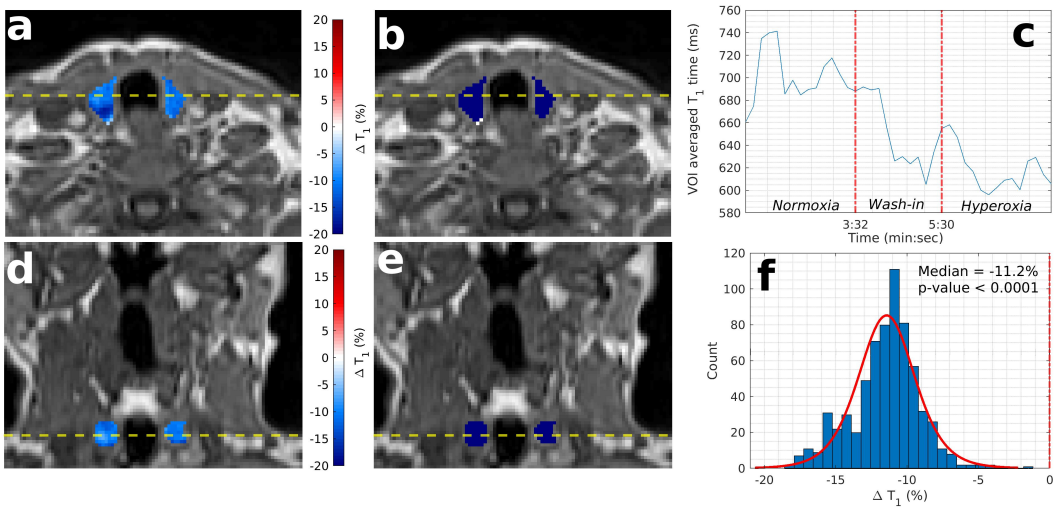

Figure 7.2: Parametric maps from thyroid gland - Example OE-MRI parametric maps of thyroid gland (patient P5). T_1 weighted VIBE image with overlaid parametric ΔT_1 map of the thyroid gland (**a**, **d**, axial and coronal plane respectively) and overlaid statistical map of ΔT_1 times (**b**, **e**). Blue colour indicates statistically significant decrease in T_1 times, white indicating no statistically significant change and red indicating statistically significant increasing T_1 times. **c** Time series of T_1 times averaged over the entire thyroid VOI. **f** Histogram of ΔT_1 times for the entire malignant nodal VOI.

Table 7.1: Characteristics of the squamous cell carcinomas for the 15 patients with histologically confirmed tumours. All histology and staging was discussed at the local head and neck cancer multidisciplinary team meeting. *HPV DNA* Human papillomavirus deoxyribonucleic acid, *N/A* Not assessed.

ID	Sex	Age (years)	Smoking	Site	Stage TNM8	p16	HPV DNA	Primary size (mL)	Lymph node masses	
									Number	Size (mL) Median (range)
1	M	54	Never	Palatine tonsil	T4aN2b	-	N/A	31.15	2	1.90 (1.31-2.50)
3	M	45	Current	Pyriform fossa	T2N2b	N/A	N/A	4.35	2	7.04 (4.27–9.81)
4	M	69	Ex	Oropharynx	T0N2	+	+	-	1	10.71
5	M	66	Never	Pyriform fossa	T2N1	+	+	3.98	2	6.26 (1.64–10.88)
6	M	46	Current	Nasopharynx	T1N2	N/A	N/A	8.83	10	2.60 (1.01–20.56)
7	M	66	Ex	Base of tongue	T4aN2	+	N/A	33.70	4	1.83 (0.37–6.44)
9	M	62	Never	Base of tongue	T1N1	+	+	1.31	1	11.98
10	M	55	Current	Base of tongue	T3N1	+	+	5.04	2	2.90 (0.26-5.55)
				Palatine tonsil	T3N0	+	+	17.69	-	-
11	M	72	Ex	Pyriform fossa	T4aN1	N/A	N/A	33.11	1	0.46
13	F	59	Current	Vallecula	T1N2c	-	-	0.54	1	9.94
14	M	56	Current	Palatine tonsil	T4aN2b	+	-	21.60	3	1.10 (0.48–8.40)
15	M	38	Current	Palatine tonsil	T1N1	+	+	2.35	7	2.62 (0.54–7.19)
16	M	65	Never	Palatine tonsil	T2N1	+	N/A	3.75	2	6.00 (0.93–11.07)
19	F	76	Never	Palatine tonsil	T2N1	+	+	4.55	1	8.35
20	M	57	Current	Larynx	T3N2b	N/A	N/A	7.20	2	1.52 (1.17–1.87)
							Median (range)	5.04 (0.26-33.70)	2 (1-10)	2.62 (0.26–20.56)
							Total number of lesions	15	41	-

Median (range) ΔT_1 times were -3.5% (-7.0% to -0.3%) for primary tumours and -2.2% (-6.5% to 1.2%) for malignant nodes. Median (range) estimated hypoxic fractions for primary tumours and malignant nodes were 30.7% (6.5% to 78.6%) and 59.9% (11.6% to 89.5%) respectively (figure 7.1). HPV related and unrelated oropharyngeal cancers had median (range) estimated hypoxic fractions of 25.6% (6.5% to 70.2%) and 52.4% (26.1% to 78.6%) respectively.

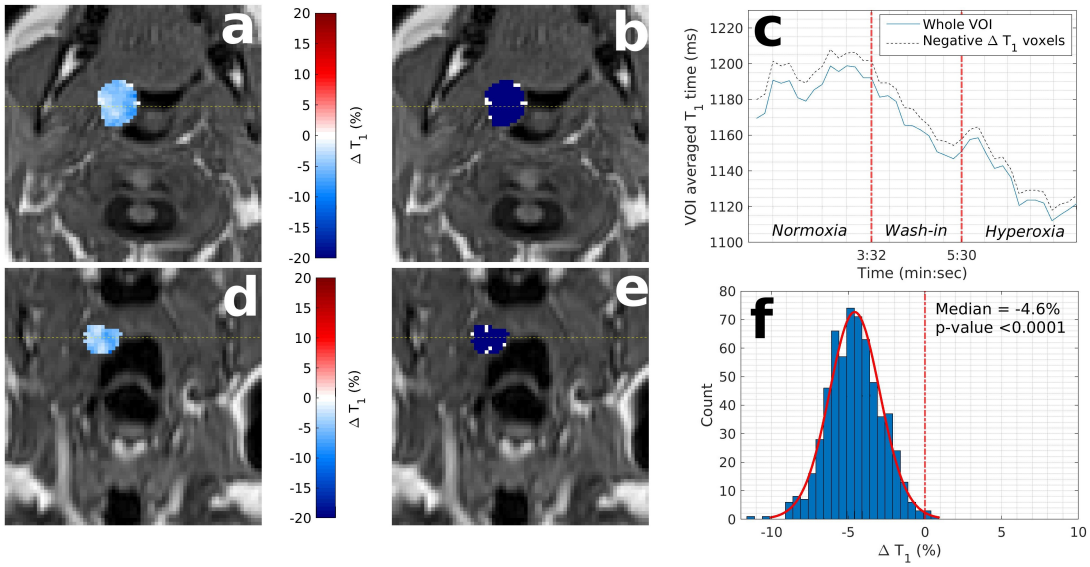

Figure 7.3: Parametric maps from normoxic primary tumour - Example OE-MRI parametric maps in a primary tumour with a complete response to radiotherapy treatment (patient P16). Low estimated hypoxic fraction (9.8%) is shown on a T_1 weighted VIBE image with overlaid parametric ΔT_1 map of the primary tumour (**a**, **d**, axial and coronal plane respectively) and overlaid statistical map of ΔT_1 times (**b**, **e**). Blue colour indicates statistically significant decrease in T_1 times, white indicating no statistically significant change and red indicating statistically significant increasing T_1 times. **c** Time series of T_1 times averaged over the entire primary tumour VOI and over those voxels with significantly decreasing T_1 times only. **f** Histogram of ΔT_1 times for the entire primary tumour VOI.

Figures 7.3 and 7.4 show example ΔT_1 parametric maps, VOI averaged T_1 time series and total VOI ΔT_1 histograms for example primary tumours with low and high estimated hypoxic fractions respectively. Plots for example malignant nodal regions with low and high estimated hypoxic fractions are given in appendix

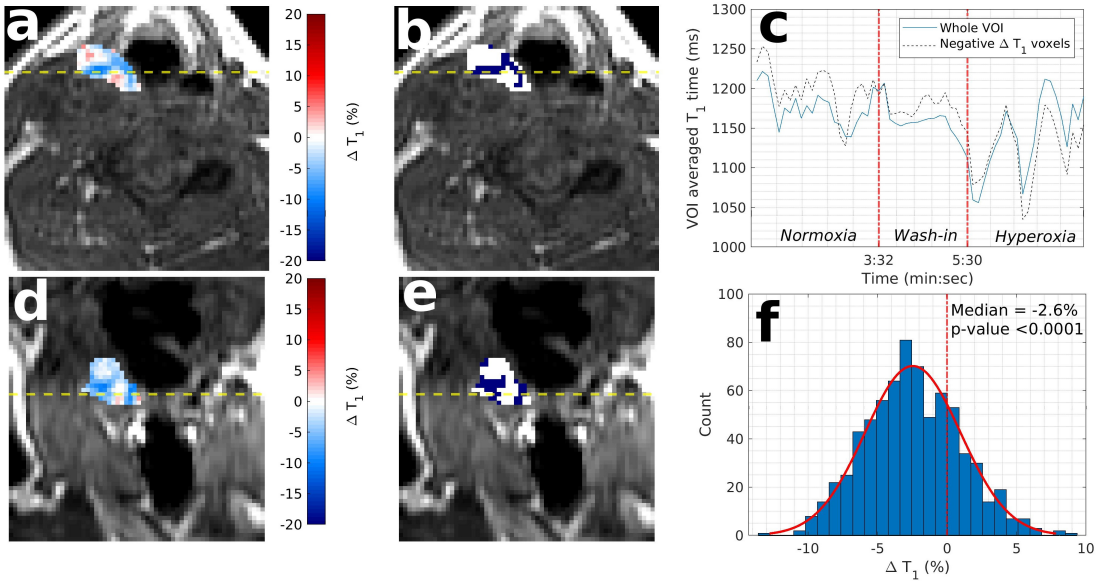

Figure 7.4: Parametric maps from hypoxic primary tumour - Example OE-MRI parametric maps in a primary tumour with residual disease post radiotherapy treatment (patient P3). High estimated hypoxic fraction (73.5%) is shown on a T_1 weighted VIBE image with overlaid parametric ΔT_1 map of the primary tumour (**a**, **d**, axial and coronal plane respectively) and overlaid statistical map of ΔT_1 times (**b**, **e**). Blue colour indicates statistically significant decrease in T_1 times, white indicating no statistically significant change and red indicating statistically significant increasing T_1 times. **c** Time series of T_1 times averaged over the entire primary tumour VOI and over those voxels with significantly decreasing T_1 times only. **f** Histogram of ΔT_1 times for the entire primary tumour VOI.

figures A.2 and A.3. Tables presenting the full T_1 and R_2^* data for all contoured primary tumours and malignant nodal masses are presented in appendix tables B.1 and B.2.

Out of 15 patients with confirmed HNSCC, 11 (73%) proceeded to curative intent radiotherapy and 9 underwent post-treatment FDG-PET scan (1 patient had post-treatment MRI scan due to clinical concerns regarding early progressive disease). Of these 10 primary tumours, 7 (70%) were responders, with 3 (30%) showing residual disease, confirmed histologically in 2 cases (table 7.2).

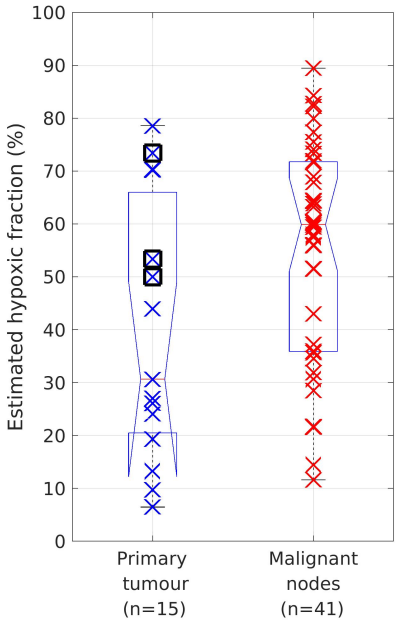

Figure 7.5: OE-MRI derived estimates of hypoxic fractions - Notched box plots with overlaid data points of estimates of hypoxic fractions (%) for malignant tissues. Data points corresponding to primary tumours with evidence of residual disease post-radiotherapy treatment are surrounded by a black box.

Median primary tumour volumes were 3.75mL (range 0.54 to 21.60mL) for responding tumours and 7.20mL (range 4.35 to 33.70mL) for non-responding tumours ($p = 0.183$, Wilcoxon rank sum) with baseline median T_1 times of 1200ms (range 716 to 1400ms) for responding and 1179 (range 1170 to 1206ms) for non-responding tumours. VOI mean ΔT_1 values were -3.8% (95% CI -5.6% to -2.0%) for responding and -3.1% (95% CI -3.5% to -2.6%) for non-responding tumours

Table 7.2: Treatment details and outcomes of post-treatment imaging for the 15 patient participants with histologically confirmed squamous cell carcinoma. Radiotherapy dose refers to that delivered to the primary tumour. Cisplatin administered as 40mg/m^2 weekly and carboplatin as AUC 1.5 weekly. *CRT* Concurrent chemoradiotherapy, *FDG-PET* ^{18}F-fluorodeoxyglucose positron emission tomography, *RT* Radiotherapy, *SACT* Systemic anticancer therapy.

ID	Intent	Modality	Treatment	Imaging outcome
1	Palliative	RT	-	N/A
3	Curative	RT	65.1Gy/30#	MRI - Residual disease in primary and nodes (no biopsy).
4	Palliative	SACT	-	N/A
5	Curative	CRT	70Gy/35# & Cisplatin	Complete response (FDG-PET).
6	Curative	CRT	70Gy/35# & Cisplatin	Complete response (FDG-PET).
7	Curative	CRT	65.1Gy/30# & Carboplatin	Residual disease in primary (FDG-PET and biopsy). Distant metastases.
9	Curative	CRT	70Gy/35# & Cisplatin	Complete response (FDG-PET).
10	Curative	CRT	70Gy/35# & Cisplatin	Died before scan.
11	Curative	Surgery	-	N/A
13	Curative	CRT	70Gy/35# & Cisplatin	Complete response (FDG-PET).
14	Curative	CRT	70Gy/35# & Cisplatin	Complete response (FDG-PET).
15	Curative	CRT	70Gy/35# & Cisplatin	Complete response in primary. Distant metastatic disease (FDG-PET).
16	Curative	CRT	70Gy/35# & Cisplatin	Complete response (FDG-PET).
19	Curative	Surgery	-	N/A
20	Curative	CRT	70Gy/35# & Cisplatin	Residual disease in primary (FDG-PET and biopsy). New malignant node outside treatment field.

(p = 0.484, unequal variance t-test). Mean estimated hypoxic fractions were 36.8% (95% confidence intervals [CI] 17.4% to 56.2%) and 59.0% (95% CI 44.6% to 73.3%) for responding and non-responding primary tumours respectively (p = 0.111, unequal variance t-test, figure 7.5). There was no correlation found between estimated hypoxic fractions and primary tumour volumes or baseline T_1 times (figure 7.6).

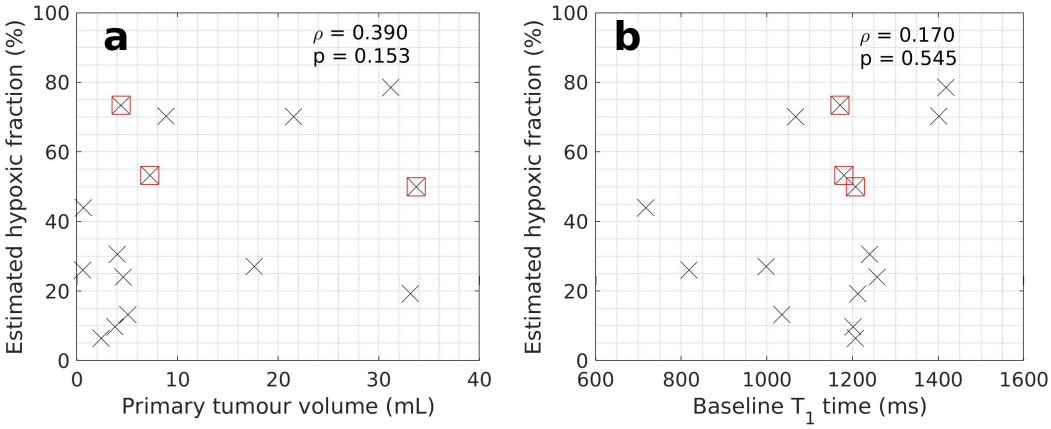

Figure 7.6: Hypoxic fractions correlation plots - Scatter plots of estimated hypoxic fractions (%) against (**a**) primary tumour volume (mL) and (**b**) average baseline primary tumour T_1 times (ms). Spearman's rank correlation coefficient (ρ) did not show any statistically significant correlation. Data points in red boxes illustrate treatment resistant tumours.

R_2^* measurements were obtained in all participants. Median (range) ΔR_2^* rates were $0.4s^{-1}$ (-29.1 to $10.7s^{-1}$) for primary tumours and $0.2s^{-1}$ (-12.7 to $24.7s^{-1}$) for malignant nodes (figures 7.7 and 7.8). In patients who had curative intent radiotherapy, mean ΔR_2^* rates were $6.3s^{-1}$ (95% CI 1.9 to $10.7s^{-1}$) and -$1.7s^{-1}$ (95% CI -8.8 to $5.4s^{-1}$) for responding and radiotherapy resistant primary tumours (p = 0.812, unequal variance t-test) with baseline mean R_2^* rates of $33.3s^{-1}$ (95% CI 15.0 to $51.5s^{-1}$) and $44.8s^{-1}$ (95% CI 42.3 to $47.3s^{-1}$) respectively (p = 0.897, unequal variance t-test). Primary tumour ΔR_2^* rates showed no statistical correlation to baseline R_2^* values (p = 0.457, Spearman rank correlation) but did show a moderate negative correlation for malignant nodal masses (ρ = -0.429, p = 0.005, Spearman rank correlation, figure 7.9).

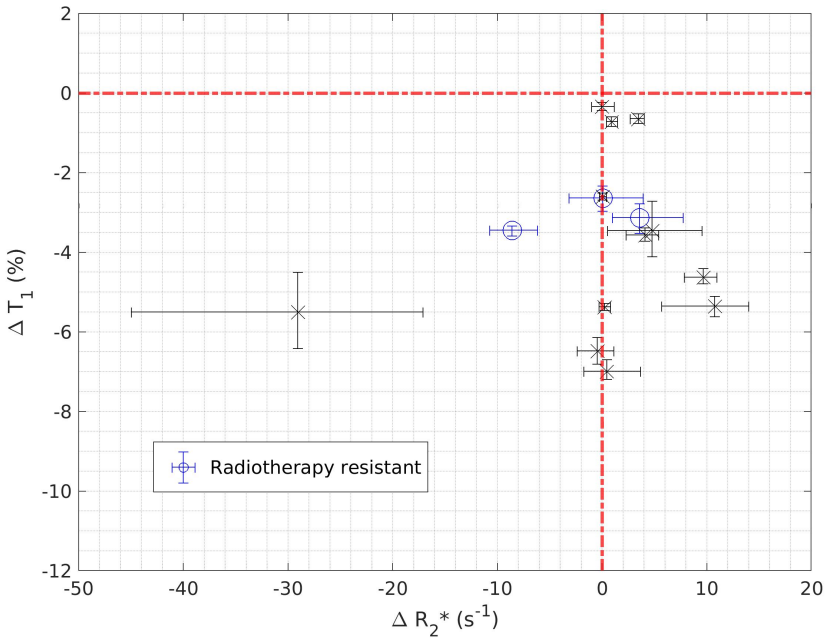

Figure 7.7: ΔT_1 versus ΔR_2^* for primary tumours - Scatter plot showing categorisation of hypoxia status of primary tumours based on VOI average median ΔT_1 times and ΔR_2^* rates with error bars indicating estimates of 95% confidence intervals derived from Bootstrap sampling with 1,000 samples. Data points corresponding to primary tumours with evidence of residual disease post radiotherapy treatment are shown with blue circles.

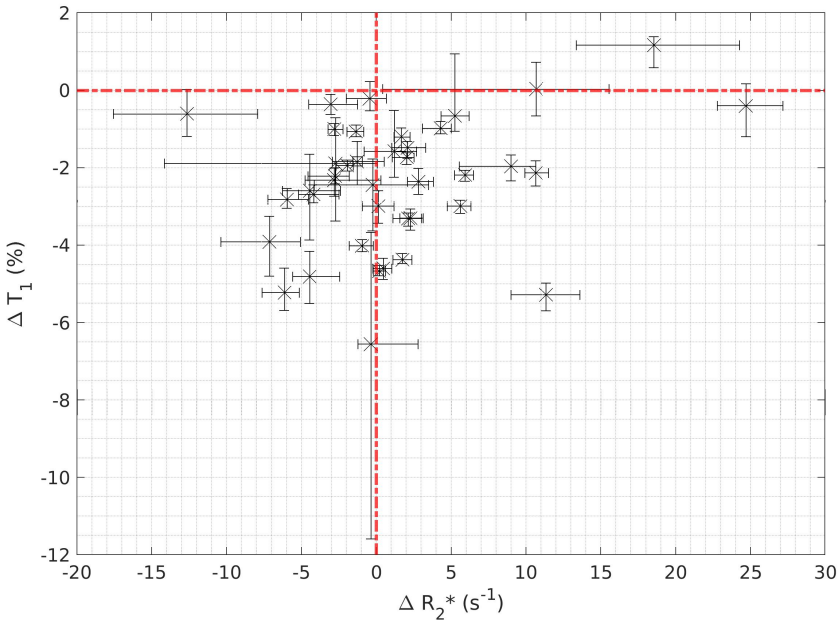

Figure 7.8: ΔT_1 versus ΔR_2^* for malignant nodes - Scatter plot showing categorisation of hypoxia status of malignant nodes based on VOI average median ΔT_1 times and ΔR_2^* rates with error bars indicating estimates of 95% confidence intervals derived from Bootstrap sampling with 1,000 samples.

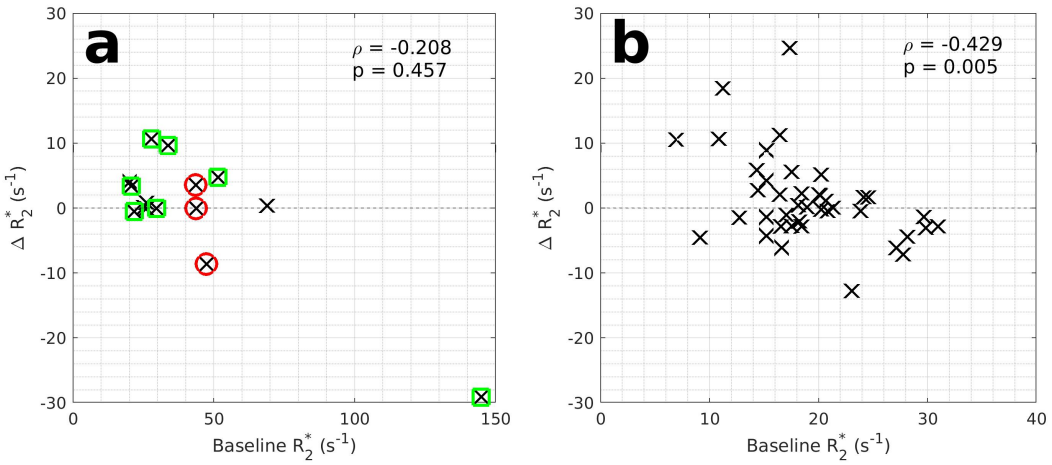

Figure 7.9: R_2^* correlation plots - Scatter plots of ΔR_2^* versus baseline R_2^* rates for primary tumours (**a**) and malignant nodal masses (**b**). Spearman's rank correlation coefficient (ρ) did not show statistical significance for primary tumours but showed a moderate negative correlation for malignant nodal masses.

7.2.3 Discussion

The OE-MRI protocol was designed to be added to a standard clinical protocol using routinely available equipment therefore making this a low cost and rapidly translatable method of hypoxia imaging in HNSCC. For this reason room air as opposed to medical air was utilised for the pre-oxygen acquisitions in order to avoid the need for medical gas supply and additional equipment in the form of gas mixers. Although this meant participants did not have the opportunity to become accustomed to the gas delivery before oxygen was commenced, no apparent disadvantages were encountered from this approach. Despite the OE-MRI sequence taking less than 10 min, it was possible to image the entire tumour volume and discern differing responses to supplemental oxygen challenge.

Normal Structures

The magnitude of oxygen induced T_1 shortening in parotid and submandibular glands is small indicating limited sensitivity of the OE-MRI technique in these structures. In contrast, the thyroid gland showed strong and consistent negative ΔT_1.

As OE-MRI relies on the absence of T_1 shortening to determine hypoxic regions, a clinically relevant quality control structure to ensure adequate oxygen delivery to organs is desirable (sections 3.4.5 and 5.5.3). The thyroid gland may represent such a structure in the head and neck and is in an anatomical location that is readily incorporable into the field of view in clinical head and neck cancer imaging. However without being able to derive measures of the actual delivered oxygen concentration (section 5.5.3) the magnitude of T_1 change in a control region that is required in order to classify an individual examination as having an acceptable level of sensitivity for detecting clinically relevant tumour hypoxia remains to be established.

Malignant tissue

The presence of hypoxia in HNSCC is well documented with oxygenation levels measured invasively using Eppendorf oxygen tension (pO2) histography showing overall median tumour pO2 of 10 mmHg corresponding to median hypoxic fractions of 21% and 32% depending upon the threshold set to define radiobiologically significant hypoxia (2.5 mmHg and 5 mmHg, respectively) (Vaupel et al. 2007). PET-based imaging assessments of tumour hypoxia in HNSCC have shown significant interlesion variability with individual tumour fractional hypoxia estimates ranging from 0% to 95% and study population median values ranging 0.9% to 66% (Mortensen et al. 2012, Zips et al. 2012, Graves et al. 2016, Thorwarth et al. 2019). In the current study, estimated hypoxic fractions also show significant inter-lesion variability but the median estimated hypoxic fraction in primary tumours of 31% is comparable to direct measurements.

Regarding treatment outcomes, radiotherapy non-responding tumours show a 29.3% greater average hypoxic fraction than responding tumours, albeit not statistically significant potentially due to the sample size of this study. There was no difference found with VOI averaged ΔT_1 times between responding and non-responding tumours. This is in keeping with OE-MRI studies in other tumour sites which have failed to identify correlations between spatially averaged changes in T_1/R_1 values and reference hypoxia markers (chapter 3). Hypoxia-imaging

biomarkers that capture information pertaining to the distribution of hypoxic regions are therefore likely to prove the most clinically relevant.

The dichotomisation of a voxel's hypoxic status based on the lack of statistically significant T_1 shortening is clearly an oversimplification of the underlying continuously varying oxygen tension present in tumours. The relationship between T_1 times and tumour pO2 is dependent on a number of physical and physiological variables meaning it is not possible to readily ascribe pO2 values to imaged voxels (Bluemke et al. 2022*a*). Consequently, it is not possible to state the effective pO2 threshold for the estimates of hypoxic fractions presented in this study.

The magnitude of the hypoxic fractions within the tumours in this study may have been overestimated due to the inclusion of any cystic, necrotic or nonperfused areas in the VOI. Using the alternative OE-MRI metric of the fraction of perfused oxygen refractory voxels, as proposed by O'Connor et al. (2016) may potentially overcome this limitation. However although the assumption is that such regions do not contain viable tumour cells and thus do not contribute to hypoxia induced radioresistance, the extent of such regions may be overestimated based upon DCE-MRI measurements and such regions may contain quiescent tumour cells that can drive radioresistance even when subsequently re-oxygenated (Menegakis et al. 2021). The hypoxic fractions in this study may also be overestimated as a consequence of the study power returned from performing individual voxel analysis on a limited number of dynamic data points. This power could be increased at the expense of scan time or with the use of higher scan acceleration.

The OE-MRI sequence was developed for in-plane and slice resolution to be adequate to facilitate fusion of acquired parametric maps to radiotherapy planning computed tomography scans with the ambition of mapping tumour hypoxia distributions to assist in radiotherapy volume delineation. Although the spatial resolution used in this study ($1.6 \times 1.6 \times 2.5$ mm^3) is higher than other clinical OE-MRI studies (chapter 3), it is still significantly coarser than the typical diffusion distance of molecular oxygen ($\sim 100\mu m$ (Hughes et al. 2019)). Although the image resolution used here may detect greater levels of variability in oxygen distribution compared to coarser acquisitions, this comes at the cost of worse

signal to noise ratio, which may reduce the ability to discern borderline normoxic voxels thus overestimating tumour hypoxic burden.

It has been suggested that negative oxygen induced ΔR_2^* rates may occur in hypoxic tumours due to decreases in deoxyhaemoglobin concentrations with supplemental oxygen and could potentially discriminate lower levels of hypoxia from normoxia in tumours with oxygen induced T_1 shortening (Cao-Pham et al. 2017, O'Connor et al. 2019). Only two primary tumours in this study showed such a decrease in R_2^* rates but only one of the three radiotherapy resistant HNSCC primary tumours had such a change. In addition, no statistically significant difference in R_2^* parameters between radiotherapy responsive and resistant primary tumours was identified. As baseline R_2^* rates are related to deoxyhaemoglobin concentrations, faster initial R_2^* rates may be associated with tumours that are less well oxygenated in the vascular compartment and therefore may also show the greatest magnitude of R_2^* shortening with supplemental oxygen. Although a moderate negative correlation between baseline R_2^* and ΔR_2^* was found for malignant nodal masses, no such association was found for primary tumours. This may be because the magnitude of R_2^* rates are also related to factors independent of deoxyhaemoglobin concentration including haematocrit, vascular volume, pH level and vessel density (Cao-Pham et al. 2017). The potential for spatial fluctuations in perfusion further serves to complicate the relationship between oxygen induced ΔT_1 times, ΔR_2^* rates and baseline R_2^* rates. As such, spatially averaged ΔR_2^* rates may not be sensitive enough to offer useful insights on tumour hypoxia.

At the commencement of this study there was no published data in the literature on oxygen induced ΔT_1 times in patients with HNSCC. However since data collection commenced in 2021, there have been two other small studies published performing OE-MRI in HNSCC. A single other study in HNSCC at 1.5T reported mean oxygen induced ΔR_1 rates of 0.019/s in 6 patients with HNSCC on a diagnostic MRI system, corresponding to ΔT_1 of -2.1% which is comparable to the median primary tumour VOI ΔT_1 of -3.5% in the study in this thesis. All 15 primary tumours in the current study showed statistically significant shortening of VOI median ΔT_1 times mirroring the observed oxygen induced increases of all VOI averaged ΔR_1 rates in the other 1.5T study (Dubec et al. 2023). In contrast, a study at 3T in 5 patients with oropharyngeal cancers reported tumour

ΔR_1 rates ranging -0.001 to 0.108/s with 2 of the mean baseline R_1 rates failing to show statistically significant change with oxygen (Bluemke et al. 2023).

Although the study presented in this thesis and the other two recent HNSCC studies all used volumetric acquisitions, the 3T study by Bluemke et al. (2023) made single T_1 measurements before and after oxygen to determine tumour ΔR_1 rates whereas the study in this thesis and the 1.5T study by Dubec et al. (2023) used dynamic acquisitions with multiple T_1 measurement time points before and after oxygen administration. These dynamic measurements allow voxel wise oxygen-induced ΔT_1 / ΔR_1 maps to be produced following image coregistration to control for participant motion. Bluemke et al. (2023) acknowledge that patient motion was a significant difficulty encountered in their study and focus their OE-MRI analysis on describing oxygen induced changes to tumour region of interest R_1 histograms. Dynamic OE-MRI acquisitions with appropriate image registration allow greater characterisation of tumour oxygenation status, however standardisation of imaging parameters and data processing approaches is clearly required for ready comparison of OE-MRI studies as has been developed in other quantitative MRI techniques (O'Connor et al. 2017, Shukla-Dave et al. 2019).

7.2.4 Limitations

The aim of this study was to evaluate the feasibility of performing OE-MRI in suspected HNSCC in a clinical environment and not to repeat the work of previous authors in demonstrating the efficacy of OE-MRI in determining tumour hypoxia (Linnik et al. 2014, O'Connor et al. 2016, White et al. 2016, Little et al. 2018, Salem et al. 2019). Nevertheless, histopathological correlation with a suitable hypoxia marker would have enabled comparison and evaluation of the accuracy of the estimated hypoxic fractions. In addition, as is routine practice in the UK, routine histological verification of malignant cervical lymph nodes is reserved for cases with equivocal radiological findings only. Without surgical treatment, no definitive histology of nodal masses is obtained hence correlation with clinical outcome in this study was limited to histologically confirmed primary tumours.

The majority of primary tumours in this study were oropharyngeal (11/15) with 82% (9/11) positive for p16 expression (high risk HPV variant DNA de-

tected in 7 cases) representing a likely selection bias in the patient recruitment design of the study. HPV related cancers are relatively more radiosensitive than HPV negative tumours and although both types display similar levels of hypoxia (Göttgens et al. 2019) pharmacological hypoxia modification therapies appear less effective in HPV positive tumours (Lassen et al. 2010, Rischin et al. 2010). The ability to stratify HPV positive tumours based on their hypoxia status may therefore be less clinically relevant with regards to therapy escalation strategies than for HPV negative tumours although may have a significant role in identifying HPV positive tumours for whom radiotherapy dose de-escalation strategies may be appropriate (section 1.4) (Lee et al. 2024*a*,).

The clinical endpoint in this study of residual disease on a 12-week post treatment FDG-PET scan is also an early assessment of treatment outcome and is therefore heavily biased towards detecting tumours with highly treatment resistant phenotypes. This end point was chosen as it is a routinely used assessment metric and time point but was also a practical outcome measure that allowed associations between hypoxic metrics and treatment resistance to be explored within the time constraints of a pilot study. Nevertheless, it is routine clinical practice to follow-up patients for at least 5 years after treatment with the highest risk of disease occurrence being within the first 2 years (Machiels et al. 2020) meaning that the end point in this study will miss those patients with later disease recurrence that could still potentially be related to hypoxia induced radioresistance. Future, larger OE-MRI in HNSCC clinical studies should therefore look at using clinical follow-up periods of at least 2 years post treatment.

The power of this study to detect differences in treatment response between patients with more or less hypoxic tumours was significantly reduced due to the study recruitment not meeting its target with only 20 patients imaged out of a planned 50. The reduced recruitment was principally due to the requirement to perform the study imaging as part of patients' routine clinical imaging without causing any delays to investigative or treatment pathways. This restriction on when the research imaging session could be performed was necessitated by the research aim of investigating whether OE-MRI can be performed in the head and neck region using routine clinical equipment (and not research MRI scanners) coupled with the significant pressures faced by the NHS and NUH during the

data acquisition phase of this study due to the COVID-19 pandemic meaning that additional scanning sessions were not available on the clinical MRI machines.

Future studies that incorporate an assessment of the practical nature of performing novel imaging in the clinical environment will need to contend with the continuing pressures faced by the UK health system therefore requiring careful and novel designs of patient recruitment and experimental imaging pathways. Nevertheless, it is important to perform such practical clinical assessments of new techniques as the clinical environment can present unique challenges that may not be fully elucidated in a pure research setting.

7.2.5 Conclusion

The implementation of dynamic, volumetric OE-MRI in the head and neck region using routinely available equipment in an acute hospital setting that was able to discern differing responses to supplemental oxygen within biopsy confirmed HNSCC has been presented. Estimates of tumour hypoxic fractions derived from the OE-MRI data were comparable to historical direct measurements of tumour oxygenation in HNSCC and showed a greater hypoxic fraction in those tumours resistant to radiotherapy treatment although the magnitude of this difference was not statistically significant potentially due to the reduced power of the study. The addition of oxygen induced ΔR_2^* rate measurements appeared to be of limited clinical benefit in assessing oxygen induced radioresistance. Further adequately powered studies are now required in HNSCC to investigate the predictive power of OE-MRI estimated tumour hypoxic fractions in discriminating patients more likely to benefit from the addition of hypoxia modification therapy to radiotherapy treatments.

7.3 Exploratory analysis

The estimates of tumour hypoxic fraction presented in section 7.2.2 were derived using two-tailed unequal variance t-tests on the dynamic data of individual voxels against the null hypothesis of no change in T_1 time. Not only does this approach have the limitations of the assumptions of the t-test but it also has a bias towards

overestimating the extent of hypoxia through lack of rejection of the null hypothesis. The t-test approach also fails to quantify the degree of certainty to which an individual voxel is labelled as normoxic. Although an increased magnitude of a voxel's decrease in T_1 time implies greater concentration of molecular oxygen, as this is dependent upon factors including the extent of blood perfusion, ΔT_1 alone does not provide a quantitative assessment of the normoxia likelihood of an individual voxel.

Bootstrapping is an alternative approach to analysing OE-MRI data that removes the bias from using a t-test. This has been proposed by Little et al. (2022) in conference abstract form to derive patient confidence intervals on the metric of fraction of perfused but refractory to oxygen voxels in rectal cancer OE-MRI. In the context of the OE-MRI data obtained in this study, once pre and post-oxygen Bootstrap samples have been obtained for a voxel, the fraction of these samples demonstrating shortening of T_1 times with oxygen can be used as an estimate of the likelihood that an individual voxel represents normoxic tumour tissue. Such voxel data can then be displayed as parametric maps and the tumour hypoxic fraction subsequently estimated dependent upon the chosen normoxia likelihood threshold level.

As previous OE-MRI studies outside of the head and neck failed to show correlations between reference hypoxia markers and spatially average ΔT_1 values (section 3.4) the analysis presented in this chapter has focussed on estimating tumour hypoxic fractions using voxel-by-voxel analysis. However, such fractions do not take any account of spatial relationship of normoxic and hypoxic voxels. For example, figure 7.10 shows 5 plots of simulated normoxia likelihood data all of which have a hypoxic fraction (at the 95% level) of 63.4%. However, the images clearly have different distributions of the hypoxic and normoxic voxels which is not captured by the hypoxic fraction metric. Such grouping or dispersion of hypoxic regions may conceivably have an impact on tumour treatment response. As such analysing the heterogeneity of the OE-MRI derived parametric maps or the so called texture of the images may provide information pertinent to clinical outcomes.

Second-order statistical texture features can be extracted by a range of different mathematical approaches. One such methodology derives metrics using the

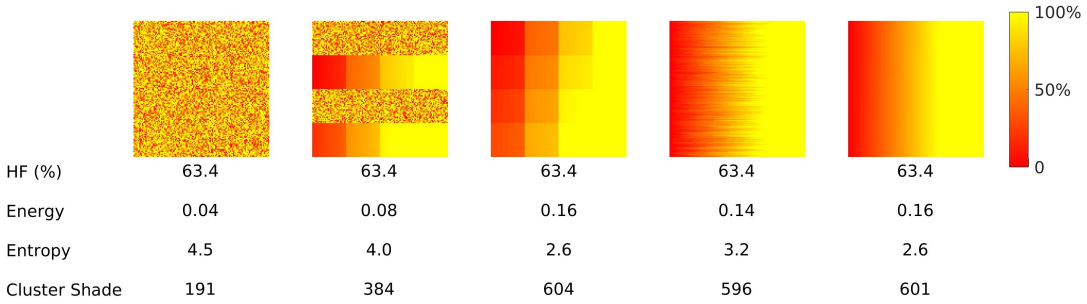

Figure 7.10: Example differing image texture - Example simulated normoxia likelihood maps (%) with different textural features for a set hypoxic fraction (HF) level of 63.4% at the 95% normoxia likelihood level. Data was generated for the first image on the far left in MATLAB using a random number generator with a positively skewed distribution over the interval [0,1]. The baseline data set was subjected to variable levels of data ordering in order to generate the subsequent images. Textural features were calculated via the GLCM approach and equations 7.2 to 7.4.

grey level co-occurrence matrix (GLCM). The GLCM is a square matrix whose size is equal to the number of quantised grey levels in the image that is being processed (N_g). Each element of the matrix $p(i,j)$ denotes how often pairs of pixels with values equal to the i^{th} and j^{th} quantised grey level occur within a specified spatial relationship. Once the GLCM has been determined, various parameters can be calculated from it to determine the underlying texture of the original image (Haralick et al. 1973, Yang et al. 2012).

There are at least 20 different parameters that can be calculated from the GLCM (Haralick et al. 1973, Soh & Tsatsoulis 1999, Pierce 2016). Three of these that are commonly described as detailing the physical properties of homogeneity and uniformity are energy, entropy and cluster shade. Energy (or angular second moment) is a measure of homogeneity with increased values representative of more homogeneous images. Entropy quantifies the extent of randomness in the image texture with a more homogeneous image having lower entropy whereas cluster shade is often quoted as a measure of image uniformity with higher values indicating asymmetric images (Haralick et al. 1973, Soh & Tsatsoulis 1999, Pierce 2016).

For a GLCM $p(i,j)$ with N_g grey levels, energy, entropy and cluster shade can be defined as (Yang et al. 2012):

$$\text{Energy} = \sum_{i=0}^{N_g-1} \sum_{j=0}^{N_g-1} p(i,j)^2 \tag{7.2}$$

$$\text{Entropy} = -\sum_{i=0}^{N_g-1} \sum_{j=0}^{N_g-1} p(i,j) \log(p(i,j)) \tag{7.3}$$

$$\text{Cluster shade} = \sum_{i=0}^{N_g-1} \sum_{j=0}^{N_g-1} (i+j-u_x-u_y)^3 p(i,j) \tag{7.4}$$

where u_x and u_y represent the means of the GLCM columns and rows respectively.

Figure 7.10 shows an example of how these parameters can vary for simulated normoxia likelihood data with the same magnitude of hypoxic fraction. For a 3D VOI, there are 26 connections between an individual voxel and surrounding voxels (6 faces, 12 edges and 8 corners) yielding a total of 13 unique directions for spatial relationships. By computing the GLCM and textural features for each of these directions, the original 3D image textural feature can be obtained by averaging over the 13 returned values (Pierce 2016).

In order to investigate the feasibility of performing textural analysis on OE-MRI data, Bootstrapping was first used to generate normoxia likelihood maps of the imaged tumour VOIs that were then discretised and GLCMs produced.

7.3.1 Method

The MATLAB command `bootstrp` was used with 1,000 data samples using sampling with replacement for the 15 data points pre and post-oxygen delivery for each voxel in the tumour VOI. The median values of the pre and post-oxygen Bootstrapped data were used to determine if each voxel sample showed a decrease in median T_1 time. The percent of the 1,000 samples that showed decreased median T_1 times was used to represent an estimate of the voxel normoxia likelihood (0 to 1 with 1 representing 100% estimated likelihood of normoxia). Normoxia

likelihood maps were used to construct estimates of primary tumour hypoxic fractions (%) based on defining hypoxic voxels as those with a normoxia likelihood value of $< 95\%$.

Textural features of energy, entropy and cluster shade were extracted from the normoxia likelihood maps for each primary tumour volumes using *'PET Oncology Radiomics Test Suite'* (Pierce 2016) within the MATLAB environment by constructing GLCMs with 16 grey levels.

Correlation between textural features and t-test derived hypoxic maps as well as between Bootstrap hypoxic fractions and t-test hypoxic fractions was performed via Spearman's rank correlation. Unequal variance t-test was used to investigate association between textural features and treatment outcomes. Bonferroni correction for multiple testing was applied with the level for statistical significance set at $p< 0.05/4 = 0.0125$.

7.3.2 Results

Voxel-wise Bootstrap sampling of the dynamic OE-MRI data was successfully performed for all participants with normoxia likelihood maps produced for all patient participants. Examples of ΔT_1 maps, t-test statistical maps of the ΔT_1 data and normoxia likelihood maps for an example primary tumour and malignant nodal mass from two different patient participants are shown in figure 7.11 and appendix figure A.4 respectively.

Spearman's rank correlation coefficient (ρ) and associated p-values for the primary tumour textural parameters and Bootstrap derived hypoxic fraction estimates against t-test derived hypoxic fractions are presented in table 7.3. Cluster shade is the only parameter which did not show a strong correlation to t-test derived hypoxic fractions (Spearman $\rho = 0.029$, p-value=0.923). Scatter plots of the textural features versus t-test based hypoxic fraction estimates are shown in figure 7.12.

Boxplots of the textural features of the hypoxia likelihood maps for the primary tumours are shown in figure 7.13. Mean (95% CI) textural parameters for responding and non-responding tumours respectively were 0.46 (0.22 to 0.70) versus 0.17 (0.06 to 0.28) for Energy, 2.0 (0.9 to 3.1) versus 3.6 (3.0 to 4.2) for

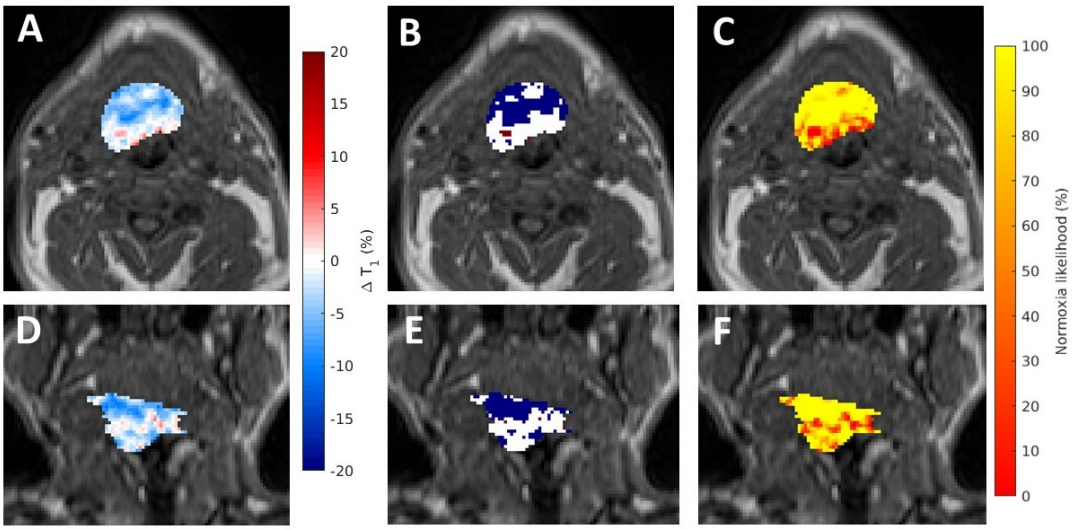

Figure 7.11: Example primary tumour Bootstrap OE-MRI parametric map - ΔT_1 maps (**A**, **D**), corresponding statistical map with blue indicating statistically significant reduction in voxel T_1 times, white no change and red statistically significant increase in T_1 times via t-test with significance at $p < 0.05$ (**B**, **E**) and normoxia likelihood maps constructed from 1,000 Bootstrap samples for each voxel from the dynamic OE-MRI data (**C**, **F**) for the primary tumour in patient ID 7. **A**, **B**, **C**: axial slice. **D**, **E**, **F**: coronal slice.

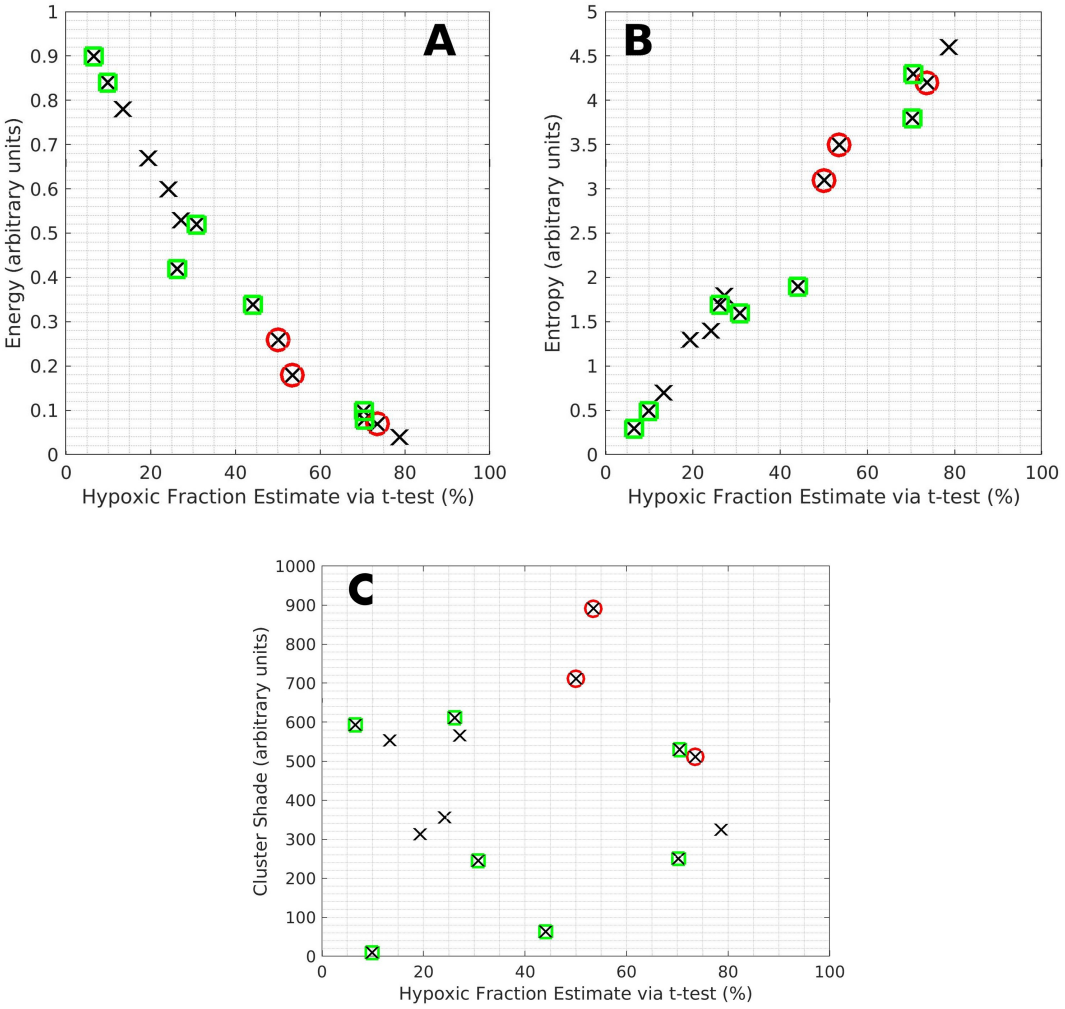

Figure 7.12: Textural features versus hypoxic fraction - Scatter plots of OE-MRI energy (**A**), entropy (**B**) and cluster shade (**C**) values derived from Bootstrap produced hypoxia likelihood maps versus hypoxic fraction estimates derived from individual voxel t-test for primary tumours. Green squares indicate primary tumours treated with curative intent radiotherapy with a complete post-treatment response and red circles those primary tumours with residual disease post radiotherapy.

Entropy, and 329 (144 to 515) versus 705 (490 to 920) for Cluster Shade. At the $p < 0.0125$ statistical level (unequal variance t-test), none of these textural parameters showed statistically significant differences between radiotherapy responsive primary tumours and radiotherapy resistant cancers.

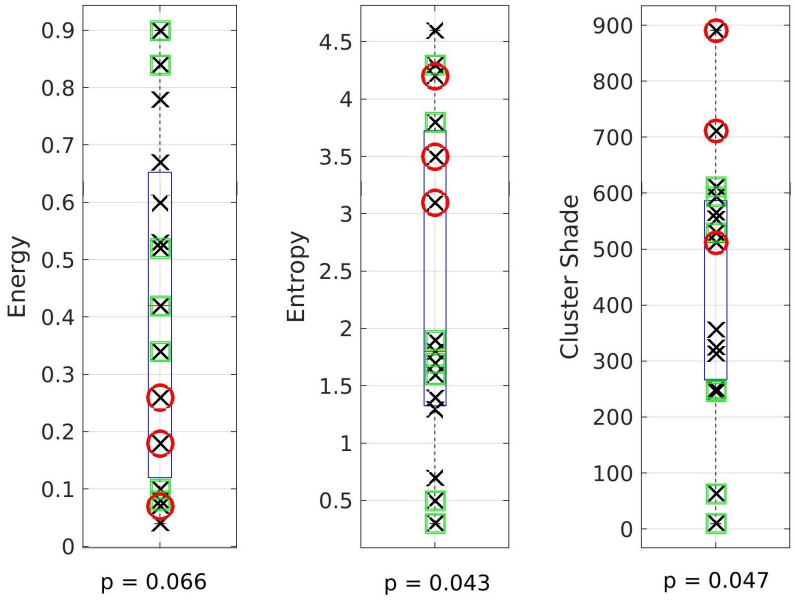

Figure 7.13: Textural analysis boxplots - Boxplots of textural parameters derived from normoxia likelihood maps for primary tumours with p-values quoted from unequal variance t-test of radiotherapy responsive versus radiotherapy resistant tumours. Green squares indicate primary tumours treated with curative intent radiotherapy with a complete post-treatment response and red circles those primary tumours with residual disease post radiotherapy.

7.3.3 Discussion

Although there is a strong correlation between the t-test and Bootstrap derived hypoxic fraction estimates, the non-biased Bootstrap method allows for quantification of the uncertainty in the labelling of a voxel as normoxic or hypoxic and may therefore better reflect the complex underlying oxygen distributions present in tumours than the binary t-test maps. As such the Bootstrap maps are well placed to serve as a base for textural analysis.

Table 7.3: Spearman ρ correlation coefficients for textural features derived from primary tumour normoxia likelihood maps compared to voxel-wise t-test hypoxic fractions with associated p-values. *HF* - hypoxic fraction.

	Correlation to t-test HF	
	Spearman ρ	p-value
Bootstrap HF	0.982	< 0.001
Energy	-0.989	< 0.001
Entropy	0.986	< 0.001
Cluster shade	0.029	0.923

Due to the number of patient data sets available, textural analysis was focussed on three parameters that were anticipated to best reflect the spatial fluctuations in hypoxia. However the GLCM that formed the basis of these measurements is only one way in which to extract textural relationships in imaging data. It was used here as an example of a mathematical method of capturing spatial relationships between voxels however other formulations such as the Grey Level Run-Length Matrix (GLRLM), Grey Level Size Zone matrix (GLSZM) and Grey Level Distance Zone matrix (GLDZM) which provide information on the runs of consecutive voxels or groups of connected neighbouring voxels may provide more sensitive measurements of biologically relevant hypoxia distribution. Alternatively fractal analysis via determination of fractal dimensions, which reflect the scale of additional structural detail with increasing magnification may serve as a suitable measure of the complexity of hypoxia distribution (Mayerhoefer et al. 2020). Due to the nature of repeated statistical testing, the evaluation of such a broad range of metrics for association with treatment related outcomes will require a large and high quality database of OE-MRI imaging.

One of the applications of textural characteristics is its use in the developing field of radiomics. Radiomics refers to the extraction of imaging features that describe shape, intensity and texture characteristics and the computer based mining of this data for predictive and prognostic biomarkers or signatures (Haider et al. 2020). Radiomics has been applied to cancer imaging including using head and neck MRI scans to both predict patient outcomes as well as to provide information on the tumour microenvironment and the expression of biomarkers and

targets for therapeutic interventions (Jethanandani et al. 2018, Li & Zhou 2022, Kang et al. 2023). Radiomic features have shown strong correlations with cellular heterogeneity and tumour aggressiveness (Mayerhoefer et al. 2020) and may therefore be potentially useful in the analysis of OE-MRI data.

Radiomic studies routinely use two datasets; one for testing and developing the radiomic signature and a second for testing this signature. Due to the repeated statistical testing that is used, large baseline datasets are required. The limited data set obtained in this study is therefore not suitable on its own for radiomic based analysis. Future OE-MRI in HNSCC studies may generate adequate data to attempt radiomic analysis however careful control of the quality of both the documented clinical data as well as consistency in the imaging acquisition is paramount and is unlikely to be obtained on a multi-institutional basis without agreed OE-MRI imaging protocols or guidelines.

The analysis presented in this section is exploratory in nature but has illustrated that in principle textural analysis of OE-MRI derived parametric maps may provide clinically useful measurements. The choice of textural parameters, image quantisation grey levels and clinical outcome measures used here are all open to debate. In addition, no textural analysis was made of metastatic lymph node OE-MRI data as the clinical outcome data was focussed on residual primary site disease post treatment. Further studies with larger datasets will therefore be needed to extract any OE-MRI radiomic signatures and the issue of standardising image acquisition, processing and analysis will need addressing.

7.4 Radiotherapy

One potential method of overcoming hypoxia induced radioresistance is to utilise targeted dose escalations via dose painting (section 1.4). Such an approach requires knowledge of the distribution of tumour hypoxic regions on the imaging used to plan the radiotherapy treatment. Although MRI only approaches to radiotherapy treatment planning in the head and neck are available (Clasen et al. 2023, *MR-only Radiotherapy Planning* 2024) they are not yet routinely available meaning co-registration of OE-MRI derived parametric maps to radiotherapy planning CT scans is required for dose painting therapeutic approaches. Such

planning CT scans are performed with slice thickness of 3mm or finer (Grégoire et al. 2018) hence the slice thickness of the OE-MRI pulse sequence in this study being set at 2.5mm.

7.4.1 Method

In order to provisionally assess the feasibility of fusing OE-MRI parametric maps with radiotherapy planning CT scans, the default deformable image registration within ANTS was utilised (see section 6.3). The first acquisition of the study dynamic T_1 weighted OE-MRI sequence was registered to the planning CT scan. The derived deformation was applied to both ΔT_1 map and primary tumour VOIs. The deformed ΔT_1 maps were displayed as on overlay on the planning CT scans for the deformed primary tumour volume allowing a visual inspection of the quality of the fusion.

As an indicator of the fusion quality, the centre of gravity displacement of the physician contoured CT planning Gross Tumour Volumes (GTV) compared to the OE-MRI based primary tumour volumes were computed. CT based contours were constructed during routine clinical practice by the treating clinical oncologist with reference to all available diagnostic pathology and imaging including the clinical MRI examination but not the research MRI sequences. They were constructed using the radiotherapy treatment planning system RayStation (version 6, RaySearch Medical Laboratories, AB Stockholm, Sweden). Estimates of primary tumour volumes were made by multiplying the number of voxels in each ROI by the voxel volumes ($1.074 \times 1.074 \times 3mm^3$ for planning CT and $1.5625 \times 1.5625 \times 2.5mm^3$ for the MRI) and compared using Wilcoxon signed rank test.

7.4.2 Results

A total of 12 clinically utilised gross tumour volumes (GTV) were available. There was no GTV available for one participant as a clinical target volume had been constructed directly without the physician contouring a GTV. Qualitatively, all of the transformed VOIs sat within the primary tumour on the planning CT with the exception of participant ID 9.

Median planning CT GTV volume was 11.3cm^3 (range 3.7cm^3 to 70.1cm^3) compared to the median OE-MRI primary tumour volume of 6.1cm^3 (range 0.6cm^3 to 33.7cm^3, p=0.001 Wilcoxon Signed Rank test, appendix table B.3). The median magnitude of distance between the planning CT and MRI derived primary tumour volumes was 5.9mm (range 2.4mm to 16.8mm) with the majority of this difference found in the slice direction which had a median difference of 5.0mm (range 0.3mm to 14.1mm) compared to the median in-plane displacement of 2.4mm (range 0mm to 7.2mm).

Example images of OE-MRI parametric maps deformed to the planning CT scans from two patient participants who had biopsy confirmed residual disease post completion of radiotherapy treatment are shown in figure 7.14 alongside a corresponding slice from the post-treatment PET scan.

7.4.3 Discussion

There was a statistically significant difference in the volume of the primary tumour between those contours performed on the study MRI sequence and the physicians treating contours performed on the planning CT scan. Such a discrepancy is a recognised issue in radiotherapy treatments for head and neck cancers (Clasen et al. 2023) which therefore significantly limits the utility of tumour contour similarity metrics as a means of assessing registration accuracy. In addition, in this study the MRI scan was generally performed prior to a diagnostic biopsy and also a significant period of time prior to commencing treatment (median time from study MRI scan to commencing radiotherapy treatment was 62 days, range 17 to 117 days). There is therefore the chance of significant tumour growth and distortion to the tumour and surrounding anatomy between the MRI and CT planning scans. Such an issue could be addressed by performing an MRI scan in the treatment position and closer in time to the radiotherapy CT scan.

Visual inspection of the transformed contours revealed good overlap with the CT based primary tumour with the exception of the one case mentioned where the registration approach had been unsuccessful and the transformed primary tumour did not reside within the tumour as visualised on the CT scan. Visual inspection revealed that the CT contours tended to be contoured on a greater

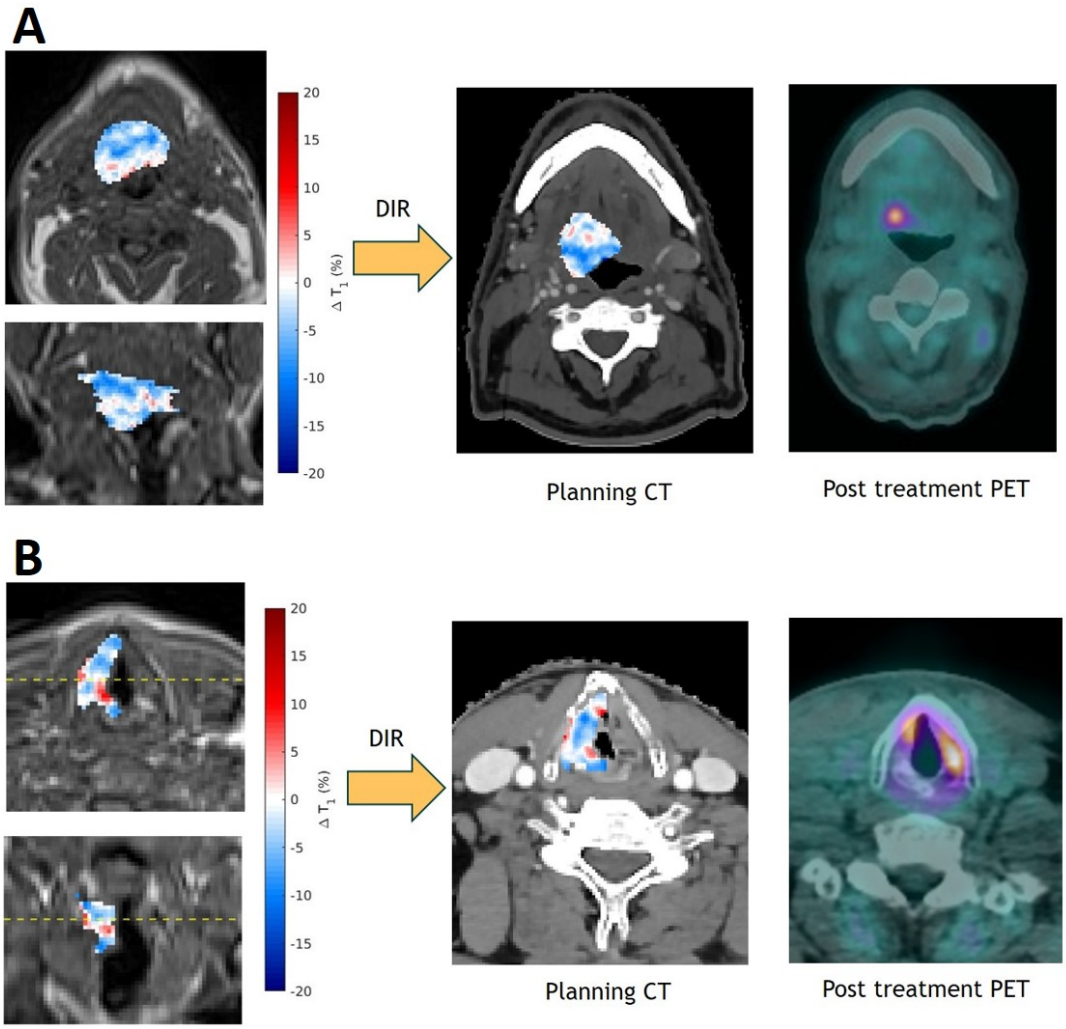

Figure 7.14: Fusion with planning CT scans - Examples from two patient participants (**A**: participant ID 7, **B**: participant ID 20) who had residual disease in their primary tumours post completion of radiotherapy. Single slice axial and coronal views of the study T_1 weighted MRI scan with overlaid ΔT_1 maps of the primary tumour are shown together with a single planning CT slice with overlaid deformed ΔT_1 map and corresponding slice on the post-treatment PET scan. Bright yellow regions on the PET scan in the right oropharynx (**A**) and right anterior glottis (**B**) were later histologically confirmed as residual squamous cell carcinoma. *DIR* - Deformable Image Registration.

number of slices than the MRI derived volumes. Given the CT slice thickness of 3mm, this imparts a significant impact on the magnitude of the contoured volumes. This finding is mirrored in the magnitude of CoG differences which imply relatively good in-plane localisation but shifts in the slice direction.

The ultimate aim for radiotherapy dose painting would be to obtain hypoxic parametric maps over the entirety of the primary tumour volume as contoured on the imaging used to plan the radiotherapy treatment. However, without being able to formally assert co-registration accuracy, it could be potentially grossly misleading to simply fuse the OE-MRI maps and use the CT based contours to extract the tumour hypoxic data. It should also be noted that the deformable registration approach used here was not optimised for cross modality registrations and therefore further work is required to develop and standardise OE-MRI and planning CT co-registration to allow for extraction of OE-MRI hypoxic parametric data for the entirety of the tumour volume used for radiotherapy planning.

In conclusion, it was possible to fuse parametric OE-MRI maps onto planning CT scans in order to give an indication of the likely distribution of hypoxic regions within primary tumours, however further work is required to develop the registration approach before performing any clinical radiotherapy dose painting studies.

Chapter 8

Tolerability of Oxygen Enhanced MRI

8.1 Abstract

Background and Method

The enclosed environs that are a design feature of the majority of clinical MRI scanners are well known to induce feelings of claustrophobia and anxiety in some patients with consequential risk of hampering clinical image acquisition. The wearing of a tight fitting oxygen mask inside such a scanner in patients with potential breathing and swallowing impairments from head and neck tumours has the potential to aggravate such negative emotions. Successful clinical implementation of OE-MRI in head and neck cancer requires this potential barrier to be assessed. All patient participants undergoing an OE-MRI scan were surveyed on their experience of the MRI scan.

Results

All patient participants except one completed the entire study scan sequence. All participants completed their subsequent clinical scan. Median anxiety scores were significantly worse with the OE-MRI sequence compared to the clinical scan ($p=0.026$ Wilcoxon signed rank) but the magnitude of this difference is small and of questionable clinical significance.

Conclusion

Overall the OE-MRI research scan sequence was well tolerated by patients with suspected head and neck cancer.

8.2 Background

MRI scanning first entered clinical practice in the 1980s and due to its lack of reliance on ionising radiation, superior ability to delineate soft tissue structures and high spatial resolution, it has rapidly become a widely used tool in clinical practice (McRobbie et al. 2017). In the year to March 2022, the NHS performed 3,845,155 individual MRI scans representing a 63.5% increase compared to the 2012/13 financial year (NHS 2023). The ability of MRI to generate image contrast based on physiological and molecular differences in addition to providing structural anatomical information has enhanced the clinical utility of MRI, especially in cancer diagnostics and evaluation. However, due to the fact that patients are often inserted head first into a relatively narrow bore tunnel whilst having receiver coils positioned close to the area of clinical interest, patient tolerance of MRI scans can be a limiting factor to their clinical utility. In addition, the on average longer duration of MRI scans compared to other diagnostic imaging modalities and the requirement for patients to lie still for the entirety of the scan whilst the machine makes a significant level of noise can cause distress and anxiety. These factors can have a negative impact on patients' ability to tolerate MRI scans and result in not only a poor patient experience making them less likely to agree to repeat scans, but also an increase in the chance of patient movement and consequential scan quality degradation which can have a significant detrimental effect on diagnostic accuracy (Madl et al. 2022).

Anxiety related distress in patients undergoing MRI scans has been well documented and researched, with a reported incidence in older style narrow bore scanners (diameter 60cm) of up to 37% (Katz et al. 1994, McIsaac et al. 1998). The causes of anxiety in MRI scanners are multifaceted but include claustrophobia, acoustic noise, pain, discomfort, having to keep still for extended periods of time and fear of what the results of the scan will reveal (Katz et al. 1994, Hewis 2015). The case series from Murphy & Brunberg (1997) on older style MRI scanners found 14.3% of patients required some form of sedation to allow

them to have an MRI scan, increasing to 16.2% for patients having a brain scan due to worry about claustrophobia with the head receiver coil. However Eshed et al. (2007) found that only 1.22% of MRI scans performed on modern design scanners (bore diameter 70cm) were terminated early due to claustrophobia with a slightly higher rate of 1.73% for patients undergoing head and neck MRI.

A variety of approaches have been explored to reduce anxiety and distress caused by MRI scanning (Munn & Jordan 2013) including modifying scanner design with technological engineering advances that enable scan quality to be maintained in machines with shorter, wider bores that patients experience a lesser degree of claustrophobia within (Tischler et al. 2008, Ahlander et al. 2020, Brunnquell et al. 2020, Iwan et al. 2020). So called "open scanners" that do not have a tunnel are often mentioned by patients as being preferred to closed, tunnel scanners however the image quality with such scanners is historically poorer than tunnel scanners due to lower magnetic field strength and increased field inhomogeneity (McRobbie et al. 2017). Educating claustrophobic patients about the image quality benefits of enclosed scanners can increase their level of acceptance of bore type scanners (Iwan et al. 2020). The physical and social environment surrounding the scanner also plays a crucial role in managing anxiety (Munn et al. 2016) as does the information provided to patients prior to their scans (Munn et al. 2015, Nakarada-Kordic et al. 2020) and the nature of the interpersonal interactions between patients and radiology staff (Carlsson & Carlsson 2013, Ajam et al. 2020).

OE-MRI scanning has the potential to cause greater scan related distress due to the requirements for patients to wear a tight-fitting oxygen mask in the scanner in addition to the MRI receiver coils. In future research studies and clinical applications of OE-MRI, it is likely to be desirable to scan patients in the radiotherapy treatment position, including with the use of radiotherapy immobilisation shells which in themselves are known to cause anxiety without being in an MRI scanner (Nixon et al. 2018, Klug et al. 2020). It is therefore important that the patient tolerability of OE-MRI with awake patients wearing an oxygen mask inside the MRI scanner is evaluated in order to fully consider interventions that may improve patient tolerance and concordance with treatment pathways. Although clinical studies of OE-MRI in solid tumours have generally reported

the scanning technique as being well tolerated by patients, formal assessment of patient experiences have not been identified in any published OE-MRI papers.

8.2.1 Patients' experience of medical imaging

Prior to developing the MRI research protocol, a quality improvement project looking at evaluating the experience of medical imaging at NUH in patients' undergoing curative intent radiotherapy for head and neck cancer was performed. A questionnaire was distributed to 50 consecutive patients undergoing curative intent radiotherapy for HNSCC asking them to recall which types of medical imaging they had undergone in the workup for their treatment. Respondents were requested to rank their experience of each scan type using a 5 point Likert scale under the domains of comfort, anxiety, pain and embarrassment (Appendix figure A.5).

Out of the 29 returned questionnaires (58% response rate), the median number of scan types undertaken prior to radiotherapy was 4 with 34% of respondents undergoing 5 different imaging modalities (planning-CT, diagnostic computed tomography (CT), MRI, PET, ultrasound scan). As seen in figure 8.1, all scans were generally well tolerated with median scores across all domains being disagree or strongly disagree that the adverse feeling was experienced. However, the domain of anxiety with the imaging modality of MRI showed the highest numbers of respondents rating agree or strongly agree to experiencing this feeling (30%) and was one of only two domains that had respondents replying that they strongly agreed that the adverse feeling was experienced.

This survey illustrates both the heavy burden of medical imaging that patients with HNSCC undergoing radiotherapy experience as well as the fact that MRI scan induced anxiety can be a potential issue in this patient group. Consequently, the OE-MRI in HNSCC study protocol incorporated a formal assessment of patient participants' reported experience of MRI induced anxiety in order to guide the future practical implementation of OE-MRI into routine clinical practice.

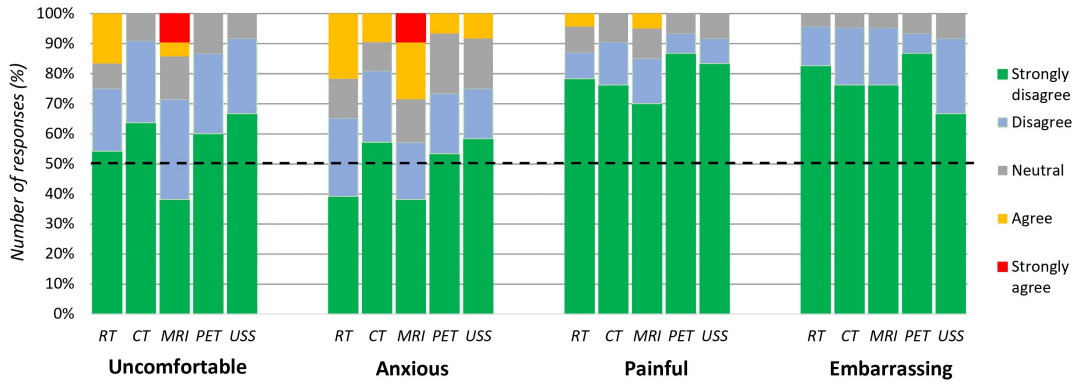

Figure 8.1: Patients' Experience of Medical Imaging - Stacked bar chart over 5 domains of patient reported experiences of medical imaging in the workup for curative intent radiotherapy treatment for head and neck cancer. RT = radiotherapy planning computed tomography, CT = computed tomography, MRI = magnetic resonance imaging, PET = positron emission tomography and computed tomography scan, USS = ultrasound scan.

8.3 Method

All patient participants in the OE-MRI study were invited to complete a questionnaire following completion of their MRI scan (figure 8.2). The questionnaire was approved as part of the research ethics committee submission but was not a mandatory component of the study meaning that patients could choose to undergo the research scan even if they declined to complete the questionnaire. The questionnaire consisted of two parts; the first pertained to the scan with the oxygen mask in-situ and the second to the routine clinical scan. Each section is based on the magnetic resonance imaging-anxiety questionnaire (MRI-AQ). This is a validated questionnaire specifically designed to assess MRI scan induced anxiety (Ahlander et al. 2016).

The scores for each of the 15 questions were summed to produce an overall measure of anxiety for the with and without oxygen mask scans (scores for questions 1, 7, 8 and 10 were inverted prior to summation as per the MRI-AQ methodology). The difference between the with and without oxygen mask score for each patient was calculated with differences between the two group assessed

Nottingham University Hospitals NHS
NHS Trust

*Study Volunteer Number*_____

PARTICIPANT QUESTIONNAIRE

(Version 1.0, 15-Jan-2021)

Evaluation of Oxygen Enhanced MRI for Identification of Hypoxia Induced Resistant Tumours in Patients with Head and Neck Cancer

Have you ever had an MRI scan before? **Yes** **No**

Below are some statements that can be used to describe your feelings. Read each statement and circle the number 1 to 4 that best describes your feelings during the MRI examination. Do not reflect too much on any statement, but respond in the way you think best corresponds to your feelings during the examination.

First part of scan (*with* oxygen mask on) 		**Not at all**	**Somewhat**	**Moderately**	**Very much**
1	I felt that I controlled the situation	1	2	3	4
2	I had palpitations (heart feeling unusual)	1	2	3	4
3	I found it hard to breathe	1	2	3	4
4	I was afraid	1	2	3	4
5	I wanted to come out	1	2	3	4
6	I panicked	1	2	3	4
7	I felt relaxed	1	2	3	4
8	I felt safe	1	2	3	4
9	I worried in advance	1	2	3	4
10	I felt calm	1	2	3	4
11	I had to force myself to manage the situation	1	2	3	4
12	Self-control was required when going through the examination	1	2	3	4
13	I needed support and encouragement	1	2	3	4
14	I wished to have someone with me	1	2	3	4
15	I needed more detailed information	1	2	3	4

When you have finished, please turn the page over.

Research & Innovation

Figure 8.2: Patient Tolerability Questionnaire - Copy of the assessment used to compare the patient experience of undergoing an OE-MRI scan versus having a standard head and neck MRI scan.

for statistical significance using the Wilcoxon signed rank test (p-value < 0.05 significant).

The free text box on the questionnaire was analysed for common themes in order to consider potential improvements to patient tolerability for future studies. Each questionnaire was reviewed by a member of the research team immediately after its completion in order to ensure that no serious issues or concerns requiring immediate attention were raised by patients.

8.4 Results

All 20 patient participants completed the study anxiety questionnaire in full. No immediate safety concerns or patient welfare issues were raised during the OE-MRI study. One patient stopped the study scan early due to discomfort (participant P012, Appendix table B.4). This participant completed the clinical scan in full and therefore suffered no adverse consequences from study participation.

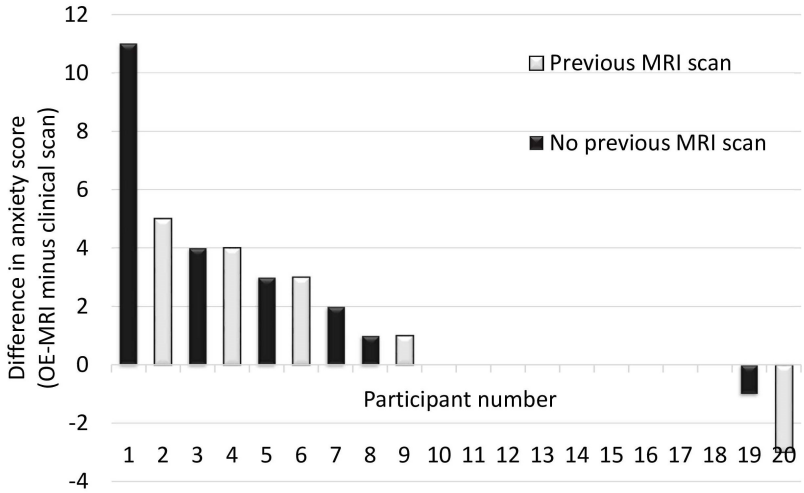

Figure 8.3: Difference in anxiety scores - Waterfall plot of the difference in anxiety scores between the OE-MRI and routine clinical MRI scan for all 20 patient participants. Larger values indicate worse reported anxiety with the OE-MRI scan. Lighter bars indicate patients who reported having undergone an MRI scan previously.

Median anxiety score were 19.5 (range 15 to 42) and 15.5 (range 15 to 45) for the scans performed with and without a mask respectively (p=0.026 Wilcoxon signed rank). There was no significant difference identified between scores for patients who had undergone a previous MRI scan compared to those who had not with median difference in anxiety scores (study scan minus clinical scan) of 0.5 and 0 respectively (p=0.871 Wilcoxon rank sum). A waterfall plot of the difference in anxiety scores per patient participant is shown in figure 8.3 with a summary of the scores for each individual domain of the questionnaire given in table 8.1.

7 patients left comments in the free text box of the questionnaire with 3 people commenting on the oxygen mask. 2 people found that the mask did not fit well and moved during the scan causing discomfort with 1 of these patients asking if the oxygen scan could be done after the clinical scan to allow them to become accustomed to the MRI environment before having to wear the oxygen mask. 1 person stated that they felt more in control without the mask on (individual patient participant results in Appendix Table B.4).

8.5 Discussion

This is the first clinical study of OE-MRI that has attempted to make a formal quantitative assessment of participants' tolerability of the study sequence. The MRI-AQ that was used to perform this assessment focuses on two factors; "anxiety symptoms" and "relaxation symptoms" (Ahlander et al. 2016). The benefit of this assessment is that it specifically assess anxiety generated by the MRI scan itself rather than non-scan related generalised anxiety as assessed by commonly used tools such as the generalised anxiety disorder assessment (GAD-7) (Spitzer et al. 2006) and the hospital anxiety and depression scale (HADS) (Zigmond & Snaith 1983).

Overall, there was a statistically significant worsening in anxiety recorded with the study sequence relative to the standard clinical scan, although the absolute magnitude of the difference is small and therefore of questionable clinical significance. All bar one participant completed the entire study sequence and all participants completed the subsequent clinical scan implying that any negative

Table 8.1: Summed scores from all patient participants for each of the 15 domains assessed in the MRI-AQ. Lowest potential summed score is 20 (lowest anxiety) to 80 (maximum anxiety). The scores for domains 1, 7, 8 and 10 have been inverted to allow ease of comparison (original scores stated in brackets).

	Total score (20 patients)		
Statement	**Mask on**	**No mask**	**Difference**
1. I felt that I controlled the situation	27 (73)	24 (76)	3
2. I had palpitations (heart feeling unusual)	24	22	2
3. I found it hard to breathe	22	23	-1
4. I was afraid	32	27	5
5. I wanted to come out	26	27	-1
6. I panicked	22	22	0
7. I felt relaxed	36 (64)	29 (71)	7
8. I felt safe	25 (75)	24 (76)	1
9. I worried in advance	35	28	7
10. I felt calm	31 (69)	27 (73)	4
11. I had to force myself to manage the situation	31	30	1
12. Self-control was required when going through the examination	38	35	3
13. I needed support and encouragement	25	25	0
14. I wished to have someone with me	26	26	0
15. I needed more detailed information	20	21	-1

emotional reaction to the study scan was manageable. Responses in the free text comments section of the questionnaire emphasise the need to ensure correct and comfortable fixing of the oxygen mask before starting the OE-MRI sequence and to explain to patients why the OE-MRI needs to be performed before routine clinical imaging that does not require an oxygen mask. One participant explicitly mentioned that the provision of a mirror above their head which allowed them to see out of the bore of the scanner during the imaging, made a significant contribution to their wellbeing. This simple intervention should be offered to all patients in the future as it has no negative impact on the image acquisition. Although this mirror was available for all participants in this study, it was not explicitly mentioned in the study protocol and therefore was not routinely used for either the oxygen enhanced scan or the routine clinical scan. Unfortunately, it was not recorded which participants had the use of this mirror and which did not therefore potentially acting as a confounding factor for differences in anxiety scores between participants.

Although the MRI-AQ is designed to given an overall anxiety score, it is interesting to note that the individual domains that showed the greatest difference in scores between the study scan and routine clinical scan were for the statements *"I felt relaxed"* and *"I worried in advance"*, both of which showed worse scores with the oxygen enhanced scan. It is maybe not overly surprising that patients reported greater worry in advance about a scan termed a *research* or *study* scan as opposed to a routine clinical scan and it maybe that if OE-MRI was used in *routine* clinical practice some of this worry would be naturally alleviated. It is also worth considering what information is provided to patients in advance of their scan and whether videos or photographs of the scan setup may be used to ameliorate pre-scan anxiety. In addition, ensuring radiography staff are fully versed in the nature of the OE-MRI sequence is critical as positive social interactions and communication from hospital staff have a significant positive influence on patients' experiences of MRI (Carlsson & Carlsson 2013, Ajam et al. 2020).

Including the published work presented in this thesis (McCabe et al. 2024a), a total of 3 papers report performing OE-MRI in patients with head and neck cancer with both of the other papers having been published after data collection for this study had been commenced. Neither of these other papers reports a formal

assessment of the patient experience. Dubec et al. (2023) note that "no adverse events were reported" in their study and managed to successfully and repeatedly scan all of their recruited patients however, Bluemke et al. (2023) reported patient motion being a significant difficulty encountered during their study and that they needed to remove a T_1 mapping sequence from their protocol part way through the study in order to reduce scanning acquisition times stating that this was "needed" by some patients. No further details on the nature of the adverse experiences that necessitated this change are provided but this highlights the potential difficulties with performing OE-MRI in the clinical setting in patients with HNSCC. Nevertheless the findings from these subsequent two studies are in concordance with the data presented here whereby the OE-MRI scan was only terminated early in one participant and clinically usable OE-MRI data was successfully obtained in all participants (chapter 7).

There are some additional significant limitations with this tolerability assessment. All participants in this study voluntarily agreed to undergo a longer MRI scan and therefore potentially represent a subset of patients less prone to MRI scan anxiety. In addition, study participants all underwent the OE-MRI study sequence prior to their diagnostic imaging sequences meaning that they may have become more accustomed to the MRI environment by the time of the diagnostic scan. This could reduce recorded anxiety levels with the diagnostic scans. Conversely, as time elapsed in the scanner patients may have experienced greater levels of discomfort which may confound the tolerability assessment as the questionnaire specifically focussed on anxiety rather than discomfort. The order of the scans was fixed due to the requirement to complete the OE-MRI protocol before the clinical imaging in order to avoid the administration of gadolinium contrast agent with the clinical scan masking changes in oxygen induced T_1 times.

A further limitation is that the MRI receiver coils used for the study and clinical scans were different in order to facilitate ready positioning of the non-rebreather oxygen mask for the study sequences. The different receiver coils used may influence the patient experience of the scans in addition to the wearing of the oxygen mask and breathing of high flow oxygen. The reason for any differences in an individual patient's anxiety scores is not elucidated by this assessment method. Finally, patients were asked about their experience of the OE-MRI and clinical

scan at the same time leading to the risk of confusion between the experiences of both parts of scan. It was however not practical nor desirable to either interview participants between scans or to perform the scans on separate days.

In conclusion, the OE-MRI scan was well tolerated by the study participants although there was a small but statistically significant worse MRI associated anxiety score with the study sequence. Further OE-MRI studies in HNSCC should be mindful of the potential burden additional or extended scans place on this group of patients who are undergoing an already significant amount of medical imaging during a psychologically challenging time.

Chapter 9

Overall Conclusions and Suggestions for Future Work

In this thesis the existing evidence behind the use of OE-MRI for the assessment of tumour hypoxia has been summarised via a scoping review of the published literature. A dynamic, volumetric OE-MRI protocol for the head and neck region using routinely available equipment in an acute hospital setting was developed and evaluated in test phantoms, non-patient volunteers and patient participants. This well-tolerated implementation of OE-MRI was able to discern differing responses to supplemental oxygen within biopsy confirmed HNSCC. Bespoke tools to process the OE-MRI data were developed and an exploration of novel analysis methods in line with current academic advancements was also performed. This thesis did not repeat the work of previous authors in establishing the utility of OE-MRI in determining regions of tumour hypoxia but focussed on developing a clinical protocol that was both practical and robust to real life challenges to make it conceivable to perform OE-MRI in the routine clinical setting in the majority of patients with HNSCC.

At the start of the research presented in this thesis there were no published papers on performing OE-MRI in HNSCC. Academic and clinical interest in the potential of OE-MRI in assessing HNSCC tumour hypoxia is however growing and other research groups have recently published on OE-MRI in the head and neck region (Bluemke et al. 2023, Dubec et al. 2023, 2024). The protocol developed in

this thesis though remains unique in its unequivocal focus on translating the OE-MRI approach into a clinically applicable imaging technique that could be readily utilised in any modern cancer centre around the world without need of specialist equipment and without adding an undue burden to patients by performing the OE-MRI sequence in less than 10 minutes. This research is also the first to explicitly test correlations between OE-MRI imaging findings and actual clinical treatment outcomes from patients with HNSCC who underwent curative intent CRT.

Although the history of tumour hypoxia assessment has been focussed around identifying tumours with a greater risk of hypoxia induced radioresistance who may benefit from the addition of hypoxia modification therapies, the significant increase in rates of HPV associated oropharyngeal HNSCC and the increased radiosensitivity of this disease compared to its non-HPV related counterparts has led to substantial interest in radiotherapy de-escalation studies in order to reduce the treatment related toxicity to healthy tissues. However as discussed in section 1.2.1, such strategies have to date proven unsuccessful in phase 3 trials with excess rates of disease recurrence and mortality in the de-escalation intervention arms. Arguably the most exciting current development in dose de-escalation trials is based around the use of hypoxic PET imaging to guide patient selection for dose de-escalation based upon lack of tumour hypoxia or early resolution of tumour hypoxia with treatment (Lee et al. 2024*a*). Although still needing verification in a phase 3 trial setting, if this de-escalation strategy proves successful it may be that OE-MRI is better placed to facilitate its wider adoption due to the greater global access to MRI than hypoxic PET imaging, especially if a 10minute, robust OE-MRI scanning protocol such as developed in this thesis were to be adopted.

The majority of imaged tumours in this thesis were HPV related, reflecting the relative prevalence of this subset of HNSCC. The practicability and tolerability assessments of the scanning protocol used in this study are therefore directly applicable to the potential for OE-MRI based HPV dose de-escalation strategies. Recently published work by Dubec et al. (2024) found that 54.6% of HPV associated tumours treated with radical radiotherapy had a reduction in OE-MRI assessed tumour hypoxic volume by the second week of treatment, increasing to 90% by week 4 leading to the hypothesis that variable levels of dose

de-escalation could be considered dependent upon the timing of the reduction in tumour hypoxic burden. However, further observational studies correlating hypoxic biomarkers to relevant clinical outcomes are required before considering any variable radiotherapy dose de-escalation trials due to the inherent risk of under-treating potentially curative patients and causing an excess of mortality. Nevertheless, it would seem reasonable to hypothesise that if hypoxic PET guided dose de-escalation strategies prove successful in HPV related oropharynx HNSCC then an OE-MRI based approach may be possible. In order to minimise the number of patients needed to be enrolled in dose de-escalation trials, ideally an OE-MRI tumour hypoxic assessment would be incorporated into the hypoxic PET based de-escalation trials. If this is not practical, correlation studies between hypoxic PET and OE-MRI imaging in patients with HPV associated oropharynx HNSCC potentially suitable for dose de-escalation should be performed as a minimum.

Outside the realm of HPV associated HNSCC, interest persists in using hypoxic imaging to stratify patients based on the likelihood of response to hypoxia modification therapy. Indeed, it has been suggested that failure to stratify based on the extent of intra-tumoural hypoxia is sufficient to account for the observed clinical futility of phase 3 trials of hypoxia-activated prodrugs (Spiegelberg et al. 2019). A pre-clinical study has demonstrated the utility of OE-MRI in assessing changes in oxygenation in tumour xenografts induced by the hypoxia modifying drugs Banoxantone (a hypoxia-activated prodrug of the topoisomerase II inhibitor AQ4) and Atovaquone (an inhibitor of mitochondrial complex III of the electron transport chain) (O'Connor et al. 2024). Combining such pre-clinical data with the evidence presented in this thesis of the utility of performing OE-MRI in HNSCC in the clinical setting suggests that OE-MRI may represent a stratification tool for future hypoxia modifying clinical trials however further evidence of the utility of this approach and standardisation of imaging protocols will be required before the pharmaceutical industry that are the principle funders and sponsors of phase 3 drug trials will be likely to adopt this strategy.

One of the greatest challenges in the non-surgical management of HNSCC is the treatment of cancers arising in the hypopharynx. Although only representing 8.4% of locally advanced HNSCC (stages III to IVb), the 3 year overall survival rate for patients with hypopharynx SCC treated with curative intent CRT in

the UK is only 47.6% (McCabe et al. 2024b). There is clearly an unmet need for this group of patients and although the specific impact of tumour hypoxia on this subgroup of HNSCC is unknown, the observed higher rates of radioresistance suggest that this is a subgroup that may benefit from OE-MRI studies; both to assess the extent and persistence of hypoxia with radiotherapy and the impact of hypoxia modifying trials including hypoxia adaptive radiotherapy studies (Ingram et al. 2024). Due to the relative lower prevalence of this subtype of HNSCC, such OE-MRI studies would need to be multi-institutional and require standardisation of imaging protocols. This is an integral step towards the wider adoption of OE-MRI and requires those researchers working in the field of tumour hypoxia OE-MRI assessment to collaborate to develop a consensus on a standardised image acquisition protocol.

Although the prognostic influence of tumour hypoxia is well proven, the relative importance of it compared to other prognostic factors needs to be considered. For example, data from the DAHANCA-19 study database found that on multivariable cox-regression, tumour hypoxia as assessed by a 15 gene hypoxic-signature failed to demonstrate statistically significant prognosis despite showing prognostic ability on univariate analysis (Horsholt Kristensen et al. 2024). Similarly, a previous German study found that the same 15 gene hypoxic classifier had greater prognostic impact only for smaller primary tumour volumes ($< 19mm^3$) (Linge et al. 2016). In this thesis 73% (11/15) of the primary tumours had volumes $< 19mm^3$. Multivariable analysis of clinical outcomes are important to discern the independent impact of tumour hypoxia however to avoid the potential of over-fitting multivariable regression models, larger detailed clinical data sets are required. Such data sets could then also be used to explore the potential role of OE-MRI textural features in prognosis and treatment stratification (see section 7.3).

One of the challenges encountered with performing OE-MRI in the head and neck region is that of movement, both gross patient movement as well as internal movement relating to normal physiological functions. As detailed in chapter 6, in this thesis a post-processing image co-registration approach was used to align successive images from the dynamic OE-MRI sequence. This approach was readily applied to the dynamic OE-MRI data resulting in measured improvement of the

consistency of OE-MRI derived hypoxia metrics. However such an approach does not compensate for degradation in image quality due to participant movement during an individual image acquisition sequence. Given the relatively small magnitude of changes in T_1 time induced by supplemental oxygen, motion induced artefacts could have a significant impact on the accuracy of ΔT_1 maps.

The VFA approach used in the OE-MRI mapping sequence in this study used conventional Cartesian k-space sampling meaning that motion during the image acquisition could induce phase offsets leading to image artefacts. The extent of motion encountered during a particular acquisition can be reduced by reducing the acquisition time through acceleration techniques (as were used in the study sequence) or through reduction in the spatial resolution or image SNR. Alternatively acquiring k-space in a non-Cartesian manner can also make an image sequence more robust to motion distortion. Kim et al. (2024) evaluated a 3D stack of stars (SOS) approach to VFA T_1 OE-MRI measurement whereby k-space is sampled using a radical trajectory in the in-plane direction with Cartesian sampling retained for the slice direction. They found that the approach improved the reliability and accuracy of T_1 determination in HNSCC patients however this approach has yet to be tested in a clinical trial correlating OE-MRI biomarkers to treatment outcomes. In addition, the authors used dedicated head and neck receiver coils and therefore the utility of performing this on the routine clinical systems and coil selection that was used in the current study requires further evaluation.

Arguably one of the most significant advances in the clinical management of HNSCC in recent years has come with the advent of immune checkpoint inhibitor therapy in the form of the programmed cell death protein 1 (PD-1) inhibitors Nivolumab and Pembrolizumab. Now widely used in the non-curative recurrent or metastatic disease setting in HNSCC they have demonstrated superior outcomes compared to conventional chemotherapy (Ferris et al. 2016, Burtness et al. 2019). Although pre-clinical studies have also suggested a synergistic effect of immunotherapy with radiotherapy, clinical trials investigating this combination have so far failed to show clinical benefits from this treatment combination (Wong et al. 2022). In addition although it is possible for patients to obtain long lasting

responses to immunotherapy treatments, such outcomes are seen in only approximately 20% of HNSCC patients, a trend also noted in other tumour types where average response rates range from 20% to 40% (Sharma et al. 2017). There is clearly therefore much to still be understood about these medications and their interaction with HNSCC of which hypoxic conditions in the tumour microenvironment is one. As discussed in section 1.1, hypoxia can drive immunosuppression and increase resistance to anti-PD-1 drugs. Knowledge of the distribution and extent of tumour hypoxia may thus yield clinically useful information pertaining to the utilisation of immunotherapy treatments in HNSCC both in the metastatic setting but also potentially for response stratification in on-going concurrent and adjuvant radical treatment immunotherapy trials. Therefore, although this thesis has focussed on patients being treated with curative intent CRT, there may be a broader role for tumour hypoxic imaging in the clinical management of HNSCC in which OE-MRI could play a significant part.

Finally, returning to the hypothesis and research aims stated in section 4.1, in this thesis the ability to perform OE-MRI on a routine clinical scanner using routinely available clinical equipment has been demonstrated via a well-tolerated volumetric implementation of OE-MRI in the head and neck region. OE-MRI derived metrics were correlated to clinical outcomes with average tumour hypoxic burden being greater in radiotherapy non-responsive tumours, albeit without statistical significance. Further adequately powered, multisite studies that would have the benefit of independent verification of OE-MRI are therefore now required to investigate the predictive power of OE-MRI hypoxic fractions and other novel OE-MRI derived biomarkers to guide treatment intensification and de-escalation strategies in the non-surgical management of HNSCC.

References

Abdel Razek, A. A. K. & Poptani, H. (2013), 'MR spectroscopy of head and neck cancer', *Eur. J. Radiol.* **82**(6), 982–989. 38

Adam, M. F., Gabalski, E. C., Bloch, D. A., Oehlert, J. W., Brown, J. M., Elsaid, A. A., Pinto, H. A. & Terris, D. J. (1999), 'Tissue oxygen distribution in head and neck cancer patients', *Head Neck* **21**(2), 146–153. 13

Aebersold, D. M., Burri, P., Beer, K. T., Laissue, J., Djonov, V., Greiner, R. H. & Semenza, G. L. (2001), 'Expression of hypoxia-inducible factor-1alpha: a novel predictive and prognostic parameter in the radiotherapy of oropharyngeal cancer', *Cancer Res.* **61**(7), 2911–2916. 32

Aherne, E., Chow, K. & Carr, J. (2020), 'Cardiac T1 mapping: Techniques and applications', *J. Magn. Reson. Imaging* **51**(5), 1336–1356. 56

Ahlander, B. M., Årestedt, K., Engvall, J., Maret, E. & Ericsson, E. (2016), 'Development and validation of a questionnaire evaluating patient anxiety during magnetic resonance imaging: the magnetic resonance Imaging-Anxiety questionnaire (MRI-AQ)', *J. Adv. Nurs.* **72**(6), 1368–1380. 173, 176

Ahlander, B. M., Engvall, J. & Ericsson, E. (2020), 'Anxiety during magnetic resonance imaging of the spine in relation to scanner design and size', *Radiography* **26**(2), 110–116. 171

Ajam, A. A., Tahir, S., Makary, M. S., Longworth, S., Lang, E. V., Krishna, N. G., Mayr, N. A. & Nguyen, X. V. (2020), 'Communication and team interactions to improve patient experiences, quality of care, and throughput in MRI', *Top. Magn. Reson. Imaging* **29**(3), 131–134. 171, 178

Albenberg, L., Esipova, T. V., Judge, C. P., Bittinger, K., Chen, J., Laughlin, A., Grunberg, S., Baldassano, R. N., Lewis, J. D., Li, H., Thom, S. R., Bushman, F. D., Vinogradov, S. A. & Wu, G. D. (2014), 'Correlation between intraluminal oxygen gradient and radial partitioning of intestinal microbiota', *Gastroenterology* **147**(5), 1055–63.e8. 2

Ang, K. K. (2010), 'More lessons learned from the suffocation of hypoxia', *J. Clin. Oncol.* **28**(18), 2941–2943. 24

Ang, K. K., Harris, J., Wheeler, R., Weber, R., Rosenthal, D. I., Nguyen-Tân,

P. F., Westra, W. H., Chung, C. H., Jordan, R. C., Lu, C., Kim, H., Axelrod, R., Silverman, C. C., Redmond, K. P. & Gillison, M. L. (2010), 'Human papillomavirus and survival of patients with oropharyngeal cancer', *N. Engl. J. Med.* **363**(1), 24–35. 27

Arai, T. J., Yang, D. M., Campbell, J. W., Chiu, T., Cheng, X., Stojadinovic, S., Peschke, P. & Mason, R. P. (2021), 'Oxygen-Sensitive MRI: A predictive imaging biomarker for tumor radiation response?', *Int. J. Radiat. Oncol. Biol. Phys.* **110**(5), 1519–1529. 65, 68

Arnold, J. F. T., Kotas, M., Fidler, F., Pracht, E. D., Flentje, M. & Jakob, P. M. (2007), 'Quantitative regional oxygen transfer imaging of the human lung', *J. Magn. Reson. Imaging* **26**(3), 637–645. 42

Atwell, D., Elks, J., Cahill, K., Hearn, N., Vignarajah, D., Lagopoulos, J. & Min, M. (2020), 'A review of modern radiation therapy dose escalation in locally advanced head and neck cancer', *Clin. Oncol.* **32**(5), 330–341. 27

Avants, B. B., Tustison, N. J., Song, G., Cook, P. A., Klein, A. & Gee, J. C. (2011), 'A reproducible evaluation of ANTs similarity metric performance in brain image registration', *Neuroimage* **54**(3), 2033–2044. 117, 133

Bader, S. B., Dewhirst, M. W. & Hammond, E. M. (2020), 'Cyclic hypoxia: An update on its characteristics, methods to measure it and biological implications in cancer', *Cancers* **13**(1). 77

Badoual, C. (2022), 'Update from the 5th edition of the world health organization classification of head and neck tumors: Oropharynx and nasopharynx', *Head Neck Pathol.* **16**(1), 19–30. 18

Baete, S. H., Vandecasteele, J. & De Deene, Y. (2011), '19 F MRI oximetry: simulation of perfluorocarbon distribution impact', *Phys. Med. Biol.* **56**(8), 2535–2557. 37

Baker, J. H. E., Moosvi, F., Kyle, A. H., Banath, J. P., Saatchi, K., Haefeli, U. O., Reinsberg, S. A. & Minchinton, A. I. (2023), 'Radiosensitizing oxygenation changes in murine tumors treated with VEGF-ablation therapy are measurable using oxygen enhanced-MRI (OE-MRI)', *Radiother. Oncol.* **187**, 109795. 78

Bane, O., Besa, C., Wagner, M., Oesingmann, N., Zhu, H., Fiel, M. I. & Taouli, B. (2016), 'Feasibility and reproducibility of BOLD and TOLD measurements in the liver with oxygen and carbogen gas challenge in healthy volunteers and patients with hepatocellular carcinoma', *J. Magn. Reson. Imaging* **43**(4), 866–876. 71

Barsoum, I. B., Koti, M., Siemens, D. R. & Graham, C. H. (2014), 'Mechanisms of hypoxia-mediated immune escape in cancer', *Cancer Res.* **74**(24), 7185–7190. 10, 11

Baumann, M., Krause, M., Dikomey, E., Dittmann, K., Dörr, W., Kasten-Pisula, U. & Rodemann, H. P. (2007), 'EGFR-targeted anti-cancer drugs in radiotherapy: Preclinical evaluation of mechanisms', *Radiother. Oncol.* **83**(3), 238–248. 21

Beeman, S. C., Shui, Y.-B., Perez-Torres, C. J., Engelbach, J. A., Ackerman, J. J. H. & Garbow, J. R. (2016), 'O_2-Sensitive MRI distinguishes brain tumor versus radiation necrosis in murine models', *Magn. Reson. Med.* **75**(6), 2442–2447. 65, 74

Belfatto, A., White, D. A., Mason, R. P., Zhang, Z., Stojadinovic, S., Baroni, G. & Cerveri, P. (2016), 'Tumor radiosensitivity assessment by means of volume data and magnetic resonance indices measured on prostate tumor bearing rats', *Med. Phys.* **43**(3), 1275–1284. 66, 68

Bernier, J., Domenge, C., Ozsahin, M., Matuszewska, K., Lefèbvre, J.-L., Greiner, R. H., Giralt, J., Maingon, P., Rolland, F., Bolla, M., Cognetti, F., Bourhis, J., Kirkpatrick, A., van Glabbeke, M. & European Organization for Research and Treatment of Cancer Trial 22931 (2004), 'Postoperative irradiation with or without concomitant chemotherapy for locally advanced head and neck cancer', *N. Engl. J. Med.* **350**(19), 1945–1952. 20

Bernstein, J. M., Homer, J. J. & West, C. M. (2014), 'Dynamic contrast-enhanced magnetic resonance imaging biomarkers in head and neck cancer: potential to guide treatment? a systematic review', *Oral Oncol.* **50**(10), 963–970. 39

Betts, G. N., Eustace, A., Patiar, S., Valentine, H. R., Irlam, J., Ramachandran, A., Merve, A., Homer, J. J., Möller-Levet, C., Buffa, F. M., Hall, G., Miller, C. J., Harris, A. L. & West, C. M. (2013), 'Prospective technical validation and assessment of intratumour heterogeneity of a low density array hypoxia gene profile in head and neck squamous cell carcinoma', *Eur. J. Cancer* **49**(1), 156–165. 33

Bezabeh, T., Odlum, O., Nason, R., Kerr, P., Sutherland, D., Patel, R. & Smith, I. C. P. (2005), 'Prediction of treatment response in head and neck cancer by magnetic resonance spectroscopy', *AJNR Am. J. Neuroradiol.* **26**(8), 2108–2113. 37

Bhandari, V., Li, C. H., Bristow, R. G., Boutros, P. C. & PCAWG Consortium (2020), 'Divergent mutational processes distinguish hypoxic

and normoxic tumours', *Nat. Commun.* **11**(1), 737. 8, 9

Bhide, S. A., Ahmed, M., Barbachano, Y., Newbold, K., Harrington, K. J. & Nutting, C. M. (2008), 'Sequential induction chemotherapy followed by radical chemo-radiation in the treatment of locoregionally advanced head-and-neck cancer', *Br. J. Cancer* **99**(1), 57–62. 87

Bhogal, A. A., Siero, J. C. W., Zwanenburg, J., Luijten, P. R., Philippens, M. E. P. & Hoogduin, H. (2017), 'Quantitative T1 mapping under precisely controlled graded hyperoxia at 7T', *J. Cereb. Blood Flow Metab.* **37**(4), 1461–1469. 107, 110

Biau, J., Lapeyre, M., Troussier, I., Budach, W., Giralt, J., Grau, C., Kazmierska, J., Langendijk, J. A., Ozsahin, M., O'Sullivan, B., Bourhis, J. & Grégoire, V. (2019), 'Selection of lymph node target volumes for definitive head and neck radiation therapy: a 2019 update', *Radiother. Oncol.* **134**, 1–9. 20

Bigos, K. J. A., Quiles, C. G., Lunj, S., Smith, D. J., Krause, M., Troost, E. G. C., West, C. M., Hoskin, P. & Choudhury, A. (2024), 'Tumour response to hypoxia: understanding the hypoxic tumour microenvironment to improve treatment outcome in solid tumours', *Front. Oncol.* **14**. 10

Blanchard, P., Baujat, B., Holostenco, V., Bourredjem, A., Baey, C., Bourhis, J., Pignon, J.-P. & MACH-CH Collaborative group (2011), 'Meta-analysis of chemotherapy in head and neck cancer (MACH-NC): a comprehensive analysis by tumour site', *Radiother. Oncol.* **100**(1), 33–40. 21

Blockley, N. P., Jiang, L., Gardener, A. G., Ludman, C. N., Francis, S. T. & Gowland, P. A. (2008), 'Field strength dependence of R1 and r2* relaxivities of human whole blood to ProHance, vasovist, and deoxyhemoglobin', *Magn. Reson. Med.* **60**(6), 1313–1320. 130

Bluemke, E., Bertrand, A., Chu, K.-Y., Syed, N., Murchison, A. G., Cooke, R., Greenhalgh, T., Burns, B., Craig, M., Taylor, N., Shah, K., Gleeson, F. & Bulte, D. (2022*a*), 'Using variable flip angle (VFA) and modified Look-Locker inversion recovery (MOLLI) T1 mapping in clinical OE-MRI', *Magn. Reson. Imaging* **89**, 92–99. 56, 62, 72, 75, 76

Bluemke, E., Bertrand, A., Chu, K.-Y., Syed, N., Murchison, A. G., Cooke, R., Greenhalgh, T., Burns, B., Craig, M., Taylor, N., Shah, K., Gleeson, F. & Bulte, D. (2023), 'Oxygen-enhanced MRI and radiotherapy in patients with oropharyngeal squamous cell carcinoma', *Clin Transl Radiat Oncol* **39**(100563), 100563. 79, 132, 153, 179, 181

Bluemke, E., Bulte, D., Bertrand, A., Ben George, Cooke, R., Chu, K.-Y., Durrant, L., Goh, V., Jacobs, C., Ng, S. M., Strauss, V. Y., Hawkins, M. A. & Muirhead, R. (2020), 'Oxygen-enhanced MRI MOLLI T1 mapping during chemoradiotherapy in anal squamous cell carcinoma', *Clin Transl Radiat Oncol* **22**, 44–49. 68, 69, 72, 75

Bluemke, E., Stride, E. & Bulte, D. P. (2022*a*), 'Modeling the effect of hyperoxia on the Spin-Lattice relaxation rate R1 of tissues', *Magn. Reson. Med.* **88**(4), 1867–1885. 83, 130, 151

Bluemke, E., Stride, E. & Bulte, D. P. (2022*b*), 'A simplified empirical model to estimate oxygen relaxivity at different magnetic fields', *NMR Biomed.* **35**(2), e4625. 111

Bluemke, E., Stride, E. & Bulte, D. P. (2022*b*), 'A general model to calculate the Spin-Lattice relaxation rate (r1) of blood, accounting for hematocrit, oxygen saturation, oxygen partial pressure, and magnetic field strength under hyperoxic conditions', *J. Magn. Reson. Imaging* **55**(5), 1428–1439. 67

Boeckman, H. J., Trego, K. S. & Turchi, J. J. (2005), 'Cisplatin sensitizes cancer cells to ionizing radiation via inhibition of nonhomologous end joining', *Mol. Cancer Res.* **3**(5), 277–285. 21

Bolland, H., Ma, T. S., Ramlee, S., Ramadan, K. & Hammond, E. M. (2021), 'Links between the unfolded protein response and the DNA damage response in hypoxia: a systematic review', *Biochem. Soc. Trans.* **49**(3), 1251–1263. 7

Bonner, J. A., Harari, P. M., Giralt, J., Azarnia, N., Shin, D. M., Cohen, R. B., Jones, C. U., Sur, R., Raben, D., Jassem, J., Ove, R., Kies, M. S., Baselga, J., Youssoufian, H., Amellal, N., Rowinsky, E. K. & Ang, K. K. (2006), 'Radiotherapy plus cetuximab for squamous-cell carcinoma of the head and neck', *N. Engl. J. Med.* **354**(6), 567–578. 21

Boult, J. K. R., Roy, U., Bernauer, C., Box, C., Howell, L., Lepicard, E. Y., Jamin, Y., O'Connor, J. P. B., Shipley., J. M. & Robinson, S. P. (2022), 'Characterising hypoxia in rhabdomyosarcoma xenografts with oxygen-enhanced MRI', *Proc. Intl. Soc. Mag. Reson. Med.* **Abstract 2754**. 65

Boumphrey, S. M., Morris, E. A. J. & Kinsella, S. M. (2003), '100% inspired oxygen from a hudson mask-a realistic goal?', *Resuscitation* **57**(1), 69–72. 106

Bourhis, J., Montay-Gruel, P., Gonçalves Jorge, P., Bailat, C., Petit, B., Ollivier, J., Jeanneret-Sozzi, W., Ozsahin, M., Bochud, F., Moeckli, R., Germond, J.-F. & Vozenin, M.-C. (2019), 'Clinical translation of FLASH radiotherapy: Why and

how?', *Radiother. Oncol.* **139**, 11–17. 26

Bradley, J. (2022), Voxel-Based approaches to evaluating the spatial and temporal SNR in dynamic and Oxygen-Enhanced magnetic resonance imaging, Master's thesis, Nottingham Trent University. 120

Brighi, C., Waddington, D. E. J., Keall, P. J., Booth, J., O'Brien, K., Silvester, S., Parkinson, J., Mueller, M., Yim, J., Bailey, D. L., Back, M. & Drummond, J. (2023), 'The MANGO study: a prospective investigation of oxygen enhanced and blood-oxygen level dependent MRI as imaging biomarkers of hypoxia in glioblastoma', *Front. Oncol.* **13**, 1306164. 77

Bristow, R. G. & Hill, R. P. (2008), 'Hypoxia and metabolism. hypoxia, DNA repair and genetic instability', *Nat. Rev. Cancer* **8**(3), 180–192. 3

Brizel, D. M., Dodge, R. K., Clough, R. W. & Dewhirst, M. W. (1999), 'Oxygenation of head and neck cancer: changes during radiotherapy and impact on treatment outcome', *Radiother. Oncol.* **53**(2), 113–117. 2, 30

Brizel, D. M., Sibley, G. S., Prosnitz, L. R., Scher, R. L. & Dewhirst, M. W. (1997), 'Tumor hypoxia adversely affects the prognosis of carcinoma of the head and neck', *Int. J. Radiat. Oncol. Biol. Phys.* **38**(2), 285–289. 2, 30

Brouwer, C. L., Steenbakkers, R. J. H. M., Bourhis, J., Budach, W., Grau, C., Grégoire, V., van Herk, M., Lee, A., Maingon, P., Nutting, C., O'Sullivan, B., Porceddu, S. V., Rosenthal, D. I., Sijtsema, N. M. & Langendijk, J. A. (2015), 'CT-based delineation of organs at risk in the head and neck region: DAHANCA, EORTC, GORTEC, HKNPCSG, NCIC CTG, NCRI, NRG oncology and TROG consensus guidelines', *Radiother. Oncol.* **117**(1), 83–90. 117, 137

Brown, J. M. & Wilson, W. R. (2004), 'Exploiting tumour hypoxia in cancer treatment', *Nat. Rev. Cancer* **4**(6), 437–447. 13

Bruijnen, T., Stemkens, B., Terhaard, C. H. J., Lagendijk, J. J. W., Raaijmakers, C. P. J. & Tijssen, R. H. N. (2019), 'Intrafraction motion quantification and planning target volume margin determination of head-and-neck tumors using cine magnetic resonance imaging', *Radiother. Oncol.* **130**, 82–88. 113

Brunnquell, C. L., Hoff, M. N., Balu, N., Nguyen, X. V., Oztek, M. A. & Haynor, D. R. (2020), 'Making magnets more attractive: Physics and engineering contributions to patient comfort in MRI', *Top. Magn. Reson. Imaging* **29**(4), 167–174. 171

Buffa, F. M., Harris, A. L., West, C. M. & Miller, C. J. (2010), 'Large meta-analysis of multiple cancers reveals a common, compact and highly prognostic hypoxia metagene', *Br. J. Cancer* **102**(2), 428–435. 33

Burrell, J. S., Walker-Samuel, S., Baker, L. C. J., Boult, J. K. R., Jamin, Y., Halliday, J., Waterton, J. C. & Robinson, S. P. (2013), 'Exploring R_2* and R_1 as imaging biomarkers of tumor oxygenation', *J. Magn. Reson. Imaging* **38**(2), 429–434. 65, 67, 74

Burtness, B., Harrington, K. J., Greil, R., Soulières, D., Tahara, M., de Castro, Jr, G., Psyrri, A., Basté, N., Neupane, P., Bratland, Å., Fuereder, T., Hughes, B. G. M., Mesía, R., Ngamphaiboon, N., Rordorf, T., Wan Ishak, W. Z., Hong, R.-L., González Mendoza, R., Roy, A., Zhang, Y., Gumuscu, B., Cheng, J. D., Jin, F., Rischin, D. & KEYNOTE-048 Investigators (2019), 'Pembrolizumab alone or with chemotherapy versus cetuximab with chemotherapy for recurrent or metastatic squamous cell carcinoma of the head and neck (KEYNOTE-048): a randomised, open-label, phase 3 study', *Lancet* **394**(10212), 1915–1928. 11, 185

Buschmann, J., Heuberger, D. M., Kivrak Pfiffner, F., Wolint, P., Jang, J.-H., Jungraithmayr, W., Giovanoli, P., Calcagni, M. & Waschkies, C. F. (2022), 'Probing vasoreactivity and hypoxic phenotype in different tumor grafts grown on the chorioallantoic membrane of the chicken embryo in ovo using MRI', *Cancers* **14**(13). 78

Busk, M., Overgaard, J. & Horsman, M. R. (2020), 'Imaging of tumor hypoxia for radiotherapy: Current status and future directions', *Semin. Nucl. Med.* **50**(6), 562–583. 29, 30, 35

Bussink, J., Kaanders, J. H., Strik, A. M. & van der Kogel, A. J. (2000), 'Effects of nicotinamide and carbogen on oxygenation in human tumor xenografts measured with luminescense based fiber-optic probes', *Radiother. Oncol.* **57**(1), 21–30. 31

Cancer statistics (2018), `https://www.cancerresearchuk.org/health-professional/cancer-statistics/statistics-by-cancer-type/head-and-neck-cancers`. Accessed: 2021-10-14. 15

Cao-Pham, T.-T., Joudiou, N., Van Hul, M., Bouzin, C., Cani, P. D., Gallez, B. & Jordan, B. F. (2017), 'Combined endogenous MR biomarkers to predict basal tumor oxygenation and response to hyperoxic challenge', *NMR Biomed.* **30(12)**(12), e3836. 65, 66, 67, 74, 83, 137, 152

Cao-Pham, T.-T., Tran, L.-B.-A., Colliez, F., Joudiou, N., El Bachiri, S.,

Gregoire, V., Leveque, P., Gallez, B. & Jordan, B. F. (2016), 'Monitoring tumor response to carbogen breathing by Oxygen-Sensitive magnetic resonance parameters to predict the outcome of radiation therapy: A preclinical study', *Int. J. Radiat. Oncol. Biol. Phys.* **96**(1), 149–160. 66, 70

Cárdenas-Navia, L. I., Mace, D., Richardson, R. A., Wilson, D. F., Shan, S. & Dewhirst, M. W. (2008), 'The pervasive presence of fluctuating oxygenation in tumors', *Cancer Res.* **68**(14), 5812–5819. 3

Carles, M., Fechter, T., Grosu, A. L., Sörensen, A., Thomann, B., Stoian, R. G., Wiedenmann, N., Rühle, A., Zamboglou, C., Ruf, J., Martí-Bonmatí, L., Baltas, D., Mix, M. & Nicolay, N. H. (2021), '18F-FMISO-PET hypoxia monitoring for Head-and-Neck cancer patients: Radiomics analyses predict the outcome of Chemo-Radiotherapy', *Cancers* **13**(14). 35

Carlsson, S. & Carlsson, E. (2013), ''the situation and the uncertainty about the coming result scared me but interaction with the radiographers helped me through': a qualitative study on patients' experiences of magnetic resonance imaging examinations', *J. Clin. Nurs.* **22**(21-22), 3225–3234. 171, 178

Carreau, A., El Hafny-Rahbi, B., Matejuk, A., Grillon, C. & Kieda, C. (2011), 'Why is the partial oxygen pressure of human tissues a crucial parameter? small molecules and hypoxia', *J. Cell. Mol. Med.* **15**(6), 1239–1253. 1

Chan, A. T. C., Hui, E. P., Ngan, R. K. C., Tung, S. Y., Cheng, A. C. K., Ng, W. T., Lee, V. H. F., Ma, B. B. Y., Cheng, H. C., Wong, F. C. S., Loong, H. H. F., Tong, M., Poon, D. M. C., Ahuja, A. T., King, A. D., Wang, K., Mo, F., Zee, B. C. Y., Chan, K. C. A. & Lo, Y. M. D. (2018), 'Analysis of plasma epstein-barr virus DNA in nasopharyngeal cancer after chemoradiation to identify high-risk patients for adjuvant chemotherapy: A randomized controlled trial', *J. Clin. Oncol.* **36**(31), JCO2018777847. 19

Chang, J. H., Wada, M., Anderson, N. J., Lim Joon, D., Lee, S. T., Gong, S. J., Gunawardana, D. H., Sachinidis, J., O'Keefe, G., Gan, H. K., Khoo, V. & Scott, A. M. (2013), 'Hypoxia-targeted radiotherapy dose painting for head and neck cancer using 18F-FMISO PET: A biological modeling study', *Acta Oncol.* **52**(8), 1723–1729. 28

Chen, L., Zhang, Z., Kolb, H. C., Walsh, J. C., Zhang, J. & Guan, Y. (2012), '[18]F-HX4 hypoxia imaging with PET/CT in head and neck cancer: a comparison with [18]F-FMISO', *Nucl. Med. Commun.* **33**(10), 1096–1102. 35

Chen, Z., Han, F., Du, Y., Shi, H. & Zhou, W. (2023), 'Hypoxic microenvironment in cancer: molecular mechanisms and therapeutic interventions', *Signal Transduct Target Ther* **8**(1), 70. 3

Choudhury, A. (2021), 'MR-BIO: A study to evaluate changes in MR imaging and biological parameters - full text view - ClinicalTrials.gov', `https://clinicaltrials.gov/ct2/show/NCT04903236`. Accessed: 2022-5-27. 62

Christiaens, M., Collette, S., Overgaard, J., Gregoire, V., Kazmierska, J., Castadot, P., Giralt, J., Grant, W., Tomsej, M., Bar-Deroma, R., Monti, A. F., Hurkmans, C. W. & Weber, D. C. (2017), 'Quality assurance of radiotherapy in the ongoing EORTC 1219-DAHANCA-29 trial for HPV/p16 negative squamous cell carcinoma of the head and neck: Results of the benchmark case procedure', *Radiother. Oncol.* **123**(3), 424–430. 25

Chua, M. L. K., Wee, J. T. S., Hui, E. P. & Chan, A. T. C. (2016), 'Nasopharyngeal carcinoma', *Lancet* **387**(10022), 1012–1024. 18

Clasen, K., Nachbar, M., Gatidis, S., Zips, D., Thorwarth, D. & Welz, S. (2023), 'Impact of MRI on target volume definition in head and neck cancer patients', *Radiat. Oncol.* **18**(1), 148. 164, 166

Cloutier, M. M. (2019), *Respiratory physiology*, ClinicalKey, second edition. edn, Elsevier. 107, 108

Colliez, F., Gallez, B. & Jordan, B. F. (2017), 'Assessing tumor oxygenation for predicting outcome in radiation oncology: A review of studies correlating tumor hypoxic status and outcome in the preclinical and clinical settings', *Front. Oncol.* **7**, 10. 38

Colliez, F., Neveu, M.-A., Magat, J., Thanh Trang Cao Pham, Gallez, B. & Jordan, B. F. (2014), 'Qualification of a noninvasive magnetic resonance imaging biomarker to assess tumor oxygenation', *Clin. Cancer Res.* **20**(21), 5403–5411. 65, 70, 74

Cosper, P. F., Bradley, S., Luo, L. & Kimple, R. J. (2021), 'Biology of HPV mediated carcinogenesis and tumor progression', *Semin. Radiat. Oncol.* **31**(4), 265–273. 15

Cosse, J.-P. & Michiels, C. (2008), 'Tumour hypoxia affects the responsiveness of cancer cells to chemotherapy and promotes cancer progression', *Anticancer Agents Med. Chem.* **8**(7), 790–797. 9

DAHANCA (2020*a*), 'DAHANCA 35: Proton versus photon therapy for head-neck cancer - full

text view - ClinicalTrials.gov', https://clinicaltrials.gov/ct2/show/NCT04607694. Accessed: 2021-10-13. 26

DAHANCA (2020*b*), 'Nimorazole. treatment with the hypoxic radiosensitizer nimorazole in squamous cell carcinoma of the head and neck', Danish Head and Neck Cancer Study Group Clinical Practice Guidelines. 24

DAHANCA (2021), 'DAHANCA 30: A randomized non-inferiority trial of hypoxia-profile guided hypoxic modification of radiotherapy of HNSCC - ClinicalTrials.gov', https://clinicaltrials.gov/ct2/show/study/NCT02661152. Accessed: 2021-10-13. 26, 33

Daniels, C. P., Liu, H. Y.-H., Bernard, A., Williams, C., Foote, M. C., Ladwa, R., McGrath, M., Panizza, B. J. & Porceddu, S. V. (2020), 'The declining role of post-treatment neck dissection in human papillomavirus-associated oropharyngeal cancer', *Radiother. Oncol.* **151**, 242–248. 16

Datta, A. (2021), 'Biomarkers for clinical hypoxia evaluation in cervical cancer', https://clinicaltrials.gov/ct2/show/NCT05029258. Accessed: 2022-5-27. 62

Datta, A., Dubec, M., Buckley, D., McHugh, D., Salah, A., Little, R., Berks, M., Cheung, S., West, C., Choudhury, A., Barraclough, L., Hoskin, P. & O'Connor, J. P. B. (2022), 'Quantifying and mapping hypoxia modification in patients with uterine cervical cancer using oxygen-enhanced MRI', *Proc. Intl. Soc. Mag. Reson. Med.* **Abstract 2584**. 62, 68, 69, 73, 74

Deacon, K., Onion, D., Kumari, R., Watson, S. A. & Knox, A. J. (2012), 'Elevated SP-1 transcription factor expression and activity drives basal and hypoxia-induced vascular endothelial growth factor (VEGF) expression in non-small cell lung cancer', *J. Biol. Chem.* **287**(47), 39967–39981. 8

Delprat, V., Tellier, C., Demazy, C., Raes, M., Feron, O. & Michiels, C. (2020), 'Cycling hypoxia promotes a pro-inflammatory phenotype in macrophages via JNK/p65 signaling pathway', *Sci. Rep.* **10**(1), 882. 3

Dengler, V. L., Galbraith, M. & Espinosa, J. M. (2014), 'Transcriptional regulation by hypoxia inducible factors', *Crit. Rev. Biochem. Mol. Biol.* **49**(1), 1–15. 6

Deoni, S. C. L., Rutt, B. K. & Peters, T. M. (2003), 'Rapid combined T1 and T2 mapping using gradient recalled acquisition in the steady state', *Magn. Reson. Med.* **49**(3), 515–526. 92

Deschuymer, S., Sørensen, B. S., Dok, R., Laenen, A., Hauben, E., Overgaard, J. & Nuyts, S. (2020), 'Prognostic value of a 15-gene hypoxia classifier in oropharyngeal cancer treated with accelerated chemoradiotherapy', *Strahlenther. Onkol.* **196**(6), 552–560. 33

Dewhirst, M. W. & Birer, S. R. (2016), 'Oxygen-Enhanced MRI is a major advance in tumor hypoxia imaging', *Cancer Res.* **76**(4), 769–772. 29, 43

Dewhirst, M. W., Cao, Y. & Moeller, B. (2008), 'Cycling hypoxia and free radicals regulate angiogenesis and radiotherapy response', *Nat. Rev. Cancer* **8**(6), 425–437. 3, 9, 60

Dice, L. R. (1945), 'Measures of the amount of ecologic association between species', *Ecology* **26**(3), 297–302. 118

Dierckx, R. A. & Van de Wiele, C. (2008), 'FDG uptake, a surrogate of tumour hypoxia?', *Eur. J. Nucl. Med. Mol. Imaging* **35**(8), 1544–1549. 35

Druker, J., Wilson, J. W., Child, F., Shakir, D., Fasanya, T. & Rocha, S. (2021), 'Role of hypoxia in the control of the cell cycle', *Int. J. Mol. Sci.* **22**(9), 4874. 8

Dubec, M., Datta, A., Little, R. A., Clough, A., Buckley, D. L., Hague, C., McHugh, D., Berks, M., Cheung, S., Salah, A., Higgins, D., Eccles, C. L., Bristow, R., Naish, J. H., Matthews, J. C., Hoskin, P., van Herk, M., Parker, G. J. M., Choudhury, A., McPartlin, A. & O'Connor, J. P. B. (2022), 'First in-human technique translation of OE-MRI for hypoxia imaging onto an MR linac system in patients with head and neck cancer', *Proc. Intl. Soc. Mag. Reson. Med.* **Abstract 0290**. 68, 69, 73, 74, 79

Dubec, M. J., Buckley, D. L., Berks, M., Clough, A., Gaffney, J., Datta, A., McHugh, D. J., Porta, N., Little, R. A., Cheung, S., Hague, C., Eccles, C. L., Hoskin, P. J., Bristow, R. G., Matthews, J. C., van Herk, M., Choudhury, A., Parker, G. J. M., McPartlin, A. & O'Connor, J. P. B. (2023), 'First-in-human technique translation of oxygen-enhanced MRI to an MR linac system in patients with head and neck cancer', *Radiother. Oncol.* **183**, 109592. 79, 132, 152, 153, 179, 181

Dubec, M., Price, J., Berks, M., Gaffney, J., Little, R., Porta, N., Sridharan, N., Datta, A., McHugh, D., Hague, C. J., Cheung, S., Manoharan, P., van Herk, M., Choudhury, A., Matthews, J. C., Parker, G. J. M., Buckley, D. L., Harrington, K. J., McPartlin, A. & O'Connor, J. P. B. (2024), 'Oxygen-enhanced MRI detects incidence, onset and heterogeneity of radiation-induced hypoxia modification in HPV-

associated oropharyngeal cancer', *Clin. Cancer Res.* . 181, 182

Dunst, J., Stadler, P., Becker, A., Lautenschlager, C., Pelz, T., Hansgen, G., Molls, M. & Kuhnt, T. (2003), 'Tumor volume and tumor hypoxia in head and neck cancers - The amount of the hypoxic volume is important', *Strahlenther. Onkol.* **179**(8), 521+. 30

Dupont, W. D. & Plummer, Jr, W. D. (1990), 'Power and sample size calculations. a review and computer program', *Control. Clin. Trials* **11**(2), 116–128. 87

EORTC (2022), 'EORTC-1219 / DAHANCA-29', `https://clinicaltrials.gov/ct2/show/NCT01880359`. Accessed: 2021-10-13. 25

Ernst, R. R. & Anderson, W. A. (1966), 'Application of fourier transform spectroscopy to magnetic resonance', *Rev. Sci. Instrum.* **37**(1), 93–102. 55

Eshed, I., Althoff, C. E., Hamm, B. & Hermann, K.-G. A. (2007), 'Claustrophobia and premature termination of magnetic resonance imaging examinations', *J. Magn. Reson. Imaging* **26**(2), 401–404. 171

Estephan, H., Tailor, A., Parker, R., Kreamer, M., Papandreou, I., Campo, L., Easton, A., Moon, E. J., Denko, N. C., Ternette, N., Hammond, E. M. & Giaccia, A. J. (2025), 'Hypoxia promotes tumor immune evasion by suppressing MHC-I expression and antigen presentation', *EMBO J.* **44**(3), 903–922. 10

Eustace, A., Mani, N., Span, P. N., Irlam, J. J., Taylor, J., Betts, G. N. J., Denley, H., Miller, C. J., Homer, J. J., Rojas, A. M., Hoskin, P. J., Buffa, F. M., Harris, A. L., Kaanders, J. H. A. M. & West, C. M. L. (2013), 'A 26-gene hypoxia signature predicts benefit from hypoxia-modifying therapy in laryngeal cancer but not bladder cancer', *Clin. Cancer Res.* **19**(17), 4879–4888. 25, 33

Evans, S. M., Du, K. L., Chalian, A. A., Mick, R., Zhang, P. J., Hahn, S. M., Quon, H., Lustig, R., Weinstein, G. S. & Koch, C. J. (2007), 'Patterns and levels of hypoxia in head and neck squamous cell carcinomas and their relationship to patient outcome', *Int. J. Radiat. Oncol. Biol. Phys.* **69**(4), 1024–1031. 129

Fabbrizi, M. R. & Parsons, J. L. (2020), 'Radiotherapy and the cellular DNA damage response: current and future perspectives on head and neck cancer treatment', *Cancer Drug Resistance* . 11

Facciabene, A., Peng, X., Hagemann, I. S., Balint, K., Barchetti, A., Wang, L.-P., Gimotty, P. A., Gilks, C. B., Lal,

P., Zhang, L. & Coukos, G. (2011), 'Tumour hypoxia promotes tolerance and angiogenesis via CCL28 and T(reg) cells', *Nature* **475**(7355), 226–230. 10

Falk, S. (2018), 'Oxygen enhanced MRI measurement in head and neck cancer: Validation and efficacy of response', `https://clinicaltrials.gov/ct2/show/NCT03646747`. Accessed: 2022-5-27. 87

Fan, Q., Tang, C. Y., Gu, D., Zhu, J., Li, G., Wu, Y. & Tao, X. (2017), 'Investigation of hypoxia conditions using oxygen-enhanced magnetic resonance imaging measurements in glioma models', *Oncotarget* **8**(19), 31864–31875. 80

Featherstone, A. K., O'Connor, J. P. B., Little, R. A., Watson, Y., Cheung, S., Babur, M., Williams, K. J., Matthews, J. C. & Parker, G. J. M. (2018), 'Data-driven mapping of hypoxia-related tumor heterogeneity using DCE-MRI and OE-MRI', *Magn. Reson. Med.* **79**(4), 2236–2245. 65, 129

Ferris, R. L., Blumenschein, Jr, G., Fayette, J., Guigay, J., Colevas, A. D., Licitra, L., Harrington, K., Kasper, S., Vokes, E. E., Even, C., Worden, F., Saba, N. F., Iglesias Docampo, L. C., Haddad, R., Rordorf, T., Kiyota, N., Tahara, M., Monga, M., Lynch, M., Geese, W. J., Kopit, J., Shaw, J. W. & Gillison, M. L. (2016), 'Nivolumab for recurrent Squamous-Cell carcinoma of the head and neck', *N. Engl. J. Med.* **375**(19), 1856–1867. 11, 185

Fram, E. K., Herfkens, R. J., Johnson, G. A., Glover, G. H., Karis, J. P., Shimakawa, A., Perkins, T. G. & Pelc, N. J. (1987), 'Rapid calculation of T1 using variable flip angle gradient refocused imaging', *Magn. Reson. Imaging* **5**(3), 201–208. 56

Gallez, B., Baudelet, C. & Jordan, B. F. (2004), 'Assessment of tumor oxygenation by electron paramagnetic resonance: principles and applications', *NMR Biomed.* **17**(5), 240–262. 38

Gaustad, J.-V., Hauge, A., Wegner, C. S., Simonsen, T. G., Lund, K. V., Hansem, L. M. K. & Rofstad, E. K. (2020), 'DCE-MRI of tumor hypoxia and Hypoxia-Associated aggressiveness', *Cancers* **12**(7). 40

Gebre-Medhin, M., Brun, E., Engström, P., Haugen Cange, H., Hammarstedt-Nordenvall, L., Reizenstein, J., Nyman, J., Abel, E., Friesland, S., Sjödin, H., Carlsson, H., Söderkvist, K., Thomasson, M., Zackrisson, B. & Nilsson, P. (2021), 'ARTSCAN III: A randomized phase III study comparing chemoradiotherapy with cisplatin versus cetuximab in patients with locoregionally advanced head and neck squamous cell cancer', *J. Clin. Oncol.* **39**(1), 38–47. 22

Gillison, M. L., Trotti, A. M., Harris, J., Eisbruch, A., Harari, P. M., Adelstein, D. J., Jordan, R. C. K., Zhao, W., Sturgis, E. M., Burtness, B., Ridge, J. A., Ringash, J., Galvin, J., Yao, M., Koyfman, S. A., Blakaj, D. M., Razaq, M. A., Colevas, A. D., Beitler, J. J., Jones, C. U., Dunlap, N. E., Seaward, S. A., Spencer, S., Galloway, T. J., Phan, J., Dignam, J. J. & Le, Q. T. (2019), 'Radiotherapy plus cetuximab or cisplatin in human papillomavirus-positive oropharyngeal cancer (NRG oncology RTOG 1016): a randomised, multicentre, non-inferiority trial', *Lancet* **393**(10166), 40–50. 22

Göttgens, E.-L., Ostheimer, C., Span, P. N., Bussink, J. & Hammond, E. M. (2019), 'HPV, hypoxia and radiation response in head and neck cancer', *Br. J. Radiol.* **92**(1093), 20180047. 16, 154

Gouel, P., Decazes, P., Vera, P., Gardin, I., Thureau, S. & Bohn, P. (2023), 'Advances in PET and MRI imaging of tumor hypoxia', *Front. Med.* **10**, 1055062. 35, 37

Graves, E. E., Hicks, R. J., Binns, D., Bressel, M., Le, Q.-T., Peters, L., Young, R. J. & Rischin, D. (2016), 'Quantitative and qualitative analysis of [(18)F]FDG and [(18)F]FAZA positron emission tomography of head and neck cancers and associations with HPV status and treatment outcome', *Eur. J. Nucl. Med. Mol. Imaging* **43**(4), 617–625. 150

Gray, L. H., Conger, A. D., Ebert, M., Hornsey, S. & Scott, O. C. (1953), 'The concentration of oxygen dissolved in tissues at the time of irradiation as a factor in radiotherapy', *Br. J. Radiol.* **26**(312), 638–648. 13

Grégoire, V., Evans, M., Le, Q.-T., Bourhis, J., Budach, V., Chen, A., Eisbruch, A., Feng, M., Giralt, J., Gupta, T., Hamoir, M., Helito, J. K., Hu, C., Hunter, K., Johansen, J., Kaanders, J., Laskar, S. G., Lee, A., Maingon, P., Mäkitie, A., Micciche', F., Nicolai, P., O'Sullivan, B., Poitevin, A., Porceddu, S., Składowski, K., Tribius, S., Waldron, J., Wee, J., Yao, M., Yom, S. S., Zimmermann, F. & Grau, C. (2018), 'Delineation of the primary tumour clinical target volumes (CTV-P) in laryngeal, hypopharyngeal, oropharyngeal and oral cavity squamous cell carcinoma: AIRO, CACA, DAHANCA, EORTC, GEORCC, GORTEC, HKNPCSG, HNCIG, IAG-KHT, LPRHHT, NCIC CTG, NCRI, NRG oncology, PHNS, SBRT, SOMERA, SRO, SSHNO, TROG consensus guidelines', *Radiother. Oncol.* **126**(1), 3–24. 21, 165

Grégoire, V., Tao, Y., Kaanders, J., Machiels, J., Vulquin, N., Nuyts, S., Fortpied, C., Lmalem, H., Marreaud, S. & Overgaard, J. (2021), 'OC-0278

accelerated CH-RT with/without nimorazole for p16- HNSCC: the randomized DAHANCA 29-EORTC 1219 trial', *Radiother. Oncol.* **161**, S187–S188. 25

Griffiths, J. R. & Robinson, S. P. (1999), 'The OxyLite: a fibre-optic oxygen sensor', *Br. J. Radiol.* **72**(859), 627–630. 30

Grimes, D. R., Warren, D. R. & Warren, S. (2017), 'Hypoxia imaging and radiotherapy: bridging the resolution gap', *Br. J. Radiol.* **90**(1076), 20160939. 13, 43, 45, 130

Gross, M. W., Karbach, U., Groebe, K., Franko, A. J. & Mueller-Klieser, W. (1995), 'Calibration of misonidazole labeling by simultaneous measurement of oxygen tension and labeling density in multicellular spheroids', *Int. J. Cancer* **61**(4), 567–573. 31

Grosu, A.-L., Souvatzoglou, M., Röper, B., Dobritz, M., Wiedenmann, N., Jacob, V., Wester, H.-J., Reischl, G., Machulla, H.-J., Schwaiger, M., Molls, M. & Piert, M. (2007), 'Hypoxia imaging with FAZA-PET and theoretical considerations with regard to dose painting for individualization of radiotherapy in patients with head and neck cancer', *Int. J. Radiat. Oncol. Biol. Phys.* **69**(2), 541–551. 27

Guo, W., Luo, D., Chen, X., Lin, M., Li, L., Zhao, Y., Yang, L., Hu, L., Zhao, X. & Zhou, C. (2017), 'Dynamic contrast-enhanced magnetic resonance imaging for pretreatment prediction of early chemo-radiotherapy response in larynx and hypopharynx carcinoma', *Oncotarget* **8**(20), 33836–33843. 87

Gurney-Champion, O. J., McQuaid, D., Dunlop, A., Wong, K. H., Welsh, L. C., Riddell, A. M., Koh, D.-M., Oelfke, U., Leach, M. O., Nutting, C. M., Bhide, S. A., Harrington, K. J., Panek, R. & Newbold, K. L. (2018), 'MRI-based assessment of 3D intrafractional motion of head and neck cancer for radiation therapy', *Int. J. Radiat. Oncol. Biol. Phys.* **100**(2), 306–316. 113

Haddock, B., Larsson, H. B. W., Hansen, A. E. & Rostrup, E. (2013), 'Measurement of brain oxygenation changes using dynamic t(1)-weighted imaging', *Neuroimage* **78**, 7–15. 107

Haider, S. P., Burtness, B., Yarbrough, W. G. & Payabvash, S. (2020), 'Applications of radiomics in precision diagnosis, prognostication and treatment planning of head and neck squamous cell carcinomas', *Cancers Head Neck* **5**, 6. 163

Hallac, R. R., Zhou, H., Pidikiti, R., Song, K., Stojadinovic, S., Zhao, D., Solberg, T., Peschke, P. & Mason, R. P. (2014), 'Correlations of noninvasive BOLD and TOLD MRI with pO_2 and relevance to tumor radiation response',

Magn. Reson. Med. **71**(5), 1863–1873. 37, 43, 65, 68, 74

Hammond, E. M., Asselin, M.-C., Forster, D., O'Connor, J. P. B., Senra, J. M. & Williams, K. J. (2014), 'The meaning, measurement and modification of hypoxia in the laboratory and the clinic', *Clin. Oncol.* **26**(5), 277–288. 11, 13

Hamy, V., Dikaios, N., Punwani, S., Melbourne, A., Latifoltojar, A., Makanyanga, J., Chouhan, M., Helbren, E., Menys, A., Taylor, S. & Atkinson, D. (2014), 'Respiratory motion correction in dynamic MRI using robust data decomposition registration - application to DCE-MRI', *Med. Image Anal.* **18**(2), 301–313. 116

Han, S., Tay, J. K., Loh, C. J. L., Chu, A. J. M., Yeong, J. P. S., Lim, C. M. & Toh, H. C. (2021), 'Epstein-barr virus epithelial cancers-a comprehensive understanding to drive novel therapies', *Front. Immunol.* **12**, 734293. 18

Hanahan, D. & Weinberg, R. A. (2011), 'Hallmarks of cancer: the next generation', *Cell* **144**(5), 646–674. 4, 6, 32

Hanna, L., Crosby, T. & Macbeth, F. (2008), *Practical clinical oncology*, Cambridge University Press, Cambridge. 15, 20

Hantzidiamantis, P. J. & Amaro, E. (2021), Physiology, alveolar to arterial oxygen gradient, *in* 'StatPearls', StatPearls Publishing, Treasure Island (FL). 107

Haralick, R. M., Shanmugam, K. & Dinstein, I. (1973), 'Textural features for image classification', *IEEE Trans. Syst. Man Cybern.* **SMC-3**(6), 610–621. 157

Hectors, S. J., Wagner, M., Bane, O., Besa, C., Lewis, S., Remark, R., Chen, N., Fiel, M. I., Zhu, H., Gnjatic, S., Merad, M., Hoshida, Y. & Taouli, B. (2017), 'Quantification of hepatocellular carcinoma heterogeneity with multiparametric magnetic resonance imaging', *Sci. Rep.* **7**(1), 2452. 71

Hendrickson, K., Phillips, M., Smith, W., Peterson, L., Krohn, K. & Rajendran, J. (2011), 'Hypoxia imaging with [f-18] FMISO-PET in head and neck cancer: potential for guiding intensity modulated radiation therapy in overcoming hypoxia-induced treatment resistance', *Radiother. Oncol.* **101**(3), 369–375. 28

Hewis, J. (2015), 'Do MRI patients tweet? thematic analysis of patient tweets about their MRI experience', *J Med Imaging Radiat Sci* **46**(4), 396–402. 170

Hockel, M., Schlenger, K., Aral, B., Mitze, M., Schaffer, U. & Vaupel, P. (1996), 'Association between tumor hypoxia and malignant progression in ad-

vanced cancer of the uterine cervix', *Cancer Res.* **56**(19), 4509–4515. 11

Hoff, C. M., Hansen, H. S., Overgaard, M., Grau, C., Johansen, J., Bentzen, J. & Overgaard, J. (2011), 'The importance of haemoglobin level and effect of transfusion in HNSCC patients treated with radiotherapy–results from the randomized DAHANCA 5 study', *Radiother. Oncol.* **98**(1), 28–33. 23

Horsholt Kristensen, M., Kristina Sørensen, M., Tramm, T., Alsner, J., Singers Sørensen, B., Maare, C., Johansen, J., Primdahl, H., Bratland, Å., Andrup Kristensen, C., Andersen, M., Kinggaard Lilja-Fischer, J., Ivalu Sander Holm, A., Samsøe, E., Rønn Hansen, C., Zukauskaite, R., Overgaard, J. & Grau Eriksen, J. (2024), 'Tumor volume and cancer stem cell expression as prognostic markers for high-dose loco-regional failure in head and neck squamous cell carcinoma – a DAHANCA 19 study', *Radiother. Oncol.* p. 110149. 184

Horsman, M. R., Mortensen, L. S., Petersen, J. B., Busk, M. & Overgaard, J. (2012), 'Imaging hypoxia to improve radiotherapy outcome', *Nat. Rev. Clin. Oncol.* **9**(12), 674–687. 27, 29, 31, 34, 35, 37

Horsman, M. R., Sørensen, B. S., Busk, M. & Siemann, D. W. (2021), 'Therapeutic modification of hypoxia', *Clin. Oncol.* **33**(11), e492–e509. 9, 11

Huang, R. & Zhou, P.-K. (2021), 'DNA damage repair: historical perspectives, mechanistic pathways and clinical translation for targeted cancer therapy', *Signal Transduct Target Ther* **6**(1), 254. 4

Huang, W., Zhang, Q., Wu, G., Pian Chen, P., Li, J., McCabe Gillen, K., Spincemaille, P., Chiang, G. C., Gupta, A., Wang, Y. & Chen, F. (2021), 'DCE-MRI quantitative transport mapping for noninvasively detecting hypoxia inducible factor-1α, epidermal growth factor receptor overexpression, and ki-67 in nasopharyngeal carcinoma patients', *Radiother. Oncol.* . 40

Huen, I., Morris, D. M., Wright, C., Parker, G. J. M., Sibley, C. P., Johnstone, E. D. & Naish, J. H. (2013), 'R1 and R2 * changes in the human placenta in response to maternal oxygen challenge', *Magn. Reson. Med.* **70**(5), 1427–1433. 56

Hughes, V. S., Wiggins, J. M. & Siemann, D. W. (2019), 'Tumor oxygenation and cancer therapy-then and now', *Br. J. Radiol.* **92**(1093), 20170955. 2, 29, 35, 60, 151

Hypoxyprobe (2024), 'Reagents for studies of tissue oxygenation and chemoprovention',

http://www.hypoxyprobe.com/. Accessed: 2024-6-19. 31

Ingram, S., Dubec, M., Price, J., O'Connor, J. & Aitkenhead, A. (2024), 'Functional image guided adaptive radiotherapy (fig-art) in pbt h+n treatment planning for changes in hypoxia using oxygen-enhanced MRI imaging', *Int. J. Part. Ther.* **12**(100190), 100190. 184

Iwan, E., Yang, J., Enders, J., Napp, A. E., Rief, M. & Dewey, M. (2020), 'Patient preferences for development in MRI scanner design: a survey of claustrophobic patients in a randomized study', *Eur. Radiol.* . 171

Iwata, H., Ogino, H., Hashimoto, S., Iwana, M., Shibata, H., Keisuke, Y., Toshito, T., Omachi, C., Tatekawa, K., Manabe, Y., Mizoe, J. & Shibamoto, Y. (2014), 'Oxygen enhancement ratio of proton beams: The precise report of the same institution's experiments using the clinical equipments', *Int. J. Radiat. Oncol. Biol. Phys.* **90**(1), S779. 26

Jackson, E., Bronskill, M., Drost, D., Och, J., Pooley, R., Sobol, W. & Clark, G. e. a. (2010), *Acceptance Testing and Quality Assurance Procedures for Magnetic Resonance Imaging Facilities. AAPM Report No. 100*, American Association of Physicists in Medicine (A A P M). 99

James D. Brierley, Mary K. Gospodarowicz, Christian Wittekind, ed. (2017), *TNM Classification of Malignant Tumours Eight Edition*, John Wiley & Sons, Ltd. 15

Jansen, M. J. A., Veldhuis, W. B., van Leeuwen, M. S. & Pluim, J. P. W. (2019), 'Motion correction of dynamic contrast enhanced MRI of the liver'. 116

Janssens, G. O., Rademakers, S. E., Terhaard, C. H., Doornaert, P. A., Bijl, H. P., van den Ende, P., Chin, A., Marres, H. A., de Bree, R., van der Kogel, A. J., Hoogsteen, I. J., Bussink, J., Span, P. N. & Kaanders, J. H. (2012), 'Accelerated radiotherapy with carbogen and nicotinamide for laryngeal cancer: results of a phase III randomized trial', *J. Clin. Oncol.* **30**(15), 1777–1783. 23, 24

Jethanandani, A., Lin, T. A., Volpe, S., Elhalawani, H., Mohamed, A. S. R., Yang, P. & Fuller, C. D. (2018), 'Exploring applications of radiomics in magnetic resonance imaging of head and neck cancer: A systematic review', *Front. Oncol.* **8**, 131. 164

Joiner, M. & van der Kogel, A., eds (2009), *Basic Clinical Radiobiology*, fourth edition edn, Hodder Arnold. 13

Jordan, B. F., Magat, J., Colliez, F., Ozel, E., Fruytier, A.-C., Marchand,

V., Mignion, L., Bouzin, C., Cani, P. D., Vandeputte, C., Feron, O., Delzenne, N., Himmelreich, U., Denolin, V., Duprez, T. & Gallez, B. (2013), 'Mapping of oxygen by imaging lipids relaxation enhancement: A potential sensitive endogenous MRI contrast to map variations in tissue oxygenation', *Magn. Reson. Med.* **70**(3), 732–744. 65, 70

Kang, W., Qiu, X., Luo, Y., Luo, J., Liu, Y., Xi, J., Li, X. & Yang, Z. (2023), 'Application of radiomics-based multi-omics combinations in the tumor microenvironment and cancer prognosis', *J. Transl. Med.* **21**(1), 598. 164

Kaplan, A. R. & Glazer, P. M. (2020), 'Impact of hypoxia on DNA repair and genome integrity', *Mutagenesis* **35**(1), 61–68. 8

Katz, R. C., Wilson, L. & Frazer, N. (1994), 'Anxiety and its determinants in patients undergoing magnetic resonance imaging', *J. Behav. Ther. Exp. Psychiatry* **25**(2), 131–134. 170

Kim, K. Y., Le, Q.-T., Yom, S. S., Ng, R. H. W., Chan, K. C. A., Bratman, S. V., Welch, J. J., Divi, R. L., Petryshyn, R. A. & Conley, B. A. (2017), 'Clinical utility of epstein-barr virus DNA testing in the treatment of nasopharyngeal carcinoma patients', *Int. J. Radiat. Oncol. Biol. Phys.* **98**(5), 996–1001. 19

Kim, S.-E., Roberts, J. A., Kholmovski, E. G., Hitchcock, Y. & Anzai, Y. (2024), 'T1 mapping for head and neck cancer patients undergoing chemoradiotherapy: Feasibility of 3D stack of star imaging', *Magn. Reson. Imaging* **112**, 38–46. 185

Kimple, R. J., Smith, M. A., Blitzer, G. C., Torres, A. D., Martin, J. A., Yang, R. Z., Peet, C. R., Lorenz, L. D., Nickel, K. P., Klingelhutz, A. J., Lambert, P. F. & Harari, P. M. (2013), 'Enhanced radiation sensitivity in HPV-positive head and neck cancer', *Cancer Res.* **73**(15), 4791–4800. 16

Kizaka-Kondoh, S. & Konse-Nagasawa, H. (2009), 'Significance of nitroimidazole compounds and hypoxia-inducible factor-1 for imaging tumor hypoxia', *Cancer Sci.* **100**(8), 1366–1373. 6, 31

Klein, T. J. & Glazer, P. M. (2010), 'The tumor microenvironment and DNA repair', *Semin. Radiat. Oncol.* **20**(4), 282–287. 3

Klug, N., Butow, P. N., Burns, M., Dhillon, H. M. & Sundaresan, P. (2020), 'Unmasking anxiety: A qualitative investigation of health professionals; perspectives of mask anxiety in head and neck cancer', *J Med Imaging Radiat Sci* **51**(1), 12–21. 171

Kousi, E., Borri, M., Dean, J., Panek, R., Scurr, E., Leach, M. O. &

Schmidt, M. A. (2016), 'Quality assurance in MRI breast screening: comparing signal-to-noise ratio in dynamic contrast-enhanced imaging protocols', *Phys. Med. Biol.* **61**(1), 37–49. 120

Kraus, R. J., Yu, X., Cordes, B.-L. A., Sathiamoorthi, S., Iempridee, T., Nawandar, D. M., Ma, S., Romero-Masters, J. C., McChesney, K. G., Lin, Z., Makielski, K. R., Lee, D. L., Lambert, P. F., Johannsen, E. C., Kenney, S. C. & Mertz, J. E. (2017), 'Hypoxia-inducible factor-1α plays roles in epstein-barr virus's natural life cycle and tumorigenesis by inducing lytic infection through direct binding to the immediate-early BZLF1 gene promoter', *PLoS Pathog.* **13**(6), e1006404. 18, 19

Krock, B. L., Skuli, N. & Simon, M. C. (2011), 'Hypoxia-induced angiogenesis: good and evil', *Genes Cancer* **2**(12), 1117–1133. 6

Lassen, P., Eriksen, J. G., Hamilton-Dutoit, S., Tramm, T., Alsner, J., Overgaard, J. & Danish Head and Neck Cancer Group (DAHANCA) (2010), 'HPV-associated p16-expression and response to hypoxic modification of radiotherapy in head and neck cancer', *Radiother. Oncol.* **94**(1), 30–35. 154

Lassen, P., Primdahl, H., Johansen, J., Kristensen, C. A., Andersen, E., Andersen, L. J., Evensen, J. F., Eriksen, J. G., Overgaard, J. & Danish Head and Neck Cancer Group (DAHANCA) (2014), 'Impact of HPV-associated p16-expression on radiotherapy outcome in advanced oropharynx and non-oropharynx cancer', *Radiother. Oncol.* **113**(3), 310–316. 16, 17

Le, Q.-T., Koong, A., Lieskovsky, Y. Y., Narasimhan, B., Graves, E., Pinto, H., Brown, J. M. & Spielman, D. (2008), 'In vivo H-1 magnetic resonance spectroscopy of lactate in patients with Stage IV head and neck squamous cell carcinoma', *Int. J. Radiat. Oncol. Biol. Phys.* **71**(4), 1151–1157. 37

Leavitt, R. J., Almeida, A., Grilj, V., Montay-Gruel, P., Godfroid, C., Petit, B., Bailat, C., Limoli, C. L. & Vozenin, M.-C. (2024), 'Acute hypoxia does not alter tumor sensitivity to FLASH radiation therapy', *Int. J. Radiat. Oncol. Biol. Phys.* . 26

Lee, C. P., Payne, G. S., Oregioni, A., Ruddle, R., Tan, S., Raynaud, F. I., Eaton, D., Campbell, M. J., Cross, K., Halbert, G., Tracy, M., McNamara, J., Seddon, B., Leach, M. O., Workman, P. & Judson, I. (2009), 'A phase I study of the nitroimidazole hypoxia marker SR4554 using 19F magnetic resonance spectroscopy', *Br. J. Cancer* **101**(11), 1860–1868. 38

Lee, N. Y., Mechalakos, J. G., Nehmeh,

S., Lin, Z., Squire, O. D., Cai, S., Chan, K., Zanzonico, P. B., Greco, C., Ling, C. C., Humm, J. L. & Schöder, H. (2008), 'Fluorine-18-labeled fluoromisonidazole positron emission and computed tomography-guided intensity-modulated radiotherapy for head and neck cancer: a feasibility study', *Int. J. Radiat. Oncol. Biol. Phys.* **70**(1), 2–13. 28

Lee, N. Y., Sherman, E. J., Schöder, H., Wray, R., Boyle, J. O., Singh, B., Grkovski, M., Paudyal, R., Cunningham, L., Zhang, Z., Hatzoglou, V., Katabi, N., Diplas, B. H., Han, J., Imber, B. S., Pham, K., Yu, Y., Zakeri, K., McBride, S. M., Kang, J. J., Tsai, C. J., Chen, L. C., Gelblum, D. Y., Shah, J. P., Ganly, I., Cohen, M. A., Cracchiolo, J. R., Morris, L. G. T., Dunn, L. A., Michel, L. S., Fetten, J. V., Kripani, A., Pfister, D. G., Ho, A. L., Shukla-Dave, A., Humm, J. L., Powell, S. N., Li, B. T., Reis-Filho, J. S., Diaz, L. A., Wong, R. J. & Riaz, N. (2024*a*), 'Hypoxia-directed treatment of human papillomavirus-related oropharyngeal carcinoma', *J. Clin. Oncol.* **42**(8), 940–950. 17, 28, 29, 154, 182

Lee, N. Y., Sherman, E. J., Schöder, H., Wray, R., White, C., Dunn, L., Hung, T., Pfister, D. G., Ho, A. L., McBride, S. M., Yu, Y., Zakeri, K., Kalman, N., Rutter, C., Morris, L., Singh, B., Boyle, J., Ganly, I., Wong, R. J. & Riaz, N. (2024*b*), 'Intra-treatment hypoxia directed major radiation de-escalation as definitive treatment for human papillomavirus-related oropharyngeal cancer', *J. Clin. Oncol.* **42**(16 suppl), 6007. 17, 29, 154

Lepicard, E., Boult, J., Jamin, Y., Zormpas-Petridis, K., Featherstone, A., Box, C., Panek, R., O'Connor, J. & Robinson, S. (2020), 'Imaging hypoxia in head and neck cancer xenografts with oxygen-enhanced MRI', *Proc. Intl. Soc. Mag. Reson. Med.* **Abstract 0276**. 65, 66

Li, S. & Zhou, B. (2022), 'A review of radiomics and genomics applications in cancers: the way towards precision medicine', *Radiat. Oncol.* **17**(1), 217. 164

Li, X., Morgan, P. S., Ashburner, J., Smith, J. & Rorden, C. (2016), 'The first step for neuroimaging data analysis: DICOM to NIfTI conversion', *J. Neurosci. Methods* **264**, 47–56. 103

Li, X., Qin, S., Liang, W., Mei, Y., Yuan, Y. & Quan, X. (2018), 'Assessment of tumor hypoxia using tissue oxygen level dependent in a rabbit VX2 liver tumor model', *Proc. Intl. Soc. Mag. Reson. Med.* **Abstract 1538**. 65

Lickliter, J. D., Ruben, J., Kichenadasse, G., Jennens, R., Gzell, C., Mason, R. P., Zhou, H., Becker, J., Unger,

E. & Stea, B. (2023), 'Dodecafluoropentane emulsion as a radiosensitizer in glioblastoma multiforme', *Cancer research communications* **3**(8), 1607–1614. 78

Lin, G. & Chung, Y.-L. (2014), 'Current opportunities and challenges of magnetic resonance spectroscopy, positron emission tomography, and mass spectrometry imaging for mapping cancer metabolism in vivo', *Biomed Res. Int.* **2014**, 625095. 38

Linge, A., Lohaus, F., Löck, S., Nowak, A., Gudziol, V., Valentini, C., von Neubeck, C., Jütz, M., Tinhofer, I., Budach, V., Sak, A., Stuschke, M., Balermpas, P., Rödel, C., Grosu, A.-L., Abdollahi, A., Debus, J., Ganswindt, U., Belka, C., Pigorsch, S., Combs, S. E., Mönnich, D., Zips, D., Buchholz, F., Aust, D. E., Baretton, G. B., Thames, H. D., Dubrovska, A., Alsner, J., Overgaard, J., Krause, M., Baumann, M. & DKTK-ROG (2016), 'HPV status, cancer stem cell marker expression, hypoxia gene signatures and tumour volume identify good prognosis subgroups in patients with HNSCC after primary radiochemotherapy: A multicentre retrospective study of the german cancer consortium radiation oncology group (DKTK-ROG)', *Radiother. Oncol.* **121**(3), 364–373. 184

Linnik, I. V., Scott, M. L. J., Holliday, K. F., Woodhouse, N., Waterton, J. C., O'Connor, J. P. B., Barjat, H., Liess, C., Ulloa, J., Young, H., Dive, C., Hodgkinson, C. L., Ward, T., Roberts, D., Mills, S. J., Thompson, G., Buonaccorsi, G. A., Cheung, S., Jackson, A., Naish, J. H. & Parker, G. J. M. (2014), 'Noninvasive tumor hypoxia measurement using magnetic resonance imaging in murine U87 glioma xenografts and in patients with glioblastoma', *Magn. Reson. Med.* **71**(5), 1854–1862. 43, 65, 67, 68, 71, 153

Little, R. A., Datta, A., Featherstone, A. K., Watson, Y., Cheung, S., Buckley, L. & Saunders, M. P. (2019), 'OE-MRI, DCE-MRI and DWI provide complementary response evaluation in patients with rectal cancer treated with chemoradiotherapy', *Proc. Intl. Soc. Mag. Reson. Med.* **Abstract 2312**. 66, 68, 69, 73

Little, R. A., Jamin, Y., Boult, J. K. R., Naish, J. H., Watson, Y., Cheung, S., Holliday, K. E., Lu, H., McHugh, D. J., Irlam, J., West, C. M. L., Betts, G. N., Ashton, G., Reynolds, A. R., Maddineni, S., Clarke, N. W., Parker, G. J. M., Waterton, J. C., Robinson, S. P. & O'Connor, J. P. B. (2018), 'Mapping hypoxia in renal carcinoma with oxygen-enhanced MRI: Comparison with intrinsic susceptibility MRI

and pathology', *Radiology* **288**(3), 739–747. 65, 66, 68, 72, 74, 83, 153

Little, R. A., Parker, G. J. M. & O'Connor, J. P. B. (2022), 'Quantifying confidence in the OE-MRI biomarker pOxy-R using bootstrap analysis', *Proc. Intl. Soc. Mag. Reson. Med.* **30**. 156

Little, R. A., Tessyman, V., Babur, M., Cheung, S., Watson, Y., Gieling, R., Finegan, K. G., Ashton, T. M., Parker, G. J. M., Gillies Mckenna, W., Higgins, G., Williams, K. J. & O'Connor, J. P. B. (2017), 'In vivo OE-MRI quantification and mapping of response to hypoxia modifying drugs banoxantrone and atovaquone in calu6 xenografts', *Proc. Intl. Soc. Mag. Reson. Med.* **Abstract 2919**. 65, 66

Liu, H., Zheng, L., Shi, G., Xu, Q., Wang, Q., Zhu, H., Feng, H., Wang, L., Zhang, N., Xue, M. & Dai, Y. (2021), 'Pulmonary functional imaging for lung adenocarcinoma: Combined MRI assessment based on IVIM-DWI and OE-UTE-MRI', *Front. Oncol.* **11**, 677942. 80

Ljungkvist, A. S., Bussink, J., Rijken, P. F., Raleigh, J. A., Denekamp, J. & Van Der Kogel, A. J. (2000), 'Changes in tumor hypoxia measured with a double hypoxic marker technique', *Int. J. Radiat. Oncol. Biol. Phys.* **48**(5), 1529–1538. 31

Lloyd, W. K., Agushi, E., Coope, D., Lewis, D., Jackson, A. & Parker, G. J. M. (2019), 'An optimised protocol for dynamic oxygen enhanced imaging of brain tumours', *Proc. Intl. Soc. Mag. Reson. Med.* **27**. 80

Löck, S., Perrin, R., Seidlitz, A., Bandurska-Luque, A., Zschaeck, S., Zöphel, K., Krause, M., Steinbach, J., Kotzerke, J., Zips, D., Troost, E. G. C. & Baumann, M. (2017), 'Residual tumour hypoxia in head-and-neck cancer patients undergoing primary radiochemotherapy, final results of a prospective trial on repeat FMISO-PET imaging', *Radiother. Oncol.* **124**(3), 533–540. 35

Lyng, H., Tanum, G., Evensen, J. F. & Rofstad, E. K. (1999), 'Changes in oxygen tension during radiotherapy of head and neck tumours', *Acta Oncol.* **38**(8), 1037–1042. 2

Machiels, J.-P., René Leemans, C., Golusinski, W., Grau, C., Licitra, L. & Gregoire, V. (2020), 'Squamous cell carcinoma of the oral cavity, larynx, oropharynx and hypopharynx: EHNS-ESMO-ESTRO clinical practice guidelines for diagnosis, treatment and follow-up', *Ann. Oncol.* **31**(11), 1462–1475. 19, 20, 91, 154

Mackay, K., Bernstein, D., Glocker, B., Kamnitsas, K. & Taylor, A. (2023), 'A review of the metrics used to assess

Auto-Contouring systems in radiotherapy', *Clin. Oncol.* **35**(6), 354–369. 118

Madl, J., Janka, R., Bay, S. & Rohleder, N. (2022), 'MRI as a stressor: The psychological and physiological response of patients to MRI, influencing factors, and consequences', *J. Am. Coll. Radiol.* **19**(3), 423–432. 170

Mallikarjuna, P., Zhou, Y. & Landström, M. (2022), 'The synergistic cooperation between TGF-β and hypoxia in cancer and fibrosis', *Biomolecules* **12**(5). 5

Martens-de Kemp, S. R., Dalm, S. U., Wijnolts, F. M. J., Brink, A., Honeywell, R. J., Peters, G. J., Braakhuis, B. J. M. & Brakenhoff, R. H. (2013), 'DNA-bound platinum is the major determinant of cisplatin sensitivity in head and neck squamous carcinoma cells', *PLoS One* **8**(4), e61555. 21

Martens, R. M., Noij, D. P., Ali, M., Koopman, T., Marcus, J. T., Vergeer, M. R., de Vet, H., de Jong, M. C., Leemans, C. R., Hoekstra, O. S., de Bree, R., de Graaf, P., Boellaard, R. & Castelijns, J. A. (2019), 'Functional imaging early during (chemo)radiotherapy for response prediction in head and neck squamous cell carcinoma; a systematic review', *Oral Oncol.* **88**, 75–83. 36

Matsumoto, S., Yasui, H., Mitchell, J. B. & Krishna, M. C. (2010), 'Imaging cycling tumor hypoxia', *Cancer Res.* **70**(24), 10019–10023. 3

Matuszak, N., Suchorska, W. M., Milecki, P., Kruszyna-Mochalska, M., Misiarz, A., Pracz, J. & Malicki, J. (2022), 'FLASH radiotherapy: an emerging approach in radiation therapy', *Rep Pract Oncol Radiother* **27**(2), 344–351. 26

Mayerhoefer, M. E., Materka, A., Langs, G., Häggström, I., Szczypiński, P., Gibbs, P. & Cook, G. (2020), 'Introduction to radiomics', *J. Nucl. Med.* **61**(4), 488–495. 163, 164

McCabe, A., Borys, D., Christian, J., Pereira, S., Rowe, S., Morgan, P. S., Shah, J., Blackshaw, E., Martin, S. & Panek, R. (2022), 'Oxygen induced T1 changes in head and neck anatomical structures', *Proc. Intl. Soc. Mag. Reson. Med.* **Abstract 2923**. 62, 73, 76

McCabe, A., Cherry, R., Knott, C., Fontrier, A.-M., Alexopoulos, T., Schoenherr, N. & Mehanna, H. (2024b), 'Real world survival outcomes and treatment patterns in patients with locally advanced squamous cell carcinoma of the head and neck (LA SCCHN): English national disease registration study', *Abstract submitted to 11th European Congress on Head and Neck Oncology* . 184

McCabe, A., Martin, S., Rowe, S., Shah, J., Morgan, P. S., Borys, D. & Panek,

R. (2024a), 'Oxygen-enhanced MRI assessment of tumour hypoxia in head and neck cancer is feasible and well tolerated in the clinical setting', *Eur Radiol Exp* **8**(1), 27. 77, 132, 178

McCabe, A., Martin, S., Shah, J., Morgan, P. S. & Panek, R. (2023), 'T1 based oxygen- enhanced MRI in tumours; a scoping review of current research', *Br. J. Radiol.* **96**(1146), 20220624. 60, 77

McCabe, A., McGrath, D., Blockley, N. & Panek, R. (2021), Does hypocapnia affect oxygen induced changes in brain T1 times at 3t?, *in* 'European Society of Magnetic Resonance in Medicine and Biology 2021'. 107, 110

McGettrick, A. F. & O'Neill, L. A. J. (2020), 'The role of HIF in immunity and inflammation', *Cell Metab.* **32**(4), 524–536. 4, 6

McIsaac, H. K., Thordarson, D. S., Shafran, R., Rachman, S. & Poole, G. (1998), 'Claustrophobia and the magnetic resonance imaging procedure', *J. Behav. Med.* **21**(3), 255–268. 170

McKeown, S. R. (2014), 'Defining normoxia, physoxia and hypoxia in tumours-implications for treatment response', *Br. J. Radiol.* **87**(1035), 20130676. 1, 2, 8, 11, 13

McLaughlin, D. P. (2007), *Human physiology*, BIOS instant notes, Taylor & Francis, New York. 107

McRobbie, D. W., Moore, E. A., Graves, M. J. & Prince, M. R. (2017), *MRI from Picture to Proton*, Cambridge University Press. 39, 41, 48, 49, 50, 55, 56, 170, 171

Mehanna, H., Robinson, M., Hartley, A., Kong, A., Foran, B., Fulton-Lieuw, T., Dalby, M., Mistry, P., Sen, M., O'Toole, L., Al Booz, H., Dyker, K., Moleron, R., Whitaker, S., Brennan, S., Cook, A., Griffin, M., Aynsley, E., Rolles, M., De Winton, E., Chan, A., Srinivasan, D., Nixon, I., Grumett, J., Leemans, C. R., Buter, J., Henderson, J., Harrington, K., McConkey, C., Gray, A., Dunn, J., Moleron, R., McArdle, O., Dyker, K., Al Booz, H., O'Toole, L., Cook, A., Husband, D., Loo, V., Soe, W., Aynsley, E., Sridhar, T., Jankowska, P., Joseph, M., Geropantas, K., Vaidya, D., Griffin, M., Hartley, A., Vijayan, R., Hwang, D., Harrington, K., Pettit, L., Whitaker, S., De Winton, E., Rolles, M., Brennan, S., Sen, M., Mendes, R., Forster, M., Chan, A., Evans, M., Buter, J., Srinivasan, D., Foran, B., Nankivell, P., Bryant, J., Sharma, N., Spruce, R., Brooks, J., Batis, N., Roques, T., Bidmead, M., Yang, H., Nutting, C., Tyler, J., Henderson, J., Baines, H., Gasnier, A., Miles, E., Clark, C.

& Evans, M. (2019), 'Radiotherapy plus cisplatin or cetuximab in low-risk human papillomavirus-positive oropharyngeal cancer (De-ESCALaTE HPV): an open-label randomised controlled phase 3 trial', *Lancet* **393**(10166), 51–60. 16, 17, 22

Mehanna, H., Wong, W.-L., McConkey, C. C., Rahman, J. K., Robinson, M., Hartley, A. G. J., Nutting, C., Powell, N., Al-Booz, H., Robinson, M., Junor, E., Rizwanullah, M., von Zeidler, S. V., Wieshmann, H., Hulme, C., Smith, A. F., Hall, P. & Dunn, J. (2016), 'PET-CT surveillance versus neck dissection in advanced head and neck cancer', *N. Engl. J. Med.* **374**(15), 1444–1454. 84, 87

Mehemed, T. M., Fushimi, Y., Okada, T., Yamamoto, A., Kanagaki, M., Kido, A., Fujimoto, K., Sakashita, N. & Togashi, K. (2014), 'Dynamic oxygen-enhanced MRI of cerebrospinal fluid', *PLoS One* **9**(6), e100723. 107, 110

Meijer, T. W. H., Kaanders, J. H. A. M., Span, P. N. & Bussink, J. (2012), 'Targeting hypoxia, HIF-1, and tumor glucose metabolism to improve radiotherapy efficacy', *Clin. Cancer Res.* **18**(20), 5585–5594. 14

Menegakis, A., Klompmaker, R., Vennin, C., Arbusà, A., Damen, M., van den Broek, B., Zips, D., van Rheenen, J., Krenning, L. & Medema, R. H. (2021), 'Resistance of hypoxic cells to ionizing radiation is mediated in part via Hypoxia-Induced quiescence', *Cells* **10**(3). 14, 151

Menegakis, A., Vennin, C., Ient, J., Klompmaker, R., Krenning, L., Friskes, A., Ilic, M., Harkes, R., Groot, A., van Rheenen, J., Vooijs, M. & Medema, R. (2023), 'OC-0511 hypoxic tumour cells drive tumour relapse after radiotherapy as revealed by a novel tracing tool', *Radiother. Oncol.* **182**, S420–S421. 14

Messroghli, D. R., Radjenovic, A., Kozerke, S., Higgins, D. M., Sivananthan, M. U. & Ridgway, J. P. (2004), 'Modified Look-Locker inversion recovery (MOLLI) for high-resolution T1 mapping of the heart', *Magn. Reson. Med.* **52**(1), 141–146. 56

Metwally, M. A. H., Frederiksen, K. D. & Overgaard, J. (2014), 'Compliance and toxicity of the hypoxic radiosensitizer nimorazole in the treatment of patients with head and neck squamous cell carcinoma (HNSCC)', *Acta Oncol.* **53**(5), 654–661. 24

Michael, B. D., Adams, G. E., Hewitt, H. B., Jones, W. B. & Watts, M. E. (1973), 'A posteffect of oxygen in irradiated bacteria: a submillisecond fast mixing study', *Radiat. Res.* **54**(2), 239–251. 13

Min, M., Lee, M. T., Lin, P., Holloway, L., Wijesekera, D., Gooneratne, D., Rai, R., Xuan, W., Fowler, A., Forstner, D. & Liney, G. (2016), 'Assessment of serial multi-parametric functional MRI (diffusion-weighted imaging and r2*) with (18)F-FDG-PET in patients with head and neck cancer treated with radiation therapy', *Br. J. Radiol.* **89**(1058), 20150530. 41

Moosvi, F., Baker, J. H. E., Yung, A., Kozlowski, P., Minchinton, A. I. & Reinsberg, S. A. (2019*a*), 'Dynamic Oxygen-Enhanced MRI (dOE-MRI) with group ICA detects increased oxygenation in murine tumours treated with VEGF-ablation therapy', *Proc. Intl. Soc. Mag. Reson. Med.* **27**. 65, 68, 78

Moosvi, F., Baker, J. H. E., Yung, A., Kozlowski, P., Minchinton, A. I. & Reinsberg, S. A. (2019*b*), 'Fast and sensitive dynamic oxygen-enhanced MRI with a cycling gas challenge and independent component analysis', *Magn. Reson. Med.* **81**(4), 2514–2525. 65, 67, 68

Mortensen, L. S., Johansen, J., Kallehauge, J., Primdahl, H., Busk, M., Lassen, P., Alsner, J., Sorensen, B. S., Toustrup, K., Jakobsen, S., Petersen, J., Petersen, H., Theil, J., Nordsmark, M. & Overgaard, J. (2012), 'FAZA PET/CT hypoxia imaging in patients with squamous cell carcinoma of the head and neck treated with radiotherapy: Results from the DAHANCA 24 trial', *Radiother. Oncol.* **105**(1), 14–20. 150

MR-only Radiotherapy Planning (2024), `https://www.siemens-healthineers.com/en-uk/magnetic-resonance-imaging/clinical-specialities/synthetic-ct`. Accessed: 2024-5-18. 164

Munn, Z. & Jordan, Z. (2013), 'Interventions to reduce anxiety, distress and the need for sedation in adult patients undergoing magnetic resonance imaging: a systematic review', *Int. J. Evid. Based Healthc.* **11**(4), 265–274. 171

Munn, Z., Pearson, A., Jordan, Z., Murphy, F., Pilkington, D. & Anderson, A. (2015), 'Patient anxiety and satisfaction in a magnetic resonance imaging department: Initial results from an action research study', *J Med Imaging Radiat Sci* **46**(1), 23–29. 171

Munn, Z., Pearson, A., Jordan, Z., Murphy, F., Pilkington, D. & Anderson, A. (2016), 'Addressing the patient experience in a magnetic resonance imaging department: Final results from an action research study', *J Med Imaging Radiat Sci* **47**(4), 329–336. 171

Murphy, K. J. & Brunberg, J. A. (1997), 'Adult claustrophobia, anxiety and sedation in MRI', *Magn. Reson. Imaging* **15**(1), 51–54. 170

Mythen, M. (2010), *Anaesthesiology: Churchill's ready reference*, Churchill's ready reference, Churchill Livingstone, Edinburgh ; New York. 108

Nagy, J. A., Chang, S.-H., Shih, S.-C., Dvorak, A. M. & Dvorak, H. F. (2010), 'Heterogeneity of the tumor vasculature', *Semin. Thromb. Hemost.* **36**(3), 321–331. 2

Nakanishi, Y., Wakisaka, N., Kondo, S., Endo, K., Sugimoto, H., Hatano, M., Ueno, T., Ishikawa, K. & Yoshizaki, T. (2017), 'Progression of understanding for the role of epstein-barr virus and management of nasopharyngeal carcinoma', *Cancer Metastasis Rev.* **36**(3), 435–447. 18, 19

Nakarada-Kordic, I., Reay, S., Bennett, G., Kruse, J., Lydon, A.-M. & Sim, J. (2020), 'Can virtual reality simulation prepare patients for an MRI experience?', *Radiography* **26**(3), 205–213. 171

NHS (2023), 'NHS diagnostic imaging dataset', `https://www.england.nhs.uk/statistics/statistical-work-areas/diagnostic-imaging-dataset/`. Accessed: 2023-5-5. 170

NICE (2018), 'Cancer of the upper aerodigestive tract: assessment and management in people aged 16 and over'. 84

NICE (2022), 'Cervical screening', `https://cks.nice.org.uk/topics/cervical-screening/`. Accessed: 2024-2-23. 16

NICE (2024), 'Infectious mononucleosis (glandular fever)', `https://cks.nice.org.uk/topics/infectious-mononucleosis-glandular-fever/`. Accessed: 2025-2-7. 17

Nickoloff, J. A., Sharma, N. & Taylor, L. (2020), 'Clustered DNA double-strand breaks: Biological effects and relevance to cancer radiotherapy', *Genes (Basel)* **11**(1), 99. 12

Nicolay, N. H., Wiedenmann, N., Mix, M., Weber, W. A., Werner, M., Grosu, A. L. & Kayser, G. (2020), 'Correlative analyses between tissue-based hypoxia biomarkers and hypoxia PET imaging in head and neck cancer patients during radiochemotherapy-results from a prospective trial', *Eur. J. Nucl. Med. Mol. Imaging* **47**(5), 1046–1055. 32

NIHR (2020), 'National institute for health research (NIHR) interactive costing tool (iCT) 2020/2021 v2.2.1'. 43

Nixon, J. L., Cartmill, B., Turner, J., Pigott, A. E., Brown, E., Wall, L. R., Ward, E. C. & Porceddu, S. V. (2018), 'Exploring the prevalence and experience of mask anxiety for the person

with head and neck cancer undergoing radiotherapy', *J Med Radiat Sci* **65**(4), 282–290. 171

Noman, M. Z., Desantis, G., Janji, B., Hasmim, M., Karray, S., Dessen, P., Bronte, V. & Chouaib, S. (2014), 'PD-L1 is a novel direct target of HIF-1α, and its blockade under hypoxia enhanced MDSC-mediated T cell activation', *J. Exp. Med.* **211**(5), 781–790. 11

Nordsmark, M., Alsner, J., Keller, J., Nielsen, O. S., Jensen, O. M., Horsman, M. R. & Overgaard, J. (2001), 'Hypoxia in human soft tissue sarcomas: adverse impact on survival and no association with p53 mutations', *Br. J. Cancer* **84**(8), 1070–1075. 11

Nordsmark, M., Bentzen, S. M., Rudat, V., Brizel, D., Lartigau, E., Stadler, P., Becker, A., Adam, M., Molls, M., Dunst, J., Terris, D. J. & Overgaard, J. (2005), 'Prognostic value of tumor oxygenation in 397 head and neck tumors after primary radiation therapy. An international multi-center study', *Radiother. Oncol.* **77**(1), 18–24. 30

Nordsmark, M., Eriksen, J. G., Gebski, V., Alsner, J., Horsman, M. R. & Overgaard, J. (2007), 'Differential risk assessments from five hypoxia specific assays: The basis for biologically adapted individualized radiotherapy in advanced head and neck cancer patients', *Radiother. Oncol.* **83**(3), 389–397. 32

Nordsmark, M. & Overgaard, J. (2000), 'A confirmatory prognostic study on oxygenation status and loco-regional control in advanced head and neck squamous cell carcinoma treated by radiation therapy', *Radiother. Oncol.* **57**(1), 39–43. 30

Nordsmark, M., Overgaard, M. & Overgaard, J. (1996), 'Pretreatment oxygenation predicts radiation response in advanced squamous cell carcinoma of the head and neck', *Radiother. Oncol.* **41**(1), 31–39. 30

Norikane, T., Yamamoto, Y., Maeda, Y., Kudomi, N., Matsunaga, T., Haba, R., Iwasaki, A., Hoshikawa, H. & Nishiyama, Y. (2014), 'Correlation of (18)f-fluoromisonidazole PET findings with HIF-1α and p53 expressions in head and neck cancer: comparison with (18)F-FDG PET', *Nucl. Med. Commun.* **35**(1), 30–35. 32

Nutting, C. M., Griffin, C. L., Sanghera, P., Foran, B., Beasley, M., Bernstein, D., Cosgrove, V., Fisher, S., West, C. M., Sibtain, A., Palaniappan, N., Urbano, T. G., Sen, M., Soe, W., Rizwanullah, M., Wood, K., Ramkumar, S., Junor, E., Cook, A., Roques, T., Scrase, C., Bhide, S. A., Gujral, D., Harrington, K. J., Mehanna, H., Miah, A., Emson, M., Gardiner, D., Morden,

J. P., Hall, E. & ART DECO Trial Management Group (2021), 'Dose-escalated intensity-modulated radiotherapy in patients with locally advanced laryngeal and hypopharyngeal cancers: ART DECO, a phase III randomised controlled trial', *Eur. J. Cancer* **153**, 242–256. 27

Nutting, C. M., Morden, J. P., Harrington, K. J., Urbano, T. G., Bhide, S. A., Clark, C., Miles, E. A., Miah, A. B., Newbold, K., Tanay, M., Adab, F., Jefferies, S. J., Scrase, C., Yap, B. K., A'Hern, R. P., Sydenham, M. A., Emson, M., Hall, E. & PARSPORT trial management group (2011), 'Parotid-sparing intensity modulated versus conventional radiotherapy in head and neck cancer (PARSPORT): a phase 3 multicentre randomised controlled trial', *Lancet Oncol.* **12**(2), 127–136. 20

O'Connor, J. P. B., Aboagye, E. O., Adams, J. E., Aerts, H. J. W. L., Barrington, S. F., Beer, A. J., Boellaard, R., Bohndiek, S. E., Brady, M., Brown, G., Buckley, D. L., Chenevert, T. L., Clarke, L. P., Collette, S., Cook, G. J., deSouza, N. M., Dickson, J. C., Dive, C., Evelhoch, J. L., Faivre-Finn, C., Gallagher, F. A., Gilbert, F. J., Gillies, R. J., Goh, V., Griffiths, J. R., Groves, A. M., Halligan, S., Harris, A. L., Hawkes, D. J., Hoekstra, O. S., Huang, E. P., Hutton, B. F., Jackson, E. F., Jayson, G. C., Jones, A., Koh, D.-M., Lacombe, D., Lambin, P., Lassau, N., Leach, M. O., Lee, T.-Y., Leen, E. L., Lewis, J. S., Liu, Y., Lythgoe, M. F., Manoharan, P., Maxwell, R. J., Miles, K. A., Morgan, B., Morris, S., Ng, T., Padhani, A. R., Parker, G. J. M., Partridge, M., Pathak, A. P., Peet, A. C., Punwani, S., Reynolds, A. R., Robinson, S. P., Shankar, L. K., Sharma, R. A., Soloviev, D., Stroobants, S., Sullivan, D. C., Taylor, S. A., Tofts, P. S., Tozer, G. M., van Herk, M., Walker-Samuel, S., Wason, J., Williams, K. J., Workman, P., Yankeelov, T. E., Brindle, K. M., McShane, L. M., Jackson, A. & Waterton, J. C. (2017), 'Imaging biomarker roadmap for cancer studies', *Nat. Rev. Clin. Oncol.* **14**(3), 169–186. 68, 69, 153

O'Connor, J. P. B., Boult, J. K. R., Jamin, Y., Babur, M., Finegan, K. G., Williams, K. J., Little, R. A., Jackson, A., Parker, G. J. M., Reynolds, A. R., Waterton, J. C. & Robinson, S. P. (2016), 'Oxygen-Enhanced MRI accurately identifies, quantifies, and maps tumor hypoxia in preclinical cancer models', *Cancer Res.* **76**(4), 787–795. 43, 65, 66, 151, 153

O'Connor, J. P. B., Jackson, A., Buonaccorsi, G. A., Buckley, D. L., Roberts, C., Watson, Y., Cheung, S., McGrath, D. M., Naish, J. H., Rose, C. J., Dark,

P. M., Jayson, G. C. & Parker, G. J. M. (2007), 'Organ-specific effects of oxygen and carbogen gas inhalation on tissue longitudinal relaxation times', *Magn. Reson. Med.* **58**(3), 490–496. 76

O'Connor, J. P. B., Naish, J. H., Parker, G. J. M., Waterton, J. C., Watson, Y., Jayson, G. C., Buonaccorsi, G. A., Cheung, S., Buckley, D. L., McGrath, D. M., West, C. M. L., Davidson, S. E., Roberts, C., Mills, S. J., Mitchell, C. L., Hope, L., Ton, N. C. & Jackson, A. (2009), 'Preliminary study of oxygen-enhanced longitudinal relaxation in MRI: a potential novel biomarker of oxygenation changes in solid tumors', *Int. J. Radiat. Oncol. Biol. Phys.* **75**(4), 1209–1215. 65, 71, 74, 83

O'Connor, J. P. B., Robinson, S. P. & Waterton, J. C. (2019), 'Imaging tumour hypoxia with oxygen-enhanced MRI and BOLD MRI', *Br. J. Radiol.* **92**(1096), 20180642. 43, 67, 83, 116, 152

O'Connor, J. P. B., Tessyman, V., Little, R. A., Babur, M., Forster, D., Latif, A., Cheung, S., Lipowska-Bhalla, G., Higgins, G. S., Asselin, M.-C., Parker, G. J. M. & Williams, K. J. (2024), 'Combined oxygen-enhanced MRI and perfusion imaging detect hypoxia modification from banoxantrone and atovaquone and track their differential mechanisms of action', *Cancer Res. Commun.* **4**(10), 2565–2574. 66, 183

O'Driscoll, B. R., Howard, L. S., Davison, A. G. & British Thoracic Society (2008), 'BTS guideline for emergency oxygen use in adult patients', *Thorax* **63 Suppl 6**, vi1–68. 106

Overgaard, J. (2007), 'Hypoxic radiosensitization: adored and ignored', *J. Clin. Oncol.* **25**(26), 4066–4074. 24, 26, 29

Overgaard, J. (2011), 'Hypoxic modification of radiotherapy in squamous cell carcinoma of the head and neck–a systematic review and meta-analysis', *Radiother. Oncol.* **100**(1), 22–32. 2, 23

Overgaard, J., Eriksen, J. G., Nordsmark, M., Alsner, J., Horsman, M. R. & Danish Head and Neck Cancer Study Group (2005), 'Plasma osteopontin, hypoxia, and response to the hypoxia sensitiser nimorazole in radiotherapy of head and neck cancer: results from the DAHANCA 5 randomised double-blind placebo-controlled trial', *Lancet Oncol.* **6**(10), 757–764. 32

Overgaard, J., Hansen, H. S., Andersen, A. P., Hjelm-Hansen, M., Jørgensen, K., Sandberg, E., Berthelsen, A., Hammer, R. & Pedersen, M. (1989), 'Misonidazole combined with split-course radiotherapy in the treatment of invasive carcinoma of larynx and pharynx: report from the DAHANCA 2

study', *Int. J. Radiat. Oncol. Biol. Phys.* **16**(4), 1065–1068. 24

Overgaard, J., Hansen, H. S., Overgaard, M., Bastholt, L., Berthelsen, A., Specht, L., Lindeløv, B. & Jørgensen, K. (1998), 'A randomized double-blind phase III study of nimorazole as a hypoxic radiosensitizer of primary radiotherapy in supraglottic larynx and pharynx carcinoma. results of the danish head and neck cancer study (DAHANCA) protocol 5-85', *Radiother. Oncol.* **46**(2), 135–146. 24

Overgaard, J., Hoff, C. M., Hansen, H. S., Specht, L., Overgaard, M., Lassen, P., Andersen, E., Johansen, J., Andersen, L. J., Evensen, J. F., Alsner, J. & Grau, C. (2018), 'DAHANCA 10 – effect of darbepoetin alfa and radiotherapy in the treatment of squamous cell carcinoma of the head and neck. a multicenter, open-label, randomized, phase 3 trial by the danish head and neck cancer group', *Radiother. Oncol.* **127**(1), 12–19. 23

Overgaard, J. & Horsman, M. R. (1996), 'Modification of Hypoxia-Induced radioresistance in tumors by the use of oxygen and sensitizers', *Semin. Radiat. Oncol.* **6**(1), 10–21. 22

Pacheco-Torres, J., Zhao, D., Saha, D., Lopez-Larrubia, P., Cerdan, S. & Mason, R. P. (2009), 'Evaluation of lung tumor oxygenation using FREDOM and TOLD', *Proc. Intl. Soc. Mag. Reson. Med.* **Abstract 2464**. 65

Pajonk, F., Vlashi, E. & McBride, W. H. (2010), 'Radiation resistance of cancer stem cells: The 4 r's of radiobiology revisited', *Stem Cells* **28**(4), 639. 14

Palmer, G. M., Fontanella, A. N., Zhang, G., Hanna, G., Fraser, C. L. & Dewhirst, M. W. (2010), 'Optical imaging of tumor hypoxia dynamics', *J. Biomed. Opt.* **15**(6), 066021. 30

Panek, R. & McCabe, A. (2021), 'Evaluation of OE-MRI in patients with head and neck cancer', `https://clinicaltrials.gov/ct2/show/NCT04724096`. Accessed: 2022-5-27. 62

Panek, R., Welsh, L., Baker, L. C. J., Schmidt, M. A., Wong, K. H., Riddell, A. M., Koh, D.-M., Dunlop, A., Mcquaid, D., d'Arcy, J. A., Bhide, S. A., Harrington, K. J., Nutting, C. M., Hopkinson, G., Richardson, C., Box, C., Eccles, S. A., Leach, M. O., Robinson, S. P. & Newbold, K. L. (2017), 'Noninvasive Imaging of Cycling Hypoxia in Head and Neck Cancer Using Intrinsic Susceptibility MRI', *Clin. Cancer Res.* **23**(15), 4233–4241. 3, 41, 129

Panek, R., Wong, K. H., Welsh, L., Riddell, A. M., Koh, D.-M., Morgan, V., Bhide, S. A., Harrington, K. J., Nutting, C. M., Schmidt, M., Leach, M. O.,

O'Connor, J. P. B., Newbold, K. L. & Robinson, S. P. (2018), 'Oxygen-Enhanced MRI for the detection of hypoxia in patients with head and neck cancer', *Proc. Intl. Soc. Mag. Reson. Med.* **Abstract 3916**. 66, 73, 87

Paulson, E. S., Erickson, B., Schultz, C. & Allen Li, X. (2015), 'Comprehensive MRI simulation methodology using a dedicated MRI scanner in radiation oncology for external beam radiation treatment planning', *Med. Phys.* **42**(1), 28–39. 134

Perez, R. C., Kim, D., Maxwell, A. W. P. & Camacho, J. C. (2023), 'Functional imaging of hypoxia: PET and MRI', *Cancers* **15**(13). 37, 40

Petrik, D., Lavori, P. W., Cao, H., Zhu, Y., Wong, P., Christofferson, E., Kaplan, M. J., Pinto, H. A., Sutphin, P., Koong, A. C., Giaccia, A. J. & Le, Q.-T. (2006), 'Plasma osteopontin is an independent prognostic marker for head and neck cancers', *J. Clin. Oncol.* **24**(33), 5291–5297. 32

Pierce, L. (2016), 'PORTS 3D image texture metric calculation package', `https://www.mathworks.com/matlabcentral/fileexchange/55587-ports`. Accessed: 2023-12-21. 157, 158, 159

Pigorsch, S. U., Wilkens, J. J., Kampfer, S., Kehl, V., Hapfelmeier, A., Schläger, C., Bier, H., Schwaiger, M. & Combs, S. E. (2017), 'Do selective radiation dose escalation and tumour hypoxia status impact the loco-regional tumour control after radio-chemotherapy of head & neck tumours? the ESCALOX protocol', *Radiat. Oncol.* **12**(1), 45. 28

Poh, S. S., Chua, M. L. K. & Wee, J. T. S. (2016), 'Carcinogenesis of nasopharyngeal carcinoma: an alternate hypothetical mechanism', *Chin. J. Cancer* **35**(1), 9. 18

Prezzi, D., Neji, R., Dregely, I., Jeljeli, S., Bassett, P., Cook, G. & Goh, V. (2022), 'Feasibility and repeatability of oxygen-enhanced T1 measurements in primary colorectal cancer: a prospective study in 22 patients', *Proc. Intl. Soc. Mag. Reson. Med.* **Abstract 3421**. 73

Price, J., Hall, E., West, C. & Thomson, D. (2020), 'TORPEdO - a phase III trial of intensity-modulated proton beam therapy versus intensity-modulated radiotherapy for multitoxicity reduction in oropharyngeal cancer', *Clin. Oncol.* **32**(2), 84–88. 26

Price, J. M., Prabhakaran, A. & West, C. M. L. (2022), 'Predicting tumour radiosensitivity to deliver precision radiotherapy', *Nat. Rev. Clin. Oncol.* . 6, 7, 12, 13

Qian, J., Yu, X., Li, B., Fei, Z., Huang, X., Luo, P., Zhang, L., Zhang, Z.,

Lou, J. & Wang, H. (2020), '*In vivo* monitoring of oxygen levels in human brain tumor between fractionated radiotherapy using oxygen-enhanced MR imaging', *Curr. Med. Imaging Rev.* **16**(4), 427–432. 68, 72

Rajendran, J. G., Schwartz, D. L., O'Sullivan, J., Peterson, L. M., Ng, P., Scharnhorst, J., Grierson, J. R. & Krohn, K. A. (2006), 'Tumor hypoxia imaging with [f-18] fluoromisonidazole positron emission tomography in head and neck cancer', *Clin. Cancer Res.* **12**(18), 5435–5441. 35

Raleigh, J. A., Chou, S. C., Arteel, G. E. & Horsman, M. R. (1999), 'Comparisons among pimonidazole binding, oxygen electrode measurements, and radiation response in C3H mouse tumors', *Radiat. Res.* **151**(5), 580–589. 31

Rasey, J. S., Koh, W. J., Evans, M. L., Peterson, L. M., Lewellen, T. K., Graham, M. M. & Krohn, K. A. (1996), 'Quantifying regional hypoxia in human tumors with positron emission tomography of [18f]fluoromisonidazole: a pretherapy study of 37 patients', *Int. J. Radiat. Oncol. Biol. Phys.* **36**(2), 417–428. 35

Ratai, E.-M., Zhang, Z., Fink, J., Muzi, M., Hanna, L., Greco, E., Richards, T., Kim, D., Andronesi, O. C., Mintz, A., Kostakoglu, L., Prah, M., Ellingson, B., Schmainda, K., Sorensen, G., Barboriak, D., Mankoff, D., Gerstner, E. R. & ACRIN 6684 trial group (2018), 'ACRIN 6684: Multicenter, phase II assessment of tumor hypoxia in newly diagnosed glioblastoma using magnetic resonance spectroscopy', *PLoS One* **13**(6), e0198548. 40

Ratcliffe, P. J. (2007), 'HIF-1 and HIF-2: working alone or together in hypoxia?', *J. Clin. Invest.* **117**(4), 862–865. 4

Remmele, S., Sprinkart, A. M., Mueller, A., Traeber, F., von Lehe, M., Gieseke, J., Flacke, S., Willinek, W. A., Schild, H. H., Senegas, J., Keupp, J. & Muertz, P. (2013), 'Dynamic and simultaneous MR measurement of R1 and r2* changes during respiratory challenges for the assessment of blood and tissue oxygenation', *Magn. Reson. Med.* **70**(1), 136–146. 65, 71

Riaz, N., Sherman, E., Pei, X., Schöder, H., Grkovski, M., Paudyal, R., Katabi, N., Selenica, P., Yamaguchi, T. N., Ma, D., Lee, S. K., Shah, R., Kumar, R., Kuo, F., Ratnakumar, A., Aleynick, N., Brown, D., Zhang, Z., Hatzoglou, V., Liu, L. Y., Salcedo, A., Tsai, C. J., McBride, S., Morris, L. G. T., Boyle, J., Singh, B., Higginson, D. S., Damerla, R. R., Paula, A. d. C., Price, K., Moore, E. J., Garcia, J. J., Foote, R., Ho, A., Wong, R. J., Chan, T. A., Powell, S. N., Boutros, P. C.,

Humm, J. L., Shukla-Dave, A., Pfister, D., Reis-Filho, J. S. & Lee, N. (2021), 'Precision radiotherapy: Reduction in radiation for oropharyngeal cancer in the 30 ROC trial', *J. Natl. Cancer Inst.* **113**(6), 742–751. 16, 17

Rich, L. J. & Seshadri, M. (2016), 'Photoacoustic monitoring of tumor and normal tissue response to radiation', *Sci. Rep.* **6**, 21237. 65, 66

Rickard, A. G., Palmer, G. M. & Dewhirst, M. W. (2019), 'Clinical and pre-clinical methods for quantifying tumor hypoxia', **1136**, 19–41. 41

Rischin, D., Peters, L. J., O'Sullivan, B., Giralt, J., Fisher, R., Yuen, K., Trotti, A., Bernier, J., Bourhis, J., Ringash, J., Henke, M. & Kenny, L. (2010*a*), 'Tirapazamine, cisplatin, and radiation versus cisplatin and radiation for advanced squamous cell carcinoma of the head and neck (TROG 02.02, HeadSTART): a phase III trial of the TransTasman radiation oncology group', *J. Clin. Oncol.* **28**(18), 2989–2995. 24

Rischin, D., Young, R. J., Fisher, R., Fox, S. B., Le, Q.-T., Peters, L. J., Solomon, B., Choi, J., O'Sullivan, B., Kenny, L. M. & McArthur, G. A. (2010), 'Prognostic significance of p16INK4A and human papillomavirus in patients with oropharyngeal cancer treated on TROG 02.02 phase III trial', *J. Clin. Oncol.* **28**(27), 4142–4148. 154

Rodrigues, L. M., Howe, F. A., Griffiths, J. R. & Robinson, S. P. (2004), 'Tumor r2* is a prognostic indicator of acute radiotherapeutic response in rodent tumors', *J. Magn. Reson. Imaging* **19**(4), 482–488. 41

Rohlfing, T. (2012), 'Image similarity and tissue overlaps as surrogates for image registration accuracy: widely used but unreliable', *IEEE Trans. Med. Imaging* **31**(2), 153–163. 120

Roy, U., Lepicard, E. Y., Boult, J. K. R., Box, C., Harrington, K. J., O'Connor, J. P. B., Jamin, Y. & Robinson, S. P. (2022), 'Imaging hypoxia in murine oral cavity squamous cell carcinomas with oxygen-enhanced MRI', *Proc. Intl. Soc. Mag. Reson. Med.* **Abstract 0289**. 65

Rudat, V., Stadler, P., Becker, A., Vanselow, B., Dietz, A., Wannenmacher, M., Molls, M., Dunst, J. & Feldmann, H. J. (2001), 'Predictive value of the tumor oxygenation by means of po2 histography in patients with advanced head and neck cancer', *Strahlenther. Onkol.* **177**(9), 462–468. 30

Rudat, V., Vanselow, B., Wollensack, P., Bettscheider, C., Osman-Ahmet, S., Eble, M. J. & Dietz, A. (2000), 'Repeatability and prognostic impact of the pretreatment pO(2) histography in patients with advanced head and neck

cancer', *Radiother. Oncol.* **57**(1), 31–37. 30

Rühle, A., Grosu, A.-L. & Nicolay, N. H. (2021*a*), 'De-Escalation strategies of (Chemo)Radiation for Head-and-Neck squamous cell Cancers-HPV and beyond', *Cancers* **13**(9). 17

Rühle, A., Grosu, A.-L., Wiedenmann, N., Stoian, R., Haehl, E., Zamboglou, C., Baltas, D., Werner, M., Kayser, G. & Nicolay, N. H. (2021*b*), 'Immunohistochemistry-based hypoxia-immune prognostic classifier for head-and-neck cancer patients undergoing chemoradiation - post-hoc analysis from a prospective imaging trial', *Radiother. Oncol.* **159**, 75–81. 32

Ruttkay-Nedecky, B., Jimenez Jimenez, A. M., Nejdl, L., Chudobova, D., Gumulec, J., Masarik, M., Adam, V. & Kizek, R. (2013), 'Relevance of infection with human papillomavirus: the role of the p53 tumor suppressor protein and E6/E7 zinc finger proteins (review)', *Int. J. Oncol.* **43**(6), 1754–1762. 16

S. Y. F. Chu, L. P. E. & Firestone, R. B. (1998), 'The Lund/LBNL nuclear data search', `http://nucleardata.nuclear.lu.se/toi/index.asp`. Accessed: 2024-6-28. 34

Sage, E. & Shikazono, N. (2017), 'Radiation-induced clustered DNA lesions: Repair and mutagenesis', *Free Radic. Biol. Med.* **107**, 125–135. 12

Saksø, M., Primdahl, H., Johansen, J., Nowicka-Matus, K., Overgaard, J. & DAHANCA (2020), 'DAHANCA 33: functional image-guided dose-escalated radiotherapy to patients with hypoxic squamous cell carcinoma of the head and neck (NCT02976051)', *Acta Oncol.* **59**(2), 208–211. 28

Salem, A., Little, R. A., Latif, A., Featherstone, A. K., Babur, M., Peset, I., Cheung, S., Watson, Y., Tessyman, V., Mistry, H., Ashton, G., Behan, C., Matthews, J. C., Asselin, M.-C., Bristow, R. G., Jackson, A., Parker, G. J. M., Faivre-Finn, C., Williams, K. J. & O'Connor, J. P. B. (2019), 'Oxygen-enhanced MRI is feasible, repeatable, and detects radiotherapy-induced change in hypoxia in xenograft models and in patients with non-small cell lung cancer', *Clin. Cancer Res.* **25(13)**(13), 3818–3829. 43, 65, 66, 68, 72, 74, 75, 83, 153

Sato, J., Kitagawa, Y., Yamazaki, Y., Hata, H., Okamoto, S., Shiga, T., Shindoh, M., Kuge, Y. & Tamaki, N. (2013), '18f-fluoromisonidazole PET uptake is correlated with hypoxia-inducible factor-1α expression in oral squamous cell carcinoma', *J. Nucl. Med.* **54**(7), 1060–1065. 32

Saunders, M. E., Dische, S., Anderson, P.

& Flockhart, I. R. (1978), 'The neurotoxicity of misonidazole and its relationship to dose, half-life and concentration in the serum', *Br. J. Cancer Suppl.* **3**, 268–270. 24

Schaner, P. E., Pettus, J. R., Flood, A. B., Williams, B. B., Jarvis, L. A., Chen, E. Y., Pastel, D. A., Zuurbier, R. A., diFlorio Alexander, R. M., Swartz, H. M. & Kuppusamy, P. (2020), 'OxyChip implantation and subsequent electron paramagnetic resonance oximetry in human tumors is safe and feasible: First experience in 24 patients', *Front. Oncol.* **10**, 572060. 30, 38

Scharping, N. E., Rivadeneira, D. B., Menk, A. V., Vignali, P. D. A., Ford, B. R., Rittenhouse, N. L., Peralta, R., Wang, Y., Wang, Y., DePeaux, K., Poholek, A. C. & Delgoffe, G. M. (2021), 'Mitochondrial stress induced by continuous stimulation under hypoxia rapidly drives T cell exhaustion', *Nat. Immunol.* **22**(2), 205–215. 10

Scott-Wittenborn, N. & Fakhry, C. (2021), 'Epidemiology of HPV related malignancies', *Semin. Radiat. Oncol.* **31**(4), 286–296. 15, 16

Seddon, B. M., Maxwell, R. J., Honess, D. J., Grimshaw, R., Raynaud, F., Tozer, G. M. & Workman, P. (2002), 'Validation of the fluorinated 2-nitroimidazole SR-4554 as a noninvasive hypoxia marker detected by magnetic resonance spectroscopy', *Clin. Cancer Res.* **8**(7), 2323–2335. 38

Semenza, G. L. (2003), 'Targeting HIF-1 for cancer therapy', *Nat. Rev. Cancer* **3**(10), 721–732. 5, 6, 32

Semenza, G. L. & Wang, G. L. (1992), 'A nuclear factor induced by hypoxia via de novo protein synthesis binds to the human erythropoietin gene enhancer at a site required for transcriptional activation', *Mol. Cell. Biol.* **12**(12), 5447–5454. 4

Servagi-Vernat, S., Differding, S., Sterpin, E., Hanin, F.-X., Labar, D., Bol, A., Lee, J. A. & Grégoire, V. (2015), 'Hypoxia-guided adaptive radiation dose escalation in head and neck carcinoma: a planning study', *Acta Oncol.* **54**(7), 1008–1016. 28

Sethumadhavan, S., Silva, M., Philbrook, P., Nguyen, T., Hatfield, S. M., Ohta, A. & Sitkovsky, M. V. (2017), 'Hypoxia and hypoxia-inducible factor (HIF) downregulate antigen-presenting MHC class I molecules limiting tumor cell recognition by T cells', *PLoS One* **12**(11), e0187314. 10

Sharma, P., Hu-Lieskovan, S., Wargo, J. A. & Ribas, A. (2017), 'Primary, adaptive, and acquired resistance to cancer immunotherapy', *Cell* **168**(4), 707–723. 186

Sherer, M. V., Lin, D., Elguindi, S., Duke, S., Tan, L.-T., Cacicedo, J., Dahele, M. & Gillespie, E. F. (2021), 'Metrics to evaluate the performance of auto-segmentation for radiation treatment planning: A critical review', *Radiother. Oncol.* **160**, 185–191. 118, 120

Shukla-Dave, A., Obuchowski, N. A., Chenevert, T. L., Jambawalikar, S., Schwartz, L. H., Malyarenko, D., Huang, W., Noworolski, S. M., Young, R. J., Shiroishi, M. S., Kim, H., Coolens, C., Laue, H., Chung, C., Rosen, M., Boss, M. & Jackson, E. F. (2019), 'Quantitative imaging biomarkers alliance (QIBA) recommendations for improved precision of DWI and DCE-MRI derived biomarkers in multicenter oncology trials', *J. Magn. Reson. Imaging* **49**(7), e101–e121. 75, 153

Soh, L.-K. & Tsatsoulis, C. (1999), 'Texture analysis of SAR sea ice imagery using gray level co-occurrence matrices', *IEEE Trans. Geosci. Remote Sens.* **37**(2), 780–795. 157

Song, D., Lian, Y. & Zhang, L. (2023), 'The potential of activator protein 1 (AP-1) in cancer targeted therapy', *Front. Immunol.* **14**, 1224892. 8

Sörensen, A., Carles, M., Bunea, H., Majerus, L., Stoykow, C., Nicolay, N. H., Wiedenmann, N. E., Vaupel, P., Meyer, P. T., Grosu, A. L. & Mix, M. (2020), 'Textural features of hypoxia PET predict survival in head and neck cancer during chemoradiotherapy', *Eur. J. Nucl. Med. Mol. Imaging* **47**(5), 1056–1064. 35

Sørensen, B. S., Alsner, J., Overgaard, J. & Horsman, M. R. (2007), 'Hypoxia induced expression of endogenous markers in vitro is highly influenced by ph', *Radiother. Oncol.* **83**(3), 362–366. 33

Sørensen, B. S., Busk, M., Horsman, M. R., Alsner, J., Overgaard, J., Kyle, A. H. & Minchinton, A. I. (2014), 'Effect of radiation on cell proliferation and tumor hypoxia in HPV-positive head and neck cancer in vivo models', *Anticancer Res.* **34**(11), 6297–6304. 17

Sørensen, B. S. & Horsman, M. R. (2020), 'Tumor hypoxia: Impact on radiation therapy and molecular pathways', *Front. Oncol.* **10**, 562. 5, 32, 33

Spencer, J. A., Ferraro, F., Roussakis, E., Klein, A., Wu, J., Runnels, J. M., Zaher, W., Mortensen, L. J., Alt, C., Turcotte, R., Yusuf, R., Côté, D., Vinogradov, S. A., Scadden, D. T. & Lin, C. P. (2014), 'Direct measurement of local oxygen concentration in the bone marrow of live animals', *Nature* **508**(7495), 269–273. 2

Spiegelberg, L., Houben, R., Niemans, R., de Ruysscher, D., Yaromina, A., Theys, J., Guise, C. P., Smaill, J. B.,

Patterson, A. V., Lambin, P. & Dubois, L. J. (2019), 'Hypoxia-activated prodrugs and (lack of) clinical progress: The need for hypoxia-based biomarker patient selection in phase III clinical trials', *Clin. Transl. Radiat. Oncol.* **15**, 62–69. 183

Spitzer, R. L., Kroenke, K., Williams, J. B. W. & Löwe, B. (2006), 'A brief measure for assessing generalized anxiety disorder: the GAD-7', *Arch. Intern. Med.* **166**(10), 1092–1097. 176

Stabile, A., Giganti, F., Rosenkrantz, A. B., Taneja, S. S., Villeirs, G., Gill, I. S., Allen, C., Emberton, M., Moore, C. M. & Kasivisvanathan, V. (2020), 'Multiparametric MRI for prostate cancer diagnosis: current status and future directions', *Nat. Rev. Urol.* **17**(1), 41–61. 39

Star-Lack, J. M., Adalsteinsson, E., Adam, M. F., Terris, D. J., Pinto, H. A., Brown, J. M. & Spielman, D. M. (2000), 'In vivo 1H MR spectroscopy of human head and neck lymph node metastasis and comparison with oxygen tension measurements', *AJNR Am. J. Neuroradiol.* **21**(1), 183–193. 37

Stikov, N., Boudreau, M., Levesque, I. R., Tardif, C. L., Barral, J. K. & Pike, G. B. (2015), 'On the accuracy of T1 mapping: searching for common ground', *Magn. Reson. Med.* **73**(2), 514–522. 55, 57, 75

Su, Z. Y., Siak, P. Y., Leong, C.-O. & Cheah, S.-C. (2023), 'The role of epstein-barr virus in nasopharyngeal carcinoma', *Front. Microbiol.* **14**, 1116143. 18, 19

Sutherland, B. M., Bennett, P. V., Schenk, H., Sidorkina, O., Laval, J., Trunk, J., Monteleone, D. & Sutherland, J. (2001), 'Clustered DNA damages induced by high and low LET radiation, including heavy ions', *Phys. Med.* **17 Suppl 1**, 202–204. 12

Swartz, H. M., Williams, B. B., Zaki, B. I., Hartford, A. C., Jarvis, L. A., Chen, E. Y., Comi, R. J., Ernstoff, M. S., Hou, H., Khan, N., Swarts, S. G., Flood, A. B. & Kuppusamy, P. (2014), 'Clinical EPR: unique opportunities and some challenges', *Acad. Radiol.* **21**(2), 197–206. 38

T1 & T2 EUROSPIN Gels (2015), `https://leedstestobjects.com/index.php/phantom/t1-t2-gels/`. Accessed: 2024-1-5. 98

Tadamura, E., Hatabu, H., Li, W., Prasad, P. V. & Edelman, R. R. (1997), 'Effect of oxygen inhalation on relaxation times in various tissues', *J. Magn. Reson. Imaging* **7**(1), 220–225. 42, 50

Tang, M., Bolderson, E., O'Byrne, K. J. & Richard, D. J. (2021), 'Tumor hy-

poxia drives genomic instability', *Front Cell Dev Biol* **9**, 626229. 9

Taylor, A. J., Salerno, M., Dharmakumar, R. & Jerosch-Herold, M. (2016), 'T1 mapping: Basic techniques and clinical applications', *JACC Cardiovasc. Imaging* **9**(1), 67–81. 75

Taylor, N. J., Baddeley, H., Goodchild, K. A., Powell, M. E., Thoumine, M., Culver, L. A., Stirling, J. J., Saunders, M. I., Hoskin, P. J., Phillips, H., Padhani, A. R. & Griffiths, J. R. (2001), 'BOLD MRI of human tumor oxygenation during carbogen breathing', *J. Magn. Reson. Imaging* **14**(2), 156–163. 41

Tharmalingham, H. & Hoskin, P. (2019), 'Clinical trials targeting hypoxia', *Br. J. Radiol.* **92**(1093), 20170966. 23

Thiruthaneeswaran, N., Bibby, B. A. S., Yang, L., Hoskin, P. J., Bristow, R. G., Choudhury, A. & West, C. (2021), 'Lost in application: Measuring hypoxia for radiotherapy optimisation', *Eur. J. Cancer* **148**, 260–276. 8, 11, 33

Thomlinson, R. H. & Gray, L. H. (1955), 'The histological structure of some human lung cancers and the possible implications for radiotherapy', *Br. J. Cancer* **9**(4), 539–549. 2, 43, 60, 129

Thomson, D. J., Slevin, N. J., Baines, H., Betts, G., Bolton, S., Evans, M., Garcez, K., Irlam, J., Lee, L., Melillo, N., Mistry, H., More, E., Nutting, C., Price, J. M., Schipani, S., Sen, M., Yang, H., West, C. M. & NIMRAD Trial Group (2023), 'Randomized phase 3 trial of the hypoxia modifier nimorazole added to radiation therapy with benefit assessed in hypoxic head and neck cancers determined using a gene signature (NIMRAD)', *Int. J. Radiat. Oncol. Biol. Phys.* . 25, 26, 33

Thomson, D., Yang, H., Baines, H., Miles, E., Bolton, S., West, C. & Slevin, N. (2014), 'NIMRAD - a phase III trial to investigate the use of nimorazole hypoxia modification with intensity-modulated radiotherapy in head and neck cancer', *Clin. Oncol.* **26**(6), 344–347. 24

Thor, M., Petersen, J. B. B., Bentzen, L., Høyer, M. & Muren, L. P. (2011), 'Deformable image registration for contour propagation from CT to cone-beam CT scans in radiotherapy of prostate cancer', *Acta Oncol.* **50**(6), 918–925. 120

Thorwarth, D. & Alber, M. (2010), 'Implementation of hypoxia imaging into treatment planning and delivery', *Radiother. Oncol.* **97**(2), 172–175. 28

Thorwarth, D., Welz, S., Mönnich, D., Pfannenberg, C., Nikolaou, K., Reimold, M., La Fougère, C., Reischl, G., Mauz, P.-S., Paulsen, F., Alber, M., Belka, C. & Zips, D. (2019),

'Prospective evaluation of a tumor control probability model based on dynamic 18F-FMISO PET for head and neck cancer radiotherapy', *J. Nucl. Med.* **60**(12), 1698–1704. 35, 150

Tischler, V., Calton, T., Williams, M. & Cheetham, A. (2008), 'Patient anxiety in magnetic resonance imaging centres: Is further intervention needed?', *Radiography* **14**(3), 265–266. 171

Tofts, P. S., Brix, G., Buckley, D. L., Evelhoch, J. L., Henderson, E., Knopp, M. V., Larsson, H. B., Lee, T. Y., Mayr, N. A., Parker, G. J., Port, R. E., Taylor, J. & Weisskoff, R. M. (1999), 'Estimating kinetic parameters from dynamic contrast-enhanced t(1)-weighted MRI of a diffusable tracer: standardized quantities and symbols', *J. Magn. Reson. Imaging* **10**(3), 223–232. 39

Tol, J. P., Dahele, M., Gregoire, V., Overgaard, J., Slotman, B. J. & Verbakel, W. F. A. R. (2019), 'Analysis of EORTC-1219-DAHANCA-29 trial plans demonstrates the potential of knowledge-based planning to provide patient-specific treatment plan quality assurance', *Radiother. Oncol.* **130**, 75–81. 25

Toustrup, K., Sørensen, B. S., Lassen, P., Wiuf, C., Alsner, J., Overgaard, J. & Danish Head and Neck Cancer Group (DAHANCA) (2012), 'Gene expression classifier predicts for hypoxic modification of radiotherapy with nimorazole in squamous cell carcinomas of the head and neck', *Radiother. Oncol.* **102**(1), 122–129. 33

Toustrup, K., Sørensen, B. S., Nordsmark, M., Busk, M., Wiuf, C., Alsner, J. & Overgaard, J. (2011), 'Development of a hypoxia gene expression classifier with predictive impact for hypoxic modification of radiotherapy in head and neck cancer', *Cancer Res.* **71**(17), 5923–5931. 33

Tozer, G. M. & Griffiths, J. R. (1992), 'The contribution made by cell death and oxygenation to 31P MRS observations of tumour energy metabolism: EFFECTS OF CELL DEATH AND OXYGENATION ON TUMOUR31P SPECTRA', *NMR Biomed.* **5**(5), 279–289. 38

Tricco, A. C., Lillie, E., Zarin, W., O'Brien, K. K., Colquhoun, H., Levac, D., Moher, D., Peters, M. D. J., Horsley, T., Weeks, L., Hempel, S., Akl, E. A., Chang, C., McGowan, J., Stewart, L., Hartling, L., Aldcroft, A., Wilson, M. G., Garritty, C., Lewin, S., Godfrey, C. M., Macdonald, M. T., Langlois, E. V., Soares-Weiser, K., Moriarty, J., Clifford, T., Tunçalp, Ö. & Straus, S. E. (2018), 'PRISMA extension for scoping reviews (PRISMA-

ScR): Checklist and explanation', *Ann. Intern. Med.* **169**(7), 467–473. 61

Vaquero, J. J. & Kinahan, P. (2015), 'Positron emission tomography: Current challenges and opportunities for technological advances in clinical and preclinical imaging systems', *Annu. Rev. Biomed. Eng.* **17**, 385–414. 34, 43

Vaupel, P., Hoeckel, M. & Mayer, A. (2007), 'Detection and characterization of tumor hypoxia using pO(2) histography', *Antioxid. Redox Signal.* **9**(8), 1221–1235. 2, 13, 150

Verduzco, D., Lloyd, M., Xu, L., Ibrahim-Hashim, A., Balagurunathan, Y., Gatenby, R. A. & Gillies, R. J. (2015), 'Intermittent hypoxia selects for genotypes and phenotypes that increase survival, invasion, and therapy resistance', *PLoS One* **10**(3), e0120958. 8

Vermorken, J. B., Remenar, E., van Herpen, C., Gorlia, T., Mesia, R., Degardin, M., Stewart, J. S., Jelic, S., Betka, J., Preiss, J. H., van den Weyngaert, D., Awada, A., Cupissol, D., Kienzer, H. R., Rey, A., Desaunois, I., Bernier, J., Lefebvre, J.-L. & EORTC 24971/TAX 323 Study Group (2007), 'Cisplatin, fluorouracil, and docetaxel in unresectable head and neck cancer', *N. Engl. J. Med.* **357**(17), 1695–1704. 21

Wang, H. Z., Riederer, S. J. & Lee, J. N. (1987), 'Optimizing the precision in T1 relaxation estimation using limited flip angles', *Magn. Reson. Med.* **5**(5), 399–416. 57

Wardman, P. (2007), 'Chemical radiosensitizers for use in radiotherapy', *Clin. Oncol.* **19**(6), 397–417. 24

Waschkies, C. F., Pfiffner, F. K., Heuberger, D. M., Schneider, M. A., Tian, Y., Wolint, P., Calcagni, M., Giovanoli, P. & Buschmann, J. (2020), 'Tumor grafts grown on the chicken chorioallantoic membrane are distinctively characterized by MRI under functional gas challenge', *Sci. Rep.* **10**(1), 7505. 65, 74, 78

Wei, W. I. & Sham, J. S. T. (2005), 'Nasopharyngeal carcinoma', *Lancet* **365**(9476), 2041–2054. 18

Welsh, L., Panek, R., McQuaid, D., Dunlop, A., Schmidt, M., Riddell, A., Koh, D.-M., Doran, S., Murray, I., Du, Y., Chua, S., Hansen, V., Wong, K. H., Dean, J., Gulliford, S., Bhide, S., Leach, M. O., Nutting, C., Harrington, K. & Newbold, K. (2015), 'Prospective, longitudinal, multi-modal functional imaging for radical chemo-IMRT treatment of locally advanced head and neck cancer: the INSIGHT study', *Radiat. Oncol.* **10**, 112. 87

Welz, S., Mönnich, D., Pfannenberg, C., Nikolaou, K., Reimold, M.,

La Fougère, C., Reischl, G., Mauz, P.-S., Paulsen, F., Alber, M., Belka, C., Zips, D. & Thorwarth, D. (2017), 'Prognostic value of dynamic hypoxia PET in head and neck cancer: Results from a planned interim analysis of a randomized phase II hypoxia-image guided dose escalation trial', *Radiother. Oncol.* **124**(3), 526–532. 35

Welz, S., Paulsen, F., Pfannenberg, C., Reimold, M., Reischl, G., Nikolaou, K., La Fougère, C., Alber, M., Belka, C., Zips, D. & Thorwarth, D. (2022), 'Dose escalation to hypoxic subvolumes in head and neck cancer: A randomized phase II study using dynamic [^{18}F]FMISO PET/CT', *Radiother. Oncol.* **171**, 30–36. 28

White, D. A., Zhang, Z., Li, L., Gerberich, J., Stojadinovic, S., Peschke, P. & Mason, R. P. (2016), 'Developing oxygen-enhanced magnetic resonance imaging as a prognostic biomarker of radiation response', *Cancer Lett.* **380**(1), 69–77. 65, 68, 153

Wiedenmann, N., Grosu, A.-L., Büchert, M., Rischke, H. C., Ruf, J., Bielak, L., Majerus, L., Rühle, A., Bamberg, F., Baltas, D., Hennig, J., Mix, M., Bock, M. & Nicolay, N. H. (2020), 'The utility of multiparametric MRI to characterize hypoxic tumor subvolumes in comparison to FMISO PET/CT. consequences for diagnosis and chemoradiation treatment planning in head and neck cancer', *Radiother. Oncol.* **150**, 128–135. 40

Winer, R. L. & Koutsky, L. A. (2004), The epidemiology of human papillomavirus infections, *in* T. E. Rohan & K. V. Shah, eds, 'Cercival Cancer: From Etiology to Prevention', Springer Netherlands, Dordrecht, pp. 143–187. 15, 16

Winter, J. D., Akens, M. K. & Cheng, H.-L. M. (2011), 'Quantitative MRI assessment of VX2 tumour oxygenation changes in response to hyperoxia and hypercapnia', *Phys. Med. Biol.* **56**(5), 1225–1242. 65, 74

Winter, S. C., Buffa, F. M., Silva, P., Miller, C., Valentine, H. R., Turley, H., Shah, K. A., Cox, G. J., Corbridge, R. J., Homer, J. J., Musgrove, B., Slevin, N., Sloan, P., Price, P., West, C. M. L. & Harris, A. L. (2007), 'Relation of a hypoxia metagene derived from head and neck cancer to prognosis of multiple cancers', *Cancer Res.* **67**(7), 3441–3449. 33

Wong, K. C. W., Johnson, D., Hui, E. P., Lam, R. C. T., Ma, B. B. Y. & Chan, A. T. C. (2022), 'Opportunities and challenges in combining immunotherapy and radiotherapy in head and neck cancers', *Cancer Treat. Rev.* **105**(102361), 102361. 185

Wong, K. H., Panek, R., Dunlop, A., Mcquaid, D., Riddell, A., Welsh, L. C.,

Murray, I., Koh, D.-M., Leach, M. O., Bhide, S. A., Nutting, C. M., Oyen, W. J., Harrington, K. J. & Newbold, K. L. (2018), 'Changes in multimodality functional imaging parameters early during chemoradiation predict treatment response in patients with locally advanced head and neck cancer', *Eur. J. Nucl. Med. Mol. Imaging* **45**(5), 759–767. 87

Wong, K. H., Panek, R., Welsh, L., Mcquaid, D. & others (2016), 'The predictive value of early assessment after 1 cycle of induction chemotherapy with 18F-FDG PET/CT and diffusion-weighted MRI for response to radical ...', *Journal of Nuclear* . 92

Wouters, B. G. & Koritzinsky, M. (2008), 'Hypoxia signalling through mTOR and the unfolded protein response in cancer', *Nat. Rev. Cancer* **8**(11), 851–864. 4, 6, 7

Wozny, A.-S., Alphonse, G., Cassard, A., Malésys, C., Louati, S., Beuve, M., Lalle, P., Ardail, D., Nakajima, T. & Rodriguez-Lafrasse, C. (2020), 'Impact of hypoxia on the double-strand break repair after photon and carbon ion irradiation of radioresistant HNSCC cells', *Sci. Rep.* **10**(1), 21357. 26

Yang, D. M., Arai, T. J., Campbell, III, J. W., Gerberich, J. L., Zhou, H. & Mason, R. P. (2019), 'Oxygen-sensitive MRI assessment of tumor response to hypoxic gas breathing challenge', *NMR Biomed.* **32**(7), e4101. 67

Yang, L. & West, C. M. L. (2019), 'Hypoxia gene expression signatures as predictive biomarkers for personalising radiotherapy', *Br. J. Radiol.* **92**(1093). 33

Yang, X., Tridandapani, S., Beitler, J. J., Yu, D. S., Yoshida, E. J., Curran, W. J. & Liu, T. (2012), 'Ultrasound GLCM texture analysis of radiation-induced parotid-gland injury in head-and-neck cancer radiotherapy: an in vivo study of late toxicity', *Med. Phys.* **39**(9), 5732–5739. 157, 158

Yoshitomi, Y., Ikeda, T., Saito-Takatsuji, H. & Yonekura, H. (2021), 'Emerging role of AP-1 transcription factor JunB in angiogenesis and vascular development', *Int. J. Mol. Sci.* **22**(6), 2804. 8

Yushkevich, P. A., Piven, J., Cody Hazlett, H., Gimpel Smith, R., Ho, S., Gee, J. C. & Gerig, G. (2006), 'User-Guided 3D active contour segmentation of anatomical structures: Significantly improved efficiency and reliability', *Neuroimage* **31**(3), 1116–1128. 117, 137

Zaharchuk, G., Busse, R. F., Rosenthal, G., Manley, G. T., Glenn, O. A. & Dillon, W. P. (2006), 'Noninvasive oxygen partial pressure measurement of

human body fluids in vivo using magnetic resonance imaging', *Acad. Radiol.* **13**(8), 1016–1024. 130

Zaharchuk, G., Martin, A. J., Rosenthal, G., Manley, G. T. & Dillon, W. P. (2005), 'Measurement of cerebrospinal fluid oxygen partial pressure in humans using MRI', *Magn. Reson. Med.* **54**(1), 113–121. 107, 110, 111

Zegers, C. M. L., Hoebers, F. J. P., van Elmpt, W., Bons, J. A., Öllers, M. C., Troost, E. G. C., Eekers, D., Balmaekers, L., Arts-Pechtold, M., Mottaghy, F. M. & Lambin, P. (2016), 'Evaluation of tumour hypoxia during radiotherapy using [18F]HX4 PET imaging and blood biomarkers in patients with head and neck cancer', *Eur. J. Nucl. Med. Mol. Imaging* **43**(12), 2139–2146. 35

Zhang, Y., Fakhry, C. & D'Souza, G. (2021), 'Projected association of human papillomavirus vaccination with oropharynx cancer incidence in the US, 2020-2045', *JAMA Oncol* p. e212907. 16

Zhao, D., Pacheco-Torres, J., Hallac, R. R., White, D., Peschke, P., Cerdan, S. & Mason, R. P. (2015), 'Dynamic oxygen challenge evaluated by NMR t_1 and t_2* - insights into tumor oxygenation', *NMR Biomed.* **28**(8), 937–947. 65, 74

Zhao, Y., Hu, X., Liu, Y., Dong, S., Wen, Z., He, W., Zhang, S., Huang, Q. & Shi, M. (2017), 'ROS signaling under metabolic stress: cross-talk between AMPK and AKT pathway', *Mol. Cancer* **16**(1), 79. 2

Zhong, X., Nickel, M. D., Kannengiesser, S. A. R., Dale, B. M., Kiefer, B. & Bashir, M. R. (2014), 'Liver fat quantification using a multi-step adaptive fitting approach with multi-echo GRE imaging: Liver fat quantification with adaptive fitting', *Magn. Reson. Med.* **72**(5), 1353–1365. 93

Zhou, H., Belzile, O., Zhang, Z., Saha, D., Wagner, J., Sishc, B., Stojadinovic, S., Brekken, R. & Mason, R. P. (2017*a*), 'Evaluation of tumor oxygenation following radiation and PS-targeting antibody therapy in an orthotopic lung cancer model', *Proc. Intl. Soc. Mag. Reson. Med.* **Abstract 4364**. 65

Zhou, H., Chiguru, S., Hallac, R. R., Yang, D., Hao, G., Peschke, P. & Mason, R. P. (2019), 'Examining correlations of oxygen sensitive MRI (BOLD/-TOLD) with [18F]FMISO PET in rat prostate tumors', *Am. J. Nucl. Med. Mol. Imaging* **9**(2), 156–167. 65

Zhou, H., Hallac, R. R., Yuan, Q., Ding, Y., Zhang, Z., Xie, X.-J., Francis, F., Roehrborn, C. G., Sims, R. D., Costa, D. N., Raj, G. V. & Mason,

R. P. (2017*c*), 'Incorporating Oxygen-Enhanced MRI into Multi-Parametric assessment of human prostate cancer', *Diagnostics (Basel)* **7**(3). 71

Zhou, H., Wilson, D., Lickliter, J., Ruben, J., Raghunand, N., Sellenger, M., Mason, R. P. & Unger, E. (2016), 'TOLD MRI validation of reversal of tumor hypoxia in glioblastoma with a novel oxygen therapeutic', *Proc. Intl. Soc. Mag. Reson. Med.* **Abstract 3576**. 68, 73, 78

Zhou, H., Zhang, Z., Denney, R., Williams, J. S., Gerberich, J., Stojadinovic, S., Saha, D., Shelton, J. M. & Mason, R. P. (2017*b*), 'Tumor physiological changes during hypofractionated stereotactic body radiation therapy assessed using multi-parametric magnetic resonance imaging', *Oncotarget* **8**(23), 37464–37477. 65

Zigmond, A. S. & Snaith, R. P. (1983), 'The hospital anxiety and depression scale', *Acta Psychiatr. Scand.* **67**(6), 361–370. 176

Zips, D., Zöphel, K., Abolmaali, N., Perrin, R., Abramyuk, A., Haase, R., Appold, S., Steinbach, J., Kotzerke, J. & Baumann, M. (2012), 'Exploratory prospective trial of hypoxia-specific PET imaging during radiochemotherapy in patients with locally advanced head-and-neck cancer', *Radiother. Oncol.* **105**(1), 21–28. 150

Zschaeck, S., Haase, R., Abolmaali, N., Perrin, R., Stützer, K., Appold, S., Steinbach, J., Kotzerke, J., Zips, D., Richter, C., Gudziol, V., Krause, M., Zöphel, K. & Baumann, M. (2015), 'Spatial distribution of FMISO in head and neck squamous cell carcinomas during radio-chemotherapy and its correlation to pattern of failure', *Acta Oncol.* **54**(9), 1355–1363. 35

Zschaeck, S., Löck, S., Hofheinz, F., Zips, D., Saksø Mortensen, L., Zöphel, K., Troost, E. G. C., Boeke, S., Saksø, M., Mönnich, D., Seidlitz, A., Johansen, J., Skripcak, T., Gregoire, V., Overgaard, J., Baumann, M. & Krause, M. (2020), 'Individual patient data meta-analysis of FMISO and FAZA hypoxia PET scans from head and neck cancer patients undergoing definitive radio-chemotherapy', *Radiother. Oncol.* **149**, 189–196. 35

Appendix A

Supplementary Figures

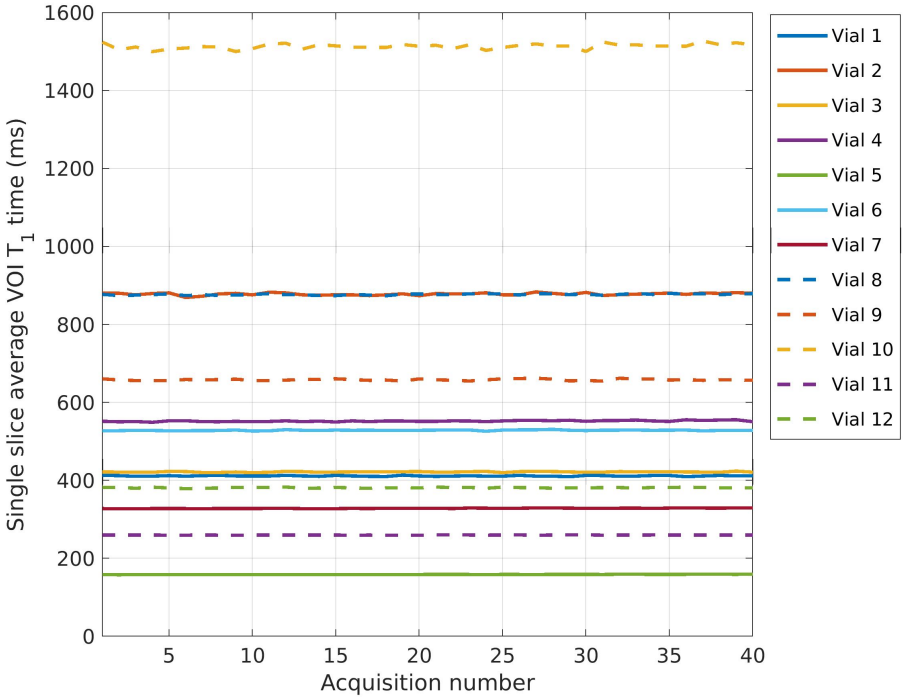

Figure A.1: Temporal stability of dynamic VIBE sequence - T_1 values for 12 gel-filled tubes in a Eurospin TO5 phantom measured over 40 dynamic acquisitions using dynamic VIBE sequence on MRI machine 1.

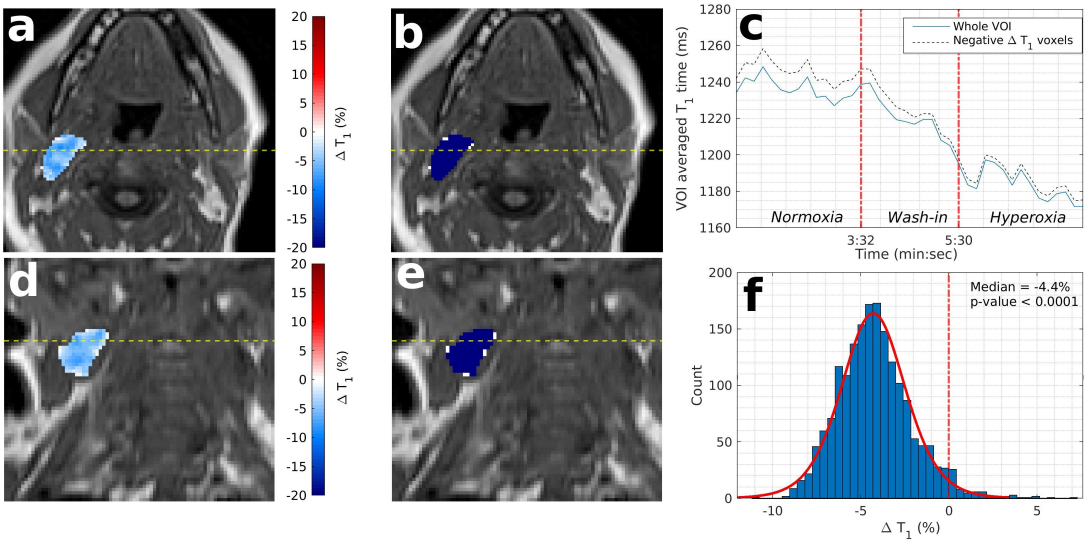

Figure A.2: Parametric maps from normoxic malignant nodal mass - Example OE-MRI parametric maps in a patient with a suspected malignant nodal mass (patient no: 16 Lymph Node no: 2). Low estimated hypoxic fraction (11.6%) is shown on a T_1 weighted VIBE image with overlaid parametric ΔT_1 map of the malignant mass (**a**, **d**, axial and coronal plane respectively) and overlaid statistical map of ΔT_1 times (**b**, **e**). Blue colour indicates statistically significant decrease in T_1 times, white indicating no statistically significant change and red indicating statistically significant increasing T_1 times. **c** Time series of T_1 times averaged over the entire malignant node VOI and over those voxels with significantly decreasing T_1 times only. **f** Histogram of ΔT_1 times for the entire malignant nodal VOI.

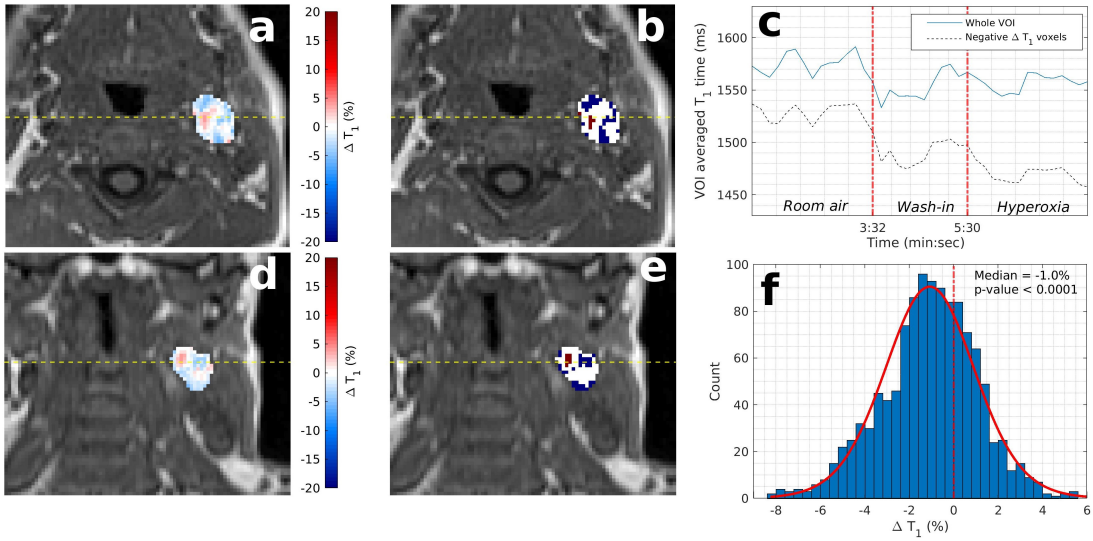

Figure A.3: Parametric maps from hypoxic malignant nodal mass - Example OE-MRI parametric maps in a patient with a suspected malignant nodal mass (patient no: 15 Lymph Node no: 7). High estimated hypoxic fraction (72.0%) is shown on a T_1 weighted VIBE image with overlaid parametric ΔT_1 map of the malignant mass (**a**, **d**, axial and coronal plane respectively) and overlaid statistical map of ΔT_1 times (**b**, **e**). Blue colour indicates statistically significant decrease in T_1 times, white indicating no statistically significant change and red indicating statistically significant increasing T_1 times. **c** Time series of T_1 times averaged over the entire malignant node VOI and over those voxels with significantly decreasing T_1 times only. **f** Histogram of ΔT_1 times for the entire malignant nodal VOI.

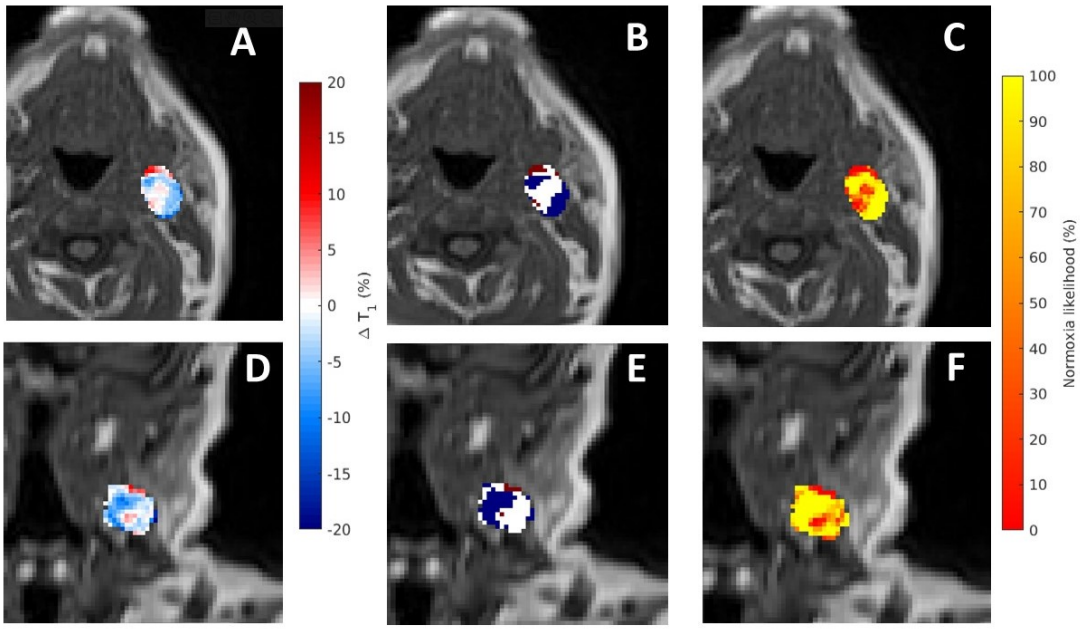

Figure A.4: Example nodal mass Bootstrap OE-MRI parametric map - ΔT_1 maps (**A**, **D**), corresponding statistical map with blue indicating statistically significant reduction in voxel T_1 times, white no change and red statistically significant increase in T_1 times via t-test with significance at $p < 0.05$ (**B**, **E**) and normoxia likelihood maps constructed from 1,000 Bootstrap samples for each voxel from the dynamic OE-MRI data (**C**, **F**) for the malignant nodal mass in patient ID 19. **A**, **B**, **C**: axial slice. **D**, **E**, **F**: coronal slice.

Evaluation and Improvement of Head and Neck Radiotherapy
Patients' Experience of Medical Imaging

NHS
Nottingham
University Hospitals
NHS Trust

1.) Thinking about your current cancer treatment, which of the following scans have you had?

		Yes	No
	**Radiotherapy planning CT** • Donut shaped machine. Scanned with radiotherapy mask. • Scan takes a few minutes. • You may have had a dye injected.	☐	☐
	**Diagnostic CT** • Donut shaped machine. No mask. • Scan takes a few minutes. • You may have had a dye injected.	☐	☐
	**PET** • Large machine with a donut shaped hole in middle. • Scan takes around 20 to 30 minutes. • Radioactive dye injected 30 to 60 minutes before.	☐	☐
	**MRI** • Large machine with a tunnel that you go into. • Scans takes around 30 to 60 minutes and is often noisy. • You may have had a dye injected.	☐	☐
	**Ultrasound** • Handheld by an operator with 'jelly' placed on skin. • Usually 15 to 30 minutes. • A tissue sample (biopsy) is sometimes taken.	☐	☐

2.) Considering each type of scan that you have had, please rate from 1(strongly disagree) to 5 (strongly agree) how much you **agree** with each of the following statements. If you have not had a particular scan then please leave that column blank:

	CT	PET	MRI	Radiotherapy planning CT	Ultrasound
(i) I found the scan uncomfortable?					
(ii) I felt anxious during the scan?					
(iii) I found the scan painful?					
(iv) I found the scan embarrassing?					

1 = strongly disagree, 2 = disagree, 3 = neither agree nor disagree, 4 = agree, 5 = strongly agree

Hospital number: K_____

We Listen
We Care

Figure A.5: Medical imaging questionnaire - Copy of the questionnaire distributed to patients with head and neck squamous cell carcinoma undergoing curative intent (chemo)radiotherapy to assess their experience of medical imaging in the workup for their radiotherapy treatment.

Appendix B

Supplementary Tables

Tables B.1 and B.2 display the full MRI derived tumour characteristics and OE-MRI metrics for all of the imaged primary tumours and all malignant nodes respectively.

Table B.1: Full tumour characteristics and MRI derived imaging parameters for all histologically confirmed squamous cell primary tumours.

PRIMARY TUMOUR				T1 time: median (ms)			R_2^* rate: median (s^{-1})		
Participant	p16	HPV DNA	Volume (cm^3)	Baseline (IQR)	ΔT1 (%) (IQR)	p-value	Hypoxic fraction (%)	Baseline (IQR)	ΔR_2^* (IQR)	p-value
1	-	N/A	31.15	1417 (294)	-0.7 (4.8)	<0.0001	78.6	26.1 (27.6)	0.9 (16.9)	0.0004
3	N/A	N/A	4.35	1170 (197)	-2.6 (4.7)	<0.0001	73.5	43.6 (35.2)	0.0 (37.0)	0.6852
5	+	+	3.98	1239 (198)	-5.4 (4.2)	<0.0001	30.7	27.8 (39.1)	10.7 (38.8)	<0.0001
6	N/A	N/A	8.83	1400 (178)	-0.6 (2.5)	<0.0001	70.4	20.6 (26.9)	3.4 (14.7)	<0.0001
7	+	N/A	33.70	1206 (239)	-3.4 (4.9)	<0.0001	50.0	47.3 (66.6)	-8.6 (55.5)	<0.0001
9	+	+	0.61	716 (152)	-3.5 (2.7)	<0.0001	44.0	51.4 (39.2)	4.8 (18.1)	0.0392
10 (i)	+	+	5.04	1034 (190)	-7.0 (3.8)	<0.0001	13.3	68.8 (57.7)	0.4 (27.6)	0.5291
10 (ii)	+	+	17.69	997 (196)	-2.6 (2.3)	<0.0001	27.1	26.1 (23.3)	0.0 (8.1)	0.0115
11	N/A	N/A	33.11	1211 (223)	-5.4 (4.4)	<0.0001	19.3	25.1 (25.4)	0.2 (25.4)	0.2705
13	-	-	0.54	817 (372)	-5.5 (6.0)	<0.0001	26.1	144.8 (73.1)	-29.1 (49.7)	<0.0001
14	+	-	21.60	1066 (146)	-0.3 (4.3)	<0.0001	70.2	29.6 (17.7)	0.0 (17.7)	0.5403
15	+	+	2.35	1206 (173)	-6.5 (3.6)	<0.0001	6.5	21.7 (27.0)	-0.5 (15.2)	0.4338
16	+	N/A	3.75	1200 (194)	-4.6 (2.3)	<0.0001	9.8	33.6 (20.5)	9.7 (17.4)	<0.0001
19	+	+	4.55	1256 (164)	-3.6 (3.0)	<0.0001	24.1	20.1 (22.2)	4.1 (18.0)	<0.0001
20	N/A	N/A	7.20	1179 (224)	-3.1 (6.4)	<0.0001	53.4	43.5 (40.5)	3.6 (45.8)	<0.0001

Table B.2: Full tumour characteristics and MRI derived imaging parameters for all nodal masses that were clinically managed as malignant.

MALIGNANT NODES

Participant	p16	HPV DNA	Volume (cm^3)	T1 time: median (ms)				R_2* rate: median (s^{-1})		
				Baseline (IQR)	ΔT1 (%) (IQR)	p-value	Hypoxic fraction (%)	Baseline (IQR)	ΔR_2* (IQR)	p-value
1 (i)	-	N/A	2.50	1353 (296)	-1.8 (5.6)	<0.0001	64.6	29.6 (12.7)	-1.3 (13.5)	0.1550
1 (ii)	-	N/A	1.31	1087 (216)	1.2 (4.1)	0.0008	82.8	11.2 (32.2)	18.5 (31.9)	<0.0001
3 (i)	N/A	N/A	4.27	1262 (429)	-3.0 (6.0)	<0.0001	63.3	21.3 (10.1)	0.1 (10.9)	0.6329
3(ii)	N/A	N/A	9.81	1327 (302)	-3.0 (4.5)	<0.0001	60.2	17.5 (15.1)	5.6 (14.9)	<0.0001
4 (i)	+	+	10.71	1339 (629)	-1.0 (4.6)	<0.0001	60.5	15.2 (18.1)	4.3 (17.3)	<0.0001
5 (i)	+	+	10.88	1343 (194)	-2.2 (3.1)	<0.0001	59.9	14.3 (8.8)	5.9 (9.8)	<0.0001
5(ii)	+	+	1.64	1177 (197)	-2.3 (3.2)	<0.0001	51.7	30.9 (19.9)	-2.8 (19.7)	0.0684
6 (i)	N/A	N/A	7.23	1547 (244)	-1.7 (2.4)	<0.0001	60.3	20.1 (14.3)	2.0 (10.5)	<0.0001
6 (ii)	N/A	N/A	3.50	1426 (146)	-1.5 (2.9)	<0.0001	56.1	20.0 (13.2)	2.1 (11.3)	<0.0001
6 (iii)	N/A	N/A	20.56	1674 (619)	-1.8 (3.7)	<0.0001	67.9	15.2 (15.8)	-1.3 (7.8)	<0.0001
(iv)	N/A	N/A	1.01	847 (654)	-2.6 (7.8)	<0.0001	63.9	28.1 (28.7)	-4.4 (8.7)	<0.0001
6 (v)	N/A	N/A	1.16	1324 (433)	-0.2 (3.1)	0.5021	77.4	20.8 (12.4)	-0.4 (6.3)	0.4582
(vi)	N/A	N/A	8.41	1345 (198)	-4.0 (3.2)	<0.0001	37.3	17.0 (7.7)	-1.0 (12.5)	<0.0001
6 (vii)	N/A	N/A	1.19	1402 (203)	-2.2 (2.1)	<0.0001	43.1	16.5 (8.4)	-2.8 (7.6)	<0.0001
6 (viii)	N/A	N/A	1.70	1455 (101)	-2.7 (2.7)	<0.0001	31.9	15.2 (11.2)	-4.2 (7.7)	<0.0001

6 (ix)	N/A	N/A	6.32	1424 (142)	-1.9 (2.3)	<0.0001	51.5	18.2 (7.8)	-2.0 (8.4)	<0.0001
6 (x)	N/A	N/A	1.54	1327 (363)	-1.2 (3.4)	<0.0001	73.4	24.5 (14.1)	1.7 (7.0)	<0.0001
7 (i)	+	N/A	0.37	1333 (392)	-1.6 (4.2)	0.0045	80.0	20.6 (12.3)	1.2 (7.5)	0.0827
7 (ii)	+	N/A	3.13	1371 (220)	-5.3 (3.8)	<0.0001	34.6	16.4 (15.0)	11.3 (19.5)	<0.0001
7 (iii)	+	N/A	6.44	1232 (288)	-0.4 (5.1)	<0.0001	84.4	29.8 (14.5)	-3.0 (21.3)	<0.0001
7 (iv)	+	N/A	0.54	903 (383)	-1.9 (6.8)	0.0059	74.2	17.5 (22.4)	-2.7 (22.1)	0.0080
9 (i)	+	+	11.98	1258 (269)	-4.7 (3.7)	<0.0001	14.5	18.9 (12.8)	0.2 (7.6)	0.0314
10 (i)	+	+	5.55	1019 (254)	-4.6 (3.6)	<0.0001	21.7	18.1 (10.6)	0.5 (7.1)	0.0104
10 (ii)	+	+	0.26	577 (187)	-6.5 (12.5)	0.0001	28.6	23.8 (12.5)	-0.4 (4.6)	0.4074
11 (i)	N/A	N/A	0.46	957 (231)	-3.9 (5.9)	<0.0001	36.0	27.7 (17.5)	-7.1 (7.6)	<0.0001
13 (i)	-	-	9.94	1567 (252)	-1.1 (3.4)	<0.0001	69.0	12.7 (12.2)	-1.4 (10.8)	<0.0001
14 (i)	+	-	8.40	1246 (177)	-3.3 (3.7)	<0.0001	35.7	16.4 (13.1)	2.1 (13.7)	<0.0001
14 (ii)	+	-	0.48	1205 (365)	-2.4 (4.8)	<0.0001	59.5	20.2 (11.6)	-0.2 (12.4)	0.6045
14 (iii)	+	-	1.10	1202 (211)	-0.6 (4.4)	0.1290	89.5	23.0 (17.5)	-12.7 (29.4)	<0.0001
15 (i)	+	+	5.93	1454 (303)	-2.8 (4.1)	<0.0001	58.0	16.6 (11.7)	-6.0 (13.8)	<0.0001
15 (ii)	+	+	0.54	1546 (330)	-4.8 (3.5)	<0.0001	21.6	9.1 (7.5)	-4.5 (6.7)	0.0002
15 (iii)	+	+	2.62	1590 (289)	-2.1 (3.5)	<0.0001	55.9	6.9 (7.3)	10.6 (8.0)	<0.0001
15 (iv)	+	+	0.62	1521 (267)	-2.0 (2.7)	<0.0001	64.4	15.2 (12.3)	9.0 (7.4)	<0.0001
15 (v)	+	+	3.40	1656 (384)	-3.3 (3.4)	<0.0001	30.7	18.4 (11.0)	2.3 (7.4)	<0.0001

15 (vi)	+	+	0.93	1664 (320)	-0.6 (3.1)	0.0012	71.7	20.2 (6.4)	5.2 (4.0)	<0.0001
15 (vii)	+	+	7.19	1577 (318)	-1.0 (2.7)	<0.0001	72.0	18.4 (11.0)	-2.8 (6.4)	<0.0001
16 (i)	+	N/A	0.93	1187 (351)	-5.2 (5.0)	<0.0001	21.7	27.1 (12.0)	-6.1 (5.8)	<0.0001
16 (ii)	+	N/A	11.07	1249 (148)	-4.4 (2.6)	<0.0001	11.6	24.1 (9.7)	1.7 (10.6)	<0.0001
19 (i)	+	+	8.35	1448 (585)	-2.3 (6.6)	<0.0001	57.5	14.4 (18.7)	2.8 (11.7)	<0.0001
20 (i)	N/A	N/A	1.87	1359 (257)	-0.4 (6.3)	0.8391	75.6	17.3 (19.9)	24.7 (16.3)	<0.0001
20 (ii)	N/A	N/A	1.17	1285 (240)	0.0 (6.2)	0.6378	82.3	10.8 (25.2)	10.7 (45.2)	0.0004

Table B.3: Primary tumour contoured volumes on OE-MRI VIBE sequence and as per treating clinician on radiotherapy planning CT scans. Volume of tumour obtained by multiplying voxels by spatial resolution ($1.5625 \times 1.5625 \times 2.5mm^3$ for the OE-MRI and $1.074 \times 1.074 \times 3mm^3$ for planning CT).

	OE-MRI Scan		Planning CT	
ID	Voxels	Volume (cm^3)	Voxels	Volume (cm^3)
1	5103	31.15	28872	99.91
3	712	4.35	1078	3.73
5	652	3.98	3346	11.58
6	1447	8.83	12951	44.82
7	5522	33.70	20270	70.14
9	100	0.61	1058	3.66
10(i)	825	5.04	2297	7.95
10(ii)	2898	17.69	15309	52.98
13	88	0.54	Missing	
14	3539	21.60	12521	43.33
15	385	2.35	1280	4.43
16	615	3.75	3025	10.47
20	1180	7.20	3185	11.02

Table B.4: Summed anxiety scores for the research scan and routine clinical scan along with free text comments from all patient participants.

		Anxiety score		
ID	**MRI before**	**Study**	**Clinical**	**Comments**
1	No	18	15	-
2	Yes	21	17	Pain in shoulder was main concern.
3	Yes	23	19	-
4	No	21	21	-
5	No	16	16	-
6	No	26	15	Mask rode up high and pushed into eyes (uncomfortable). Came tight to face when oxygen on and made face itch. Felt tight on nose and difficult at times. Could you do non-mask scan before mask to get used to scanner?
7	Yes	16	15	Bit noisy.
8	No	25	24	-
9	Yes	26	27	Not a particularly enjoyable experience but I was fully informed and supported throughout with professionalism and kindness.
10	No	15	15	Mirror makes a big difference.
11	No	15	15	-
12	Yes	42	45	Prefer to have someone in the room until in and positioned.
13	Yes	30	30	-
14	No	15	15	-
15	No	15	15	-
16	No	15	15	-
17	Yes	26	26	-
18	No	20	15	-
19	Yes	17	15	-
20	No	19	16	Try make mask more comfortable - pushed up into eyes. Something that fits to face better would be more comfortable.

Appendix C

ANTs Code

Script for affine co-registration of dynamic OE-MRI images (script name OEMRIaffine.sh).

```
#!/usr/bin/bash
# script expect 2 parameters :
# $1 - DIRECTORY with .nii input files
# $2 - filename in $1 DIRECTORY which will be FIXED (others will be MOVING-coregistered to the FIXED file)

‘cd $1‘

pathData=$1
fname=$2

ls ${pathData} | grep .nii >> ${pathData}/files.txt
file_fixed=${pathData}/${fname}.nii

# number of computing cores
Ncores=4
# --------------------------------------------------------------
# PERFORM REGISTRATION using : rigid+affine

parallel --jobs ${Ncores} "antsRegistrationSyNQuick.sh \
        -d 3  -n 2 \
        -f ${file_fixed} \
        -m ${pathData}/{} \
        -o ${pathData}/{} \
        -t a" :::: ${pathData}/files.txt

# create subDIRS for registration results :
# AffineWarped - registration results  / AffineWarps - for transformation matrix
mkdir ${pathData}/AffineWarped
mkdir ${pathData}/AffineWarps

# MOVE registration results and deformation fields/matrix
mv ${pathData}/*.niiWarped.nii.gz ${pathData}/AffineWarped
mv ${pathData}/*.gz ${pathData}/AffineWarps
mv ${pathData}/*.mat ${pathData}/AffineWarps
# UNPACK .gz files
ls ${pathData}/AffineWarped | grep .gz | parallel --jobs ${Ncores} gunzip ${pathData}/AffineWarped/{}
```

Script for non-rigid co-registration of dynamic OE-MRI images (script name OEMRInonrigid.sh)

```
#!/usr/bin/bash
# script expect 2 parameters :
# $1 - DIRECTORY with .nii input files
# $2 - filename in $1 DIRECTORY which will be FIXED (others will be MOVING-coregistered to the FIXED file)

‘cd $1‘

pathData=$1
fname=$2

ls ${pathData} | grep .nii | grep -v "r" |grep -v "mean" >> ${pathData}/files.txt
file_fixed=${pathData}/${fname}.nii

# number of computing cores
Ncores=4
# ----------------------------------------------------------------------------------------------
# PERFORM REGISTRATION using : rigid + affine + deformable SyN (non-rigid/elastic)
parallel --jobs ${Ncores} "antsRegistrationSyNQuick.sh \
        -d 3  -n 2 \
        -f ${file_fixed} \
        -m ${pathData}/{} \
        -o ${pathData}/{} \
        -t s" :::: ${pathData}/files.txt

# create subDIRS for registration results:
# Warped - registration results  / Warps - for deformation fields and transformation affine matrix
mkdir ${pathData}/Warped
mkdir ${pathData}/Warps

# MOVE registration results and deformation fields/matrix
mv ${pathData}/*.niiWarped.nii.gz ${pathData}/Warped
mv ${pathData}/*.gz ${pathData}/Warps
mv ${pathData}/*.mat ${pathData}/Warps
# UNPACK .gz files
ls ${pathData}/Warped | grep .gz | parallel --jobs ${Ncores} gunzip ${pathData}/Warped/{}
```